Autorul tezei de abilitare: Conf. dr. ing. Dan Moldovanu
Domeniul: Ingineria Autovehiculelor

PORTOFOLIU DE LUCRĂRI ÎN DOMENIUL DE DOCTORAT VIZAT

1. Burnete, Nicolae Vlad, Florin Mariasiu, Christopher Depcik, Istvan Barabas, and **Dan Moldovanu**. "Review of thermoelectric generation for internal combustion engine waste heat recovery." Progress in Energy and Combustion Science 91 (2022): 101009. https://www.webofscience.com/wos/woscc/full-record/WOS:000798843400002

2. **Moldovanu, Dan**, and Nicolae Burnete. "Computational fluid dynamics simulation of a single cylinder research engine working with biodiesel." Thermal Science 17, no. 1 (2013): 195-203. https://www.webofscience.com/wos/woscc/full-record/WOS:000315175600018

3. Burnete, Nicolae Vlad, Florin Mariasiu, **Dan Moldovanu**, and Christopher Depcik. "Simulink model of a thermoelectric generator for vehicle waste heat recovery." Applied Sciences 11, no. 3 (2021): 1340. https://www.webofscience.com/wos/woscc/full-record/WOS:000615001000001

4. Cărăuşan, H., B. O. Varga, **D. Moldovanu**, and A. A. Sirca. "Comparative analysis of fuel cell and electric public for transport busses." In IOP Conference Series: Materials Science and Engineering, vol. 1256, no. 1, p. 012041. IOP Publishing, 2022. https://www.scopus.com/record/display.uri?eid=2-s2.0-85167868865&origin=recordpage

5. **Moldovanu, Dan**, Florin Mariaşiu, Bogdan Ovidiu Varga, Adela Ioana Borzan, Horaţiu Cărăuşan, and Dan Doru Micu. "Analysis of the modes of operation of an electric vehicle on energy consumption." In 2023 10th International Conference on Modern Power Systems (MPS), pp. 1-5. IEEE, 2023. https://www.scopus.com/record/display.uri?eid=2-s2.0-85167868865&origin=recordpage

6. Mattson, Jonathan, Nicolae Vlad Burnete, Christopher Depcik, **Dan Moldovanu**, and Nicolae Burnete. "Second law analysis of waste cooking oil biodiesel versus ULSD during operation of a CI engine." Fuel 255 (2019): 115753. https://www.webofscience.com/wos/woscc/full-record/WOS:000479141700113

7. **Moldovanu, Dan**, A. Molea, and I. Barabás. "Preliminary results on nano-diamond and nano-graphite testing as additive for an engine lubrication oil." In IOP Conference Series: Materials Science and Engineering, vol. 724, no. 1, p. 012047. IOP Publishing, 2020. https://www.webofscience.com/wos/woscc/full-record/WOS:000619349400047

8. Mariasiu, Florin, Nicolae V. Burnete, **Dan Moldovanu**, Bogdan O. Varga, Calin Iclodean, and Levente Kocsis. "Effects of bioethanol ultrasonic generated aerosols application on diesel engine performances." Thermal science 19, no. 6 (2015): 1931-1941. https://www.webofscience.com/wos/woscc/full-record/WOS:000367565400007

10.07.2025 Conf.Dr.Ing. Dan MOLDOVANU

Progress in Energy and Combustion Science 91 (2022) 101009

Contents lists available at ScienceDirect

Progress in Energy and Combustion Science

journal homepage: www.elsevier.com/locate/pecs

Review of thermoelectric generation for internal combustion engine waste heat recovery

Nicolae Vlad Burnete [a,*], Florin Mariasiu [a], Christopher Depcik [b], Istvan Barabas [a], Dan Moldovanu [a]

[a] Automotive Engineering and Transports Department, Technical University of Cluj-Napoca, Muncii Street, 103-105, Cluj-Napoca 400641, Romania
[b] Department of Mechanical Engineering, University of Kansas, 1530 W.15th Street, 3138 Learned Hall, Lawrence, KS 66045, USA

ARTICLE INFO

Keywords:
Thermoelectric module
Thermoelectric generator
Internal combustion engine
Waste heat recovery
Exhaust heat recovery
Energy conversion

ABSTRACT

With the current emphasis on electrified vehicles, the use of internal combustion engines (ICEs) as the main propulsion source is challenged, especially for passenger cars. Even though this is not yet the case for freight transportation and the internal combustion engine is still considered the short to mid-term solution, significant improvements in its efficiency and pollutant emissions are required. An energy distribution analysis shows that the internal combustion engine already has two important heat rejection sources representing approximately 65–70% of the energy input: the exhaust gas system (~35–40%) and the radiator (~30%). Partially recovering some of this otherwise wasted heat can improve overall thermal efficiency. Compared to other thermal energy recovery methods (Organic Rankine Cycle, mechanical or electrical turbocompounding, etc.), thermoelectric generators have numerous advantages: environmentally friendly, no moving parts, little to no noise and vibration, no working fluids, high reliability (when working temperatures are not exceeded), low maintenance, scalable, modular, ability to operate over a wide range of transient temperature conditions, and the direct conversion of thermal energy into electrical energy. This effort seeks to bring together all aspects concerning the use of thermoelectric generators for internal combustion engine waste heat recovery in a comprehensive overview on the issue while aiding researchers and engineers in the development of efficient systems. This is accomplished by delivering two thorough summaries of both experimental and simulation results including, but not limited to the power output and parasitic losses, as well as the gain in efficiency and reduction in fuel consumption. Furthermore, this effort includes a recap of hot side heat exchanger design (e.g., external shape, internal structure, material, test temperature and gas flow velocity, etc.). As a result, the use of thermoelectric generators installed on the exhaust system and in other regions that can provide heat for power generation (i.e., radiator and exhaust gas recirculation) are fully described.

1. Introduction

According to the Lawrence Livermore National Laboratory [1], in 2018 the amount of rejected energy resulting from the residential, commercial, industrial, and transportation sectors in the United States (U.S.) totaled 45.65 EJ, of which 23.63 EJ came from the transportation sector. This analysis shows the significant potential for energy recovery systems and that by recouping a part of this energy from internal combustion engines (ICEs), overall transportation efficiency could be meaningfully increased.

Internal combustion engines are one of the largest fossil fuel consumers due to their widespread use in transportation along with stationary power units and industrial and agricultural machinery [2]. Despite significant technological advances and improvements, there is a limit to internal combustion engine efficiency, namely the efficiency of the constant volume cycle. Due to geometrical constraints, this efficiency is already below the reference efficiency for a heat engine operating between high temperature and low temperature reservoirs, namely the Carnot efficiency. Consequently, it is impossible for an internal combustion engine to achieve the efficiency of an electric motor or fuel cell due to unavoidable irreversibilities. Partially recovering some of the otherwise wasted heat is important in improving thermal efficiency. Here, the waste heat recovery (WHR) process seeks to capture and

Abbreviations: TEM, Thermoelectric module; TEG, Thermoelectric generator; ICE, Internal combustion engine; WHR, Waste heat recovery.

* Corresponding author.
E-mail address: nicolae.vlad.burnete@auto.utcluj.ro (N.V. Burnete).

https://doi.org/10.1016/j.pecs.2022.101009
Received 12 March 2021; Received in revised form 22 March 2022; Accepted 24 March 2022
Available online 1 April 2022
0360-1285/© 2022 Elsevier Ltd. All rights reserved.

Nomenclature

Abbreviations

ACO	Air coflow
ACOU	Air counterflow
ATS	Exhaust gas aftertreatment system
B5	95% diesel + 5% biodiesel (V/V)
B10	90% diesel + 10% biodiesel (V/V)
BSFC	Brake specific fuel consumption
CFD	Computation fluid dynamics
CPM	Constant property model
DC	Direct current
DCTEG	Direct contact thermoelectric generator
DMPPT	Distributed maximum power point tracking
DPP	Differential power processing
EES	Engineering equation solver
EGR	Exhaust gas recirculation
EPA	Environmental Protection Agency
eTEG	Electric turbo-generator
FC	Fuel consumption
HEV	Hybrid electric vehicle
HVAC	Heating ventilation and air conditioning
HX	Heat exchanger
ICE	Internal combustion engine
ISG	Integrated starter generator
MPP	Maximum power point
MPPT	Maximum power point tracking
NEDC	New European Driving Cycle
NRTC	Non-road Transient Cycle
PCM	Phase change material
PEM	Proton exchange membrane
RDE	Real driving emissions
SASTEG	Segmented asymmetrical thermoelectric generator
STEG	Segmented thermoelectric generator
TC	Thermocouple
TE	Thermoelectric
TEG	Thermoelectric generator
TEM	Thermoelectric module
U.S.	United States
UDDS	Urban Dynamometer Driving Schedule
WCO	Water coflow
WCOU	Water counterflow
WHR	Waste heat recovery
WLTC	Worldwide Harmonized Light Vehicles Test Cycle
WLTP	Worldwide Harmonized Light Vehicle Test Procedure
WTVC	World Transient Vehicle Cycle

convert heat that would otherwise end up unused in the environment, in some other form of useful energy [3].

An internal combustion engine energy distribution analysis shows that approximately 65–70% of the energy input is lost through exhaust gases (~35–40%) and through dissipation in cooling circuits (~30%) [4]. In other words, the internal combustion engine already has two important heat sources: the exhaust gas system and the radiator. To further underline the potential and importance of waste heat recovery for internal combustion engines, a study performed by the Fiat Research Center [5] estimated that recovering 400–500 W of waste thermal energy as electrical energy can lead to a reduction of carbon dioxide (CO_2) emission values by 6–7 gm/km. Furthermore, simulations performed by Stobart et al. [6] in 2010 considering the technology available at that time for waste heat recovery predicted fuel savings of 3.9–4.7% for various passenger cars and up to 7.4% for a transit bus.

There are numerous methods available for recovering a part of the energy otherwise wasted through the exhaust gases like the Organic Rankine Cycle, mechanical or electrical turbocompounding, thermoelectric (TE) generators, etc. However, if they are not properly designed, all these methodologies can also result in parasitic power losses (either directly or indirectly through the added weight of the system) that can become significant. Of these options, thermoelectric generation is a promising method since it uses solid-state devices with relatively low maintenance. Compared to other thermal energy recovery methods, thermoelectric generators (TEGs) have several advantages [7–9]: environmentally friendly, no moving parts, little to no noise and vibration, no working fluids, high reliability (when working temperatures are not exceeded), low maintenance, scalable, modular, ability to operate over a wide range of transient temperature conditions, and the direct conversion of thermal energy into electrical energy. Furthermore, the same thermoelectric module can be used for both cooling and heating along with thermoelectric generation. However, recovering high temperature waste heat also poses challenges concerning the reliability and durability of thermoelectric generators devices like oxidation, sublimation, degradation of the thermal and electrical interface, as well as mismatches due to thermal expansion [10–17]. The main limitations of thermoelectric generators for automotive applications are [7–9]: low efficiency, high cost, insufficient extraction and non-uniform heat distribution on the hot side, insufficient (/inappropriate) heat dissipation (method) on the cold side, installation space, high added weight as a result of the low efficiency of each individual element, the unsteady nature of the heat source (in case of exhaust gas waste heat recovery), as well as a large number of required connections.

As presented prior, the advantages of utilizing thermoelectric generators in automotive applications are numerous with studies predicting even a possible replacement of the alternator in passenger vehicles [18]. Therefore, if enough electrical energy is generated, the added mass of the TEG system could be balanced by removing this device. Another possibility is to use thermoelectric generators as a replacement for currently available heating ventilation and air conditioning (HVAC) systems. Here, switching between heating and cooling is done by reversing the current while offering high control flexibility [19]. In addition, partially recovering waste heat as electrical energy could significantly benefit engine performance, efficiency, reliability, and design [20]. As a result, the stress on the battery could be lowered with the aim of increasing its lifetime.

Currently, there are a few review papers that endeavor to summarize the literature for utilizing thermoelectric generators when recovering the waste thermal energy of internal combustion engines. Rodriguez et al. [3] cover several aspects of waste heat recovery using thermoelectric generators, namely the possible locations for thermoelectric generator installation, a description of the thermoelectric technology, the typical components used to build a thermoelectric generator, aspects of exhaust gas thermoelectric generator modeling required to predict power output, experimental results, and future trends. Zheng et al. [19] have a more general approach to the use of thermoelectric generators for recovering waste heat. In other words, these authors review the status of material development with respect to function, commercialization, and high efficiency thermoelectric generator development, as well as possible application areas in different industries. With respect to the automotive industry, the authors briefly present the use of the thermoelectric devices for climate control and waste heat recovery from exhaust gases. Shen et al. [4] perform a comprehensive review of thermoelectric generators installed on the exhaust pipe of vehicles with respect to the country where the study was performed taking into account the proposed research objectives, test conditions, system features, as well as study outcomes. In addition, these authors cover the challenges of thermoelectric generator design like heat extraction and

dissipation, connection modes, available space, weight, and other items, but also present a summary of previous studies. The paper ends with proposed future directions. Alghoul et al. [21] focused on classifying and clarifying the differences between thermoelectric systems used for power generation with respect to design and performance, but also the test rigs employed by researchers. Aspects of thermoelectric generator use for automotive exhaust gas heat recovery are covered only briefly. In their review, Champier [8] reviews the possible application areas of thermoelectric generators in general; thus, only succinctly covering their use for automotive waste heat recovery . Saidur et al. [20] review the technologies that can be used to recover the exhaust gas waste heat of internal combustion engines, like thermoelectric generation, a six-stroke internal combustion engine cycle, or a Rankine bottoming cycle and turbocharging. With respect to thermoelectric generators, the authors cover some of their general aspects for the automotive industry, the main challenges, and a few advances in the technology. Yang [22] presents specific potential applications of thermoelectric waste heat recovery in vehicles and its potential to reduce fuel consumption. Patil et al. [23] begin with a description of thermoelectric materials, but then concentrate their study on the design of thermoelectric generators heat exchangers with respect to the heat transfer rate, temperature distribution, and pressure drop. Orr et al. [24] review the advantages and limitations of using heat pipes in conjunction with thermoelectric generators as a means to improve the system efficiency. This is achieved by decreasing the pressure losses in the gas stream, thermal resistance, as well as allowing for a more flexible design and temperature control. Like Saidur et al. [20], Hatami et al. [25] start by covering waste heat recovery technologies for internal combustion engines, but then they focus their review on the hot side heat exchanger design studies as a means to improve the thermoelectric generator system efficiency.

In contrast to the presented literature, this effort seeks to bring together all aspects concerning the use of thermoelectric generators for internal combustion engine waste heat recovery to provide a comprehensive overview on the issue while aiding researchers and engineers in the development of efficient systems. This is accomplished by delivering a thorough summary of experimental results that highlights the goal of the study, the applied test method and obtained temperature gradient, the design of the TEG system (thermoelectric materials, number of thermoelectric modules, system mass, hot side structure, and cooling method), the power output and parasitic losses, as well as the gain in efficiency and reduction in fuel consumption. A similar summary is also supplied for simulation studies. The authors have also included efforts covering the hot side heat exchanger design (external shape, internal structure, material, test temperature and gas flow velocity, average interface temperature, uniformity of temperature distribution, and pressure drop). Furthermore, it has been found that the focus of literature is on TEG systems installed on the exhaust system due to high temperatures of the exhaust gases, simplicity and a relatively low influence on engine operation (the last two reasons strongly depend on the design of the thermoelectric generator). In contrast, this review includes studies covering other regions that can provide heat for power generation (i.e., radiator and exhaust gas recirculation).

2. Fundamentals of thermoelectric generators

A thermoelectric generator module is a solid-state device that converts thermal energy directly into electrical energy based on the Seebeck principle (the creation of an electric potential between two connected semiconductors when these components are subjected to a temperature difference). The reversed process of transforming electrical energy into thermal energy is also possible and is based on the Peltier effect. These effects happen by using charge carriers (electrons and holes) moving in the material, which are particles with the ability to transport heat and electric charge. Their movement requires an energy input, but when they recombine, energy is released. A thermoelectric module (TEM) consists of many thermocouples (up to hundreds) positioned between two (usually) ceramic plates that serve as electric insulators and thermal conductors. Throughout this effort TEG is used to refer to the system made up of one or more thermoelectric modules (operating as thermoelectric generators) and (but not always) hot and cold side heat exchangers. Considering T_{hot} the temperature of the hot side junction and T_{cold} the temperature of the cold side junction, under open circuit conditions, the Seebeck voltage (V_{OC}) is:

$$V_{OC} = \alpha \cdot \Delta T = \alpha \cdot (T_{hot} - T_{cold}) \tag{1}$$

where $\alpha = V_{OC} / \Delta T$ is the Seebeck coefficient that is specific to the material and it can be either positive or negative. For the rest of the paper, α designates the junction Seebeck coefficient, unless otherwise mentioned.

The Peltier effect is the reverse of the Seebeck effect, namely it is the conversion of current flow into a temperature difference between two dissimilar materials and is defined by the Peltier coefficient (π_P):

$$\pi_P = \frac{Q_{h/c}}{I} \tag{2}$$

where $Q_{h/c}$ is the rate of heating or cooling and I is the current. The Peltier effect is undesirable for thermoelectric generation since it causes an increased transport of heat from the hot side to the cold side; thus, decreasing the temperature gradient. An additional effect that must be considered for thermoelectric generators is the Thomson effect (defined as the heating or cooling of a current-carrying material when subjected to a temperature difference). In device modeling, this effect is regarded as minor compared to the Joule effect (discussed next) and is often neglected. Here, some authors [26,27] have shown that it does not alter the internal resistance, but can reduce the thermoelectric generator power output by hindering the voltage output.

The Joule effect correlates heat and electrical energy as follows:

$$Q_J = I^2 \cdot R_{cond} \tag{3}$$

where R_{cond} is the conductor resistance, while Q_J is heat released along the length of a conductor when electric current flows through it. The Joule effect is independent of the current flow direction, which is thermodynamically irreversible and accounted for as a heat loss [26,27]. The Seebeck, Peltier, and Thomson (τ) coefficients are connected through the Kelvin relationships:

$$\pi_P = \alpha \cdot T_{junction} \tag{4}$$

$$\tau = \overline{T} \cdot \frac{d\alpha}{dT} \tag{5}$$

where $T_{junction}$ is the temperature of the junction and $\overline{T}$ is the average temperature of the material. Consequently, the amount of heat transferred due to the Peltier effect is:

$$Q_{h/c} = \alpha \cdot I \cdot T_{junction} \tag{6}$$

In general, three scenarios exist for operation of a TEG system: constant heat, "dynamic" heat and constant temperature. The constant temperature scenario requires maintaining steady temperature values for the hot and cold side. This is accomplished by varying the amount of energy input by heat with respect to changes in electrical load. One way of achieving this situation is by employing phase-change materials (see Section 7.2) that can release the stored heat at variable rates corresponding to the electrical and thermal operating conditions. The constant heat scenario is usually found in waste heat applications, where there is a uniform amount of energy input by heat, while the temperatures of the hot and cold side can vary depending on parasitic effects driven by the load current. Finally, the "dynamic" heat scenario varies the amount of energy input by heat in a timeframe shorter than the thermal time constant (i.e., response) of the TEG system. For automotive applications all these scenarios are possible. For example, exhaust gas

waste heat recovery is typically of the type "dynamic" heat, whereas radiator waste heat recovery is often the constant heat variety.

3. Efficiency

3.1. General considerations

The primary parameter used to describe the potential of thermoelectric devices is the figure of merit (Z) [8]:

$$Z = \frac{(\alpha_p - \alpha_n)^2}{\left(\sqrt{\kappa_p \cdot \rho_p} + \sqrt{\kappa_n \cdot \rho_n}\right)^2} \tag{7}$$

where ρ is the electrical resistivity and κ is the thermal conductivity which consists of two parts: lattice thermal conductivity (κ_L) and electronic thermal conductivity (κ_e) [28]. The subscripts $_p$ and $_n$ indicate the corresponding two materials of the thermocouple (p-type and n-type, respectively). To characterize the material thermoelectric performance, the dimensionless figure of merit ($z\overline{T}$) is used. For simplification, it is often assumed that $Z\overline{T}$ (device figure of merit - see Eq. (7)) and $z\overline{T}$ (material figure of merit) are equal [29]; thus, leading to:

$$Z\overline{T} = \frac{\alpha^2 \sigma}{\kappa}\overline{T} = \frac{\alpha^2}{\rho\kappa}\overline{T} \tag{8}$$

where $\overline{T} = (T_{hot} + T_{cold})/2$ and σ is the electrical conductivity ($\sigma = 1/\rho$).

The efficiency of a thermoelectric module operating as a generator [8] is defined as the ratio of the electrical energy output ($W_{electric}$) to the thermal energy supplied to the hot side (Q_{hot}):

$$\eta_{TEM,generator} = \frac{W_{electric}}{Q_{hot}} = \frac{T_{hot} - T_{cold}}{T_{hot}} \cdot \frac{\sqrt{1 + Z\overline{T}} - 1}{\sqrt{1 + Z\overline{T}} + \frac{T_{cold}}{T_{hot}}} \tag{9}$$

As an example, the variation of thermal efficiency for a thermoelectric generator installed on the exhaust pipe or exhaust gas recirculation cooler when the cold side is cooled with engine coolant (the coolant average temperature is considered to be 353.15 K [30]) is presented in Fig. 1, where C is the Carnot efficiency and 0.5, 1, 2, and 5 are example $Z\overline{T}$ values. Depending on engine load, the temperature difference can reach values as high as 650 K [31,32]. In such cases the efficiency would range between 9.2% for a $Z\overline{T}$ of 0.5 and 33.5% for a $Z\overline{T}$ of 5. It is important to note here that the current (market) state of the art $Z\overline{T}$ for thermoelectric materials is less than 2 [33]. However, limiting the discussion to a value of 2 will mitigate the importance and potential of research in this field [33]. Previous research [28,34–36], as well as ongoing research projects, like the Horizon 2020 project UncorrelaTEd [37] showed that it is possible to decouple the Seebeck coefficient and the electrical conductivity, thus allowing for an increase in the power factor by a factor of 4 or more [38]. Consequently, the limit of 5 presented in Fig. 1 was chosen to highlight the importance of developing high performance thermoelectric generators, considering the high energy efficiency that can be achieved in these conditions. Currently, commercially available, and widely used thermoelectric modules use bismuth telluride (Bi_2Te_3) that have a $Z\overline{T}$ of approximately 1, subsequently leading to a conversion efficiency of ~2–10% (based on the scenarios presented prior and the references presented in Tables 6 and 7 in Section 10). Some researchers estimate that reaching a $Z\overline{T}$ value of 2 can lead to an approximately 9–10% improvement in fuel consumption [39].

As indicated, to be useful in thermoelectric applications for internal combustion engine waste heat recovery, a material should have a large $Z\overline{T}$ value. Considering Eqn. (8), this means the material must have a high power factor $\alpha^2\sigma$ and a low thermal conductivity. Here, the power factor characterizes the heat to electricity conversion of the charge carriers. Maximizing these characteristics is a difficult task since it involves a compromise between parameters that are interdependent (although there are studies [28,34–36,38] which have shown that it is possible to overcome these barriers): i.e., Seebeck coefficient, electrical conductivity (or electrical resistivity), and thermal conductivity (see Eqs. (4) and (5)). The low thermal conductivity requirement also conflicts with the heat flux requirements and ultimately with the power output of the system [40], which represents a percentage of the heat flux through the thermoelectric devices. As a result, decreasing the thermal conductivity of the thermoelectric material to increase the $Z\overline{T}$ negatively impacts the heat flux through the devices, thus limiting the amount of power it can produce. Subsequently, to recover this power, more thermoelectric devices are required resulting in an increase in the overall size and weight of the system that can be detrimental to fuel economy of the vehicle.

To determine overall TEG system efficiency, more factors beyond just the specific thermoelectric module efficiency have to be included (see Eqs. (1) and (2) from [4]). This includes the efficiency of the hot ($\eta_{HX,hot}$) and cold side ($\eta_{HX,cold}$) heat exchangers (HX), needed for automotive waste heat recovery applications, along with the efficiency of the electrical converter and its ability to optimize the electrical load (not included here) [41]:

$$\eta_{TEG,system} = \eta_{hot\ HX}\eta_{TEM}\eta_{cold\ HX} \tag{10}$$

It must be noted that, generally, heat exchangers are evaluated according to their effectiveness, but Fakheri has showed in his work [42] that, if the effectiveness is known, it is possible to determine a corresponding heat exchanger efficiency. Furthermore, contact resistances between the heat exchangers and the thermoelectric module (accounted for by the coefficients $\zeta_{hot\ HX\text{-}TEM,contact\ loss}$, $\zeta_{TEM\text{-}cold\ HX,contact\ loss}$) must be added (to Eq. (10)) along with the additional heat losses from the side

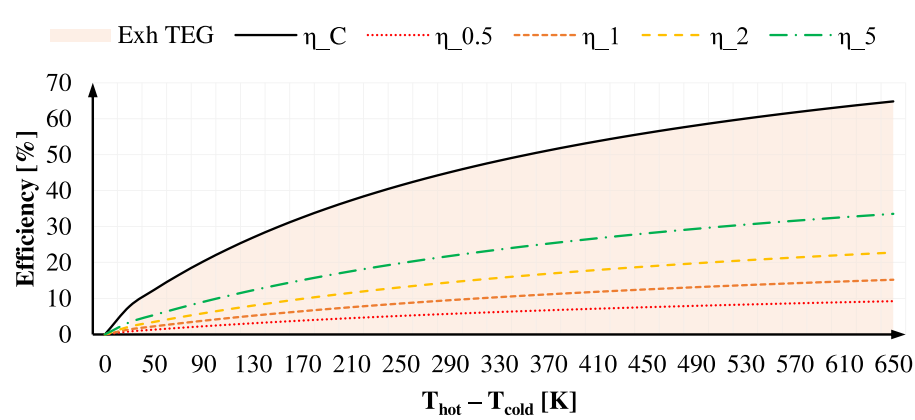

Fig. 1. Theoretical variation of η_{TEG} for different $Z\overline{T}$ values when $T_{cold} = 353.15[K]$ (specific to exhaust gas thermoelectric generators with coolant cooling) – heat exchanger efficiency and other practical losses are neglected.

surfaces of both the heat exchangers and the thermoelectric module legs (accounted for by the coefficients $\zeta_{hot\ HX,side}$ and $\zeta_{TEM,side}$):

$$\eta_{TEG,system} = \zeta_{hot\,HX,side} \cdot \eta_{hot\,HX} \cdot \zeta_{hot\,HX-TEM,contact} \cdot \zeta_{TEM,side} \cdot \eta_{TEM} \cdot \zeta_{TEM-cold\,HC,contact} \cdot \eta_{cold\,HX} \quad (11)$$

If the heat exchanger on the cold side is operating at temperatures above the ambient, heat losses to the ambient could improve the temperature gradient and heat flux through the thermoelectric device; thus, improving its efficiency.

3.2. Analysis of efficiency

As described in the previous section, the findings illustrate that there are significant differences in the presentation of the underlying equations for thermoelectric generation. Furthermore, the analysis also highlighted numerous situations where it was not clear how the equations were obtained. In both cases, it is possible to cause confusion and/or the arrival of the reader at erroneous conclusions (this is also valid for Sections 5 and 9). With respect to the efficiency of thermoelectric devices, research and innovation should be focused on the identification of new solutions, technologies and materials that can further improve the figure of merit to reach a value of at least 5, although even a lower value might suffice for internal combustion engine waste heat recovery applications. By doing so, the efficiency of the devices will be significantly increased, thus making them more attractive for vehicle manufacturers, especially for heavy-duty vehicles used in road transport. Achieving this target requires solutions to break the correlation between the three factors influencing $Z\overline{T}$: Seebeck coefficient, electrical resistivity, and thermal conductivity.

4. Thermoelectric modules design

4.1. Materials

When it comes to thermoelectric materials, the main challenges for researchers and manufacturers alike are: growth of material operating range to work at higher temperature differences, improvement of $Z\overline{T}$, and/or development of low-cost materials to counteract the effects of low efficiency [8]. Other technological challenges involving the use of thermoelectric generators for high temperature operation (not only automotive), like the diffusion of atoms at the boundary of the semiconductor and the metal, control of the mechanical stress, etc., are presented by Yazawa and Shakouri [43]. Note that there are several literature reviews regarding thermoelectric materials that deliver excellent classifications, thermoelectric properties, and material structures [3,19,33,44]; hence, their comprehensive presentations are not presented in this effort.

According to Zheng et al. [19], there has been no significant breakthrough in developing commercially available materials with high $Z\overline{T}$ values that are capable of replacing Bi_2Te_3 or other materials that are currently in use. The main causes identified are:

- Tested materials have been manufactured in form factors specific to some type of specialized testing equipment, thus limiting testing;
- Testing of thin film (1–10 μm) samples may require a difficult and time-consuming correction of end values to account for surface dislocations, substrate interactions or even stress-induced effects;
- Test errors and/or the use of inadequate equipment;
- Measuring individual properties at large time intervals. Since these can vary in time and/or due to exposure to the test conditions, the resulting $Z\overline{T}$ value may be incorrect;
- Measuring just two of the properties, with the third being extrapolated or chosen from literature, which can also lead to incorrect $Z\overline{T}$ values.

Although peak $Z\overline{T}$ values of common thermoelectric materials vary in the range of 1–2.6 (Fig. 2 - top), one must be aware that these values are also a function of temperature. Typically, values provided in the literature are mainly the peak values but their change with temperature is equally important to consider (Fig. 2 - bottom) [3] since in many applications, like internal combustion engine exhaust waste heat recovery, the temperature of the heat source varies over a wide range. With respect to automotive applications, primary material requirements are: large $Z\overline{T}$ values, high reliability, low producing cost, high availability, low environmental impact, and large-scale manufacturing capabilities [45].

4.1.1. Thermomechanical properties

Mechanical properties of thermoelectric materials are essential to consider along with their thermoelectric properties. Overall, to resist different external forces (bending, shaking, compression, etc.) and ensure long-term reliability of thermoelectric materials, a high elastic modulus is required [46]. Generally, thermoelectric generator modules used in automotive applications for waste heat recovery have to resist over 10,000 thermal cycles (i.e., variable thermal gradients from the cold start and the hot stop of the engine, temperature variations caused by the variable engine load) along with withstanding the mechanical vibration and shocks generated by the internal combustion engine, moving parts of the transmission, and unevenness of the road surface [4,47,48]. Since most thermoelectric materials are brittle, fracture strength (σ_f) is crucial to evaluate mechanical failure. Other mechanical properties, such as Young's modulus (E), hardness (H_V), toughness (K_C), Poisson's ratio (ν), thermal shock resistance ($R_{th,shock}$), and coefficient of thermal expansion ($\alpha_{th,exp}$) are required for optimal design of thermoelectric modules [22,47].

4.1.2. Cost

LeBlanc et al. [49] generated a comprehensive analysis of the material, manufacturing, and system costs for 30 thermoelectric materials with respect to the conversion efficiency. The authors estimated the cost of power generation in $/W by considering material, manufacturing, and heat exchanger costs for five scenarios involving different temperatures (thermoelectric cooling – $\overline{T}$ = 10 °C, low temperature heat recovery – $\overline{T}$ = 60 °C, solar thermal generator – $\overline{T}$ = 135 °C, automotive exhaust – $\overline{T}$ = 275 °C, and industrial furnace heat recovery – $\overline{T}$ = 425 °C). Furthermore, an appropriate device geometry is determined with respect to cost and performance. Note that the dominant design parameters consider the ratio of the total area covered by the active thermoelectric material to the plate area, designated as the fill factor (F) and the leg length (L), respectively. Since there is a trade-off between material volume and power output, it can be concluded that an optimum geometry can be determined for minimum costs and maximum power output. The results for each of the scenarios involving power generation are presented in Table 1. Specific discussion involving the advantages and disadvantages of the materials provided in Table 1 can be found in the works of Yang et al. [33], Liu et al. [50], and Wei et al. [51].

In a different study, Ouyang and Li [52] analyzed the cost-performance ratio and the corresponding power output density and efficiency of multiple materials (with operating temperatures in the range 300–1000 K) from the following categories: skutterudites, half-Heusler, SiGe alloy, and chalcogenides. The authors modeled various segmented thermoelectric generators by considering temperature dependent material properties, as well as electrical and thermal contact resistances for every interface between thermoelectric elements and between the thermoelectric element and the electrode. They arrived at the conclusion that thermoelectric materials exhibiting high power factors (e.g., half-Heuslers and Yb filled skutterudites) are preferable for applications where the cost is not a major concern. However, if there are cost limitations, the use of segmented thermoelectric generators that include thermoelectric materials with a high $Z\overline{T}$ can lead to a

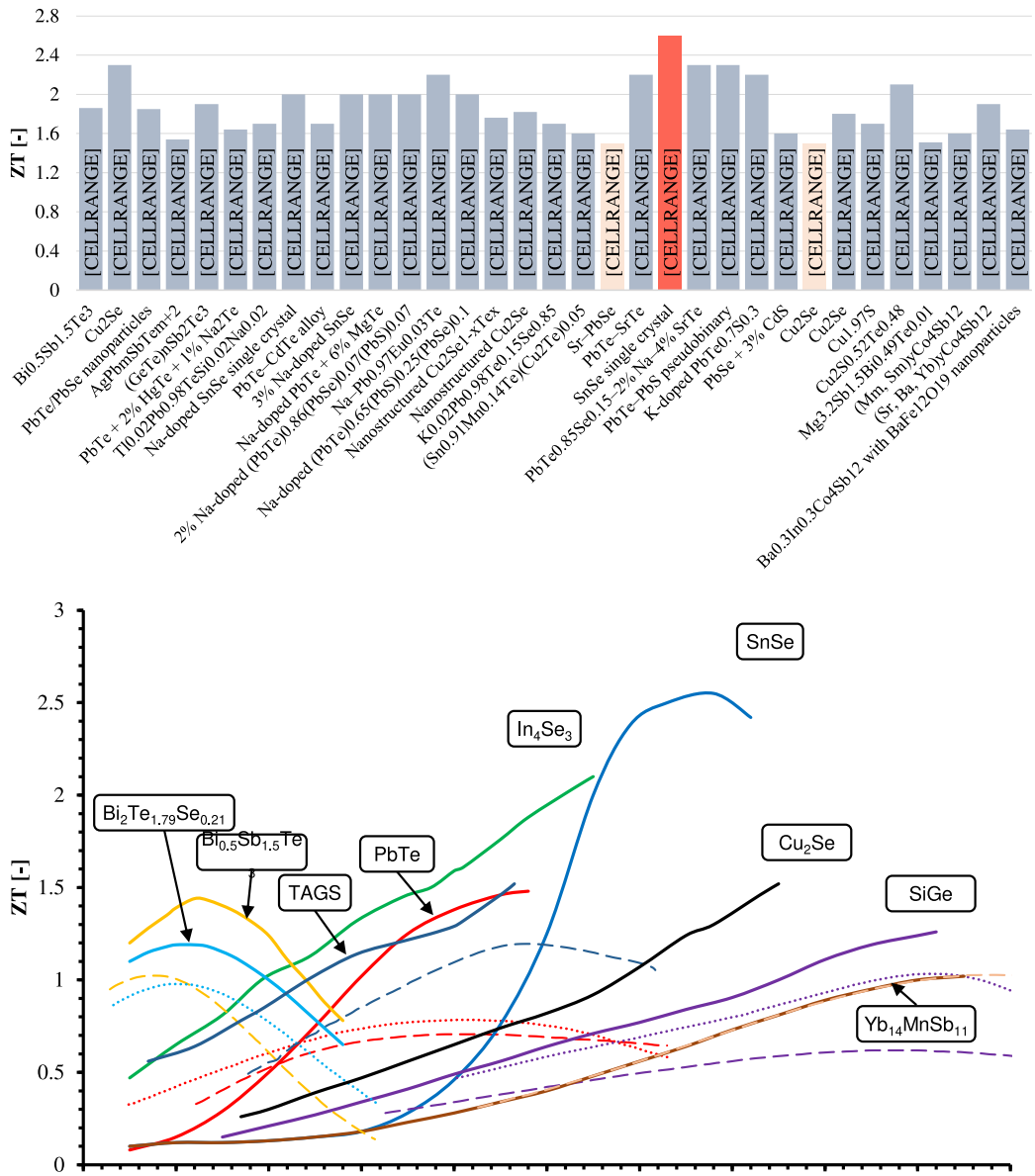

Fig. 2. Peak $Z\overline{T}$ values (*top* – adapted from [33]) and comparison of state of the art $Z\overline{T}$ *(bottom)* in 2008 (marked with dashed lines (p-type) and dotted lines (n-type) – adapted from [29]) and 2017 (marked with continuous lines – adapted from [33]).

Table 1.
Cost of different thermoelectric generators with respect to material, manufacturing type and mean temperature [49].

Scenario	Mean temperature [°C]	Materials with lowest cost	Manufacturing type	Cost
Low temperature	60	Bi_2Te_3	Bulk	< 100$/W
		$Bi_{0.52}Sb_{1.48}Te_3$	Bulk	
		$Bi_{0.52}Sb_{1.48}Te_3$	Nanobulk	
Medium-Low temperature	135	$Bi_{0.52}Sb_{1.48}Te_3$	Bulk	< 20$/W
		$Bi_{0.52}Sb_{1.48}Te_3$	Nanobulk	
		$AgPb_{18}SbTe_{20}$	Bulk	
Medium-High temperature	275	$(Na_{0.0283}Pb_{0.945}Te_{0.9733})$	Nanobulk	< 6$/W
		$(Ag_{1.11}Te_{0.555})$	Bulk	
		$AgPb_{18}SbTe_{20}$	Bulk	
		$Yb_{0.2}In_{0.2}Co_4Sb_{12}$	Bulk	
		$Zr_{0.25}Hf_{0.25}Ti_{0.5}NiSn_{0.994}Sb_{0.006}$		
High temperature	425	$(Na_{0.0283}Pb_{0.945}Te_{0.9733})$	Nanobulk	< 6$/W
		$(Ag_{1.11}Te_{0.555})$	Bulk	
		$AgPb_{18}SbTe_{20}$	Bulk	
		$Mg_2Si_{0.6}Sn_{0.4}$	Bulk	
		$Zr_{0.25}Hf_{0.25}Ti_{0.5}NiSn_{0.994}Sb_{0.006}$		

cost-performance ratio of approximately 0.86 \$/W, an efficiency of 17.8%, and a power density of 3.0 W/cm^2. This makes them a possible solution for internal combustion engine exhaust gas thermoelectric generators.

To estimate the power generation cost (G) on a \$/W basis, the LeBlanc et al. [49] applied the same equation as Yee et al. [53]:

$$G = \frac{C}{P_{el}} = \frac{4}{\alpha^2\sigma(T_{hot}-T_{cold})^2}\frac{(m+1)^2}{m}\left[\left(C_{M,B}+C_B\right)\rho_{mat}L^2+\left(C_{M,A}\right)L+\frac{C_{HX}h_TL}{F}\right] \tag{12}$$

where C is the overall cost in \$, P_{el} the output power in W, and $m = R_{Load}/R_{TEG}$. Here, C_B is the cost associated with the bulk material, $C_{M,B}$ the manufacturing cost associated with processing the bulk material while ρ_{mat} is the density of the active material. The sum of $C_{M,B}$ and C_B is designated as volumetric cost. $C_{M,A}$ represents the cost that scales with the area of the module, or areal module costs. Finally, C_{HX} is the cost of both heat exchangers and h_T their overall heat transfer coefficient.

Hendricks et al. [54] expanded on the works of Yee et al. [53] and LeBlanc et al. [49] by removing key assumptions and constraints to account for heat exchanger heat flux effects and differences in thermal characteristics of the hot and cold side heat exchangers. This was accomplished while invoking the cold to hot side heat exchanger conductance ratio (≥10) developed in [55] to arrive at a more detailed cost equation:

$$G = \frac{4}{\alpha^2\sigma(T_{hot}-T_{cold})^2}\frac{(m+1)^2}{m}\left[\frac{1.1\cdot\kappa\cdot A_{HX,TE_interface}\cdot F}{K_{HX,hot}}+L\right]^2\left[\left(C_{M,B}+C_B\right)\rho_{mat}+\frac{C_{M,A}}{L}+\frac{C_{HX}UA_{HX}}{A_{HX,TE_interface}L\cdot F}\right] \tag{13}$$

where $A_{HX,TE_interface}$ is the interface area between the heat exchanger and the thermoelectric element, UA_{HX} the UA value of the heat exchanger, and $K_{HX,hot}$ the thermal conductance of the hot side heat exchanger. Using this equation, Hendrix [56] established the dependency of the optimum cost and fill factor on heat exchanger performance and heat exchanger flux. They concluded that, for the overall TEG system cost to drop below 3\$/W, heat exchanger costs must be lower than 1\$/(W/K) in comparison to thermoelectric material and manufacturing costs. Other efforts by Anderson and Brandon [57] concluded that it is unlikely that a reduction in material cost will contribute to a significant reduction in the overall cost, due to the high costs associated with module manufacturing (also supported by [19]).

Finally, Hendricks et al. [54] determined for internal combustion engine exhaust gas TEG systems that the costs are usually determined by:

- exhaust gas temperature,
- ratio of the cold side to the hot side junction temperature,
- $Z\overline{T}$ of the thermoelectric module (mainly the thermal conductivity and separately the module power factor),
- hot side thermal conductance and the ratio of the cold side to hot side thermal conductance,
- heat exchanger cost factor expressed in \$/(W/K), and
- parasitic thermal losses.

Reviewing the literature presented in this section finds efforts regarding a system cost analysis for thermoelectric generators installed on the exhaust gas recirculation system or on the radiator with both as possible heat sources (see Section 6).

4.2. Design and manufacturing

The material covered in Sections 2, 3, and 9 of this effort highlights that the typical metrics for thermoelectric generators are its figure of merit (usually reported based on the material properties), efficiency, and power output. However, a thermoelectric module is comprised of more than just the thermoelectric conversion material and, therefore, a device-level discussion is required. According to Liu and Bai [58], the final assembled module can be split with respect to the key materials involved: thermoelectric conversion materials (used for the conversion of thermal to electrical energy), thermoelectric interface materials (used for ensuring a reliable transport of heat and electricity between the electrode strip and the thermoelectric elements with a minimum loss of energy), package material (used to prevent the evaporation of the thermoelectric conversion material and/or as thermal insulation), housing material (used to provide structural support as well as electrical insulation), and brazing or soldering material. This leads to multiple challenges that must be overcome to ensure durability and the desired module operating performance (e.g., the stresses that an automotive exhaust gas waste heat recovery thermoelectric generator must withstand as discussed in Section 4.1): the development of a corresponding contact layer with respect to the thermoelectric material (since the thermomechanical stress at the semiconductor-metal interface is one of the main failure mechanism [59]), mitigating contact issues due to the mismatch of thermal expansion coefficients, appropriate packaging, etc. [60]. Considering these aspects, the manufacturing process that depends on the thermoelectric material employed becomes of particular importance. For bulk materials, the traditional manufacturing process involves the following steps [61,62]:

- Ball milling powders of the constituent elements followed by mixing,
- Hot pressing or spark plasma sintering of the thermoelectric material into ingots,
- Dicing of the ingots to form thermoelectric elements (legs) – for this step, the material brittleness is of great concern because any chipping or cracking of the thermoelectric element influences its thermal and electrical resistance [61],
- Metallization,
- thermoelectric element dicing,
- Brazing or soldering of electrode strips and thermoelectric elements, and
- Module assembly.

Regarding thermoelectric module design, Glatz et al. [63] suggested that there are three approaches, depending on the heat flow through the device and the layout of the thermocouples:

(a) Planar design – lateral heat flow with laterally fabricated thermocouples have the advantage of flexibility in terms of thermocouple thickness and length (an increased length increases the thermal resistance and consequently the temperature gradient), as well as suitability for thin film deposition [64],
(b) Vertical design – vertical heat flow with vertically fabricated thermocouples are the most commercialized type due to their simplicity, high thermocouple integration, and high output voltage [64], and
(c) Mixed design – vertical heat flow with laterally fabricated thermocouples.

A more thorough presentation of thermoelectric modules design and manufacturing can be found in the effort of He et al. [60], where the authors discuss the following architectures: flat bulk, cylindrical bulk, thin- and thick-film, as well as flexible. Additionally, their effort covers thermoelectric generators used in wearable applications, thermoelectric generators with hot side pn junctions, as well as devices with orthogonal heat and electrical current flux directions.

Further details concerning the manufacturing process, both traditional and alternative, can be found in the works of LeBlanc [61], El-Desouky et al. [62], Jaziri et al. [64], and Du et al. [65]. With respect to device-level challenges, the efforts of He et al. [60], Liu and Bai [58], and Aswal et al. [66] provide thorough analyses. Finally, Araiz [67] discusses synergistic efforts regarding the assembly of thermoelectric generators and how it can impact their performance.

4.3. Commercially available thermoelectric generators

A selection based on operating temperature and output of commercially available thermoelectric modules is presented in Table 2 to provide an understanding of current TEM technology. For each manufacturer, only thermoelectric modules with a power output greater than 8 W were included. The price evaluation was done considering 50 $ a respectively medium price level.

4.4. Multistage and functionally graded thermoelectric generators

4.4.1. Segmented thermoelectric generators

The strong correlation between the figure of merit and temperature limits the thermal stability of thermoelectric generators to a narrow temperature range and ultimately its use in internal combustion engine exhaust waste heat recovery applications considering that the exhaust gas temperature depends on the operating conditions (e.g., city traffic versus highway travelling). A possible solution to this issue is to use a series of segments (layers) made of different types of thermoelectric materials that work in narrower temperature ranges [78]. When these segments are in thermal and electric contact, they form a segmented leg (aka segmented thermoelectric generator or STEG [79]) that is able to work with a larger thermal gradient, subsequently producing greater

Table 2.
Selection of commercially available thermoelectric modules.

Manufacturer	Designation	Material	No. of TCs	Size (width x length x height) [mm x mm x mm]	Continuous / max power [W]	T_c / T_h for continuous power [°C]	Maximum allowable temperature [°C]	Efficiency at T_h-T_c for continuous power [%]	TEM Mass [g]	Price
Custom Thermoelectric [68]	1261G-7L31-24CX1	$(Bi, Sb)_2(Te, Se)_3$	126	56 × 56 × 5	19.1	25/320	320	N/A	60	high
European Thermodynamics [69]	GM250-241-10-12	N/A	N/A	40 × 40 × 3.4	9.32	30/250	250	N/A	N/A	high
European Thermodynamics [69]	GM200-127-28-12	N/A	N/A	62.5 × 62.5 × 4	15.6	30/200	200	N/A	N/A	medium
European Thermodynamics [69]	GM250-127-28-10	N/A	N/A	62.5 × 62.5 × 4	28.3	30/250	250	N/A	N/A	high
Everredtronics Limited [70]	TEG126-60A	$(Bi, Sb)_2(Te, Se)_3$	N/A	56.5 × 56.5	14.6	30/300	400	~ 4	N/A	N/A
Hi-Z Technology Inc. [71]	HZ 20	$(Bi, Sb)_2(Te, Se)_3$	71	74.68 × 74.68	20 / 36	50/250	350	~ 5	102	medium
Hi-Z Technology Inc. [71]	HZ 14HV	$(Bi, Sb)_2(Te, Se)_3$	126	61.05 × 71.05 × 7.87	17 / 25	50/250	350	~ 3	66	low
Marlow Industries Inc. [72]	TG12-8-01	N/A	N/A	40.13 × 44.70 × 3.76	7.95	50/200	230	~ 5	N/A	low
P&N Technology Co. Ltd. [73]	TEG-127020-40 × 44-200	N/A	127	40 × 44 × 3.3	8.5	30/200	250	N/A	23	medium
TEGpro [74]	TE-MOD-22W7V-56	$(Bi, Sb)_2(Te, Se)_3$	N/A	56.5 × 56.5 × 5	21.6	30/330	400	N/A	N/A	medium
TEGpro [74]	TGMT-19W-4V	$(Bi, Sb)_2(Te, Se)_3$	N/A	56 × 56 × 5	19.3	30/330	400	N/A	N/A	medium
TECTEG MFR [75]	TEG1-12610-4.3	$Bi_{,2}Te_3$	126	40 × 40 × 4.3	5.2	30/300	320	N/A	N/A	low
TECTEG MFR [75]	TEG1-24111-6.0	$Bi_{,2}Te_3$	241	56 × 56 × 6.0	17.6	30/300	320	N/A	N/A	medium
TECTEG MFR [75]	TEG1B-12610-5.1	$Bi_{,2}Te_3$	126	40 × 40 × 5.1	7.1	30/300	320	N/A	N/A	low
TECTEG MFR [75]	TEG1-12611-8.0	$Bi_{,2}Te_3$	126	56 × 56 × 8.0	13	30/300	320	N/A	N/A	high
TECTEG MFR [75]	TEG1-12611-6.0	$Bi_{,2}Te_3$	126	56 × 56 × 6.0	14.7	30/300	320	N/A	N/A	medium
Thermonamic [76]	TELBP1-12656-0.45	$(Bi, Sb)_2(Te, Se)$	N/A	56.5 × 56.5	21.7	30/350	400	N/A	N/A	N/A
TXL Group [77]	TXL-199-02Q	$(Bi, Sb)_2(Te, Se)$	199	40 × 40 × 4.4	N/A	30/200	200	N/A	21	low

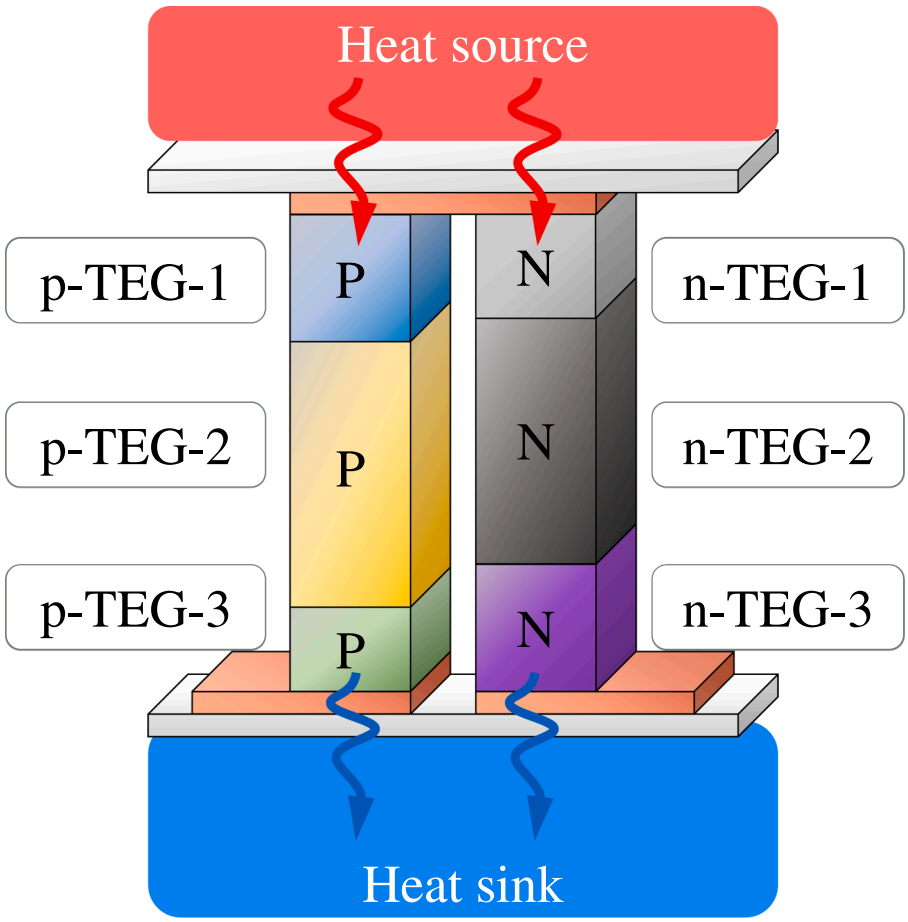

Fig. 3. A typical segmented thermoelectric generator.

power as compared to an unsegmented thermoelectric generator under the same thermal condition [78]. A typical example of a segmented thermoelectric generator is shown in Fig. 3. Generally, in the case of a segmented thermoelectric generator, the pairs of two *p* and *n* legs consist of two or more segments made of different types of thermoelectric materials. For example, skutterudite can be used for the medium-temperature segment and combined with bismuth telluride for the low-temperature segment [80]. However, to obtain the highest possible efficiency of segmented thermoelectric generators by ensuring the proper temperature range for each segment, it is necessary to consider the operating conditions of the internal combustion engine and its application (e.g., a truck travelling at constant speed on the highway).

For a segmented thermoelectric generator, the length ratio of the different segments that form the legs can affect its performance. Consequently, to achieve enhanced performance, differentiated segmentation of the p-leg and n-leg is needed because of their respectively dissimilar thermal conductivity values. Generally, the parts of a segmented thermoelectric generator are connected both thermally and electrically in series. Subsequently, the same current and comparable

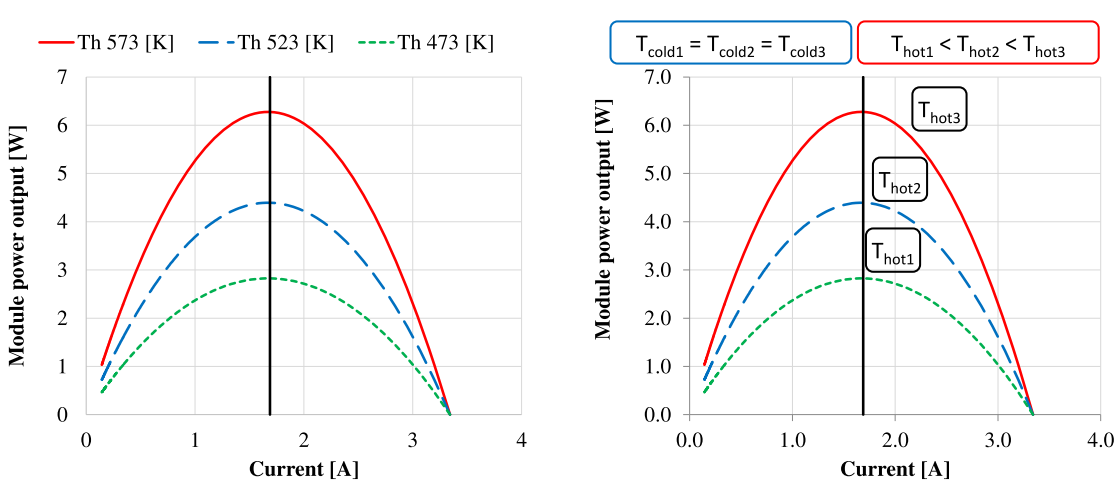

Fig. 4. Method to mitigate the compatibility conflict in the direction of flow.

conduction of heat flows through each segment [81]. When the optimum power output of the individual segments forming the segmented thermoelectric generator appears at different current densities, a compatibility issue occurs. In the case of severe incompatibility, certain segments can actually deliver negative power output at a current that is optimal for other segments [82]. To avoid this problem, Snyder and Ursell [81] introduced a compatibility factor (Eq. (14)) as the value of the relative current density u ($=\frac{J}{\kappa\sqrt{T}}$) where the thermoelectric generator reaches its highest performance:

$$s=\frac{\sqrt{1+Z\overline{T}}-1}{\alpha\overline{T}} \tag{14}$$

If the compatibility factors differ by a factor of 2 or more, the maximum efficiency of the segmented thermoelectric generator might decrease [81].

To mitigate this compatibility issue, Crane and Bell [82] recommend to vary the aspect ratio of individual segments by keeping their cross sections constant and varying their length until the value of the current matches the value for the best power output (Fig. 4). This way, the temperature difference for each segment can be set to a near-optimum.

4.4.2. Cascaded thermoelectric generators

Another potential solution to the energy conversion efficiency-heat source temperature issue is to use several independent thermoelectric modules installed in two or three cascade stages (Fig. 5). This design has the benefit of a respectively simple structure and easier manufacturing. Furthermore, it is recommended for high temperature heat sources like the exhaust gas of internal combustion engines.

Each stage is made of thermoelectric modules adapted to the input temperature. The main challenge in manufacturing cascade thermoelectric generators is the appropriate choice of thermoelectric modules (usually made of different materials) since their combination affects the overall energy conversion efficiency [83]. In this area, Zhang et al. [83] analyzed two- and three-stage cascaded thermoelectric generators. For the first stage (the low temperature stage), the authors used $Bi_2(Se,Te)_3$ and $(Bi,Sb)_2Te_3$ at a working temperature of 523 K. The second stage (the mid-temperature stage) materials were $Na_xCo_2O_4$ and SLTO that worked with a relatively hot side temperature of 825 K. For the third stage (the high temperature stage), the authors chose $TiO_{1.1}$ and ZnAlO as suitable materials for temperatures as high as 1223 K. For the two-stage thermoelectric generator, the efficiency was 13.2%; whereas, for the three-stage thermoelectric generator it increased to 13.5%. Since there is only a small difference between the two, they state it is preferable to use the two-stage design due to lower costs and a simpler build.

4.5. Analysis of thermoelectric modules design

Analyzing the findings described in the previous section, it can be concluded that materials are the basis for increasing thermal to electrical energy conversion efficiency, but one must also consider the device-level integration. Improvements in this area can also increase the number of potential applications for thermoelectric devices. Consequently, it is necessary to continue researching new materials, technical and manufacturing solutions that will allow improving efficiency, reducing the costs and the specific weight, while also eliminating polluting solutions that are currently used (like thermoelectric modules using lead). Additionally, considering the added cost of the system and

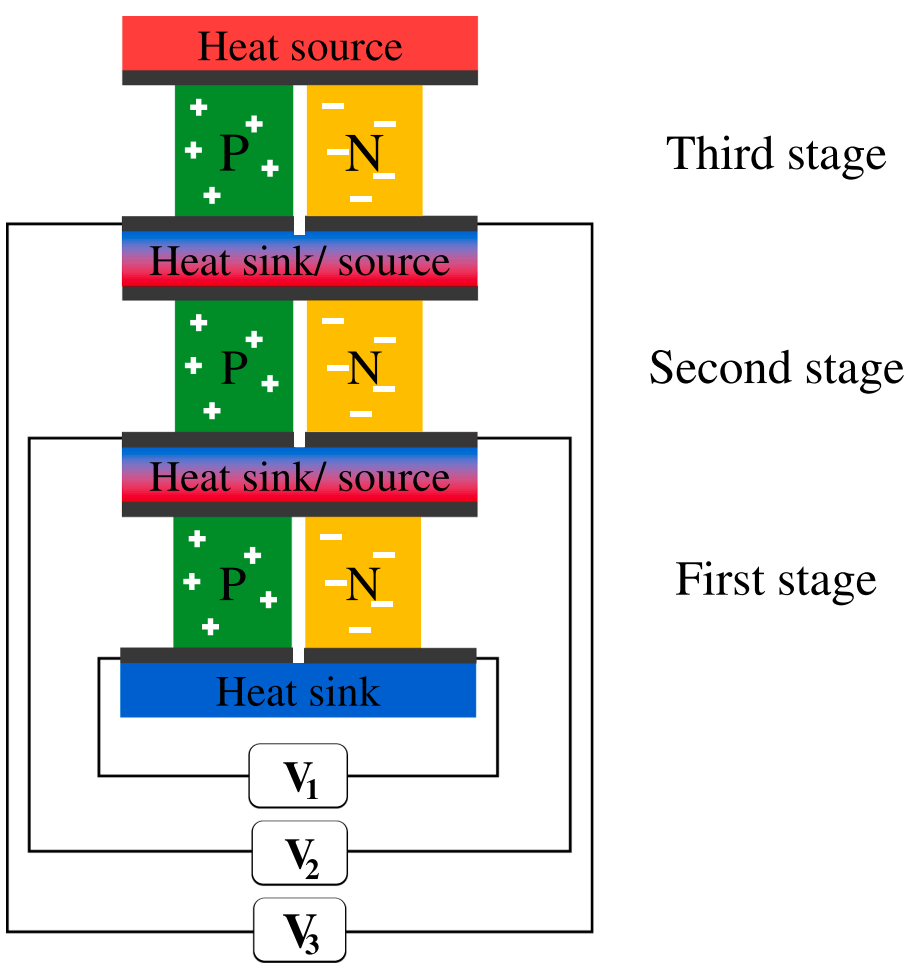

Fig. 5. Cascaded thermoelectric generator design.

therefore the long periods for recovering of the investment, the use of thermoelectric generators for vehicle waste heat recovery requires the evaluation of the mechanical and thermal stress in specific conditions of vehicle operation for a better assessment of the thermoelectric generator durability and maintenance requirements. Multistage and functionally graded thermoelectric generators have proven to provide superior conversion efficiency, but they also require additional optimization effort and have higher costs. Therefore, research should focus on a new design approach that combines the benefits of segmented and cascaded segmented thermoelectric generators for a further increase in efficiency while ensuring the optimal temperature operating range for each component.

5. Electrical and thermal characterization of thermoelectric generators

5.1. Electrical characterization of thermoelectric generators

For a constant temperature gradient across the thermoelectric module, at steady state, there is an almost linear relationship between electrical parameters. This allows for an electrical circuit analog modeling of the thermoelectric module as a series connection between a Direct Current (DC) source and an internal resistance (see Fig. 6). It must be noted that the internal resistance (R_{TEG}) and the voltage of a thermoelectric generator depend on the temperature gradient and the average temperature. More specifically, for a given temperature gradient, $\overline{T}$ should be as low as possible to minimize the influence on the internal resistance and consequently, on the voltage and power output [84]. When connecting a load (Fig. 6) the current passing through the circuit and the output will be:

$$I_{Load} = \frac{V_{OC}}{R_{TEM} + R_{Load}} = \frac{\alpha \cdot \Delta T}{R_{TEM} + R_{Load}} \tag{15}$$

where V_{Load} is the load voltage. Finally, the power of the load (P_{Load}) is:

$$P_{Load} = V_{Load} \cdot I_{Load} = R_{Load} \cdot I_{Load}^2 = R_{Load} \left(\frac{\alpha \cdot \Delta T}{R_{TEM} + R_{Load}} \right)^2 \tag{16}$$

Often, thermoelectric generators used in automotive exhaust waste heat recovery applications are made of many thermoelectric modules (Fig. 6 – right) to increase the output. However, since the temperature gradient across the thermoelectric generators (Fig. 7) is often not uniform [86,87], this can cause circulating currents in the array of thermoelectric modules that decreases system efficiency.

5.2. Thermal characterization of thermoelectric generators

The heat flow through the thermoelectric generator device is governed by its electrical and thermal conductivity. To maintain a temperature gradient across the module, the thermal conductivity must be respectively low [88]; however, this conflicts with heat flux requirements. As mentioned in Section 3, a low thermal conductivity decreases the heat flux through the devices and limits its power output [40]. In the case of a system with a minimum required power output, this can increase the number of thermoelectric modules and consequently the total weight, which, for automotive waste heat recovery applications would reduce the net output of the system. In addition, electrical conductivity influences the temperature gradient by means of the Joule effect (see Section 2, Eq. (3)). To minimize this influence, electrical conductivity should be as high as possible. Neglecting the spreading thermal resistance and contraction thermal resistance between the thermoelectric modules and the heat exchangers, as well as the fin efficiency, Fig. 8 shows the equivalent thermal circuit of a thermoelectric generator installed on the exhaust system of an internal combustion engine, which consists of a hot side heat exchanger, a thermoelectric module, and a cold side heat exchanger with coolant cooling.

If a load is connected to the module, the Thomson effect and the heat transferred from the hot side to the cold side around the legs are considered negligible; however, the Peltier (Eq. (6)) and Joule (Eq. (3)) effects cannot be neglected. Hence, the amounts of energy transferred by heat at the two junctions are:

$$Q_{TEM,\,hot} = K_{TEM} \cdot (T_{hot} - T_{cold}) + \alpha I T_{hot} - \frac{1}{2} I^2 R_{TEM} = K_{HX,hot} \cdot (T_{hot,source} - T_{hot}) \tag{17}$$

$$Q_{TEM,\,cold} = K_{TEM} \cdot (T_{hot} - T_{cold}) + \alpha I T_{cold} + \frac{1}{2} I^2 R_{TEM} = K_{HX,cold} \cdot (T_{cold} - T_{cold,sink}) \tag{18}$$

where K_{TEM} is the thermoelectric module conductance, while $K_{HX,\,hot}$ and $K_{HX,\,cold}$ designate the thermal conductance of the hot side and cold side heat exchangers, respectively.

5.3. Analysis of electrical and thermal characterization

The complexity and multitude of physical parameters that govern the operating efficiency of thermoelectric generators requires a thorough understanding of the interactions between their thermal and electrical

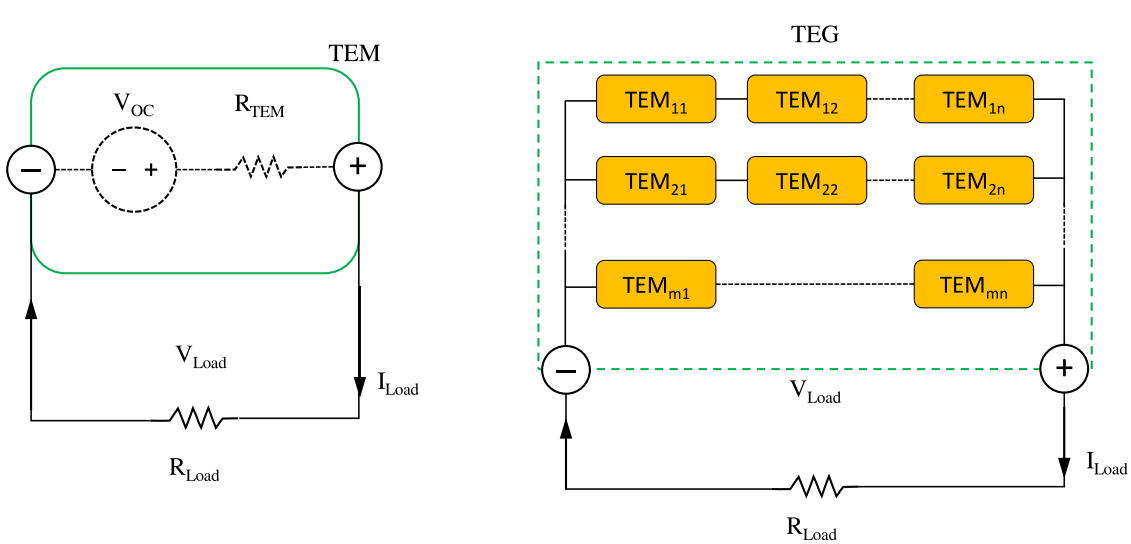

Fig. 6. Equivalent electric circuit of a thermoelectric module (left) and generalized structure of thermoelectric generators (right) (adapted from [85]).

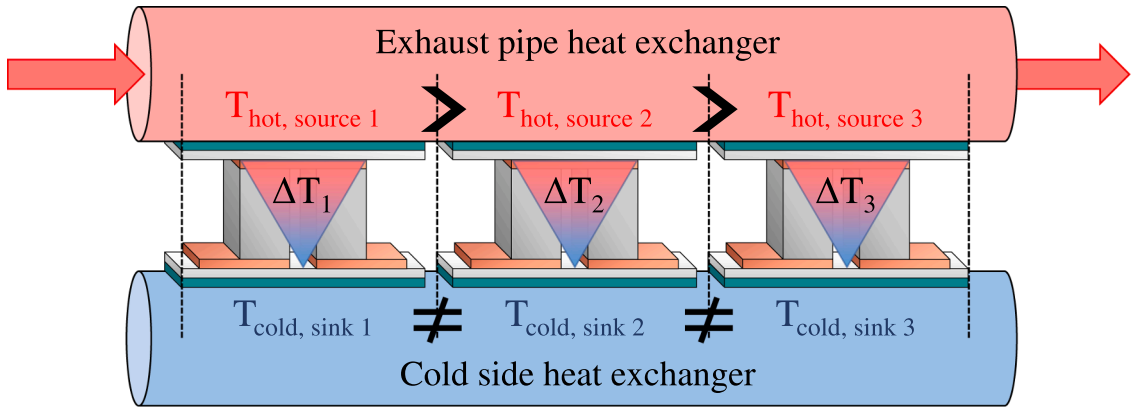

Fig. 7. Differences in temperature gradient across different modules of a thermoelectric generator.

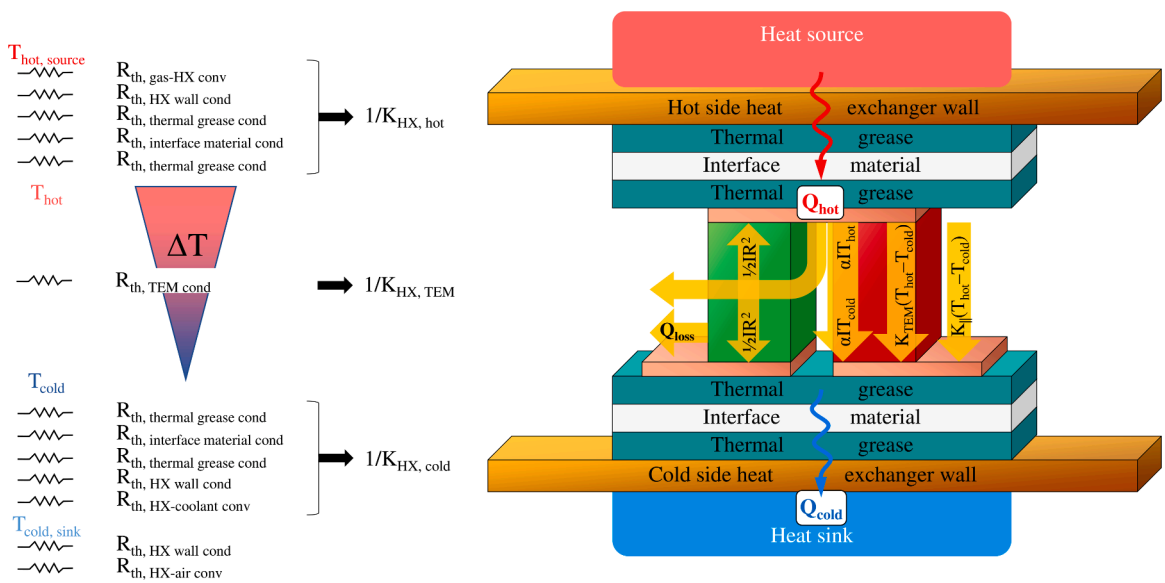

Fig. 8. Equivalent thermal circuit of an automotive exhaust gas thermoelectric generator.

characteristics and the conflicting requirements for achieving high performance. This section sought to present these aspects with an adequate level of detail, as means of underlining the importance of interdisciplinary research for thermoelectric generator development. Possible research directions can arise from the primary parameter used to describe the potential of thermoelectric materials: the figure of merit. This links the Seebeck coefficient, electrical conductivity, and thermal conductivity or, in other words, the electrical and thermal characteristics. Consequently, to overcome the low efficiency barrier of thermoelectric generators, future research should focus on decoupling the Seebeck coefficient and the electrical conductivity to increase the power factor without negatively influencing thermal characteristics. With respect to the thermal conductivity, additional research is required to determine the optimum compromise between a large temperature gradient across the thermoelectric generator and a high heat flux.

6. Design considerations for automotive thermoelectric generators

A general schematic of a TEG system is presented in Fig. 9 and

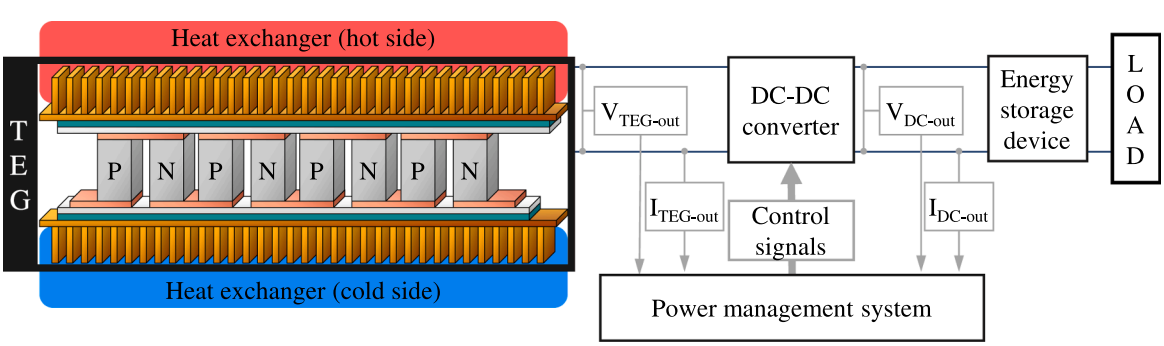

Fig. 9. General schematic of a thermoelectric generator system.

consists of the following [85]:

- Hot side heat exchanger – used to extract the maximum possible amount of heat from the heat source to ensure a high temperature on the hot side of the thermoelectric modules.
- Thermoelectric generator – the material and number of thermoelectric modules, as well as the size of the thermoelectric generator are chosen considering the operating temperature range and required power output.
- Cold side heat exchanger – used to reject heat to ensure a low temperature on the cold side and, therefore, a significant temperature gradient across the module.
- Power management system – processes the electrical output of the thermoelectric generator and delivers the resulting electrical power at a suitable voltage level for the loads. Generally, it consists of a DC-DC converter and a control algorithm responsible for maximizing or stabilizing the electrical power delivered to the loads.
- Energy storage device – usually a battery that must compensate for any mismatch between the load demand and the generated power.

When considering the use of thermoelectric generators for waste heat regeneration from an internal combustion engine, one important question that arises is whether the thermoelectric generator system is compatible with the original design of the heat source (i.e., exhaust system, exhaust gas recirculation, radiator, etc.) regarding the amount of heat that can be supplied to the thermoelectric generator, or does the latter have to be modified to allow for an optimum heat transfer to the thermoelectric generator [21]. Here, a suggested TEG system design approach [8] is the following:

- Research thermoelectric materials to achieve the highest possible $Z\overline{T}$ through the operating temperature range of the thermoelectric generator,
- Analyze heat exchanger designs and their coupling to the thermoelectric modules,
- Examine the possible connection modes (series / parallel / mixed) and the algorithm (maximum efficiency point tracking or maximum power point tracking) employed to optimize the thermoelectric generator operating point and transfer maximum power to the load,
- Complete numerical studies to optimize the thermoelectric generator.

One key factor in this process is acknowledging the fact that, in practical applications, the power generated by a specific module for a certain temperature gradient may differ from the datasheet specifications. One reason for this dissimilarity can be the testing method (i.e., the lack of a standard testing method [89–91]). Sometimes testing is done under vacuum and, in this case, convection losses are lower compared to testing in air; hence, the reported thermoelectric generator performance is higher. Consequently, it is recommended to test one module using application specific conditions to determine any discrepancies with the datasheet [85].

Another important factor is the specific cost per W of the TEG system (see Eqs. (12, 13)) and the rate of return. A series of studies performed by FIAT and Chrysler as part of the HEATRECAR (reduced energy consumption by massive thermoelectric waste heat recovery in light-duty trucks) project [92] estimated a specific cost per W of electrical power of approximately 8.4€/W of which approximately 20% is the cost of Bi_2Te_3 and 73% the manufacturing cost. The same study underlined a maximum accepted cost for thermoelectric generation depending on vehicle type:

- Personal car or gasoline-hybrid taxi: 0.5€/W
- Light-duty truck or freightliner in USA: 0.7€/W
- Light-duty diesel truck or freightliner: 1.5€/W
- Conventional diesel taxi: 3€/W

A more recent study performed by Heber and Schwab [93] showed that at peak power output it is possible to achieve a cost as low as 1.2€/W but this is not always achieved during normal vehicle operation. The authors also highlighted that the thermoelectric modules currently available on the market cannot be used to achieve an amortization period of less than three years. In another study, Kober [94] demonstrated that it is possible to achieve both a high performance and low cost of the thermoelectric generator by applying a holistic approach that demands a highly integrated thermoelectric generator design, consideration of all system interactions, weight, and installation space, optimization of the thermoelectric generator in driving cycles, as well as cost modelling. Using this method, he was able to achieve a cost-benefit ratio of 81.3€/(g/km) (or 2.9 CO_2 g/km) for a conventional vehicle and 54.8€/(g/km) (or 5.4 CO_2 g/km) for a hybrid vehicle over the World Harmonized Light Vehicles Test Cycle (WLTC).

Reviewing the literature and the efforts of Schock et al. [95] and Zheng et al. [19], it was found that there are several challenges to overcome before thermoelectric generators can become viable for automotive usage:

- Developing thermoelectric materials with high efficiencies and an appropriate cost to power ratio for the defined operating temperature ranges [52],
- Ensuring an appropriate heat transfer on the hot side (Section 7) and an appropriate cooling solution (Section 8) with minimum parasitic losses [96,97] (see also Table 4),
- Mitigating engine/road induced vibrations that influence thermoelectric generator components [19],
- Improving robustness, since failure of a single coupling leads to failure of the entire module [60,95] (see also Fig. 9), and
- Diminishing interface failures from mismatches in thermal expansion coefficients and/or poor bonding [95].

In addition to these general challenges, the use of thermoelectric generators installed on the exhaust pipe, exhaust manifold [98], or the exhaust gas recirculation system of an internal combustion engine poses the following issues:

- Temperature of the exhaust gases can be as low as 90°C while also possibly exceeding 1000°C (see Figs. 16 and 17 as well as Table 3),
- Both the exhaust gas mass flow and temperature are influenced by load and speed, which are further influenced by the driving conditions and/or style [19,93],
- Gas temperature decreases along the exhaust pipe (see Fig. 7),
- Exhaust pipes are usually annular (consequently, high compatibility and performance would require an annular thermoelectric generator [99]), and
- Due to the high temperatures involved, thermoelectric generators are prone to sublimation issues [19,95].

For radiator thermoelectric generators, the main additional issue is that the source temperature is relatively low (80–100 °C [30]) and consequently the temperature gradient is small. This leads to lower efficiencies as compared to thermoelectric generators using exhaust gas as energy source.

Another critical issue of thermoelectric generators for automotive applications is its added weight that negatively impacts fuel consumption. According to Rowe et al. [100], the power penalty is approximately 12 W/kg, meaning that the power output of the TEG system must exceed this value, otherwise it will lead to an undesired increase in fuel consumption.

Considering the prior mentioned factors, TEG system development should focus on:

Table 3
Maximum temperature slopes for different engines

Engine / Fuel	Exhaust gas temperature at idle [°C]	Exhaust gas temperature at high load [°C]	Maximum temperature slope [°C/s]
SI / Gasoline	90	1000 [110]	45.50
SI / Ethanol	90	775 [111]	34.25
SI / CNG	90	900 [112]	45.50
SI / LPG	90	765 [113]	33.75
SI / H_2	90	450 [114]	18.00
CI / Diesel	90	850	38.00
CI / Biodiesel	90	600 [115]	25.50

- Stabilization and uniform distribution of temperature on the hot side to avoid fluctuations and overheating of the thermoelectric modules (see Section 7);
- Appropriate selection of thermoelectric materials with respect to operating conditions to lower costs and achieve the maximum possible efficiency (good thermomechanical properties, environmentally friendly, low cost, high figure of merit, investigation of segmented legs and cascaded thermoelectric generators, etc. – see Section 4);
- A holistic approach for the thermoelectric generator optimization together with the consideration of all system interactions, weight, and installation space, optimization of the thermoelectric generator in driving cycles, as well as cost modelling [94],
- Testing of the TEG system under the thermal and mechanical stresses caused by driving conditions with the aim of providing optimum thermal conductivity and a long lifetime [19,93]; and
- Lightweight thermoelectric generator development (see Section 6.2).

6.1. Installation position and operating conditions

For automotive applications, several factors must be considered when choosing TEG system installation position:

- Ensuring the maximum possible performance of the system (temperature and mass flow rate must be considered) [19],
- Space limitations (depending on the installation location) [19,93],
- Design of cooling system (depending on the type of cooling fluid) [101–103],
- Avoiding thermoelectric generator damage from exposure to high temperatures [95], and
- Mitigating the negative effect of the TEG system on internal combustion engine performance and aftertreatment devices (see Section 6.2).

There are several possible locations where the exhaust pipe appears to be the most attractive due to high temperatures (Figs. 10 and 11 – it must be noted that the temperature values presented in these figures are specific to compression ignition engines; in contrast, the temperature values encountered in the exhaust system of spark ignition engines are usually higher) and mass flow rates. However, this poses some challenges:

- The variable nature of vehicle internal combustion engine operation leads to unsteady exhaust gas temperatures and mass flow rates. Consequently, the temperature on the hot side of the thermoelectric generator elements varies constantly. Two issues arise from this:
  - Fluctuation of generated power – note: this can be addressed with the control algorithm (see Section 9),
  - Under specific engine operating conditions, the temperature of the exhaust gas may exceed the maximum threshold of the thermoelectric generator, thus damaging it; this issue can be solved with a bypass (see references [104,105]), heat pipes (see Section 7.1), or phase change thermal storage (see Section 7.2).
- Interference with the exhaust gas aftertreatment system (ATS). The use of thermoelectric generators before the exhaust gas aftertreatment system can cause a significant decrease of the exhaust gas temperature and hinder the operation of catalytic converters, particulate filters, etc. This can be avoided by either limiting the amount of extracted heat or by installing the thermoelectric generator after the exhaust gas aftertreatment system.

A good overview of manufactured and tested exhaust gas thermoelectric generator systems can be found in the efforts of Shen et al. [4] and Orr et al. [24]. It must be noted that there are studies which highlighted the benefits of using thermoelectric generators with an exhaust gas aftertreatment system. For example, a recent study performed by Massaguer et al. [106] showed that it is possible to use the energy recovered with the TEG system to improve the performance of the exhaust gas aftertreatment system during cold starts events. A different study, performed by Wan et al. [107] illustrated that the thermoelectric generator, catalytic converter, and muffler could be combined to form a single unit with benefits in terms of temperature distribution uniformity, as well as weight.

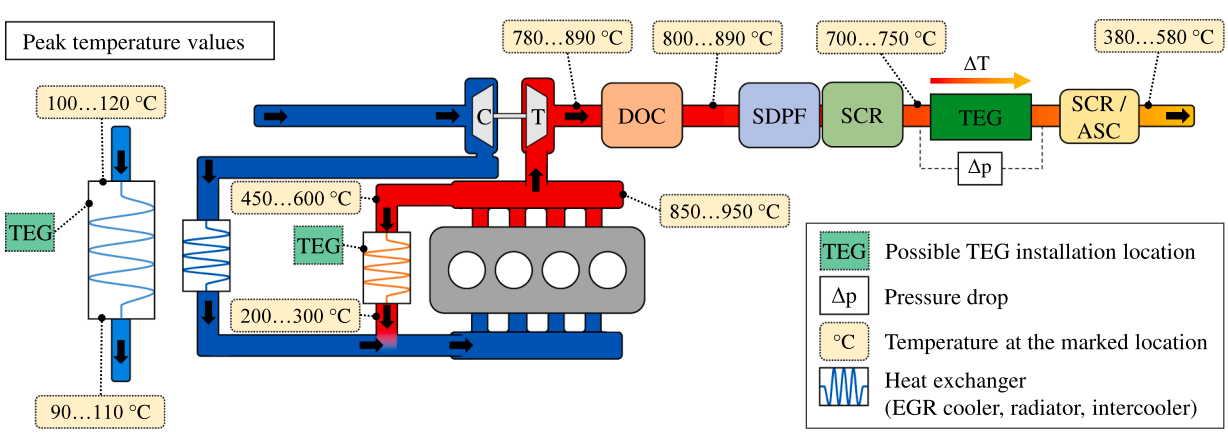

Fig. 10. Example of TEG installed on the exhaust pipe of a compression ignition engine – peak temperature values.

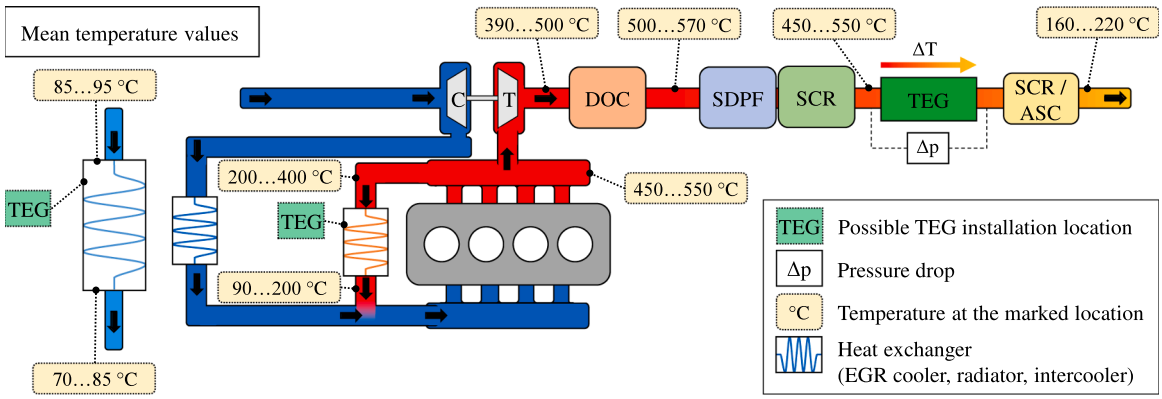

Fig. 11. Example of thermoelectric generator installed on the exhaust pipe of a compression ignition engine – mean temperature values.

Approximately 30% of the energy rejected by the internal combustion engine (Section 1) is lost through dissipation in the cooling circuits; hence, other possible waste recovery locations exist. Such a potential location is the radiator, where the coolant containing the larger part of the heat rejected through the cylinder walls is cooled. The main advantage is that there is no need for an additional heat exchanger. However, one must consider the lower temperatures of the coolant as compared to the exhaust gas.

As one of the main means to reduce nitrogen oxides (NO_x) emissions, modern engines employ exhaust gas recirculation. In this case, a part of the hot exhaust gases (high pressure exhaust gas recirculation) is directed back into the cylinder through an exterior pipe that connects the exhaust manifold with the intake pipe. Furthermore, to allow for an additional NO_x reduction, cooling of these exhaust gases is employed by using an exhaust gas recirculation cooler. Since hot exhaust gases (with temperatures on the order of 600–850 K [95]) pass through a heat exchanger (the cold side is ensured by the coolant), this becomes an attractive installation location for the thermoelectric generator.

6.2. Thermoelectric generator systems installed on automotive internal combustion engine exhaust

One of the biggest challenges when using thermoelectric generators installed on the vehicle exhaust pipe is to determine the optimum trade-off between heat extraction and power loss (due to an increased exhaust backpressure, as well as its added weight). In the case of forced convection liquid/air cooling systems, the additional power consumption of the pump/fan must also be included. Moreover, if engine coolant is used as the cooling fluid, this puts additional stress on the radiator due to the increased heat input (i.e., extracted by the thermoelectric generator from the tailpipe and rejected to the coolant), which could ultimately increase the power consumption of the radiator fan. This is of critical importance for a correct evaluation of the efficiency benefit to recover wasted thermal energy. In this sense, Ezzitouni et al. [108] find that by using current thermoelectric materials there is only a limited operating range where the use of a thermoelectric generator can lead to an increase in global efficiency.

Considering that the measured power output of the thermoelectric generator is P_{TEG}, the net power P_{net} produced by a coolant-cooled system can be expressed as [101–103]:

$$\begin{aligned} P_{net} &= P_{TEG} - P_{wt_loss} - P_{\Delta p_loss} - P_{pump_loss} - P_{other_loss} \\ &= P_{TEG} - \frac{W_{TEG} \cdot f_{roll} \cdot v_{vehicle}}{\eta_{transm}} - \dot{V}_{exh} \cdot \Delta p - P_{pump_loss} - P_{other_loss} \\ &= P_{TEG} - \frac{W_{TEG} \cdot f_{roll} \cdot v_{vehicle}}{\eta_{transm}} - \frac{\dot{m}_{exh}}{\rho_{exh}} \Delta p - P_{pump_loss} - P_{other_loss} \end{aligned} \tag{19}$$

where P_{wt_loss} is power loss due to the added weight of the thermoelectric generator, $P_{\Delta p_loss}$ is the power loss due to the pressure drop across the hot side heat exchanger of the thermoelectric generator, P_{pump_loss} the cooling pump power consumption (for a forced convection air-cooled system, this becomes the fan power), P_{other_loss} the additional power losses that can be caused by increasing the heat input to the radiator (and/or power requirement of power electronics [61]), $\dot{V}_{exh}$ the volumetric flow of exhaust gas, Δp the pressure drop across the hot side heat exchanger of the thermoelectric generator, $\dot{m}_{exh}$ the mass flow of exhaust gas, and ρ_{exh} the density of exhaust gases. Since installing the thermoelectric generator usually involves a change in the cross-section of the exhaust pipe, the pressure drop can be expressed as:

$$\Delta p = \frac{\dot{m}_{exh}}{\rho_{exh}} \cdot h_{L_total} \cdot \rho_{exh} \cdot g = \dot{m}_{exh} \cdot \left(K_{L_inlet} \cdot \frac{v_{inlet}^2}{2} + f \frac{L_{TEG,HX}}{D_{TEG,HX}} \frac{v_{TEG,HX}^2}{2} + K_{L_exit} \cdot \frac{v_{exit}^2}{2} \right) \tag{20}$$

where h_{L_total} is the total head loss (comprised of expansion, friction, and contraction losses), K_{L_inlet} and K_{L_exit} are the loss coefficients for the inlet and exit section respectively, f is the Darcy–Weisbach friction factor, $L_{TEG,HX}$, $D_{TEG,HX}$, $v_{TEG,HX}$ the length, hydraulic diameter, and average exhaust gas flow velocity inside the TEG heat exchanger, respectively, while v_{inlet} and v_{exit} are the average flow velocities at the thermoelectric generator heat exchanger inlet and exit, respectively.

The efficiency (η_e) of an internal combustion engine can be expressed as:

$$\eta_e = \frac{P_e}{\dot{m}_f \cdot LHV} \tag{21}$$

where P_e is the brake power of the engine in kW, $\dot{m}_f$ the fuel consumption in kg/s and LHV the lower heating value of the fuel in kJ/kg. The amount of fuel burnt to produce the electrical power P_{el} by using the alternator can be expressed as:

$$\dot{m}_{f_alt} = \frac{P_{el}}{\eta_{alt} \eta_e LHV} \tag{22}$$

For example, Massaguer et al. [109] determined that, for a mid-size

vehicle under the WLTP cycle, the fuel burnt due to alternator usage can be as much as 4.26%. By using an exhaust thermoelectric generator with 34 bismuth telluride thermoelectric modules and water cooling they were able to achieve a 0.53% improvement in fuel consumption.

When installing a TEG system, the amount of fuel burnt to produce the same amount of electrical power depends on the pressure loss across the hot side heat exchanger of the thermoelectric generator:

$$\dot{m}_{f_TEG} = \frac{P_{\Delta p_loss}}{\eta_e LHV} \tag{23}$$

By extracting enough electrical energy to replace the alternator (assuming the same weight for the TEG system and the alternator), the efficiency of the internal combustion engine can be improved. For the same amount of fuel burnt, the efficiency of the engine (see Eqs. (19–23)) can be expressed as (Eq. (24)):

$$\eta_{e_TEG} = \eta_e \cdot \left(1 + \frac{P_{net}}{P_e}\right) \tag{24}$$

One other challenge in automotive systems is the dynamic modulation in exhaust pipe surface temperature and the peak surface temperature. For example, an internal combustion engine can rapidly switch from idle to high loads; thus, leading to dramatic temperature changes. Based on exhaust gas temperatures usually encountered for various engine types, assuming the time interval to achieve maximum operating temperature is 20 s, the estimated maximum temperature slopes for several engines are given in Table 3:

Chen et al. [116] analyzed, among others, the simulated influence of temperature oscillation (sinusoidal) at the hot side surface on the performance of thermoelectric generators. Their findings showed that the power output can increase when the temperature fluctuates, especially under low temperature gradients. The efficiency was found to either decrease (negligibly) or remain constant. Shittu et al. [117] arrived at similar conclusion, but they used a rectangular pulsed heat input. In contrast, Fan and Gao [118], found that for an annular segmented thermoelectric generator, if the total heat flow is constant, a pulsed heat input improves only the peak power output values without any change to the mean values. However, this increases the von Mises stress and affects its reliability. In another study, Chen et al. [119] determined that thermoelectric generator performance is not influenced by the period of fluctuation, but only by the amplitude; i.e., the higher the amplitude, the greater the output. Furthermore, the authors analyzed only a single p-n coupling. In case of a TEG system, temperature fluctuations decrease performance since there will be modules performing under different (lower temperature gradient) operating conditions; thus, leading to an electrical mismatch of the interconnected thermoelectric modules. There are solutions proposed to solve this issue, like the adaptive removal and revival method proposed by Chen [120] or the dynamic reconfiguration of thermoelectric modules proposed by Baek et al. [121], both of which are covered in more detail in Section 9.

The exhaust pipe peak surface temperature has a significant influence on TEG system design decisions, since it allows the system designer to estimate the maximum heat flux, as well as identify the worst-case operating temperature situation. For example, test cycles like the NEDC are inadequate [122] because the engine load and, consequently, the exhaust gas temperature are well below the optimum values (Fig. 12).

6.3. TEG systems for other engine components (radiator, exhaust gas recirculation path, and oil pan)

Kim et al. [123] and Baatar and Kim [124] investigated the possibility of replacing the radiator with a thermoelectric generator using engine coolant as the heat source and air-cooling for heat rejection. The thermoelectric generator uses a sandwich structure that comprises a hot side block through which coolant flows and two cold side blocks with 128 integrated heat pipes connected to air-cooled heat sinks. The thermoelectric generator has a width of approximately 80 mm, a height of 250 mm and a length of 740 mm, thus allowing 72 40 mm x 40 mm Bi_2Te_3 modules to be installed. For the study, the system was integrated in a vehicle with a 2.0 L engine, which itself was part of a vehicle simulator. The tests were performed at idle and at a vehicle speed of 80 km/h. At idle, the measured hot-side temperature ranged from 90 to 95 °C; whereas, the cold side temperature was approximately 70 °C. In this case, the authors determined a maximum output power of 28.5 W (30 V and 3.8 A) for a module efficiency of 0.9%. At 80 km/h, the hot side temperature increased to 95–100 °C, while the cold side temperature decreased to approximately 45 °C. In this case, the system generated 75 W (50 V and 6 A) for a module efficiency of 2.1%. The overall efficiency was estimated to be around 0.3%.

More recently, Abderezzak and Randi [125] investigated the potential of a Bi_2Te_3 radiator thermoelectric generator using three analysis methods: simulation (one-dimensional steady state model), experimental work on a vehicle (the thermoelectric module installed between the radiator and an additional heat sink), and experimental work on a test bench (the thermoelectric module is installed between two water HXs in controlled conditions). The experimental results showed a maximum output power of 1.68 W for the vehicle test and 1.79 W for the test bench test. In contrast, the calculated power was 1.88 W. The authors noted that the peak efficiency was 3.85%.

Similar low thermoelectric generator efficiency was found by Schock

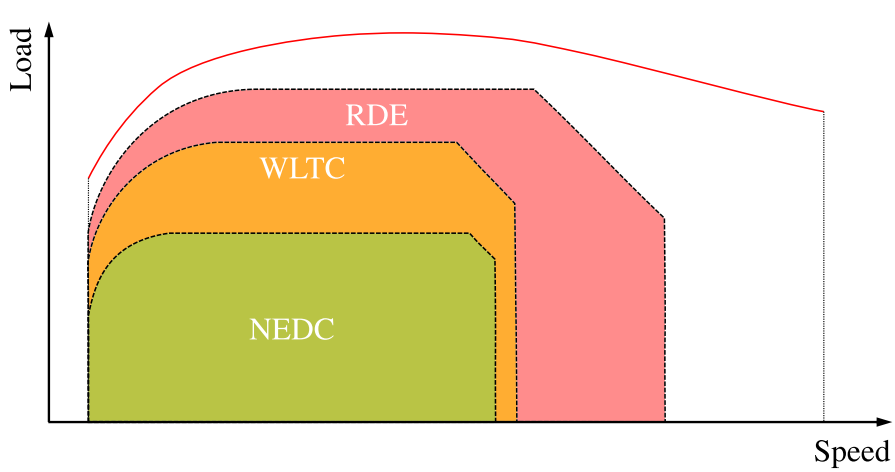

Fig. 12. Load and speed range covered by different test cycles.

et al. [95] who implemented a skutterudite thermoelectric generator in the exhaust gas recirculation cooler of a Cummins ISX engine equipping a class 8 truck. A 10 module thermoelectric generator was developed which, when operated under a temperature gradient of 550°C, produced 50.12 W of power. The measured module efficiency was 4%, while overall efficiency of the thermoelectric generator was estimated at 0.7%.

Analogous work done by Lan et al. [105] studied a TEG system mounted in the exhaust gas recirculation path of a CAT C6.6 heavy-duty engine. To avoid subjecting the thermoelectric generator to damaging temperatures, the authors modified the exhaust gas recirculation valve operation to control the exhaust gas flow rate. Four thermoelectric modules connected in series were mounted on both sides of the hot side heat exchanger. The cold side temperature was maintained using chilled water. Based on engine test bench data, the authors validated a simulation that predicted output power of 170–224 W for a thermoelectric generator using 20 thermoelectric modules. The authors also noted that optimizing the hot side heat transfer can increase system power output by as much as 25.8%. Here, it is worth noting that thermoelectric generators installed in exhaust gas recirculation coolers (EGR-TEG) have a significant advantage compared to exhaust gas pipe thermoelectric generators in terms of cost, since the components required for a TEG system (e.g., hot side heat exchanger, coolant flow) are already present.

Interestingly, Aljaghtham and Celik [126] find that it is possible to recover waste thermal energy from the oil pan. Using Multiphysics simulations (without experimental validation of the TEG system), the authors analyzed three oil pan geometries (flat, with a single step, and with multiple steps) with and without fins. Furthermore, they performed an optimization study to identify the optimum thermoelectric module size, number of thermoelectric modules, and the design (shape and size) of the oil pan. The cooling of the thermoelectric modules was accomplished using the air flow caused by the movement of the vehicle (standard passenger car and heavy-duty vehicle). Considering a constant engine oil temperature of 110 °C, 192 thermoelectric modules installed on the multiple steps oil pan with cooling fins and a vehicle speed of 120 km/h, the authors showed that it is possible to achieve a output power of 751 W at an ambient air temperature of 0 °C and 453 W at 25 °C, respectively, for the passenger car. The efficiency of the thermoelectric generator ranged between 5 and 9% for temperature gradients of 43 to 76 °C. Additionally, the authors analyzed a 6-cylinder compression ignition Cummins ISX engine with 2100 thermoelectric modules. At a vehicle speed of 110 km/h, the peak output power was 2713 W at 0 °C and 1636 W at 25 °C. Furthermore, the authors predicted an emission reduction of 11 g CO_2/km for the passenger car and 38 g CO_2/km for the heavy-duty vehicle. It must be noted that removing this much heat from the oil pan can cause unintended adverse effects on internal combustion engine operation due to a decrease in oil temperature which leads to a higher viscosity. This will then cause a lower engine efficiency, as well as increased pollutant emissions due to lower combustion chamber surface temperatures. The solution proposed by Aljaghtham and Celik [126] could be combined with the one proposed by Lan et al. [127] that suggests a thermoelectric generator can operate both as waste heat recovery system and a heat pump to reduce the engine warm-up time. By operating the thermoelectric generator in engine warm up mode, they were able to illustrate through simulations a 7 °C higher oil temperature in the first 100 s after start as compared to the baseline. Their study also showed that the engine oil reached 100 °C at 188 s (25%) and 88 °C at 431 s (38%) earlier than the baseline over the NEDC. However, to recover the energy used during the warm-up phase, longer waste heat recovery operating durations are required.

6.4. Analysis of design considerations for automotive thermoelectric generators

The use of thermoelectric generators for waste heat recovery in vehicles requires multiple compromises and optimizations, which opens numerous possibilities for further research and innovation. In this sense, it necessary to continue researching low impact solutions (tested in real driving conditions) that solve the conflict between the efficient use of thermoelectric generators for exhaust gas waste heat recovery and the operation of the exhaust gas aftertreatment system. For example, one possible solution for fast catalyst heat-up is to employ a close-coupled three-way catalyst, which reduces heat losses and ensures high exhaust gas temperatures during the engine cold start. However, after the warm-up phase has ended, the close-coupled catalyst is subjected to high temperatures that can cause sintering of the active material; thus, limiting the amount and type of material used and ultimately its efficiency. Consequently, a thermoelectric generator, with a bypass, could be installed before this catalyst to extract a part of the thermal energy contained in the exhaust gases before it reaches the catalyst. This will help control the exhaust gas temperature and, at the same time, generate electrical energy. A similar approach could be applied before the exhaust gas recirculation cooler, which could allow for reducing the stress on the cooling system.

The low efficiency of the system and the lack of efficient solutions for vehicle waste heat recovery is also owing to the nonuniform temperature distribution, the large overall dimensions of thermoelectric generators, as well as the negative impact on internal combustion engine operation (increasing heat exchanger efficiency comes at the cost of increased backpressure). Consequently, research efforts should be directed in these directions as well. Additional benefits could be obtained by solving the issue of thermoelectric module efficiency at low temperature gradients, which would make it possible to extend the use of radiator thermoelectric generators. Finally, considering that city traffic leads to large periods of exhaust gas recirculation operation and that there are significant efforts to increase the operating range of exhaust gas recirculation for highway vehicles, more effort should be directed towards the use of EGR thermoelectric generators. The main advantage of these solutions is the presence of the exhaust gas recirculation cooler that uses coolant for lowering exhaust gas temperature and therefore providing all required elements in one location. As described in the previous section, the use of the engine oil pan as a heat source has shown potential but strongly depends on the vehicle velocity and the ambient temperature.

7. Heat extraction and temperature distribution on the hot side

For some applications, direct exposure of the thermoelectric modules hot side to the heat source can be difficult or even impossible without a major system redesign. Therefore, an additional element, usually a heat exchanger, is required to extract thermal energy from the heat source and transfer it to the hot side of the thermoelectric modules. As a result, not all available heat is transferred to the hot side of the thermoelectric modules. The amount of heat transferred between the heat source and the thermoelectric material, and ultimately the system efficiency, depends on the heat exchanger efficiency. In other words, system efficiency cannot be predicted solely based on the efficiency values of the modules or the corresponding materials (see Eq. 11) [41]. In this sense, even if commercially available thermoelectric modules have an efficiency of 5–10%, system efficiency will be lower. Consequently, the heat extraction ability of the hot side heat exchanger is decisive for system operation.

Another critical factor for thermoelectric generator operation is the temperature distribution [87]. More precisely, a uniform temperature distribution is desired since TEG systems are usually comprised of an array of thermoelectric modules connected to a single power converter. As more thermoelectric modules are added, the surface area covered by the thermoelectric generator increases, and the position of the modules relative to the thermal energy source becomes asymmetric. As a result, it is possible for the thermoelectric modules to be subjected to different temperature gradients [86]. The possible causes of the uneven temperature distribution are thermal variability of the heat source (exhaust gases), uneven distribution of the mechanical clamping force among the

modules, or different conduction coefficients of the modules.

Considering a given number of identical thermoelectric module working in the same environment and with the same cold side temperature, if the temperature distribution on the hot side is not uniform, this leads to a different temperature gradient across each thermoelectric module (Fig. 7). Using Eq. (9) to determine the efficiency, it can be stated the efficiencies of the considered thermoelectric modules will be different. Furthermore, having dissimilar temperature gradients across each thermoelectric module leads to different power outputs [128,129] and this, combined with the connection mode, can cause a system output lower than the sum of the individual thermoelectric module outputs (see Section 9).

The heat extraction method on the hot side (with respect to the heat transfer mechanism) strongly depends on the heat source. For automotive applications, it can be both conduction (hot surfaces of the engine block, radiator, oil pane etc.) and convection (exhaust gases). For exhaust gas waste heat recovery systems, one challenge is to overcome the relatively large thermal resistance between the exhaust gases and the hot side of the thermoelectric generator. This is a result of the low heat transfer coefficient, specific to the gas-solid heat transfer, the thermal resistance of the heat exchanger and the contact resistance between the surfaces of the hot side heat exchanger and the thermoelectric generator hot side. In combination with a relatively small heat transfer area, the ability to extract heat is therefore limited. As a result, a temperature gradient between the hot exhaust gases and the hot side of the thermoelectric generator is established, which reduces the possible contribution to the power output and efficiency of the thermoelectric generator.

There are various methods of reducing the thermal resistance between the exhaust gases and the hot side of the thermoelectric generator: e.g., heat pipes (see Section 7.1), improved heat exchanger materials and/or design etc. For example, Kempf and Zhang [130] studied the use of silicon carbide (SiC) for the heat exchanger and found that it has a 25% higher efficiency than a stainless steel heat exchanger. In parallel, Jang and Tsai [131] studied the influence of heat exchanger wall thickness noting that increased thickness can favor axial heat conduction and the surface temperature distribution on the hot side. Other studies, like the one of Liu et al. [132] found that, if the hot side heat exchanger is placed between the catalytic converter and the muffler, the pressure drop is at its lowest and the temperature is uniformly distributed. In a different heat exchanger design study, Stobart et al. [96] started with an open-pipe design using computational fluid dynamics (CFD), but ended up adopting a plate-fin design, specific to that of exhaust gas recirculation coolers equipping heavy duty engines due to their respectively high power output (2–3 kW/kg). Using eight thermoelectric modules, the authors analyzed ten cases in terms of hot gas mass flows and temperatures, coolant mass flows and temperatures, as well as $Z\overline{T}$ values. Their design led to a 90% decrease in the pressure drop compared to a conventional exhaust gas recirculation cooler under normal operating conditions. The thermoelectric generator with plate-fin HX resulted in a power output of 139.1 W and a temperature gradient of 86.1 K as compared to the thermoelectric generator with open-pipe HX with only 13.3 W and 35.0 K. With respect to the use of fins for enhancing HX performance, He et al. [133] showed that the spacing and height of the fins have a greater influence than their thickness. Marvao et al. [134] arrived at a similar conclusion while also highlighting the importance of having a small fin thickness both from a thermal point of view and via thermoelectric generator net power output. Furthermore, the authors showed that heat exchanger optimization alone is not enough to achieve the maximum net power output, rather it must be combined with optimization of thermoelectric modules. In a different study, Karana and Sahoo [135] investigated the use of a twisted tape as a means of improving the heat transfer. They showed that geometric parameters, like the pitch ratio, twist ratio, and tilt angle have a significant influence on HX performance. Of the studied designs, the authors selected a pitch ratio of 8, twist ratio of 4, and tilt angle of 60°, for which they obtained a 0.65% improvement in the brake specific fuel consumption (BSFC). Other authors like Lou et al. [136] have sought to improve thermoelectric generator performance by using a convergent HX design. Using simulations, the authors concluded that for mass flows greater than 37.25 g/s, an inclination angle of 2° provides the optimum trade-off between the power output and pressure drop across the HX. With this design, the net power increase was 5.96%. A later simulation study of Lou et al. [137] further improved on the concept and achieved, at an inlet temperature of 500 K and a mass flow rate of 30 g/s, a net power increase of 20.2% over the conventional thermoelectric generator design. Another important aspect has been highlighted by Bou Nader [21] who found that, in addition to ensuring a sufficient and efficient supply of heat, heat exchangers must also allow for the expansion of thermoelectric modules with respect to their weight and occupied space and be dynamically stable. In this regard, there have been numerous studies for the improvement of heat exchangers covering design (geometry, size, and weight), materials, installation location, and cooling methods among other parameters.

Table 4 presents the results of several literature studies concerned with heat exchanger design and thermoelectric generators. It must be noted that not all materials used in these studies are directly suitable for the conditions found in the exhaust system of internal combustion engines (specifically the high temperature of exhaust gases). However, these studies can be useful to understand ways to obtain a more uniform temperature distribution when designing heat exchangers. Furthermore, considering that pressure drop is a significant concern in the exhaust of internal combustion engines, these studies can provide useful insight into what pressure drops are encountered by heat exchangers designed for thermoelectric generators.

7.1. Heat pipes

Heat pipes (Fig. 13) are solid state devices with a relatively high thermal conductivity (potentially higher than heat exchangers) used for transporting heat remotely with minimal losses. From a design point of view, a heat pipe is a metallic pipe sealed at both ends partially filled with a working fluid at near vacuum pressure. This causes the fluid to change phase at low temperatures. A heat pipe can be divided in three main sections: evaporator, adiabatic section, and condenser. Applying heat to the evaporator section causes the working fluid to evaporate and travel towards the condenser section. Since the condenser section is colder, this causes the fluid to condense back to liquid, which returns to the evaporator section through a wick using the capillary effect [24].

Heat pipes can be used with TEG systems installed on the engine exhaust pipe to: eliminate the need for a direct contact between the thermoelectric generator elements and the exhaust pipe (as a result, the installation location of the thermoelectric generator can be freely chosen [4]), improve heat extraction from the hot exhaust gases (reduced thermal resistance) while lowering the pressure losses, ensure a quasi-constant temperature of the hot side (see reference [150]), and improve uniformity of the temperature distribution. Consequently, effort can be redirected towards designing waste heat recovery systems with increased efficiency, without altering/redesigning the structure/build of the exhaust system.

The main issues associated with using heat pipes for exhaust gas waste heat recovery are [4,24]:

- Heat pipes have a maximum rate of heat transfer; hence, for high heat transfer rates, the system can become impractically large,
- Increased attention must be paid to the heat extraction side design to avoid high pressure drop values,
- The working temperature needs to be limited to avoid damage due to high pressure inside the pipe; for temperatures higher than 300 °C, fluids other than water need to be used and this can increase the cost significantly,

Table 4.
Literature studies of thermoelectric generator hot side heat exchangers.

Ref.	External shape	Internal structure	Material	Test conditions T_{gas} °C	w_{gas} m/s	Average interface temperature °C	Uniform temperature distribution	Pressure drop Δp kPa
[138]	Hexagonal-prism Plate-shaped	Maze-shaped baffles	Brass	300 sim.	20 sim.	120	ref.	N/A
		Fishbone-shaped baffles	Brass	300 sim.	20 sim.	>240	++	
			Iron	+ exp.	+ exp.	>200	+	
				300 sim. + exp.				
[87]	Plate-shaped	Parallel-fin-shaped baffles	N/A	300 sim.	15	~172	ref.	0
		Fishbone-shaped baffles		+ exp.	15	~177	+	0
				300 sim. + exp.				
[139]	Rectangular	Square with fins	Al	300 sim.	12	~200	-	N/A
		Square with fins + slopping block		+ exp.	12	~240	+	
				300 sim. + exp.				
[132]	Plate-shaped placed after, between and before TWC	Two small fins at inlet and small fins disorderly set further back	N/A	350 sim.	20	210	ref.	ref.
				+ exp.	20	270	+	127
				350 sim.	20	280	++	695
				+ exp.				
				350 sim. + exp.				
[140]	Plate-shaped	Fishbone-shaped	N/A	400 sim.	20	~295	ref.	N/A
		Accordion-shaped		+ exp.		~287	-	
		Scatter-shaped		400 sim.		~278	–	
				+ exp.				
				400 sim. + exp.				
[141]	Plate-shaped	Fishbone-shaped baffles	Brass	350	15.2	~244	ref.	N/A
		Chaos-shaped baffles				~252	+	
[142]	Plate-shaped	Scatter-shape inserted fins	Brass	290 sim.	~20	~214	ref.	1.697
		Dimpled surface				~215	+	1.348
[143]	Rectangle	Empty cavity	N/A	400 exp.	N/A	N/A	ref.	ref.
		Muffler like structure with pipes, 1 in, 2 out					-	1.004
							+	2.157
		Muffler like structure with pipes, 2in, 2 out						
[144]	Rectangle	Empty cavity	Al	~519	17	N/A	ref.	0.045
		Bafflers at 10°		exp.			++	0.067
		Bafflers at 20°					+	0.113
		Bafflers at 30°					+	0.251
		Bafflers at 40°					-	0.675
[2]	Rectangle	Waffle type labyrinth	N/A	300 sim.	20	~250	ref.	1.2
		Offset strip fins	N/A	N/A	N/A	N/A	-	2
[145]	Rectangle longitudinal	Fins	Cu	550	N/A	N/A	ref.	0.268
	Rectangle transversal						+	0.182
	Hexagonal						–	0.775
	Cylindrical						-	0.753
[146]	Rectangle	Fishbone, Config. 1	N/A	500	N/A	299.6	ref	1.29
		Fishbone, Config. 2				296.2	-	0.91
		Fishbone, Config. 3				294.8	+	0.78
[147]	Rectangle	Cylindrical grooves	N/A	400	N/A	117.83	-	1.300
		Random distributed inserted fins				127.83	ref	2.187
		Empty cavity with 2 deflectors				110.3	–	1.190
[148]	Rectangular octogon	Fishbone type 1	Brass	340 sim.	20	229.6	ref	N/A
		Fishbone type 2				227.9	+	
		Clip type fins				228.4	+	
		Labyrinth type fins				240.2	++	
[149]	Octagon	Empty cavity	N/A	327 sim.	22.6	209	ref.	N/A
		Parallel fins				265	+	
		Perpendicular fins				255	+	
		Skewed fins (streamwise arrangements)				271	++	

ref – represents the reference heat exchanger for the study. For all other heat exchangers "+" marks an improvement while "–" a decrease compared to the reference case.
N/A – not available

- Designing heat pipe systems is a complex process that must consider system particulars,
- Due to the unsteady nature of internal combustion engine operation, it is not possible to ensure high exhaust gas temperatures and mass flows in all cases; this leads to areas with decreased efficiency as compared to classical systems,
- Added weight of the heat pipes, which ultimately reduces the net output of the system.

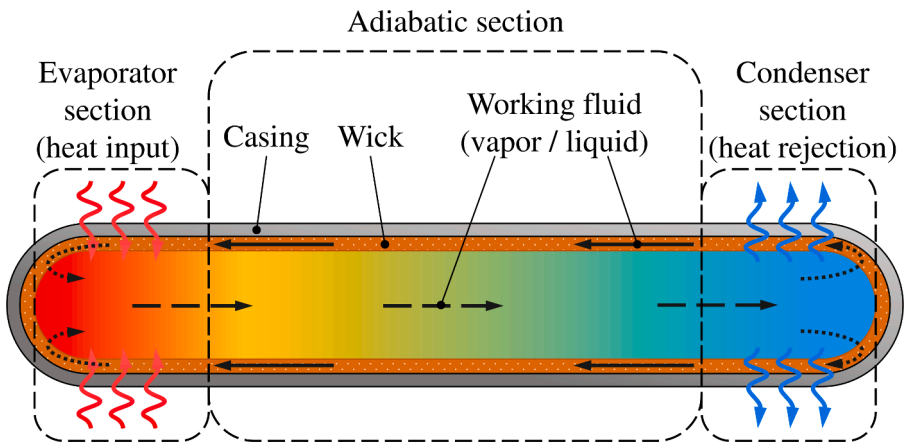

Fig. 13. Heat pipe working principle.

With respect to the use of heat pipes and TEG systems, Cao et al. [151] showed, both experimentally and through simulation, that TEG system efficiency increases, especially for high exhaust gas temperatures and mass flows. The authors were able to achieve an efficiency of 2.58% for a temperature of 300 °C and a mass flow of 80 kg/h. To control the heat transfer temperature, Brito et al. [152] designed and tested a variable conductance heat pipe. The authors added an expansion tank to control the pressure inside the pipe, and consequently the fluid boiling temperature. By controlling the pressure, the authors modulated the active length of the condenser that causes thermoelectric modules to operate at optimal temperatures. Using a Yanmar L100N DI compression ignition engine and a thermoelectric generator with 12 bismuth telluride modules, the authors were able to extract approximately 38 W at a heat pipe temperature of approximately 168 °C and a cold side (water cooled) temperature of approximately 28 °C. In contrast, Jang et al. [153] proposed a different design with a wickless loop heat pipe (loop thermosyphon) for waste heat recovery in hybrid vehicles. In their effort, the evaporator section (designed with fins to improve heat extraction) is placed inside the exhaust pipe; whereas, thermoelectric modules are placed between the plate-shaped condenser section (made of copper) and an aluminum block cooled with air. The authors found that the power output of this solution is lower than that of a system installed directly on the exhaust pipe with convective heat transfer, but it has the advantage in that it can transfer heat to remote locations; thus, bypassing the space limitations. The authors have also analyzed the influence of the volume of working fluid on the system output. Of the analyzed cases (20, 30, 40 and 50% filled volume of the total volume), they found that the best performance is obtained when the working fluid fills 30% of the total available volume. In a more recent study, Pacheco et al. [154] embedded corrugated exhaust pipes and variable conductance heat pipes (to act as a thermal spreader) in a cast aluminum matrix. The authors simulated the output of the TEG system (with 64 commercially available thermoelectric modules – GM250-49-45-25 in the first case and GM250-127-28-10 in the second case) installed in a generic light-duty vehicle (1400 kg, 1.6 L engine with 118 hp) under two cycles: a custom highway cycle and a standard WLTC Class 3 cycle. The results showed that, at high exhaust gas inlet temperatures, the setup can offer an improved temperature distribution, protection of the thermoelectric modules against overheating, as well as high power outputs (888 W for GM250-49-45-25 and 1536 W for GM250-127-28-10). The main disadvantage was the high pressure drop across the thermoelectric generator, but this can be solved by utilizing a by-pass valve. Finally, the authors estimated 5.4% savings in fuel consumption and CO_2 emissions over the highway cycle and 4.2% over the WLTC Class 3 cycle.

7.2. TEG systems with phase change materials

In general, optimal performance of a thermoelectric generator is strongly linked to a quasi-constant temperature on the hot side. This is difficult to obtain for internal combustion engine waste heat recovery applications due to its unsteady nature. This can be partly compensated by using systems with phase change materials (PCMs). The operating principle of a phase change material can be described as follows: when a respectively high temperature is supplied, the material starts to melt/vaporize, thus storing thermal energy; as the temperatures drops, the material needs to release heat to solidify/liquify again. The main criteria for choosing an appropriate phase change material are highlighted in [155] and include: type of phase change (solid-liquid or liquid-gas), phase change temperature (application specific), amount of stored heat, heat conductivity, volume variations during phase change, specific cost of phase change material, and environmental impact. Furthermore, Huang et al. [156] showed that it is important to consider a longer heating duration when including phase change materials in the thermoelectric generator design.

Using this principle in thermoelectric generator applications, heat can be extracted from the hot exhaust gases and stored in the phase change material as internal energy. When the temperature of the exhaust gases decreases, the phase change material releases heat on the hot side of the thermoelectric generator, thus leading to a quasi-constant temperature (it must be noted that the damping depends on the phase change material accumulator's thickness [157]). Furthermore, the phase change material can provide thermal protection in case of temperature extremes that could damage the thermoelectric generator [4, 155]. For example, Klein et al. [155] experimentally showed the benefits of using a phase change material in conjunction with a thermoelectric generator. For an inlet temperature variation between approximately 420 and 920 °C, the hot side temperature of the thermoelectric module varied in the interval of 350–410 °C. Furthermore, the authors showed (through simulation over the Artemis motorway cycle) that the PCM-TEG setup can be 29% more efficient than a conventional thermoelectric generator. Other authors, like Zhao et al. [158] used simulations to show that heat could be provided to the thermoelectric modules by boiling and condensation of a fluid, which is itself heated by the exhaust gases. This solution has the advantage of a limited hot side temperature, thus avoiding overheating of the thermoelectric modules.

Finally, if the stored heat in a phase change material is not converted to electrical energy, it can be used to heat the engine coolant and/or the lubricating oil of the internal combustion engine or battery pack (in case of hybrid vehicles) that ultimately leads to lower pollutant emission values and increased durability.

7.3. Analysis of heat extraction and temperature distribution on the hot side

The hot side heat exchanger of the thermoelectric generator influences both the operation of internal combustion engine, due to the increased backpressure, as well as the heat flow to the thermoelectric modules. Furthermore, it also limits the possible installation locations of the thermoelectric generator. Research efforts to counteract the downsides and to increase the amount of heat extracted from the heat sources are essential for improving overall benefits of the TEG system. This requires low impact solutions with low thermal resistance. Heat pipes solve the limitations with respect to the installation position, but they require lightweight design, increase of operating ranges and reduction of costs. One promising solution, but which requires further development is the use of phase change materials. This direction should be pursued since it offers the possibility to provide not only thermoelectric generator protection at high operating temperatures, but also a quasi-constant and uniform temperature distribution.

8. Heat rejection on the cold side

8.1. General considerations

To ensure a high heat flux through the thermoelectric generator, heat rejection on the cold side is critically important. In their study, Hendricks [55] determined that, for an optimized power output, the cold side heat exchanger needs to have a thermal resistance 10–30 times lower than the hot side heat exchanger. In general, there are three fluids commonly used in literature (see for example Tables 6 and 7) for cold side cooling: air, water, and engine coolant. Each of these has its benefits and downsides as presented in Table 5 [4]:

The main issue with air cooling is the low convective heat transfer coefficient of air which does not allow for a sufficiently low temperature on the cold side, thus impacting thermoelectric generator performance. For example, Elghool et al. [159] determined the maximum limiting heat flux for air cooled thermoelectric generators (air speed variation 0 to 5 m/s) varied between 40.3 and 76.7 W/m^2. Water cooling involves the issue of additional equipment to ensure the flow of water (tank, pump, pipes, and radiator) and consideration of the space required. In comparison, using engine coolant requires a redesign of the engine cooling system to avoid possible engine damage (due to an increased thermal stress on the system) and a decrease in performance; hence, demanding more power from the coolant pump. Here, it was proven via experimental measurements [105] that by maintaining the temperature of the coolant around 80 °C, with a flow of 0.2 kg/s, and a difference of around 50°C between the hot and the cold side, the generated power can vary between 178 and 224 W, when using GM250-127-28-10 thermoelectric modules on the non-road transient cycle (NRTC). In a different type of study, Lei et al. [160] analyzed the optimum flow rate of the coolant to achieve maximum performance with respect to pump energy consumption, thermoelectric generator output power, and exhaust backpressure. Their investigation showed that the optimum coolant flow rate depends on the temperature gradient across the thermoelectric modules.

Table 5
Advantages and disadvantages of different cooling methods for heat rejection on the cold side.

Fluid	Advantages	Disadvantages
Air	• Low cost • Simple design / structure • Limited effect on engine performance	• Low heat transfer rates • Relatively large power consumption (when using fans)
Water	• High heat transfer rates • Limited effect on engine performance	• Additional space required • High cost • Increased complexity
Engine coolant	• High heat transfer rates • Does not require additional devices	• Engine cooling system must be redesigned

8.2. Analysis of heat rejection

Like the extraction of heat from the exhaust gases, heat rejection is of equal importance for achieving high system performance considering the dependency of the power output on the heat flux through the thermoelectric generator. However, there are only a limited number of studies endeavoring to cover cooling facets (i.e.., cooling method, additional losses, etc.) of thermoelectric generation. As described in the previous section, as well as in Section 10, the findings illustrate that the currently employed cooling methods (with water, engine coolant or air, each with its own advantages and disadvantages in terms of cooling performance, complexity, and parasitic losses) are directly linked to the cooling processes of internal combustion engines. Furthermore, it was found that the solutions are not suitable for all applications and they need to be application specific (i.e., passenger car, heavy-duty vehicle, stationary engine, etc.). Consequently, a possible research direction would be the development of a dual cooling system (with low parasitic losses) that is able to adapt to vehicle operating conditions (e.g., city traffic or traveling at constant speed on the highway). It is also necessary to analyze the potential of solutions proposed for other applications like refrigerant cooling for battery thermal management in hybrid-electric vehicles [161]. Finally, instead of rejecting the heat to the environment, this energy could be stored in phase change materials for later use (e.g., cold starts) to further improve the overall efficiency.

9. TEG system output

9.1. General considerations

The output of a thermoelectric generator depends on several factors, such as the number of thermocouples in the module, the number of modules, the configuration/connection of the modules, the thermoelectric materials properties, and the temperature gradient. Building on Section 5.1 (Eqs. (15, 16)), the power output of one thermoelectric module (P_{TEM}) [3] can be written as:

$$P_{TEM} = \underbrace{\Big(\underbrace{\alpha \cdot \Delta T}_{open\ circuit\ voltage} - IR_{TEM}\Big)}_{output\ voltage} I = \alpha(T_{hot} - T_{cold})I - I^2 R_{TEM} \tag{25}$$

where I [A] is the current flow and R_{TEM} [Ohm] the internal resistance (see Section 5). Since the power output depends on the temperature gradient between the two sides of the thermoelectric module, it can be deduced that it is desirable to increase ΔT. However, one must also consider the Peltier effect and Joule heating (see Section 2) which can negatively affect thermoelectric module operation. This makes it desirable for thermoelectric modules to operate with lower current values.

Theoretically, the power output of a TEG system (P_{device}) is the sum of the individual power output of each thermoelectric module (P_{TEM}- Eq. (25)) and can be expressed as:

$$P_{device} = \sum_{i=1}^{n_{TEM}} P_{i,TEM} = \sum_{i=1}^{n_{TEM}} \frac{(\alpha_{i,p} - \alpha_{i,n})^2 \cdot (T_{i,hot} - T_{i,cold})^2}{R_{i,Load}\left(\frac{R_{i,TEM}}{R_{i,Load}} + 1\right)^2} \tag{26}$$

where i is the ith thermoelectric module, n_{TEM} the total number of thermoelectric modules, and R_{Load} the external load.

Furthermore, the dynamics of the generated power are proportional to the rates of change of the temperature gradient input (see Section 6.1). Consequently, when modeling a TEG system, the associated thermal time constants need to be considered. This issue is addressed by using appropriated control algorithms to accurately track the maximum

power point (MPP) during transient phases. One significant challenge that needs to be addressed by the control method is the interaction between the convertor MPP set-point and the parasitic Peltier effect, since the latter causes a slow temperature change response on both the hot side and the cold side of the thermoelectric generator (e.g., such delayed responses have been reported by Luo et al. [162]). In turn, this leads to a gradual temperature gradient change and affects system power output. Overall, thermoelectric generator current response is on the order of nanoseconds; whereas, the thermal effect can take up to a few minutes to manifest [85].

For engine exhaust thermoelectric generators, adding more thermoelectric modules does not necessarily increase the power output due to two reasons [4]:

- Thermal resistance and the corresponding temperature difference between the two sides of thermoelectric modules (Eqs. (17, 18)) decrease along the exhaust pipe affecting the individual power output as a result of the sandwich arrangement between the hot and the cold side, as well as the parallel thermal connection;
- Temperature along the exhaust pipe and, consequently, the temperature of the hot side of consecutive thermoelectric modules decreases due to heat extraction and losses. Furthermore, there is an uneven distribution of temperature between adjacent thermoelectric modules causing these to operate at different voltage-current points, which in turn leads to a decrease in generated current, voltage, and power along the flow direction. The employed connection mode leads to a power loss and to *internal losses*, where the total power output of the system is less than the sum of the individual thermoelectric module output.

Stevens et al. [9] developed a model that estimates the theoretical limit of the maximum power output of a thermoelectric system in contact with a hot stream by using a variational model. The model predicts an optimum number of thermoelectric modules that can be used to generate the maximum possible power of any system. The optimum number of thermoelectric modules is influenced by several factors like the temperature and mass flow rate of the exhaust gas, the heat extraction/dissipation ability of the hot/cold side etc. In another study, Li et al. [163] demonstrated that there is an optimum number of thermoelectric modules that provides the maximum power output. The authors highlighted the importance of their optimization process (a 3-step process), which led to an 53.05% and 110.07% increase in power output and conversion efficiency, respectively, as compared to the initial design.

Different thermoelectric generator designs, optimized heat exchangers and operating strategies have been studied for the purpose of reducing the internal losses and lowering the thermal resistance between the exhaust gases and the hot side of the thermoelectric generator. Another factor that needs consideration is the pressure drop, which should be lower than 15-40 kPa to avoid impairing engine operation. Furthermore, when analyzing the temperature distribution of heat exchangers used in TEG systems with the aid of simulations, thermoelectric modules must also be included [143,144].

Alghoul et al. [21] identified several elements affecting the output of thermoelectric generators:

- Heat exchanger (or stabilizer)
  - captures energy and transfers it to the thermoelectric module;
  - acts as a thermal spreader, meaning that it must provide a uniform distribution of temperature for the hot side of the thermoelectric module;
- Interfaces (between thermoelectric module and the hot and cold sides)
  - critical importance since they define the contact thermal resistance;
- Contact pressure
  - influences the operation of the module since, if the applied pressure is not evenly distributed and/or is too large, this can lead to a deformation or even permanent damage of the module, thus causing a non-uniform temperature distribution and consequently, poor performance;
- Insulation
  - clamping method has a significant influence on parasitic heat losses;
- Cooling
  - passive or active; passive cooling is done using natural air convection (metal plate, finned heat sink) and/or heat pipes; active cooling is using a forced air/water/coolant cooling with the aid of a fan/pump;
  - influences the amount of heat that can be rejected on the cold side and ultimately the cold side temperature, thus being of critical importance for the device efficiency;
  - for most applications active cooling is preferred since it allows for a larger heat flux compared to passive cooling.
- Thermoelectric module integrity
  - extracting the maximum power from a thermoelectric module is possible by choosing an optimum ratio between the external load resistance and its internal resistance, the latter being a function of temperature;
  - the external and internal resistances are equal when the load voltage is half of the open circuit voltage, the latter being measurable by breaking the circuit;
  - the resistor voltage can be measured once the thermoelectric module temperature is stabilized and the external load resistor is connected;
  - matching loads corresponding to the optimal power output can be linked in series;
  - after the load has been connected, the value of the temperature difference between the hot and the cold side of the thermoelectric module decreases due to the Peltier, Thomson, and Joule effects.

Ultimately, the authors identified four factors that cause the low levels of extracted power:

- Low value of the temperature gradient between the hot and the cold sides;
- Immature thermoelectric module integrity;
- Inaccurate measurement of the temperature difference (in some cases);
- Improper selection of thermoelectric modules.

To achieve maximum performance (power and efficiency), a good design and control algorithm are required. Currently, there two main directions for thermoelectric generator optimization, namely maximum power point tracking and maximum efficiency point tracking. According to the maximum power transfer theorem, power is maximized when $m = 1$. Conversely, the maximum efficiency condition is $m = \sqrt{1+Z\overline{T}}$. Considering $m = 1$, for a single module this leads to:

$$R_{TEM} = R_{Load} = R$$
$$P_{max} = RI_{Load}^2 = \frac{(\alpha\Delta T)^2}{4R} \tag{27}$$

For a TEG system with n_{total} modules Eqs. (26, 27) become:

$$R_{Generator} = R_{Load} = \frac{n_{series} \cdot R_{TEM}}{n_{parallel}} = R$$
$$P_{max,\,generator} = RI_{Load}^2 = \frac{n_{total}(\alpha\Delta T)^2}{4R} \tag{28}$$

For a given temperature gradient, thermoelectric generator outputs the maximum possible power (Eq. (28)) for the load when:

$$V_{Load} = \frac{1}{2}V_{OC} \text{ or } I = \frac{1}{2}I_{SC}$$

where I_{SC} is the short-circuit current.

However, Baranowski et al. [164] show that during the design stage it is possible to achieve both maximum power and maximum efficiency, provided that the thermoelectric module leg length is a design variable. Considering a constant property model (CPM) generator, the authors prove that the electrical condition for maximum efficiency is also the condition for maximum: power, power density, power/cost of thermoelectric material, and power to weight ratio of thermoelectric material. Achieving maximum power output and maximum efficiency at the same operating point of the CPM generator requires that $m = \sqrt{1+\overline{ZT}}$. Compared to $m = 1$ the result is an improved generator that has better performance and is lighter while having a lower material cost. Based on their calculations, achieving maximum thermoelectric generator performance requires optimizing thermoelectric generator geometry, electrical operating conditions (current and load resistance), and heat exchanger design.

There are various solutions proposed to solve the connection mode issue, each with its advantages and disadvantages:

- Distributed MPPT (DMPPT) – this means individual control of each module or, in other words, a MPPT power converter for each module. The downsides of this solution are the added size, cost, weight and complexity;
- Differential power processing (DPP) – power convertors are connected to neighboring modules. Compared to the DMPPT solutions, this needs one less converter;
- Removal and revival method – Chen [120] proposed and tested the removal from the array of thermoelectric modules working under lower temperature gradients. More specifically, when the temperature gradient of some thermoelectric modules decreases so that the system would produce more power without them, these are removed from the array. If the temperature gradient increases enough to increase the power output of the complete system, the removed thermoelectric modules are reconnected. The removal or revival of the thermoelectric modules is determined based on the predicted behavior (which is dominantly determined by temperature) of thermoelectric module models [165];
- Dynamic TEG reconfiguration – using measured data an algorithm developed by Baek et al. [121] seeks to find the optimal thermoelectric module array configuration (series and parallel connections) for the current condition. The optimal configuration is changed dynamically with the aid of a reconfigurable switch network.

Various authors have studied the effect of electrical configuration (connection modes) of thermoelectric modules on system output. During operation, individual thermoelectric modules are subjected to different temperature gradients or, in other words, they are working under a thermal imbalance condition (uneven temperature distribution) that leads to dissimilar outputs. Thermoelectric modules with lower power output will consume power from thermoelectric modules with higher power output and, as a result, the system output will be lower than the sum of individual outputs (Eq. (26)). Furthermore, the wiring and connectors used contribute to an increase in electrical resistance, thereby reducing the total power output.

In this area, Montecucco et al. [129] studied the electro-thermal effects occurring in arrays of three thermoelectric modules connected in series and parallel when individual modules are subjected to different temperature gradients (100, 150, and 200 °C). They found that series connections lead to lower values of Joule heating losses as compared to parallel connections. This could be associated with the lower current values found in series connections. The temperature mismatch created for the experiments led to a power reduction of 9.22% for the series connection and 12.9% for the parallel connection as compared to the sum of individual power outputs.

Other efforts by Vadstrup et al. [166] studied power losses for both connection modes using four thermoelectric generators. The authors used the MPPT algorithm applied at both stack and module level. The authors found that, when the conditions are the same (for example the modules are subjected to the same temperature gradient), applying MPPT at the stack level does not have any downsides in terms of power output in comparison to the case where it is applied at module level. If, however, there is a temperature difference, the authors noted a maximum decrease of 8.4% in power output for the series connection and 16.7% for the parallel connection when MPPT is applied at stack level instead of the module level.

Negash et al. [128] tested eight different electrical configurations of thermoelectric modules on thermoelectric generator power output. Their experiments showed that system output can decrease by more than 41% as compared to the reference power output determined by summing individual thermoelectric module outputs (34.2 W). For a constant inlet temperature, the authors noted that the number of junctions in the circuitry and an unbalanced number of thermoelectric modules in the arrays also decreases the power output of the system. For the series configuration, the power output decreased by 6%; whereas, for the parallel configuration, the system generated 11.5% less power. By balancing the number of thermoelectric modules in the arrays and minimizing the number of junctions, power losses were reduced to 4.6%.

Overall, the main idea that can be drawn from these results is that connecting the modules in parallel causes higher power losses.

9.2. Analysis of TEG system output

The output of a TEG system depends on more than just the thermoelectric modules. It is also influenced by the connection modes, the overall design of the thermoelectric generator, as well as the control algorithm. Based on a critical analysis of the literature in this section it can be concluded that efforts are still required to identify solutions with low overall dimension and high reliability for optimizing thermoelectric generator operation with respect to the operating conditions. More specifically, these solutions should be able to remove low performance thermoelectric modules (either due to the lower temperature gradients, or potential failure) from the grid, to reconfigure the connections without causing parasitic losses, and finally to solve the issue of the optimum number of thermoelectric generators with respect to the operating point and/or application.

10. Experimental and simulation results concerning thermoelectric generators in automotive applications

10.1. General findings

With the current emphasis on electrified vehicles [167,168], direct conversion of waste heat into electrical energy could provide a strategic advantage for automobile manufacturers. Studies like the one performed by Dabadie et al. [169] have shown possible improvements in fuel consumption for all considered cases (diesel hybrid electric vehicle (HEV), gasoline HEV, and Compressed Natural Gas HEV) at -25, -7, 20 and 35 °C over four cycles (NEDC, Urban, Road, and Motorway). Oetringer et al. [170] analyzed the potential of thermoelectric generator in HEVs and showed that it is possible to obtain a 3% improvement in fuel consumption over all ECE R101 test cycles (3.018% for WLTP). In addition, under optimum driving conditions, the power output of a thermoelectric generator can be increased as compared to a conventional vehicle since the engine load grows in HEV applications; thus, providing respectively high exhaust gas temperatures. Wang et al. [171] compared three mild hybrid cases: without thermoelectric generator, with thermoelectric generator, and with a thermoelectric generator and refined mode transition strategy between three possible modes (engine-only, charge, and hybrid mode). The authors found that the

thermoelectric generator can help improve fuel consumption by up to 3.64% on the Urban Dynamometer Driving Schedule (UDDS) driving cycle and 2.17% on the Environmental Protection Agency (EPA) Highway Fuel Economy Test Cycle. Hussain et al. [172] performed a numerical study on a 2.5 L gas-electric hybrid vehicle after determining the optimal thermoelectric generator design with respect to channel length, channel number, channel width, and thermoelectric layer thickness. They found that it is possible to generate 300 to 400 W of electric power, which is sufficient to improve fuel economy – provided that the back-pressure offset is kept at minimum. Kim et al. [173] investigated both experimentally and through simulations the potential of using a thermoelectric generator with heat pipes to transport heat from the hot exhaust gases to the hot side surface of the thermoelectric generators as a means of improving hybrid vehicle efficiency. The authors found that, for a hot side temperature of 170 °C and a cold side temperature of 22.5 °C, it is possible to recover up to 350 W. In this case, the offset due to the added system weight (51.5 kg) was not considered. Fang et al. [174] reported a 14.7% improvement in NEDC cycle fuel economy for the integrated starter-generator (ISG)-type hybrid electric vehicle with thermoelectric generator installed on the exhaust pipe over the conventional system for a 2.0 L engine. Deng et al. [175] compared three vehicle models: a conventional internal combustion engine, an ISG-type 42-V, and an ISG-type 42-V with TEG model. Both hybrid models showed significant improvement over the conventional internal combustion engine model both in terms of fuel consumption (~7% for ISG-type model and ~8.3% for the ISG-type with TEG model) and pollutant emissions (32.2% HC, 37.4% CO, and 38.5% NO for ISG-type model and 32.2% HC, 37.6% CO, and 40% NO for the ISG-type with TEG model) over the NEDC. Lan et al. [176] investigated the potential of a thermoelectric generator to improve fuel consumption for a mild hybrid vehicle. After validating the model against experimental and literature data, it was found that for the NEDC cycle the amount of energy recovered varies between 80 and 200 W, which translates into a 3.4% fuel economy benefit (approximately 253 € over the vehicle lifetime). The authors also estimated an annual reduction in CO_2 emissions of 39.4 kg. Muralidhar et al. [177] simulated the benefits of installing a thermoelectric generator on a hybrid electric bus using real world engine operating parameters (speed and torque). They estimated that fuel consumption can be lowered by 7.2% for a Skutterudite-based thermoelectric generator and by 6.5% for a silicon germanium-based thermoelectric generator over the Nuremberg cycle. In a recent study, Nader [97] studied the possibility of replacing the internal combustion engine range extender of an hybrid electric vehicle with an auxiliary power unit using a thermoelectric generator as energy converter. Several designs were analyzed and the most promising design was found to be a two-stage recuperator reheat thermoelectric generator, which was able to achieve an efficiency of 39%. The simulation results showed that in both modes (Plug-In and Self-Sustaining), the fuel consumption decreased by approximately 7.7% as compared to an internal combustion engine baseline. Finally, Sulaiman et al. [178] devised an experiment to show that it is possible to use a thermoelectric generator even for energy recovery in Proton Exchange Membrane (PEM) fuel cells. Using a 2 kW open-cathode PEM fuel cell and a single thermoelectric module, the authors achieved a peak output of 218.79 mW for a hot side temperature of 36.7 °C and a temperature gradient of 7.7 °C. Other relevant findings found in literature are presented in Tables 6 and 7 and the results have been split in experimental and simulation findings.

10.1.1. Main findings for experimental results

For the efforts presented in Table 6, most tests were performed in the laboratory, either with engines (approx. 57%) or using test benches (approx. 23%), while the remaining 20% were performed using vehicles. Furthermore, only a few vehicle tests were done under real driving conditions. Considering the variations in atmospheric conditions (pressure, temperature, humidity), vehicle/engine operating conditions due to traffic, road grade, etc., as well as the effects of adding the generated power into the electrical system of the vehicle, some aspects of thermoelectric generator operation are not included. For example, road induced vibrations can cause interface failures and the possibility of using the relative speed between the vehicle and the surrounding air can generate an added cooling effect. The preferred thermoelectric material, used in more than 70% of studies, was Bi_2Te_3 (Fig. 14). Other materials, like PbTe, half-Heusler, and $SnTe_{1-x}Se_x$ were also used. The laboratory tests illustrate possible fuel improvements of approximately 1 to 7.38%; however, only two of the presented efforts provided the parasitic losses which varied from 20 to 50 W. Hence, more focus should be placed on highlighting all aspects of energy flows, both positive and negative. Based on the data reported in Table 6, laboratory tests indicate significantly higher efficiency values as compared to vehicle results. This could be attributed to the fact that unlike on-road testing, where the engine usually operates under transient conditions, laboratory testing involves operating the engine under steady state conditions and disregarding the additional mass of the system. This issue could be solved by employing hardware-in-the-loop testing with and without the thermoelectric generator.

In terms of system power output, this varied greatly (from 0.8 to 1002.6 W), depending on the number of thermoelectric modules (ranging from 1 to 458). Considering the values reported by the authors, it was found that the power ranged from 0.80 to 9.83 W/TEM, with a maximum specific output of 41.6 W/kg. Analyzing Fig. 14 and considering the operating ranges, it appears that Bi_2Te_3 remains the most promising solution, but only in the low temperature range (up to approx. 250 °C). The preferred medium of cooling employed water or coolant, with only a few efforts reporting air as the cooling fluid. One potential extension of this work could be to investigate Diesel Exhaust Fluid as a possible cooling medium for compression ignition engine-based studies. Another possible solution that requires investigating is the use of refrigerant cooling, since it does not depend on engine type. In contrast with the laboratory tests, the efforts covering vehicle tests reported fuel consumption improvements of 0.25 to 4.00% and one case of increased fuel consumption (in all cases where the speed was below 110 km/h). For the analyzed cases, the outputs varied between 0.6 and 618.0 W, depending on the number of thermoelectric modules (ranging from 1 to 240). Furthermore, it was found that the power ranged from 0.6 to 28.13 W/TEM, with a maximum specific output of 11.25 W/kg. Unfortunately, only a few of the efforts provided a cost-to-power ratio, which makes it difficult to compare the cost of thermoelectric generation to current fuel prices. Hence, it is important to also provide the cost analysis for the break-even point between adding a TEG system and the time required to recover the investment (due to a reduced fuel consumption) to be highlighted.

10.1.2. Main findings for simulation results

For the efforts presented in Table 7, it was found that the used simulation application/environment varied greatly: COMSOL, Matlab-Simulink, FloTHERM, ADVISOR, ANSYS-CFX, and other. The input data for thermoelectric generator models were obtained either using an internal combustion engine simulation environment (e.g., AVL Boost and GT-Power) or from experiments. Like the experimental testing of thermoelectric generators, the material of choice in more than 50% of studies, was Bi_2Te_3 (Fig. 15). The rest of the studies concentrated their efforts on half-Heuslers, skutterudites, PbTe, $SnTe_{1-x}Se_x$, SiGe, and others. The simulation tests findings illustrate possible fuel improvements of up to 11%; thus, highlighting a significantly greater benefit than real-world testing scenarios. There are several aspects that result in this enhanced benefit of thermoelectric generators in a simulation environment:

- electrical and thermal properties are estimated based on average p-type and n-type legs values,
- heat radiation, air gaps between the thermoelectric module legs and/or the Thomson effect are neglected,

Table 6
Review of literature results – experimental results.

Ref.	Goal	Method Exp./ Sim.	Description	ΔT [°C]	Test bench / engine (lab. / vehicle)	TEG system design TEM / material	No. of TEMs	Syst. mass [kg]	Structure on the hot side	Cooling method	Power Output [W]	Parasitic losses [W]	Eff. / FC gain [%]
[6]	Investigate the possibility of replacing the alternator with TEGs and an economic analysis	Sim. + Exp.	Experimental test on a 1.9 L TDI engine with the TEG installed at approx. 2 m from the turbine outlet	~175	Engine (lab.)	HZ-14	8	-	Longitudinally finned stainless steel	Chilled coolant	68	-	3,88 – 7,38% (FC)
[2]	Test the recovery potential of a TEG installed in the exhaust system of a single cylinder engine	Sim. + Exp.	Experimental test on a single cylinder 4 stroke engine Fuels used: Diesel, B5 and B10	-	Engine (lab.)	TEG1-12610-5.1	20	-	Waffle heat exchanger with 2 × 5 TEG mounted on each side	Water	Max 72 (for Diesel) Max 80 (for B5) Max 86 (for B10)	-	2.28 – 2.4% (for Diesel) 2.36 – 2.61% (for B5) Max 2.46 – 3% (for B10) (conversion efficiency)
[179]	Measure the vehicle wasted heat (brake disc and exhaust) and experiment on a TEM in the lab. Use fuzzy logic algorithm to produce the extra data for various conditions.	Exp.	Experimental test on a vehicle (make and model not mentioned) with data from the exhaust and brake disc for highway and city driving	-	Vehicle (model not mentioned)	TEG SP1848	1	-	Measurement on one TEM, in a testing lab, on a test bench	Water	0.6 – 0.9 (TEG on disc) 2 – 2.5 (TEG on exhaust)	-	-
[124]	Fabricate a TEG prototype that replaces the radiator of an internal combustion engine	Exp.	Experimental test on a 2.0 L diesel engine, mounted on a test vehicle driving at 80 km/h.	25	Test vehicle with diesel engine, front wheel drivetrain and electric power brake system	Bi_2Te_3	72	-	80mm x 250mm x 740mm prototype TEG system	Chilled coolant	75	-	10% TEG efficiency 0.4% overall efficiency
[180]	Create an experimental testing bench for TEMs	Exp	Two testing benches were created, one for small scale 4-6 TEMs and one for 100 TEMs, with controlled temperature hot and cold sides.	125	Experimental testing bench	TG12-4	Case 1: 4-6 Case 2: 100	-	TEMs were sandwiched between aluminum fluid channels containing a hot and cold heat transfer fluid	Water	Case 1: 8-12 Case 2: 130	-	4.1%
[181]	Proof of concept of a lightweight heat exchanger design (made of sheet metal) with integrated modules	Exp.	Test bench with a diesel hot-gas generator, and the operating temperatures between 600°C and 700°C for PbTe and between 400°C and 600°C for Bi_2Te_3.	400	Experimental testing bench	1. PbTe 2. Bi_2Te_3	20	4.3-5.8	TEMs were mounted on a brazed exhaust system.	Water	1. 2.25 – 4 (temperature dependent) 2. 1.8 – 3.9	-	-
[151]	Design and test a heat pipe assisted TEG prototype	Exp.	Test bench with an electric heater that was used to heat the air. Experiments were done on two	max. ~280	Experimental testing bench	Bi_2Ti_3 (TEP1-142T300)	36		TEMs were sandwiched between alternating hot and cold layer.	Water	6.5 -13 (for 300°C on the hot side and cold water flow rate of 50 L/h)	-	2.58

(*continued on next page*)

Table 6 (*continued*)

Ref.	Goal	Method Exp./ Sim.	Description	ΔT [°C]	Test bench / engine (lab. / vehicle)	TEG system design TEM / material	No. of TEMs	Syst. mass [kg]	Structure on the hot side	Cooling method	Power Output [W]	Parasitic losses [W]	Eff. / FC gain [%]
			prototypes, with and without heat pipes. Temperatures varied between 100-300°C and coolant (water, 18.4°C) flow rate between 10-50 L/h										
[182]	Test a TEG with custom TEMs and plate-type porous medium with different porosity	Exp.	Experimental test on a 6-cylinder turbocharged diesel engine, with the TEG mounted on the exhaust. Experiments were done at 1000, 1200 and 1400 rot/min.	-	Engine (lab.)	Bi_2Te_3	30	-	Fabricated TEG was installed in the middle of the tailpipe of the engine at a distance of 1.5m from the engine exhaust manifold.	Water	98.3 @ 1400 rot/min, for the plate with the lowest porosity (0.121).	-	2.83% @ 1400 rot/min, for the plate with the porosity of 0.461 (second highest porosity).
[101]	Comparative study between TEG and Electric Turbo-Generator (eTG)	Exp.	Two engines were used, with TEG and eTG mounted to determine the electrical power recovery potential. Case 1. Nissan YD22, 2.2 L diesel engine Case 2. Ford Ecoboost, 1.6 L gasoline engine.		Engines (lab.)	Bi_2Te_3	40	-	TEGs installed on the exhaust of the engines.	Engine coolant at 50°C	Case 1. 55.4 (full-load conditions) Case 2. 126.9 (full-load conditions)	-	-
[183]	Test a new low-temperature waste heat thermoelectric generator setup	Exp.	A test bench was constructed to test standard commercial TEMs. The test bench allows two cases of study: Case 1. With natural convection cooling Case 2. With forced convection cooling	Case 1. 4 Case 2. 18	Test bench (lab.)	TEC1-03180T125	10	-	Recirculating hot water bath.	Air (Heat sink and axial fan)	Case 1. 0.015 Case 2. 0.85	-	-
[139]	Simulate energy recovery from a prototype and validate the results using a test bench	Sim. + Exp.	A second-generation prototype was created and tested to measure the energy recovery of commercial TEMs.	30	Test bench and prototype	TMH400302055 (Bi_2Te_3)	24	-	Exhaust gases (exhaust pipe going through the prototype)	Air (Heat sinks with axial fans)	12.41	-	-
[184]	Simulate and construct a TEG system	Sim. + Exp.	A prototype was created and then simulated that has 8 TEMs mounted on the exhaust pipe. The simulations were done for three cases, with different number of fins on the	88.3 (at 3500 rpm)	Prototype mounted on an engine exhaust	Bi_2Te_3	8	-	Exhaust gases	Air (Heat sinks with axial fans)	44.13 (at 3500 rpm)	-	-

(*continued on next page*)

Table 6 (*continued*)

Ref.	Goal	Method Exp./ Sim.	Description	ΔT [°C]	Test bench / engine (lab. / vehicle)	TEG system design TEM / material	No. of TEMs	Syst. mass [kg]	Structure on the hot side	Cooling method	Power Output [W]	Parasitic losses [W]	Eff. / FC gain [%]
			cold side, and for a variation of engine speed with 500 rpm increments from 1000 to 3500 rpm.										
[185]	Simulate and validate a three-dimensional resistance analysis model	Sim. + Exp.	Calculus, simulation using FloTHERM and real measurements were done on a heat recovery system. Cases taken into consideration: Case 1. Natural convection Case 2 Forced convection	80 (max)	Prototype on an experimental testbench	TMH400302055	8	-	Heater and blower	Air, cooling fan	Case 1. 3.21 Case 2. 9.28	-	-
[186]	Underline the influence of the heat sink pillars shape on power generation	Exp.	Experiments were made on a diesel engine with prototype heat sinks with triangle and rectangular shape pillars. Engine was kept at a constant speed of 1500 rpm with loads from 6 kg•m to 18 kg•m. Case 1: triangular, forward direction (a triangle tip facing the exhaust flow) Case 2. triangular, reverse direction (a triangle side facing the exhaust flow) Case 3. rectangular.	80 to 120	Prototype on an experimental testbench	HZ-14 × 10 HZ-20 × 10	20	0.082	Exhaust gases	Constant temperature water bath	200 to 260 for all 20 TEGs	-	-
[187]	Underline the differences between two TEG types	Exp.	An SUV with a TEG mounted on the exhaust was tested at different velocities, to determine how much energy can be obtained and how does the fuel efficiency improve. Experiments were done at ~ 50, 80 and 115 km/h	~320 - 480 (depending on the velocity)	Vehicle	Bi_2Te_3 based Case 1: HZQW Case 2: HZ20M	16	40	Exhaust gases	Engine coolant	Case 1: 100 - 450 Case 2: 33 - 140 (depending on the velocity)	-	Case 1: 1.1 – 1.5% Case 2: -0.25 - 0% (depending on the velocity)
[123]	Measure the output of a fabricated TEM mounted on an engine	Exp.	A 2 L engine was used to measure the output of a prototype TEG that is placed	~55	Lab measurements on a vehicle	Bi_2Te_3	72	-	Engine coolant	Engine coolant	75		2.1%

(*continued on next page*)

Table 6 (*continued*)

Ref.	Goal	Method Exp./ Sim.	Description	ΔT [°C]	Test bench / engine (lab. / vehicle)	TEG system design TEM / material	No. of TEMs	Syst. mass [kg]	Structure on the hot side	Cooling method	Power Output [W]	Parasitic losses [W]	Eff. / FC gain [%]
			instead of the conventional radiator of an engine. The vehicle was driven at 80 km/h (on the test bench).										
[188]	Measure the power generation of a TEG with hexagonal internal fins.	Exp.	An engine mounted on the test bench was used to generate the heat (loaded by a dynamometer) recovered by the hexagonal TEG. Engine was operated in a steady state mode (on a speed characteristic), until exhaust temperature was relatively constant.	~240 (@ 3000 rpm)	Engine (lab.)	1261G-7L31-05CQ	18	-	Prototype hexagonal fins placed in the exhaust	Engine coolant	21.2 - 98.8 (depending on the speed of the engine 1200 – 3000 rpm)	-	1.3 - 2.6%
[189]	Experimentally investigate the waste heat recovery performance of a TEG	Exp.	A turbocharged 6-cylinder diesel engine was used as the heat source and the TEG was mounted on the exhaust. Engine was operated at 1000, 1500 and 2000 rpm.	~300	Engine (lab.)	Bi_2Te_3	40	-	Exhaust gases	Water from a cooling tower	119 (max @ 2000 rpm)	-	2.8%
[190]	Experimentally investigate a direct contact thermoelectric generator (DCTEG) on a diesel engine	Sim. + Exp	A diesel engine was used as a heat generator for the experimental measurements, taken at three speeds (1700, 2000 and 2300 rpm) and different loads. The cold side of the TEG was kept at 25, 35 and 45°C respectively. Case 1: 25°C Case 2: 35°C Case 3: 45°C	Case 1: 342 Case 2: 352 Case 3: 362 (@2300 rpm)	Engine (lab.)	Bi_2Te_3	40	-	Exhaust gases	50–50% water and ethylene glycol mixture cooled separately	Case 1: ~28 – 43 Case 2: ~22 – 36 Case 3: ~20 – 32 (varies with the speed of the engine 1700 – 2300 rpm)	-	1 – 2%
[191]	Create and validate a model of TEG and underline its performance	Exp. + Sim.	A 6.6 L engine was used as the heat source to validate the model of a TEG. Gas-in temperature was varied, obtaining three cases:	Case 1: 197 Case 2: 224 Case 3: 250	Engine (lab.)	HZ-14 (Bi_2Te_3)	2	-	EGR Path	Coolant @4°C	Case 1: ~9.8 Case 2: ~6.2 Case 3: ~2.5 (max values)	-	-

(*continued on next page*)

Table 6 (*continued*)

Ref.	Goal	Method Exp./ Sim.	Description	ΔT [°C]	Test bench / engine (lab. / vehicle)	TEG system design TEM / material	No. of TEMs	Syst. mass [kg]	Structure on the hot side	Cooling method	Power Output [W]	Parasitic losses [W]	Eff. / FC gain [%]
			Case 1: 181°C Case 2: 228°C Case 3: 254°C										
[192]	Determine the benefits of using an intermediate fluid to damp the dynamic heat input of the vehicle engine exhaust	Exp.	An engine was used as a heat source, operating at different speeds and torques. The TEG was mounted with an intermediary oil circuit on the hot side, that exchanges heat with the exhaust.	~300 (max)	Engine (lab.)	Bi_2Te_3	105	-	Oil circuit (independent from the engine oil circuit)	Engine coolant	51 – 551.2	-	
[193]	Measure the power output of a TEG installed in a vehicle	Exp.	A vehicle was operated on a dynamometer at 80 – 125 km/h in 5th gear (equivalent to road test) with a TEG system mounted on the exhaust.	Case 1: ~90 Case 2: ~185 Case 3: 240	Whole vehicle on dynamometer	Bi_2Te_3	240	-	Exhaust gases	Water from tanks	Case 1: ~150 Case 2: ~550 Case 3: 944	-	1.28 – 1.85%
[194]	Waste heat recovery performance of a TEG installed in a light commercial vehicle	Exp.	A vehicle equipped with a 2.3 L diesel engine was operated on different driving cycles and different vehicle speeds to determine the benefit of the system. The system was also tested on the test bench.	390 on the bench 270 on the vehicle	Engine on test bench and after that vehicle on dynamometer	Bi_2Te_3	504	4 (core weight)	Exhaust gasses pass through 63 tubes	Water at 60°C	482 on the test bench 220 on the WLTP cycle	-	4% fuel economy improvement on the WLTP cycle
[195]	A method to assess the fuel economy of an automotive TEG	Exp. + Sim.	A TEG was installed in the exhaust system of a 1.4 L TSI engine, after the TWC, to analyze the fuel economy improvement of such a system. The engine equipped a virtual vehicle operating at four different driving speeds.	Case 1: 63.4 Case 2: 153.3 Case 3: 259.5 Case 4: 255.8	Engine on dyno (lab.)	TELBP1-12656-0.45 PbTe-Bi_2Te_3	12	7	Exhaust gasses pass trough a heat exchanger with 6 circular channels	Water	Case 1: 5.5 Case 2: 37.7 Case 3: 111.3 Case 4: 106.8	-	0.18%, after weight penalty is considered
[87]	Optimize TEG internal structure for ICE WHR	Exp.	The study analyzes the thermal performance of ETEGs with differing internal structures (see cases) to outline interface	~250	Engine (lab.)	-	8	-	Plate shaped with fishbone fins	Water	Case 1: ~27 Case 2: ~18	-	-

(*continued on next page*)

Table 6 (*continued*)

Ref.	Goal	Method Exp./ Sim.	Description	ΔT [°C]	Test bench / engine (lab. / vehicle)	TEG system design TEM / material	No. of TEMs	Syst. mass [kg]	Structure on the hot side	Cooling method	Power Output [W]	Parasitic losses [W]	Eff. / FC gain [%]
			temperature and thermal uniformity.										
[142]	Evaluate the performance of an automotive TEG with different internal structures	Exp. + Sim.	4 TEGs were installed on a 3.9 L diesel vehicle and tests were conducted with two different internal structures. The internal structure was modified to reduce the pressure drop compared to the reference case.	Case 1: 205 Inserted fins Case 2: 205 Dimpled surface	Vehicle	Bi_2Te_3	240	200 190	Plate shaped with fins Plate shaped with dimples	Coolant	Case 1: 609 Case 2: 618	-	0.25% eff. Increase 0.68% eff. increase
[196]	Experimentally demonstrate the possibility to recover 1kW of electrical energy using TEMs	Exp. + Sim.	A high-power-density TEG was installed in the exhaust of a Caterpillar engine and tested to highlight the energy recovery efficiency of nanostructured TEMs.	339	Engine (lab.)	half-Heusler elements	400	30	Plate fin heat exchanger with Nickel alloy fins	Coolant	1002.6	-	2.1% heat to electricity efficiency
[197]	Performance analysis of a TEG system used in diesel engines	Exp.	The performance of a TEG was analyzed on a FIAT 1.9 L engine. The speed varied between 1500 and 3500 min^{-1}, while the applied load was 50 and 100 Nm respectively in each case.	145 max 50 Nm 170 max 100 Nm	Engine (lab.)	-	40	-	Plate and cylinder type, turned into an octagonal structure	Water	- 156.7	20	-
[86]	Assess the performance of half-Heusler TEG in automotive applications	Exp.	A half-Heusler TEG was installed in a 2.0 L gasoline engine running on premium gasoline. The engine was operated after a matrix of steady-state engine operating conditions.	520-820	Engine (lab.)	half-Heusler	72	~20	Rectangle finned heat exchanger with 6 passages	Coolant	Max. 250	~50	1-2% fuel economy improvement
[198]	Modeling, simulating, and validating a TEG on a diesel engine	Sim. + Exp.	A TEG was modeled and the results were validated on a 4 cylinder diesel engine	317 (max)	Engine (lab.)	Bi_2Te_3	28	-	Prototype mounted on the exhaust	Flowing water in a copper tubing network	42	-	-
[199]	Test the influence of TEGs on the exhaust backpressure	Exp.	A Nissan diesel engine was tested on NEDC, WLTP and in different operation	(not of interest in the article)	Engine (lab.)	Bi_2Te_3	80	-	Prototype mounted on the exhaust	Coolant	68	-	-

(*continued on next page*)

Table 6 (*continued*)

Ref.	Goal	Method Exp./ Sim.	Description	ΔT [°C]	Test bench / engine (lab. / vehicle)	TEG system design TEM / material	No. of TEMs	Syst. mass [kg]	Structure on the hot side	Cooling method	Power Output [W]	Parasitic losses [W]	Eff. / FC gain [%]
			points to determine the power generation and the pumping losses when using TEGs in the exhaust.										
[108]	Test a TEG prototype installed in the exhaust of a diesel engine	Exp.	A Nissan diesel engine was tested on NEDC, WLTP and in different operation points to underline the power generation and the pumping losses that TEGs have on the exhaust.	350 (max) @2400 rpm, 110 Nm	Engine (lab.)	Bi_2Te_3	80	-	Prototype mounted on the exhaust	Coolant at 50°C	70 (max) @2400 rpm, 110 Nm	-	1.8% (max)
[93]	Test a TEG installed in the exhaust of a heavy-duty natural gas engine	Sim. + Exp.	Results were compared (experimental and simulation results) for a single-channel TEG, at a single operating point, with emphasis on the economical approach.	465	Test bench	$SnTe_{1-x}Se_x$	56	6-6.8	Prototype mounted on the exhaust	Cooling system	282.9	-	3%
[156]	Determine the influence of a PCM on TEG operation	Exp.	An experimental test rig was built to analyze the effect of using a PCM in conjunction with a TEM to improve transient performance. The results with and without the PCM were compared: Case 1. Without PCM Case 2. With PCM	180	Test bench	Bi_2Te_3	1	-	Heating plate	Water from a water bath	Case 1. 2.859 Case 2. 2.892	-	-
[200]	Test the power output of a TEG prototype with 6 TEMs installed in an Audi 80	Exp.	The hot side of the TEG is the coolant system, and the cold side of the TEG is the fuel recirculated inside the prototype. Measurements were done in mixed driving conditions, over a period of more than 30 minutes.	43	Vehicle engine	TEC1–12710 (Bi_2Te_3)	6	-	Prototype mounted on the coolant (antifreeze)	Cooling by circulating the fuel in the TEM prototype	12	-	-
[201]	Analyze the power output of a TEG installed in the exhaust system of a	Exp.	The shape and the dimensions of the TEG prototype were optimized to meet	~150-198	HEV Engine	1261G-7L31-05CQ (Bi_2Te_3)	12	-	Prototype mounted on the exhaust	Engine coolant	18-118		2.1%

(*continued on next page*)

Table 6 (*continued*)

Ref.	Goal	Method Exp./ Sim.	Description	ΔT [°C]	Test bench / engine (lab. / vehicle)	TEG system design TEM / material	No. of TEMs	Syst. mass [kg]	Structure on the hot side	Cooling method	Power Output [W]	Parasitic losses [W]	Eff. / FC gain [%]
	hybrid electric vehicle		the maximum allowable pressure drop of a 2 L 4-cylinder engine operating between 1200 and 3400 rpm under different loads										
[202]	Determine the power output of two TEGs when installed in the exhaust system of an engine	Exp.	The 1.4 L diesel engine was operated at different loads and speeds (2000-3500 rpm). TEGs used: Case 1: TEG12-8 Case 2: TEG1-199	65-70	Engine (lab.)	Case 1: TEG12-8 Case 2: TEG1-199	1	-	Exhaust gases	Electrical blower	Case 1: 0.8 Case 2: 0.9	-	-
[203]	Analyze the influence of the location and porosity of a TEG system	Exp.	The TEG was installed in the exhaust pipe of a 6-cylinder engine, with different flow straighteners at different distances from the TEG inlet.	125	Engine (6-cylinder diesel engine)	Bi_2Te_3	30	-	Exhaust gases	Coolant from a chiller	52 (without flow straightener) – 83 (with E type flow straightener al 265mm from TEG inlet)	-	-
[204]	Determine the TEG output installed in the exhaust system of a diesel engine operating with three different fuels.	Exp.	The experimental design included nine operation points of the engine, for all the fuels. The emissions were also monitored. The fuels were: Case 1. Diesel Case 2. B5 Case 3. B10	Case 1. 218 (avg) Case 2. 228 (avg) Case 3. 236 (avg)	Engine (lab.)	TEG1-12610-5.1	20	-	Exhaust gases	Chilled water	Case 1. 57.99 (max) Case 2. 65.59 (max) Case 3. 71.18 (max)	-	-
[205]	Determine the heat flow and power output of a TEG installed in the exhaust system of a gasoline engine	Sim. + Exp.	Using a 0.4 L gasoline engine the experiments were done at full load and different speeds: Case 1. 1250 rpm Case 2. 1750 rpm Case 3. 2250 rpm	Case 1. 50 Case 2. 75 Case 3. 100	Engine (lab.)	automotive TEG	20	-	Exhaust gases	Water	Case 1. 7.36 Case 2. 21.52 Case 3. 32.8	-	-
[206]	Analyze the performance of a hexagonal shaped housing TEG	Exp. + Sim.	A comparison was made between two heat exchangers with a hexagonal cross section and a traditional (round) cross section. The experiments were done using a 3.8 L V6 SI engine.	10-85	Engine (lab.)	BiTe	6	-	Exhaust gases	Coolant	14.1-45.4	-	-
[103]		Exp.					34	8	Exhaust gases	Coolant		-	-

(*continued on next page*)

Table 6 (*continued*)

Ref.	Goal	Method Exp./ Sim.	Description	ΔT [°C]	Test bench / engine (lab. / vehicle)	TEG system design TEM / material	No. of TEMs	Syst. mass [kg]	Structure on the hot side	Cooling method	Power Output [W]	Parasitic losses [W]	Eff. / FC gain [%]
	Assess the fuel economy improvement of a TEG based on the power generation, backpressure and ATEG weight		A vehicle equipped with a 1.5 L 3-cylinder engine and automatic gearbox was tested at different speeds and loads. Case 1. 50 km/h Case 2. 80 km/h Case 3. 100 km/h Case 4. 120 km/h	Case 1. 27.3 Case 2. 45.6 Case 3. 57.8 Case 4. 126.2	ATEG on real vehicle	ATEG (H-199-14-06L2)					Case 1. 38.65 Case 2. 76.38 Case 3. 101.09 Case 4. 197.77		
[207]	Determine the power output of a TEG for a diesel generator	Exp. + Sim.	Different cases were studied, with different positioning of the TEG. The fuel for the generator was 20% mahua oil biodiesel. The whole system was validated as a cogeneration system (electricity and heated water).	Case 1. 9.2 Case 2. 9.45 Case 3. 35.67 Case 4. 41.81	Generator diesel engine	Bi_2Te_3	Case 1. 458 Case 2. 455 Case 3. 102 Case 4. 100	-	Case 1. Heated wall from water from exhaust Case 2. Heated water from exhaust Case 3. Exhaust tube Case 4. Exhaust gases	Case 1. Air Case 2. Rectangular tube – air Case 3. Water-tube-air Case 4. Exhaust tube-heated water-air	Case 1. 7.74 Case 2. 8.11 Case 3. 25.86 Case 4. 34.62	-	-
[208]	Analyze the power output, temperature distribution, efficiency, internal resistance and backpressure of a TEG installed in the exhaust system of an SUV with respect to vehicle speed, clamping pressure, engine coolant flow, andambient temperature	Exp.	The vehicle, equipped with a 3.9 L 4-cylinder diesel engine, was tested on the highway at speeds ranging from 80 to 125 km/h. The engine speed ranged from 1600 to 2500 rpm.	60-170 (speed dependent)	Engine	Bi_2Te_3	240	-	Exhaust gases	Coolant	100 – 608.85 (speed dependent)	-	-

FC – Fuel consumption

Table 7
Review of literature results – simulation results.

Ref.	Goal	Method Exp./ Sim.	Description	ΔT [°C]	TEG system design TEM / material	No. of TEMs	Syst. mass [kg]	Structure on the hot side	Cooling method	Power Output [W]	Parasitic losses [W]	Eff. / FC gain [%]
[6]	Investigate the possibility of replacing the alternator with TEG and an economic analysis	Sim. + Exp.	The vehicle was modeled using Simulink. The exhaust and TEG heat transfer was analyzed using CFD. The TEG model was validated against experimental data.	~175 (Exp.)	HZ-14	8	-	Longitudinally finned stainless steel	Chilled coolant	68	-	3,88 – 7,38% (FC)
[209]	Recover the heat from an exhaust of a combustion chamber designed for heating water	Sim. + Exp.	Experimental test on a prototype with two levels of recovery. ANSYS Fluent simulation of the prototype, to compare the temperature loss and the thermoelectric generation to the experimental values.	68 – 92.7 (depending on the mass flow and input temperature) (Sim.)	-	-	-	4-sided exhaust x 2 TEM x 2 levels	Air (finned surfaces)	11.21 – 26.39 (depending on the mass flow and input temperature)	-	-
[122]	Modelling and analyzing the integration of TEG in a conventional vehicle for exhaust gases WHR	Sim.	Numerical simulation of a TEG installed in a Fiat Punto 1.3 L diesel engine with the exhaust gas as the hot side of the TEG and the engine coolant as the cool side of the TEG. The testing was done under the NEDC, FUDS and FHDS cycles.	-	Bi_2Te_3	80 TC	-	-	Engine coolant	60-90	-	17-24% electric energy savings 15-20% alternator energy
[210]	Determine the hypothetical thermoelectric performance and operating characteristic of a TEG mounted on a medium-duty turbocharged diesel engine	Sim.	Modelling the TEG and different configurations and placements of TEG systems, with real input data from a 6.7 L Cummins diesel engine working at 2000 rpm, 475Nm torque load. TEG configurations: Case 1: TEG before turbine; Case 2: TEG after turbine; Case 3: TEG after aftertreatment system; Case 4: TEGs before and after aftertreatment system; Case 5: TEGs before turbo and after after-treatment system;	~280	MnSi1.75 for the p-type leg Mg2Si0.5Sn0.5 for the n-type leg	26 for basic heat exchanger module, 26 for finned configuration, 78 for multiple parallel duct counterflow configuration	-	TEG types: basic heat exchanger module, finned configuration, and multiple parallel duct counterflow configuration	Engine coolant	320 for basic heat exchanger module 975 for finned configuration, 1060 for multiple parallel duct counterflow configuration	-	-
[116]	Simulate the differences	Sim.	Three cases were considered: I. where cold surface was	25 - 175	Case 1. Bi_2Te_3 Case 2. $(Bi_{0.2}Sb_{0.8})_2Te_3$	1	-	TEG installed between hot and cold surface	-	Case 1. 8.2 Case 2. 4.1	-	Case 1. 6.8 % Case 2. 5.6%

(*continued on next page*)

Table 7 (*continued*)

Ref.	Goal	Method Exp./ Sim.	Description	ΔT [°C]	TEG system design TEM / material	No. of TEMs	Syst. mass [kg]	Structure on the hot side	Cooling method	Power Output [W]	Parasitic losses [W]	Eff. / FC gain [%]
	between four types of TEMs		fixed at 25°C and the hot surface varies from 50-200°C. II. where the difference is fixed at 100°C, and the cold surface varies from 5-25°C with a pace of 5°C. III. Sine wave variation of the hot surface with mean values of 50, 100 and 150°C, with the cold surface fixed at 25°C		Case 3. $Cu_{11}Ni_1Sb_4S_{13}$ Case 4. $Ag_xSb_{2-x}Te_{3-x}$ x=0.93					Case 3. 3 Case 4. 0.5		Case 3. 4.6% Case 4. 1.2%
[211]	Demonstrate the efficiency of novel combined thermoelectric materials	Sim.	Three different Perovskite-type oxide combined thermoelectric materials ($CaMn_{0.98}Nb_{0.02}O_3$, $La_{1.98}Sr_{0.02}CuO_4$ and $GdCo_{0.95}Ni_{0.05}O_3$) were selected and analyzed numerically. Two configurations were considered, with different lengths and diameters. Simulation was done in COMSOL.	321 - 445	Case 1. $CaMn_{0.98}Nb_{0.02}O_3$ as n-type, $La_{1.98}Sr_{0.02}CuO_4$ as p-type. Case 2. $CaMn_{0.98}Nb_{0.02}O_3$ as n-type, $GdCo_{0.95}Ni_{0.05}O_3$ as p-type.	-	-	TEG installed in the exhaust of an ICE	Engine coolant.	Case 1. 158.4 @ ΔT=409°C Case 2. 55.6 @ ΔT=409°C	-	Case 1. 0.51% @ ΔT=409°C Case 2. 0.18% @ ΔT=409°C
[212]	Simulate and compare results to a previous paper (Exp.)	Sim.	Simulation was done for a vehicle with a 11.2 L turbocharged diesel engine (303 kW), on the world transient vehicle cycle (WTVC). The TEG was used in two modes: Case 1. cooperative with a smaller alternator. Case 2. thermostat mode (alternator passes the electricity to the battery and electrical loads intermittently).	-	Bi_2Te_3	240	115 (from a previous Exp. paper)	-	-	995	-	Case 1. 2.92% Case 2. 4.1%
[213]	Investigate the output of a TEM for different hot and cold side conditions	Sim.	A simulation was made using the CFD software Fluent. The influence of the cooling type, coolant flow rate, length, number and location of bafflers, and flow arrangement were investigated	494	-	20 TEM	-	TEGs were sandwiched on the exhaust	Case 1. ICE coolant/water Case 2. Air @ 30km/h Case 3. Air @ 60km/h Case 4. Air @ 100km/h	Case 1. 15.2 Case 2. 12.2 Case 3. 10.5 Case 4. 12.1	Case 1. 0.005 Case 2. 0.57 Case 3. 1.64 Case 4. 4.04	-
[214]	Underline the recuperation	Sim.	Based on real measurements done on	-	TEG model (half-Heusler	-	-		Cooling water	Case 1. 150 Case 2. 30	-	-

(*continued on next page*)

Table 7 (*continued*)

Ref.	Goal	Method Exp./ Sim.	Description	ΔT [°C]	TEG system design TEM / material	No. of TEMs	Syst. mass [kg]	Structure on the hot side	Cooling method	Power Output [W]	Parasitic losses [W]	Eff. / FC gain [%]
	potential of half-Heusler thermoelectric materials		WLTC, simulations were done to evaluate the energy recovery potential of half-Heusler thermoelectric materials, for two locations of the TEG: Case 1. Before turbocharger Case 2. After the ATS		thermoelectric materials)			TEGs installed in the exhaust system				
[215]	Model TEGs used for WHR from the exhaust of a diesel engine	Sim.	Engineering equation solver (EES) software was used to simulate a non-transient drive cycle. The model was validated against experimental data of two commercial TEMs.	-	TEG Model (Mg_2Si/ Zn_4Sb_3 for the high temperature Bi_2Te_3 for the low temperature)	Authors varied the number of thermoelements (maximum 10000) for a fixed TEG size.	-	TEMs installed in the exhaust system	Water	Up to 1200	-	
[216]	TEG Modelling and optimization	Sim.	A simulation was done in GT-POWER for a 2 L engine to provide input data for a TEG Model. Two temperatures were taken into consideration for the hot side: Case 1. 120°C Case 2. 150°C	Case 1. 40 Case 2. 70	Bi_2Te_3-based TEM	56	-	TEG was fixed on the exhaust with copper plates for conductivity	Coolant	Case 1. 70 Case 2. 150	-	-
[217]	Underline the power output depending on the cooling method	Sim.	A numerical analysis was done with four cooling methods for the TEG heat recovery system: the water coflow (WCO), water counterflow (WCOU), Case 3. air coflow (ACO), and air counterflow methods (ACOU). The model was validated by comparing the power output with experimental data. Both for hot and cold side, either water or air was used.	520	TEG1-127-1.4-1.6 40 × 40 × 3.8 mm	1	-	Numeric calculation for the given surface.	Case 1. the water coflow (WCO), Case 2. water counterflow (WCOU), Case 3. air coflow (ACO), Case 4. air counterflow methods (ACOU)	Case 1. 320 Case 2. 320 Case 3. 100 Case 4. 120	-	-
[184]	Simulate and build a TEG for exhaust gas WHR	Sim. + Exp.	A TEG prototype with 8 TEMs for the exhaust pipe was built and simulated. The simulations were done for different number of fins on the cold side, and for various engine speeds	88.3 (at 3500 rpm)	Bi_2Te_3	8	-	Exhaust gases	Air (Heat sinks with axial fans)	Case 1. 36.74 Case 2. 51.36 Case 3. 55.11	-	-

(*continued on next page*)

Table 7 (*continued*)

Ref.	Goal	Method Exp./ Sim.	Description	ΔT [°C]	TEG system design TEM / material	No. of TEMs	Syst. mass [kg]	Structure on the hot side	Cooling method	Power Output [W]	Parasitic losses [W]	Eff. / FC gain [%]
			ranging from 1000 to 3500 rpm with a 500 rpm increment. Cases: Case 1. 10 fins Case 2. 22 fins Case 3. 44 fins									
[185]	Simulate and validate a three-dimensional resistance analysis model	Sim. + Exp.	Simulations of the WHR system in FloTHERM were validated with experimental data. Cases: Case 1. Natural convection Case 2 Forced convection	Case 1: 55 (max) Case 2: 85 (max)	TMH400302055	8	-	Heater and blower	Air, cooling fan	Case 1: 4 (max) Case 2: 11 (max)	-	-
[130]	Simulate the conversion of heat to energy for automotive applications, with different aspect ratios	Sim.	Experimental results for a vehicle driving on the highway and introduced were used as input data for the simulation. The simulation was done for different aspect ratios (sandwiching between hot and cold side) Case 1: 1/72, Case 2: 2/36, Case 3: 3/24, Case 4: 4/18, Case 5: 6/12. Furthermore, the height of the hot side heat exchanger fins was varied from 10mm to 40mm.	~620	Nanostructured bulk half-Heusler TEG	72	-	Exhaust gases	Water	Case 1: 155 to 185 Case 2: 190 to 215, Case 3: 205 to 225, Case 4: 210 to 230, Case 5: 220 to 240 (for 40 to 10mm fins)	-	-
[176]	Analyze the WHR potential from an ICE of a hybrid vehicle	Sim.	A simulation was developed to determine the energy recovery potential from a hybrid vehicle. The heat input from the ICE (hot side of TEG on the catalyst) is converted into electrical which is then fed to the battery of the vehicle. The vehicle is simulated on the NEDC. The TEG model was validated with experimental data.	~ 125 – 480 (overall on all NEDC)	GM250-127-28-10 (Bi_2Te_3)	4	-	Exhaust gases	Chilled water from a laboratory recirculation chiller (for validation of TEG)	80 – 200 (overall on all NEDC)	-	3.4% fuel saving
[127]	Study the feasibility of a TEG to generate energy, and	Sim.	Measurements from a 2 L diesel engine (under the NEDC) were used as input data for a	-	GM250-127-28-10 (Bi_2Te_3)	1	20	Exhaust pipe	Engine oil circuit	Case 1: max 110 Case 2: max	-	-

(*continued on next page*)

Table 7 (*continued*)

Ref.	Goal	Method Exp./ Sim.	Description	ΔT [°C]	TEG system design TEM / material	No. of TEMs	Syst. mass [kg]	Structure on the hot side	Cooling method	Power Output [W]	Parasitic losses [W]	Eff. / FC gain [%]
	bifunctional TEM development		simulation. The TEM model was also validated experimentally. Following validation, the module was used for heat recovery and for engine warmup. Case 1: strategy with warmup and recovery Case 2: strategy without warmup, with recovery							150 (on NEDC)		
[105]	Validate a TEG model for exhaust gas WHR	Sim.	The data from a 6.6-liter engine running on NRTC and was used as input for the simulation model. Two scenarios with different coefficients for heat transfer, electrical contact resistance and thermal contact conductance were considered.	~ 200	GM250-127-28-10 (Bi_2Te_3)	20	-	Exhaust pipe	Engine coolant	170 – 224 (averages for scenario 1 and 2)	-	-
[218]	Predict fuel economy potential when using TEGs	Sim.	A previously validated skutterudite TEG model was integrated in a semi-empirical model comprising a quasi-static light-duty vehicle model, and dynamic models for the exhaust, coolant and TEG. Six simulation cases were considered: Case 1: NEDC Case 2: WLTP Case 3: FTP-75 Case 4: FTP-highway Case 5: 90km/h constant Case 6: 120 km/h constant Also, there are two scenarios, then the TEG is mounted before (A) and after (B) the catalytic converter.	~ 200	Skutterudite TEM	400	20	Exhaust pipe	Engine coolant	Case 1: (A) 144, (B) 71 Case 2: (A) 209, (B) 119 Case 3: (A) 157, (B) 80 Case 4: (A) 275, (B) 145 Case 5: (A) 327, (B) 190 Case 6: (A) 661, (B) 461 (average values for the specific cycles)	-	Case 1: (A) 1.7%, (B) 0.5% Case 2: (A) 3.1%, (B) 1.4% Case 3: (A) 2.1%, (B) 0.5% Case 4: (A) 3.3%, (B) 2.1% Case 5: (A) 3.1%, (B) 1.6% Case 6: (A) 3.6%, (B) 2.4% (average values for the specific cycles) (FC)
[102]	Simulate the energy generation of a TEG for three types of engines	Sim.	For the three engine types (see cases), simulations were done in ADVISOR for vehicle speeds ranging from 10 to 120 km/h with a TEG system installed in the exhaust.	Case 1: ~160 - 180 Case 2: ~160 - 240 Case 3: ~160 – 240 (but a bigger average than case 2)	Bi_2Te_3	10	-	Exhaust pipe	Air flow	Case 1: ~18 - 82 Case 2: ~18 - 110 Case 3: ~22 – 110 (but a bigger average than case 2)	-	1 – 1.028% (energy eff. gain)

(*continued on next page*)

Table 7 (*continued*)

Ref.	Goal	Method Exp./ Sim.	Description	ΔT [°C]	TEG system design TEM / material	No. of TEMs	Syst. mass [kg]	Structure on the hot side	Cooling method	Power Output [W]	Parasitic losses [W]	Eff. / FC gain [%]
			Case 1: light duty vehicle Case 2: midsize vehicle Case 3: heavy-duty vehicle	(all depending on the velocity of the vehicle)						(all depending on the velocity of the vehicle)		
[219]	Investigate the optimal STEG ratio to enhance system performance	Sim.	A segmented TEG was validated based on experimental results in order to underline the effects of structural and thermodynamic conditions on a optimal segmented ratio design. After that, the potential of power generation in consideration of disparate p-n segmented ratios is studied. Finally, the performance improvement at the system level by applying optimal segmented ratio is investigated	350 for validation ~160 when the performance improvement is investigated	TEP1-12656-0.6 $CoSb_3(p_1/n_1)$ $Bi_2Te_3(p_2/n_2)$	108	-	Exhaust pipe	Engine coolant	78.9 in the traditional layout 83.4 in the optimizes layout	-	-
[195]	Validating a TEG design to highlight potential fuel consumption improvements	Sim. + Exp.	A TEG module was validated to simulate its behavior under various vehicle operating conditions. Four cases were simulated: Case 1: 50 km/h constant Case 2: 80 km/h constant Case 3: 100 km/h constant Case 4: 120 km/h constant	Case 1: 60.6 Case 2: 172 Case 3: 235 Case 4: 244	TELBP1-12656-0.45 $PbTe-Bi_2Te_3$	12	~7	Exhaust gasses pass through a heat exchanger with six circular channels	Water	Case 1: 5.47 Case 2: 34.35 Case 3: 102.9 Case 4: 94.9	-	0.18% fuel saving
[177]	Hybrid electric heavy-duty vehicle energy recovery using TEG	Sim.	A hybrid bus was modelled and used on the Nuremberg cycle and engine operating parameters were collected to provide inputs to the engine simulation software (AVL BOOST). Those inputs were then used to simulate energy recovery and fuel saving using two different TEGs (MATLAB-SIMULINK).	277	SiGe Skutterudite	96	-	Exhaust gas is passed through a rectangular heat exchanger	Heatsink	SiGe – 1618 Skutterudite – 1926.7	-	SiGe: 6.5% Skutterudite: 7.2%
[142]	Evaluate the performance of an automotive TEG	Sim. + Exp.	4 TEGs were installed on a 3.9 L diesel vehicle and tests were conducted with two different	205 Inserted fins 205 Dimpled surfaces	Bi_2Te_3	240	200 190	Plate shaped with fins Plate shaped with dimples	Coolant	612 -	-	-

(*continued on next page*)

Table 7 (*continued*)

Ref.	Goal	Method Exp./ Sim.	Description	ΔT [°C]	TEG system design TEM / material	No. of TEMs	Syst. mass [kg]	Structure on the hot side	Cooling method	Power Output [W]	Parasitic losses [W]	Eff. / FC gain [%]
	with different internal structures		internal structures. The internal structure was modified to reduce the pressure drop compared to the reference case.									
[144]	Optimizing the design of an ETEG for ICE	Sim.	The heat exchanger of an ETEG was optimized to fully exploit the potential of the system. The modified parameter was the angle of the baffles.	427	Bi_2Te_3	20	-	Rectangle with internal baffles	Coolant	Empty: 63 BA 10°: 65 BA 20°: 74 BA 30°: 83 BA 40°: 95	-	~0.6% lower fuel consumption
[220]	Evaluate the performance of a TEG with respect to driving conditions	Sim.	A vehicle equipped with a TEG was simulated on the Japanese 10-15, NEDC and UDDS cycle.	10-15 cycle: 25.8 NEDC: 46 UDDS: 144.3	HZ-20, Bi_2Te_3	16	-	-	-	13.1 41 32.1	-	0.52% 0.78% 0.74% increase in power output
[171]	Performance investigation and energy optimization of a TEG for a mild hybrid vehicle	Sim.	A mild hybrid vehicle equipped with a TEG was simulated under the UDDS and HWFET driving cycle. Simulations were also done without the TEG to have a reference case. The electric motor was a 10 kW ISG type.	UDDS A: 623 HWFET A: 656 UDDS C: N/A HWFET C: N/A	PbTe Quinary alloy	20	14.3	Rectangle heat exchanger placed after the TWC	Coolant	277.3 max. 149.6 avg. 250.9 max. 184 avg. - -	-	3.64% 2.17% reduction in fuel consumption
[221]	Investigate the possibility of combining a TEG with a TWC and optimize the model to achieve uniform temperature distribution and low backpressure	Sim.	A simulation model of a TEG integrated into a TWC was validated and different cases with respect to TWC positioning were explored to achieve optimum conditions for the TEG. The TWC was positioned in front, middle and at the back of the TEG heat exchanger.	Front: 60 Middle: 70 Rear: 90	TEP1-12656-0.6 Bi_2Te_3	7	-	Hexagonal heat exchanger with hollow center body, which also contains the TWC	-	Front: 17.42 Middle: 22.28 Rear: 27.28	-	16% increased power output of the TEG with integrated TWC with respect to a conventional configuration
[222]	Simulate the impact on fuel economy of a TEG installed in a hybrid and a conventional vehicle	Sim.	A TEG installed in a conventional and in a hybrid vehicle was simulated using MATLAB-SIMULINK to assess the fuel economy potential under the ECE, EUDC, HWFET and FTP driving cycles.	-	-	60	-	Rectangular heat exchanger	Coolant	ECE: 430.7 EUDC: 644.6 HWFET: 700 FTP: 466.5	-	2.5% and 7.5% fuel economy improvement for the parallel hybrid and conventional vehicle respectively
[223]	Modeling, simulation, and validation of a	Sim. + Exp.	An electro-thermo-structural coupled numerical analysis was done using ANSYS-CFX	Case 1. 270 Case 2. 370 Case 3. 470 Case 4. 570	Skutterudite	12	-	Different designs of fins.	Coolant water	Case 1. 5.5 Case 2. 11.5 Case 3. 20 Case 4. 32	-	-

(*continued on next page*)

Table 7 (*continued*)

Ref.	Goal	Method Exp./ Sim.	Description	ΔT [°C]	TEG system design TEM / material	No. of TEMs	Syst. mass [kg]	Structure on the hot side	Cooling method	Power Output [W]	Parasitic losses [W]	Eff. / FC gain [%]
	TEG on a testbench		to evaluate the thermal, electrical, and structural performances of a prototype TEG. Simulations were done at different temperatures for the hot side, with different designs.									
[133]	Analyze the performance of a TEG for exhaust WHR	Sim.	A mathematical model was developed, and several structural influences were analyzed.	248-396	TEP1-1264-3.4	126 pair of p and n type semiconductors	-	Multi layered exhaust/coolant	Cooling water	185-605	-	3.3-4.1%
[93]	Simulate a TEG installed in the exhaust of a heavy-duty natural gas engine	Sim. + Exp.	Results were compared (experimental and simulation results) for a single-channel TEG, in an operating point, with emphasis on the economical approach.	465	$SnTe_{1-x}Se_x$	56	6-6.8	Prototype mounted on the exhaust	Cooling system	405	-	3.4%
[224]	Development of a TEG model to analyze the power output for light, mid and heavy-duty engines	Sim.	The engine power and relative power caused by the application of TEG system for traditional cars were modeled. Simulations were made for all three types of engines/vehicles at vehicle speeds ranging from 10 to 120 km/h: Case 1: Light duty Case 2: Midsize Case 3: Heavy-duty.	Case 1: 301 Case 2: 376 Case 3: 356 (max @ 120 km/h)	Bi_2Te_3	20	3.5	Prototype mounted on the exhaust	Cooled by air flows from the front grill of the vehicle	Case 1: 82 Case 2: 110 Case 3: 108 (max @ 120 km/h)	-	-
[225]	Optimize the output of a TEM using thermal-electric multiphysics simulation	Sim.	An air to water system was used to model the CFD performance of the TEM. Model was also validated with a test rig.	200	Bi_2Te_3	1	-	Exhaust simulation	Cooling device	3.5	-	-
[226]	Develop a converging heat exchanger design for TEG WHR	Sim. + Exp.	A multiphysics fluid-thermoelectric coupled field was used to simulate the TEG. The model was validated using a test rig. A comparison was made between the conventional and the converging TEG: Case 1. Conventional Case 2. Converging	~190	TEG-127020	16	-	Air heater	Water chiller	Case 1. 11.5 (max) Case 2. 12.5 (max)	-	-
[227]		Sim.		-	-	-	-	Exhaust	-		-	-

(*continued on next page*)

Table 7 (*continued*)

Ref.	Goal	Method Exp./ Sim.	Description	ΔT [°C]	TEG system design TEM / material	No. of TEMs	Syst. mass [kg]	Structure on the hot side	Cooling method	Power Output [W]	Parasitic losses [W]	Eff. / FC gain [%]
	Several heat exchanger designs were studied for TEMs		For all the structures of the heat exchanger, the simulation was made for a light-duty vehicle on NEDC.							250 to 650 (increase in power of ICE) depending on the structure		
[117]	Compare the performance of conventional TEM with a segmented asymmetrical thermoelectric generator (SASTEG)	Sim	The COMSOL 5.3 multiphysics software was used to optimize the electrical performance for transient and steady conditions of the SASTEG. Different duty cycles were simulated by applying transient and pulsed heat inputs. Simulations cases: Case 1. TEG Case 2. SASTEG	Case 1. 206 (max) Case 2. 286 (max)	Bi_2Te_3	1	-	-	-	Case 1. 0.06 (max) Case 2. 0.125 (max)	-	-
[228]	Simulated the power output of roof TEG from a parked vehicle exposed to the sun	Sim. + Exp.	Results showed that in both the real vehicle and the model temperature inside the cabin rose sufficiently in comparison to the outside so that TEMs can be mounted to recover the energy.	-	eTEG HV37	-	-	Inside of a vehicle cabin	Outside of a vehicle cabin	280 (for a roof area of 1 m^2 covered in TEMs)	-	-
[229]	Simulated the power output of a TEG installed in the exhaust of a diesel engine	Sim.	The TEG structure was installed in a 3.2 L 4-cylinder turbocharged engine exhaust for validation.	218.8-232.6	BiTe	112	-	Engine exhaust	Cooling water	- (focus on the temperature difference)	-	-
[230]	The concept of net power ratio was introduced to properly evaluate the heat transfer enhancement of a TEG HX	Sim. + Exp.	An annular TEG model installed in the exhaust of an engine was developed and validated by using experimental data.	225-525	HZ-20-type thermoelectric material	30	-	Hot air	Cooling water	9-43	-	-
[231]	Simulate the effect of varying model parameters of a two-stage TEG using the Latin hypercube sampling method	Sim.	It was determined that the output power and efficiency can be improved by improving the heat transfer coefficient of the cold source and mean heat exchange area. Results were validated by comparing the values with experimental measurements from another paper.	300	-	1	-	-	-	3.55	-	-

(*continued on next page*)

Table 7 (*continued*)

Ref.	Goal	Method Exp./ Sim.	Description	ΔT [°C]	TEG system design TEM / material	No. of TEMs	Syst. mass [kg]	Structure on the hot side	Cooling method	Power Output [W]	Parasitic losses [W]	Eff. / FC gain [%]
[232]	Simulate a hybrid vehicle equipped with a TEG for exhaust gas WHR	Sim.	The purpose was to analyze the power output of the TEG, for different cases in the 1000 – 5200 rpm speed range of the engine. The vehicle was simulated on the NEDC and WLTC cycles, and fuel economy values were validated. Simulations were done with different number and different sizes of the TEMs.	~600	High Seebeck coefficient material	1 (25 × 25 mm module)	-	Exhaust gases	Coolant	60-75 (for high-speed tests 4000-5200 rpm)	-	11% (4000-5200 rpm)

- thermoelectric modules models are validated against manufacturer data without experimental testing from the authors (see Section 6),
- the figure of merit is often considered independent of temperature leading to an overestimation of the power output at low temperatures and underestimation at high temperatures,
- the contact pressure (and therefore thermal contact resistance) is disregarded or considered constant resulting in an overestimation of heat flow values,
- for thermoelectric generator systems consisting of many thermoelectric modules, validation is done for a single module and not the system as a whole, thus disregarding the additional losses (due to non-uniform temperature distribution and consequently temperature gradients) and requirements for providing the proper voltage levels for the storage system and/or load,
- the parasitic losses (exhaust backpressure, added weight of the system and/or auxiliary components, efficiency of the DC-DC converter, different power outputs of the individual modules etc.) associated with the thermoelectric generator system are neglected or underestimated,
- simulation models usually consist of many submodels that are individually validated – in many cases each submodel overestimates the performance and consequently, the complete model provides more optimistic results.

When including realistic assumptions, simulations yielded results closer to real-world testing values. Thus, more focus should be placed on incorporating the real aspects of employing thermoelectric generators in on-road operation to simulations. Only one effort estimated parasitic losses: for a thermoelectric generator with 20 thermoelectric modules, the maximum losses were estimated at 4 W. Again, like the experimental findings, more focus should be placed on highlighting all energy flows. Compared to the experiments (Table 6), simulations (Table 7) showed possible outputs of up to 1926.7 W, depending on the number of thermoelectric modules (ranging from 1 to 240). This value was achieved for a thermoelectric generator with 96 thermoelectric modules or 20.1 W/TEM. The maximum specific output was the same as in the case of laboratory tests since it was obtained by the same authors 41.6 W/kg. For cooling, the authors used in their studies coolant, water, and air.

Given that the experimental results find improvements in fuel consumption are possible, as stated prior in Section 6, research should focus on current hindrances, such as the stabilization and uniform distribution of temperature on the hot side, testing of the TEG system under the thermal and mechanical stresses, lightweight development, and the appropriate selection of the thermoelectric material.

10.2. Analysis of experimental and simulation results concerning thermoelectric generators in automotive applications

As described in the previous section, the findings covering experimental research of thermoelectric generators illustrate that most efforts are concentrated on the use of thermoelectric generators for exhaust gas waste heat recovery, with a limited number of studies covering exhaust gas recirculation and radiator thermoelectric generators. Furthermore, the testing is done in laboratory conditions, which limits the possibility to identify all the challenges of using thermoelectric generators as well as to quantify the benefits. Further advances in the field can be obtained by employing RDE testing, which can provide a more comprehensive understanding of the benefits and challenges of using thermoelectric generators in this field. With respect to the simulation of thermoelectric generators for vehicle waste heat recovery, the proposed models are generally only briefly presented (therefore limiting the possibility to reproduce the results), cover only particular problems of thermoelectric generator use, and are not integrated with specialized software for the automotive industry. Consequently, directing research efforts towards the integration of such simulation solutions in specialized software, as well as providing more detailed presentations of the models can

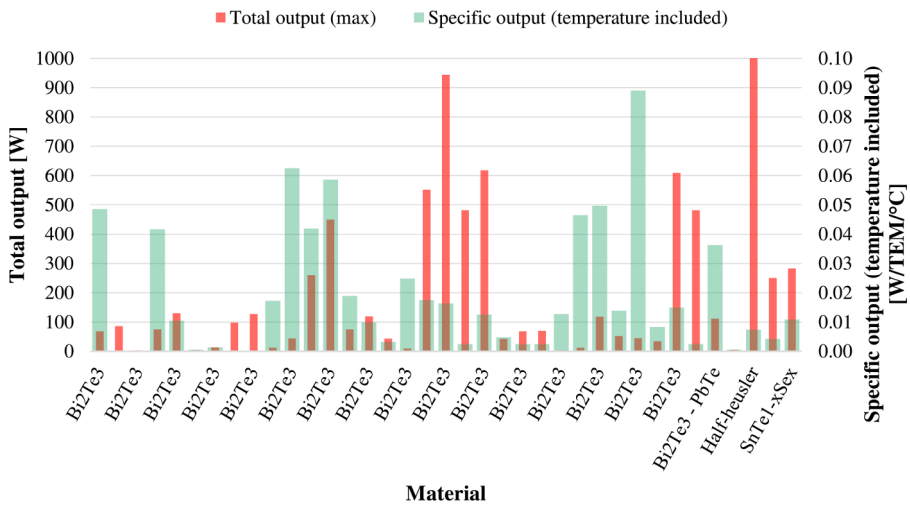

Fig. 14. Power output results for a selection of cases (based on available data) presented in Table 6 (experimental results).

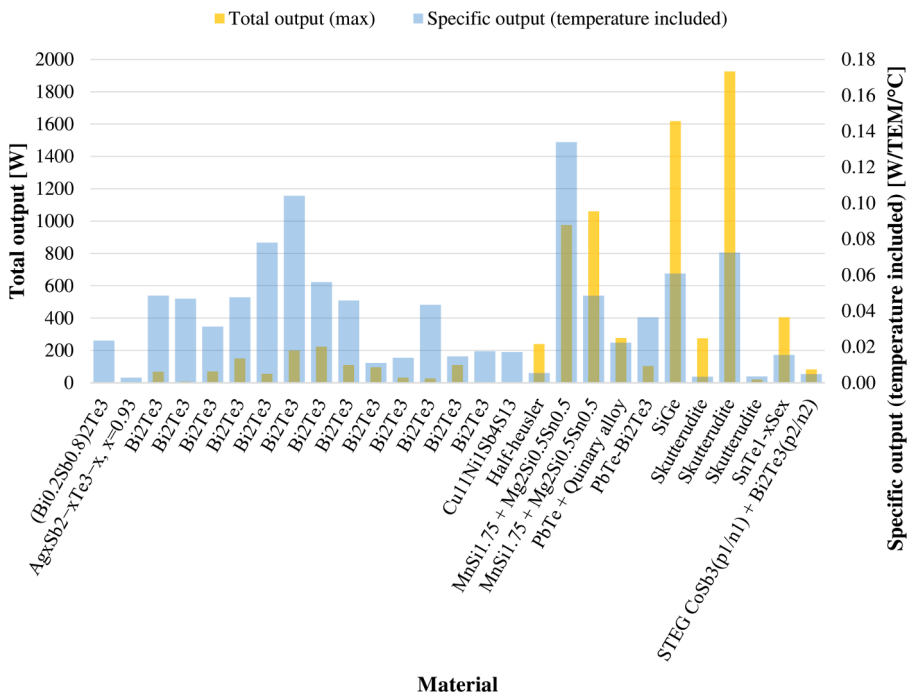

Fig. 15. Power output results for a selection of cases (based on available data) presented in Table 7 (simulation results).

positively impact the interest in further developing efficient solutions to use thermoelectric generators for vehicle waste heat recovery. Finally, it must be noted that recent developments in the automotive sector are pushing (and therefore gradually limiting) internal combustion engines research and development in the direction of hard-to-electrify applications. Furthermore, the technologies that are being deployed for internal combustion engines are pushing the efficiency limits. Since this requires that more heat is converted into useful work, the result will be lower exhaust gas temperatures and ultimately, lower thermoelectric generator efficiencies.

11. Conclusions

Since the beginning of the 20th century, the internal combustion engine has been the main propulsion source for both passenger cars and freight transport. However, its future is uncertain due to its negative impact on climate change and the current proliferation of electrified vehicles. While the issue of pollutant emissions can be solved by modern aftertreatment systems, the efficiency problem is harder to rectify, mainly due to the unavoidable losses accompanying the conversion of heat into work. Therefore, by partially recovering some of this otherwise wasted heat, the energy balance could be significantly improved. Of the thermal energy recovery methods options proposed for internal combustion engines, thermoelectric generators have several advantages: lack of moving parts and working fluids, environmentally friendly, high reliability, the direct conversion of thermal energy into electrical energy and other. Despite all these advantages, the use of such systems has not seen general adoption mainly due to its poor efficiency. However, recent advances in thermoelectric materials could provide the required breakthrough resulting in their continued need for study with an emphasis on achieving high energy efficiency.

The present study has sought to aid this effort by bringing together all aspects concerning the use of thermoelectric generators for internal combustion engines waste heat recovery as well as delivering two thorough summaries of both experimental and simulation results. Finally, this effort covers aspects regarding both thermoelectric generators installed on the exhaust system, which are usually preferred due to high temperatures of the exhaust gas, and in other regions that can

provide heat for power generation (i.e., radiator and exhaust gas recirculation).

Making thermoelectric generators more attractive for vehicle manufactures, especially for heavy-duty vehicles used in road transport, requires a significant boost in their efficiency. Consequently, research efforts should be focused on the identification of new solutions, technologies, and materials that can further improve the figure of merit to reach a value of at least 5. However, the complexity and multitude of physical parameters that govern the operating efficiency of thermoelectric generators make it difficult to achieve such a high figure of merit. This requires a thorough understanding of the interactions between their thermal and electrical characteristics and conflicting requirements (e.g., heat flux vs. thermal conductivity). Therefore, achieving this target requires solutions to break the correlation between the three factors influencing $Z\overline{T}$: Seebeck coefficient, electrical resistivity, and thermal conductivity.

The design of thermoelectric modules seeks to solve the problem of module efficiency with respect to its application. In this respect, researchers and manufacturers alike need to overcome several challenges with respect to thermoelectric materials: improvement of Z (by solving the conflicting requirements of the electrical and thermal characteristics), growth of operating range, and/or development of low-cost materials, while also considering environmental impact, mechanical vibrations, and shocks. Thermoelectric module efficiency can also be increased by using segmented thermoelectric generators, which use a series of segments made of different types of thermoelectric materials that work in narrower temperature ranges, but at the cost of increased manufacturing and optimization efforts. As opposed to segmented thermoelectric generators, cascaded thermoelectric generators use several independent thermoelectric modules installed in two or three cascade stages, thus benefiting from a simpler structure and easier manufacturing. The main challenge is the appropriate selection of the thermoelectric modules.

Reviewing the literature, it has been found that there are numerous challenges to overcome before thermoelectric generators can become viable for automotive usage: development of thermoelectric materials with high efficiencies appropriate for the internal combustion engine operating temperature ranges, ensuring an appropriate heat transfer on the hot side, improving robustness, lightweight design (not an issue for applications using stationary engines) and others. In addition to these general challenges, there are specific challenges depending on the installation position of the thermoelectric generator system (exhaust pipe, the exhaust gas recirculation system, radiator, and oil pan): decreasing temperature along the flow direction, too high or too low hot side temperatures, non-uniform distribution of temperature, etc. The positioning of the thermoelectric generator system also requires consideration of other factors like the availability of installation space and mitigating the negative effect of the thermoelectric generator system. Furthermore, depending on the installation location there is the issue of heat extraction and uniform temperature distribution (compared to the exhaust gas thermoelectric generator, the radiator and exhaust gas recirculation thermoelectric generators do not require an additional hot side heat exchanger). Exhaust gas and exhaust gas recirculation thermoelectric generators pose further issues due to the large thermal resistance between the exhaust gases and the hot side of the thermoelectric generator. Several methods have been proposed to solve these issues like heat pipes, improved heat exchanger materials and/or design, as well as phase change materials. Heat exchanger materials and design can significantly impact the power output of the system, but also the performance of the engine (due to the increased backpressure). The ability of heat pipes to transport heat at remote locations have made it possible to solve several issues: eliminate the need for a direct contact between the thermoelectric generator elements and the exhaust pipe, reduce the thermal resistance while lowering the pressure losses, and improve uniformity of the temperature distribution. However, their use also poses some challenges like the limited rate of heat transfer, high design effort, added weight etc. Phase change materials have the advantage that they can store and release heat, thus maintaining a quasi-constant temperature. Furthermore, phase change materials can provide thermal protection in case of temperature extremes that could damage the thermoelectric generator. However, they would also increase the cost and weight of the system.

As described in the previous sections, the findings illustrate that the output of a thermoelectric generator depends on several factors, such as the number of thermocouples in the thermoelectric modules, the number of thermoelectric modules, the configuration/connection of the modules, the thermoelectric materials properties, and the temperature gradient. Therefore, to achieve maximum performance (power and efficiency), a good design and control algorithm are required.

Finally, the use of thermoelectric generators for waste heat recovery in vehicles requires multiple compromises and optimizations, which opens numerous possibilities for further research and innovation. For example, solving the conflict between the efficient use of thermoelectric generators for exhaust gas waste heat recovery and the operation of the exhaust gas aftertreatment system. One example could involve the use of thermoelectric generators for both electrical energy generation and temperature control for a close-coupled three-way catalyst. Another could consider that city traffic leads to large periods of exhaust gas recirculation operation and that there are significant efforts to increase the operating range of exhaust gas recirculation for highway vehicles; hence, use of thermoelectric generators could reduce stress on the exhaust gas recirculation cooler. In addition, solving the issue of thermoelectric module efficiency at low temperature gradients can extend their use to radiator thermoelectric generators. Research efforts should also be directed towards lowering the negative impact on internal combustion engine operation where increasing heat exchanger efficiency comes at the cost of an increased backpressure. Here, the use of the engine oil pan as a heat source can be a solution but its performance strongly depends on the vehicle velocity and the ambient temperature.

Overall, the findings presented in this effort illustrate that it is feasible to use thermoelectric generation to partially recover the waste heat of internal combustion engines, but there are still important barriers that must be overcome before this solution can be commercially adopted for vehicles.

CRediT authorship contribution statement

Nicolae Vlad Burnete: Conceptualization, Resources, Writing – original draft, Writing – review & editing, Visualization. **Florin Mariasiu:** Writing – original draft. **Christopher Depcik:** Conceptualization, Writing – review & editing. **Istvan Barabas:** Writing – original draft. **Dan Moldovanu:** Resources.

Declaration of Competing Interest

The authors declare that they have no known competing financial interests or personal relationships that could have appeared to influence the work reported in this paper.

Acknowledgment

This paper was supported by the Project POCU/380/6/13/123927 “Entrepreneurial competences and excellence research in doctoral and postdoctoral programs - ANTREDOC”, project co-funded by the European Social Fund. The authors also wish to thank Richard Balint for his help in collecting the data for this effort.

References

[1] Lawrence Livermore National Laboratory. Energy Flow Charts: Charting the Complex Relationships among Energy. Water, and Carbon 2019. https://flowcharts.llnl.gov/ (accessed November 6, 2019).

[2] Ramírez R, Gutiérrez AS, Cabello Eras JJ, Valencia K, Hernández B, Duarte Forero J. Evaluation of the energy recovery potential of thermoelectric generators in diesel engines. J Clean Prod 2019;241:118412. https://doi.org/10.1016/J.JCLEPRO.2019.118412.

[3] Rodriguez R, Preindl M, Cotton JS, Emadi A. Review and trends of thermoelectric generator heat recovery in automotive applications. IEEE Trans Veh Technol 2019;68:5366–78. https://doi.org/10.1109/TVT.2019.2908150.

[4] Shen ZG, Tian LL, Liu X. Automotive exhaust thermoelectric generators: current status, challenges and future prospects. Energy Convers Manag 2019;195: 1138–73. https://doi.org/10.1016/J.ENCONMAN.2019.05.087.

[5] Brignone M, Ziggiotti A. Impact of novel thermoelectric materials on automotive applications. AIP Conf Proc 2012;1449:493. https://doi.org/10.1063/1.4731601.

[6] Stobart RK, Wijewardane A, Allen C. The potential for thermo-electric devices in passenger vehicle applications. SAE Tech Pap 2010. https://doi.org/10.4271/2010-01-0833. SAE International.

[7] Stobart R, Milner D. The Potential for Thermo-Electric Regeneration of Energy in Vehicles. SAE Technical Paper 2009. https://doi.org/10.4271/2009-01-1333. 2009-01-1333.

[8] Champier D. Thermoelectric generators: a review of applications. Energy Convers Manag 2017;140:167–81. https://doi.org/10.1016/J.ENCONMAN.2017.02.070.

[9] Stevens RJ, Weinstein SJ, Koppula KS. Theoretical limits of thermoelectric power generation from exhaust gases. Appl Energy 2014;133:80–8. https://doi.org/10.1016/j.apenergy.2014.07.075.

[10] Battiston S, Boldrini S, Fiameni S, Famengo A, Fabrizio M, Barison S. Multilayered thin fi lms for oxidation protection of Mg 2 Si thermoelectric material at middle – high temperatures. Thin Solid Films 2012;526:150–4. https://doi.org/10.1016/j.tsf.2012.10.114.

[11] Bennett GL, Skrabek EA. Power performance of U.S. space radioisotope thermoelectric generators. In: Proceedings of the 15th international conference on thermoelectrics; 1996. https://doi.org/10.1109/ICT.1996.553506.

[12] Goodson K, Nolas GS, Kozinsky B. NSF-DOE Thermoelectrics Partnership: Automotive Thermoelectric Modules with Scalable Thermo- and Electro-Mechanical Interfaces. 2012, https://www.energy.gov/sites/prod/files/2014/03/f10/ace067_goodson_2012_o.pdf (accessed November 6, 2019). https://www.energy.gov/sites/prod/files/2014/03/f13/goodson.pdf.

[13] Gao Y, Marconnet AM, Panzer MA, Leblanc S, Dogbe S, Ezzahri Y, Shakouri A, Goodson KE. Nanostructured interfaces for thermoelectrics. Journal of Electronic Materials 2010;39:1456–62. https://doi.org/10.1007/S11664-010-1256-7.

[14] Goodson PK, Barako MT, Marconnet A, Park W, Leblanc S. Novel nanostructured interface solution for automotive thermoelectric modules application. Dep Energy 2012.

[15] Leszczynski J, Wojciechowski KT, Malecki AL. Studies on thermal decomposition and oxidation of $CoSb_3$. J Therm Anal Calorim 2011;105:211. https://doi.org/10.1007/s10973-011-1461-5.

[16] Li F, Huang X, Jiang W, Chen L. Microstructure and contact resistivity of (Bi, Sb) 2Te 3/Sb interface. AIP Conf Proc 2012;1449:458–62. https://doi.org/10.1063/1.4731595.

[17] Salvador JR, Cho JY, Ye Z, Moczygemba JE, Thompson AJ, Sharp JW, König JD, Maloney R, Thompson T, Sakamoto J, et al. Thermal to Electrical Energy Conversion of Skutterudite-Based Thermoelectric Modules. J. Electron. Mater. 2013;42:1389.

[18] Crane D, Jackson G, Holloway D. Towards Optimization of automotive waste heat recovery using thermoelectrics. SAE Tech Pap 2001. https://doi.org/10.4271/2001-01-1021. SAE International.

[19] Zheng XF, Liu CX, Yan YY, Wang Q. A review of thermoelectrics research – recent developments and potentials for sustainable and renewable energy applications. Renew Sustain Energy Rev 2014;32:486–503. https://doi.org/10.1016/J.RSER.2013.12.053.

[20] Saidur R, Rezaei M, Muzammil WK, Hassan MH, Paria S, Hasanuzzaman M. Technologies to recover exhaust heat from internal combustion engines. Renew Sustain Energy Rev 2012;16:5649–59. https://doi.org/10.1016/J.RSER.2012.05.018.

[21] Alghoul MA, Shahahmadi SA, Yeganeh B, Asim N, Elbreki AM, Sopian K, et al. A review of thermoelectric power generation systems: roles of existing test rigs/prototypes and their associated cooling units on output performance. Energy Convers Manag 2018;174:138–56. https://doi.org/10.1016/J.ENCONMAN.2018.08.019.

[22] Yang J. Potential applications of thermoelectric waste heat recovery in the automotive industry. In: Proceedings of the 24th international conference on thermoelectrics. 2005; 2005. p. 170–4. https://doi.org/10.1109/ICT.2005.1519911.

[23] Patil DS, Arakerimath RR, Walke PV. Thermoelectric materials and heat exchangers for power generation – a review. Renew Sustain Energy Rev 2018;95: 1–22. https://doi.org/10.1016/J.RSER.2018.07.003.

[24] Orr B, Akbarzadeh A, Mochizuki M, Singh R. A review of car waste heat recovery systems utilising thermoelectric generators and heat pipes. Appl Therm Eng 2016; 101:490–5. https://doi.org/10.1016/J.APPLTHERMALENG.2015.10.081.

[25] Hatami M, Ganji DD, Gorji-Bandpy M. A review of different heat exchangers designs for increasing the diesel exhaust waste heat recovery. Renew Sustain Energy Rev 2014;37:168–81. https://doi.org/10.1016/J.RSER.2014.05.004.

[26] Kusano D, Hori Y. Effects of PbTe doping on the thermoelectric properties of $(Bi_2Te_3)_{0.2}(Sb_2Te_3)_{0.8}$. In: Twenty-First International Conference on Thermoelectrics, 2002. Proceedings ICT '02.; 2002. p. 13–6. https://doi.org/10.1109/ICT.2002.1190254.

[27] Zhu P, Imai Y, Isoda Y, Shinohara Y, Jia X, Zou G. Enhanced thermoelectric properties of PbTe alloyed with Sb_2Te_3. J Phys Condens Matter 2005;17:7319–26. https://doi.org/10.1088/0953-8984/17/46/015.

[28] Chen ZG, Han G, Yang L, Cheng L, Zou J. Nanostructured thermoelectric materials: current research and future challenge. Prog Nat Sci Mater Int 2012;22: 535–49. https://doi.org/10.1016/j.pnsc.2012.11.011.

[29] Snyder GJ, Toberer ES. Complex thermoelectric materials. Nat Mater 2008;7: 105–14. https://doi.org/10.1038/nmat2090.

[30] Yoo K, Simpson K, Bell M, Majkowski S. An engine coolant temperature model and application for cooling system diagnosis. SAE transactions 2000;950-960. https://doi.org/10.4271/2000-01-0939.

[31] Cairns A, Fraser N, Blaxill H. Pre versus post compressor supply of cooled EGR for full load fuel economy in turbocharged gasoline engines (No. 2008-01-0425). SAE Technical Paper 2008. https://doi.org/10.4271/2008-01-0425.

[32] Cairns A, Blaxill H, Irlam G. Exhaust gas recirculation for improved part and full load fuel economy in a turbocharged gasoline engine (No. 2006-01-0047). SAE Technical Paper. 2006. https://doi.org/10.4271/2006-01-0047.

[33] Yang L, Chen ZG, Dargusch MS, Zou J. High performance thermoelectric materials: progress and their applications. Adv Energy Mater 2018;8:1701797. https://doi.org/10.1002/aenm.201701797.

[34] Pei Y, Gibbs ZM, Gloskovskii A, Balke B, Zeier WG, Snyder GJ. Optimum carrier concentration in n-Type PbTe thermoelectrics. Adv Energy Mater 2014;4: 1400486. https://doi.org/10.1002/aenm.201400486.

[35] Pei Y, LaLonde AD, Wang H, Snyder GJ. Low effective mass leading to high thermoelectric performance. Energy Environ Sci 2012;5:7963–9. https://doi.org/10.1039/C2EE21536E.

[36] Pei Y, Heinz NA, Snyder GJ. Alloying to increase the band gap for improving thermoelectric properties of Ag2Te. J Mater Chem 2011;21:18256–60. https://doi.org/10.1039/C1JM13888J.

[37] UncorrelaTEd Project - Solid-liquid thermoelectric systems with uncorrelated properties, http://uncorrelated.uji.es/documents/ (accessed October 12, 2021). http://uncorrelated.uji.es/.

[38] Hamawandi B, Batili H, Paul M, Ballikaya S, Kilic NI, Szukiewicz R, et al. Minute-made, high-efficiency nanostructured Bi2Te3 via high-throughput green solution chemical synthesis. Nanomater 2021:11. https://doi.org/10.3390/nano11082053.

[39] Crane D, Lagrandeur J. Automotive waste heat conversion to power program—2011 vehicle technologies program annual merit review. DOE OVT Review. 2011 https://www.energy.gov/sites/prod/files/2014/03/f11/ace051_lagrandeur_2011_o_0.pdf.

[40] Love ND, Szybist JP, Sluder CS. Effect of heat exchanger material and fouling on thermoelectric exhaust heat recovery. Appl Energy 2012;89:322–8. https://doi.org/10.1016/j.apenergy.2011.07.042.

[41] Ikoma K, Munekiyo M, Furuya K, Kobayashi M, Izumi T, Shinohara K. Thermoelectric module and generator for gasoline engine vehicles. In: Proceedings of the 17th international conference on thermoelectrics; 1998. p. 464–7. https://doi.org/10.1109/ICT.1998.740419.

[42] Fakheri A. Efficiency and effectiveness of heat exchanger series. J Heat Transf 2008;130. https://doi.org/10.1115/1.2927404.

[43] Yazawa K, Shakouri A. Fuel-burning thermoelectric generators for the future of electric vehicles. Energy Convers Manag 2021;227:113523. https://doi.org/10.1016/j.enconman.2020.113523.

[44] Soleimani Z, Zoras S, Ceranic B, Shahzad S, Cui Y. A review on recent developments of thermoelectric materials for room-temperature applications. Sustain Energy Technol Assessments 2020;37:100604. https://doi.org/10.1016/j.seta.2019.100604.

[45] Schönecker A, Pichon PY, König J, Jägle M, den Heijer M, Kraaijveld B. Novel process for metal silicide nanostructures regarding cheap and large-scale material synthesis BT. In: Proceedings of the 11th European conference on thermoelectrics; 2014. p. 43–51. Amaldi A, Tang F, editors., Cham: Springer International Publishing.

[46] Zhang L, Rogl G, Grytsiv A, Puchegger S, Koppensteiner J, Spieckermann F, et al. Mechanical properties of filled antimonide skutterudites. Mater Sci Eng B 2010; 170:26–31. https://doi.org/10.1016/j.mseb.2010.02.022.

[47] Liu W, Jie Q, Kim HS, Ren Z. Current progress and future challenges in thermoelectric power generation: from materials to devices. Acta Mater 2015;87: 357–76. https://doi.org/10.1016/J.ACTAMAT.2014.12.042.

[48] Yang J, Stabler FR. Automotive applications of thermoelectric materials. J Electron Mater 2009;38:1245–51. https://doi.org/10.1007/s11664-009-0680-z.

[49] LeBlanc S, Yee SK, Scullin ML, Dames C, Goodson KE. Material and manufacturing cost considerations for thermoelectrics. Renew Sustain Energy Rev 2014;32:313–27. https://doi.org/10.1016/J.RSER.2013.12.030.

[50] Liu W, Hu J, Zhang S, Deng M, Han CG, Liu Y. New trends, strategies and opportunities in thermoelectric materials: a perspective. Mater Today Phys 2017; 1:50–60. https://doi.org/10.1016/J.MTPHYS.2017.06.001.

[51] Wei J, Yang L, Ma Z, Song P, Zhang M, Ma J, et al. Review of current high-ZT thermoelectric materials. J Mater Sci 2020;55:12642–704. https://doi.org/10.1007/s10853-020-04949-0.

[52] Ouyang Z, Li D. Design of segmented high-performance thermoelectric generators with cost in consideration. Appl Energy 2018;221:112–21. https://doi.org/10.1016/J.APENERGY.2018.03.106.

[53] Yee SK, LeBlanc S, Goodson KE, Dames C. $ per W metrics for thermoelectric power generation: beyond ZT. Energy Environ Sci 2013;6:2561–71. https://doi.org/10.1039/C3EE41504J.
[54] Hendricks TJ, Yee S, LeBlanc S. Cost scaling of a real-world exhaust waste heat recovery thermoelectric generator: a deeper dive. J Electron Mater 2016;45:1751–61. https://doi.org/10.1007/s11664-015-4201-y.
[55] Hendricks TJ. Integrated thermoelectric–thermal system resistance optimization to maximize power output in thermoelectric energy recovery systems. MRS Proc 2014;1642. https://doi.org/10.1557/opl.2014.443. mrsf13-1642-bb02-04.
[56] Hendricks TJ. New paradigms in defining optimum cost conditions in thermoelectric energy recovery designs. Mater Today Proc 2019;8:613–24. https://doi.org/10.1016/J.MATPR.2019.02.061.
[57] Anderson K, Brandon N. Techno-economic analysis of thermoelectrics for waste heat recovery. Energy Sources Part B Econ Plann Policy 2019;14:147–57. https://doi.org/10.1080/15567249.2019.1632976.
[58] Liu W, Bai S. Thermoelectric interface materials: a perspective to the challenge of thermoelectric power generation module. J Mater 2019;5:321–36. https://doi.org/10.1016/j.jmat.2019.04.004.
[59] Barako MT, Park W, Marconnet AM, Asheghi M, Goodson KE. Thermal cycling, mechanical degradation, and the effective figure of merit of a thermoelectric module. J Electron Mater 2013;42:372–81. https://doi.org/10.1007/s11664-012-2366-1.
[60] He R, Schierning G, Nielsch K. Thermoelectric devices: a review of devices, architectures, and contact optimization. Adv Mater Technol 2018;3:1700256. https://doi.org/10.1002/admt.201700256.
[61] LeBlanc S. Thermoelectric generators: linking material properties and systems engineering for waste heat recovery applications. Sustain Mater Technol 2014;1–2:26–35. https://doi.org/10.1016/J.SUSMAT.2014.11.002.
[62] El-Desouky A, Carter M, Andre MA, Bardet PM, LeBlanc S. Rapid processing and assembly of semiconductor thermoelectric materials for energy conversion devices. Mater Lett 2016;185:598–602. https://doi.org/10.1016/J.MATLET.2016.07.152.
[63] Glatz W, Schwyter E, Durrer L, Hierold C. Bi2Te3-based flexible micro thermoelectric generator with optimized design. J Microelectromech Syst 2009;18:763–72. https://doi.org/10.1109/JMEMS.2009.2021104.
[64] Jaziri N, Boughamoura A, Müller J, Mezghani B, Tounsi F, Ismail M. A comprehensive review of thermoelectric generators: technologies and common applications. Energy Rep 2020;6:264–87. https://doi.org/10.1016/J.EGYR.2019.12.011.
[65] Du Y, Chen J, Meng Q, Dou Y, Xu J, Shen SZ. Thermoelectric materials and devices fabricated by additive manufacturing. Vacuum 2020;178:109384. https://doi.org/10.1016/J.VACUUM.2020.109384.
[66] Aswal DK, Basu R, Singh A. Key issues in development of thermoelectric power generators: High Fig.-of-merit materials and their highly conducting interfaces with metallic interconnects. Energy Convers Manag 2016;114:50–67. https://doi.org/10.1016/J.ENCONMAN.2016.01.065.
[67] Araiz M, Catalan L. The importance of the assembly in thermoelectric generators. Rijeka: IntechOpen; 2018. p. 7. https://doi.org/10.5772/intechopen.75697. editorCh.
[68] Custom Thermoelectric, https://customthermoelectric.com/products/thermoelectric-power-generators/tegs (accessed October 12, 2021).
[69] European Thermodynamics Ltd., https://www.europeanthermodynamics.com/products/thermoelectric-modules/seebeck-generator (accessed February 15, 2021).
[70] EVERREDtronics Ltd, Thermoelectric Generator, http://everredtronics.com/thermoelectric.generator.html (accessed October 12, 2021).
[71] Products - Hi-Z Technology - San Diego https://hi-z.com/products/ (accessed October 12, 2021).
[72] Marlow Industries Inc., https://www.digikey.com/en/product-highlight/m/marlow/thermoelectric-generator-tg-series (accessed October 12, 2021).
[73] P&N Technology, http://www.pengnantech.com/power-generator.html (accessed October 12, 2021).
[74] TEGpro, https://www.tegmart.com/index.php?p=catalog&mode=manufacturer&mid=2 (accessed October 12, 2021).
[75] TECTEG MFR, thtps://thermoelectric-generator.com/product-category/teg-modules/ (accessed October 18, 2021).
[76] 江西纳米克热电电子股份有限公司, TEHP series is the bismuth telluride based thermoelectric modules for converting heat into electricity. It is designed to optimize its performance for around 250-300C heat source n.d. http://www.thermonamic.com/pro_view.asp?id=801 accessed October 12, 2021.
[77] TE generators, TXL Group, Inc. n.d. https://txlgroup.com/te-generators/ accessed October 12, 2021.
[78] Hadjistassou C, Kyriakides E, Georgiou J. Designing high efficiency segmented thermoelectric generators. Energy Convers Manag 2013;66:165–72. https://doi.org/10.1016/J.ENCONMAN.2012.07.030.
[79] Kishore RA, Sanghadasa M, Priya S. Optimization of segmented thermoelectric generator using Taguchi and ANOVA techniques. Sci Rep 2017. https://doi.org/10.1038/s41598-017-16372-8.
[80] Tian H, Sun X, Jia Q, Liang X, Shu G, Wang X. Comparison and parameter optimization of a segmented thermoelectric generator by using the high temperature exhaust of a diesel engine. Energy 2015;84:121–30.
[81] Snyder GJ, Ursell TS. Thermoelectric Efficiency and Compatibility. Phys Rev Lett 2003;91:148301. https://doi.org/10.1103/PhysRevLett.91.148301.
[82] Crane DT, Bell LE. Progress towards maximizing the performance of a thermoelectric power generator. In: Proceedings of the 25th international conference on thermoelectrics; 2006. p. 11–6. https://doi.org/10.1109/ICT.2006.331259.
[83] Zhang L, Tosho T, Okinaka N, Akiyama T. Design of cascaded oxide thermoelectric generator. Mater Trans 2008;49:1675–80. https://doi.org/10.2320/matertrans.MRA2008085.
[84] Risseh AE, Nee HP, Goupil C. Electrical power conditioning system for thermoelectric waste heat recovery in commercial vehicles. IEEE Trans Transp Electrif 2018. https://doi.org/10.1109/TTE.2018.2796031.
[85] Man EA. Design considerations for thermoelectric power generation. Aalborg Universitetsforlag; 2016. https://doi.org/10.5278/vbn.phd.engsci.00132.
[86] Szybist J, Davis S, Thomas J, Kaul BC. Performance of a Half-Heusler thermoelectric generator for automotive application. Society of Automotive Engineers Technical Paper Series 2018;1(01). https://www.sae.org/publications/technical-papers/content/2018-01-0054/.
[87] Su CQ, Zhan WW, Shen S. Thermal optimization of the heat exchanger in the vehicular waste-heat thermoelectric generations. J Electron Mater 2012;41:1693–7. https://doi.org/10.1007/s11664-012-2095-5.
[88] Yin Y, Baskaran K, Tiwari A. A review of strategies for developing promising thermoelectric materials by controlling thermal conduction. Phys Status Solidi 2019;216:1800904. https://doi.org/10.1002/pssa.201800904.
[89] Wang H, McCarty R, Salvador JR, Yamamoto A, König J. Determination of thermoelectric module efficiency: a survey. J Electron Mater 2014;43:2274–86. https://doi.org/10.1007/s11664-014-3044-2.
[90] Wang H, Porter WD, Böttner H, König J, Chen L, Bai S, et al. Transport properties of bulk thermoelectrics: an international round-robin study, part II: Thermal diffusivity, specific heat, and thermal conductivity. J Electron Mater 2013;42:1073–84. https://doi.org/10.1007/s11664-013-2516-0.
[91] Wang H, Porter WD, Böttner H, König J, Chen L, Bai S, et al. Transport properties of bulk thermoelectrics—an international round-robin study, part I: seebeck coefficient and electrical resistivity. J Electron Mater 2013;42:654–64. https://doi.org/10.1007/s11664-012-2396-8.
[92] European Commission (EC), CORDIS: Final Report Summary - HEATRECAR - Reduced energy consumption by massive thermoelectric waste heat recovery in light-duty trucks, 2013. https://cordis.europa.eu/project/id/218541/reporting (accessed February 15, 2021).
[93] Heber L, Schwab J. Modelling of a thermoelectric generator for heavy-duty natural gas vehicles: techno-economic approach and experimental investigation. Appl Therm Eng 2020;174:115156. https://doi.org/10.1016/j.applthermaleng.2020.115156.
[94] Kober M. Holistic development of thermoelectric generators for automotive applications. J Electron Mater 2020;49:2910–9. https://doi.org/10.1007/s11664-020-07966-6.
[95] Schock H, Brereton G, Case E, D'Angelo J, Hogan T, Lyle M, et al. Prospects for Implementation of thermoelectric generators as waste heat recovery systems in class 8 truck applications. J Energy Resour Technol 2013;135. https://doi.org/10.1115/1.4023097.
[96] Stobart R, Wijewardane MAA, Yang Z. Comprehensive analysis of thermoelectric generation systems for automotive applications. Appl Therm Eng 2017;112:1433–44. https://doi.org/10.1016/j.applthermaleng.2016.09.121.
[97] Bou Nader W. Thermoelectric generator optimization for hybrid electric vehicles. Appl Therm Eng 2020;167:114761. https://doi.org/10.1016/J.APPLTHERMALENG.2019.114761.
[98] Royale A, Simic M, Lappas P. Engine exhaust manifold with thermoelectric generator unit. Int J Engine Res 2020:1468087420932779. https://doi.org/10.1177/1468087420932779.
[99] Zhang M, Wang J, Tian Y, Zhou Y, Zhang J, Xie H, et al. Performance comparison of annular and flat-plate thermoelectric generators for cylindrical hot source. Energy Rep 2021;7:413–20. https://doi.org/10.1016/j.egyr.2021.01.008.
[100] Rowe DM, Smith J, Thomas G, Min G. Weight penalty incurred in thermoelectric recovery of automobile exhaust heat. J Electron Mater 2011;40:784. https://doi.org/10.1007/s11664-011-1571-7.
[101] Fernández-Yáñez P, Armas O, Kiwan R, Stefanopoulou AG, Boehman AL. A thermoelectric generator in exhaust systems of spark-ignition and compression-ignition engines. A comparison with an electric turbo-generator. Appl Energy 2018;229:80–7. https://doi.org/10.1016/J.APENERGY.2018.07.107.
[102] Luo D, Wang R, Yu W, Sun Z, Meng X. Theoretical analysis of energy recovery potential for different types of conventional vehicles with a thermoelectric generator. Energy Procedia 2019;158:142–7. https://doi.org/10.1016/j.egypro.2019.01.061.
[103] Comamala M, Massaguer A, Massaguer E, Pujol T. Validation of a fuel economy prediction method based on thermoelectric energy recovery for mid-size vehicles. Appl Therm Eng 2019;153:768–78. https://doi.org/10.1016/j.applthermaleng.2019.03.004.
[104] Crane D, LaGrandeur J, Jovovic V, Ranalli M, Adldinger M, Poliquin E, et al. TEG on-vehicle performance and model validation and what it means for further TEG Development. J Electron Mater 2013;42:1582–91. https://doi.org/10.1007/s11664-012-2327-8.
[105] Lan S, Yang Z, Chen R, Stobart R. A dynamic model for thermoelectric generator applied to vehicle waste heat recovery. Appl Energy 2018;210:327–38. https://doi.org/10.1016/J.APENERGY.2017.11.004.
[106] Massaguer A, Pujol T, Comamala M, Massaguer E. Feasibility study on a vehicular thermoelectric generator coupled to an exhaust gas heater to improve aftertreatment's efficiency in cold-starts. Appl Therm Eng 2020;167:114702. https://doi.org/10.1016/j.applthermaleng.2019.114702.

[107] Wan Q, Liu X, Gu B, Bai W, Su C, Deng Y. Thermal and acoustic performance of an integrated automotive thermoelectric generation system. Appl Therm Eng 2019; 158:113802. https://doi.org/10.1016/j.applthermaleng.2019.113802.
[108] Ezzitouni S, Fernández-Yáñez P, Sánchez L, Armas O. Global energy balance in a diesel engine with a thermoelectric generator. Appl Energy 2020;269:115139. https://doi.org/10.1016/j.apenergy.2020.115139.
[109] Massaguer E, Massaguer A, Pujol T, Comamala M, Montoro L, Gonzalez JR. Fuel economy analysis under a WLTP cycle on a mid-size vehicle equipped with a thermoelectric energy recovery system. Energy 2019;179:306–14. https://doi.org/10.1016/j.energy.2019.05.004.
[110] Rood S, Eslava S, Manigrasso A, Bannister C. Recent advances in gasoline three-way catalyst formulation: a review. Proc Inst Mech Eng Part D J Automob Eng 2019;234:936–49. https://doi.org/10.1177/0954407019859822.
[111] Costa RC, Sodré JR. Compression ratio effects on an ethanol/gasoline fuelled engine performance. Appl Therm Eng 2011;31:278–83. https://doi.org/10.1016/j.applthermaleng.2010.09.007.
[112] Jahirul MI, Masjuki HH, Saidur R, Kalam MA, Jayed MH, Wazed MA. Comparative engine performance and emission analysis of CNG and gasoline in a retrofitted car engine. Appl Therm Eng 2010;30:2219–26. https://doi.org/10.1016/j.applthermaleng.2010.05.037.
[113] Çinar C, Şahin F, Can Ö, Uyumaz A. A comparison of performance and exhaust emissions with different valve lift profiles between gasoline and LPG fuels in a SI engine. Appl Therm Eng 2016;107:1261–8. https://doi.org/10.1016/j.applthermaleng.2016.07.031.
[114] Kahraman E, Cihangir Ozcanlı S, Ozerdem B. An experimental study on performance and emission characteristics of a hydrogen fuelled spark ignition engine. Int J Hydrog Energy 2007;32:2066–72. https://doi.org/10.1016/j.ijhydene.2006.08.023.
[115] AL-Shemmeri TT, Oberweis S. Correlation of the NOx emission and exhaust gas temperature for biodiesel. Appl Therm Eng 2011;31:1682–8. https://doi.org/10.1016/j.applthermaleng.2011.02.010.
[116] Y.X.Y.L. Chen WH, Lin YL, Wang XD, Lin YL. A comprehensive analysis of the performance of thermoelectric generators with constant and variable properties Appl Energy 2019;241:11–24. https://doi.org/10.1016/J.APENERGY.2019.02.083.
[117] Shittu S, Li G, Zhao X, Ma X, Akhlaghi YG, Ayodele E. Optimized high performance thermoelectric generator with combined segmented and asymmetrical legs under pulsed heat input power. J Power Sources 2019;428: 53–66. https://doi.org/10.1016/j.jpowsour.2019.04.099.
[118] Fan S, Gao Y. Numerical analysis on the segmented annular thermoelectric generator for waste heat recovery. Energy 2019;183:35–47. https://doi.org/10.1016/J.ENERGY.2019.06.103.
[119] Chen WH, Huang SR, Wang XD, Wu PH, Lin YL. Performance of a thermoelectric generator intensified by temperature oscillation. Energy 2017;133:257–69. https://doi.org/10.1016/J.ENERGY.2017.05.091.
[120] Chen M. Adaptive removal and revival of underheated thermoelectric generation modules. IEEE Trans Ind Electron 2014;61:6100–7. https://doi.org/10.1109/TIE.2014.2304934.
[121] Baek D, Ding C, Lin S, Shin D, Kim J, Lin X, et al. Reconfigurable thermoelectric generators for vehicle radiators energy harvesting. In: Proceedings of the IEEE/ACM international symposium on low power electronics and design (ISLPED); 2017. p. 1–6. https://doi.org/10.1109/ISLPED.2017.8009166.
[122] Arsie I, Cricchio A, Marano V, Pianese C, De Cesare M, Nesci W. Modeling analysis of waste heat recovery via thermo electric generators for fuel economy improvement and CO2 reduction. Small Diesel Engines 2014;7:246–55. https://doi.org/10.4271/2014-01-0663.
[123] Kim SS, Park S, Kim SS, Rhi SH. A thermoelectric generator using engine coolant for light-duty internal combustion engine-powered vehicles. J Electron Mater 2011;40:812. https://doi.org/10.1007/s11664-011-1580-6.
[124] Baatar N, Kim S. A Thermoelectric generator replacing radiator for internal combustion engine vehicles. TELKOMNIKA 2011;9:523–30.
[125] Abderezzak B, Randi S. Experimental investigation of waste heat recovery potential from car radiator with thermoelectric generator. Therm Sci Eng Prog 2020;20:100686. https://doi.org/10.1016/j.tsep.2020.100686.
[126] Aljaghtham M, Celik E. Design optimization of oil pan thermoelectric generator to recover waste heat from internal combustion engines. Energy 2020;200:117547. https://doi.org/10.1016/j.energy.2020.117547.
[127] Lan S, Smith A, Stobart R, Chen R. Feasibility study on a vehicular thermoelectric generator for both waste heat recovery and engine oil warm-up. Appl Energy 2019;242:273–84. https://doi.org/10.1016/J.APENERGY.2019.03.056.
[128] Negash AA, Kim TY, Cho G. Effect of electrical array configuration of thermoelectric modules on waste heat recovery of thermoelectric generator. Senso Actuators A Phys 2017;260:212–9. https://doi.org/10.1016/J.SNA.2017.04.016.
[129] Montecucco A, Siviter J, Knox AR. The effect of temperature mismatch on thermoelectric generators electrically connected in series and parallel. Appl Energy 2014;123:47–54. https://doi.org/10.1016/J.APENERGY.2014.02.030.
[130] Kempf N, Zhang Y. Design and optimization of automotive thermoelectric generators for maximum fuel efficiency improvement. Energy Convers Manag 2016;121:224–31. https://doi.org/10.1016/j.enconman.2016.05.035.
[131] Jang JY, Tsai YC. Optimization of thermoelectric generator module spacing and spreader thickness used in a waste heat recovery system. Appl Therm Eng 2013; 51:677–89. https://doi.org/10.1016/j.applthermaleng.2012.10.024.
[132] Liu X, Deng YD, Chen S, Wang WS, Xu Y, Su CQ. A case study on compatibility of automotive exhaust thermoelectric generation system, catalytic converter and muffler. Case Stud Therm Eng 2014;2:62–6. https://doi.org/10.1016/j.csite.2014.01.002.
[133] He M, Wang E, Zhang Y, Zhang W, Zhang F, Zhao C. Performance analysis of a multilayer thermoelectric generator for exhaust heat recovery of a heavy-duty diesel engine. Appl Energy 2020;274:115298. https://doi.org/10.1016/j.apenergy.2020.115298.
[134] Marvão A, Coelho PJ, Rodrigues HC. Optimization of a thermoelectric generator for heavy-duty vehicles. Energy Convers Manag 2019;179:178–91. https://doi.org/10.1016/J.ENCONMAN.2018.10.045.
[135] Karana DR, Sahoo RR. Performance assessment of the automotive heat exchanger with twisted tape for thermoelectric based waste heat recovery. J Clean Prod 2021;283:124631. https://doi.org/10.1016/j.jclepro.2020.124631.
[136] Luo D, Wang R, Yu W, Sun Z, Meng X. Modelling and simulation study of a converging thermoelectric generator for engine waste heat recovery. Appl Therm Eng 2019;153:837–47. https://doi.org/10.1016/J.APPLTHERMALENG.2019.03.060.
[137] Luo D, Wang R, Yu W, Zhou W. Performance optimization of a converging thermoelectric generator system via multiphysics simulations. Energy 2020;204: 117974. https://doi.org/10.1016/j.energy.2020.117974.
[138] Deng YD, Liu X, Chen S, Tong NQ. Thermal optimization of the heat exchanger in an automotive exhaust-based thermoelectric generator. J Electron Mater 2013;42: 1634–40. https://doi.org/10.1007/s11664-012-2359-0.
[139] Hsu CT, Huang GY, Chu HS, Yu B, Yao DJ. Experiments and simulations on low-temperature waste heat harvesting system by thermoelectric power generators. Appl Energy 2011;88:1291–7. https://doi.org/10.1016/J.APENERGY.2010.10.005.
[140] Su CQ, Wang WS, Liu X, Deng YD. Simulation and experimental study on thermal optimization of the heat exchanger for automotive exhaust-based thermoelectric generators. Case Stud Therm Eng 2014;4:85–91. https://doi.org/10.1016/j.csite.2014.06.002.
[141] Liu X, Deng YD, Zhang K, Xu M, Xu Y, Su CQ. Experiments and simulations on heat exchangers in thermoelectric generator for automotive application. Appl Therm Eng 2014;71:364–70. https://doi.org/10.1016/j.applthermaleng.2014.07.022.
[142] Wang Y, Li S, Xie X, Deng Y, Liu X, Su C. Performance evaluation of an automotive thermoelectric generator with inserted fins or dimpled-surface hot heat exchanger. Appl Energy 2018;218:391–401. https://doi.org/10.1016/J.APENERGY.2018.02.176.
[143] Lu H, Wu T, Bai S, Xu K, Huang Y, Gao W, et al. Experiment on thermal uniformity and pressure drop of exhaust heat exchanger for automotive thermoelectric generator. Energy 2013;54:372–7. https://doi.org/10.1016/j.energy.2013.02.067.
[144] Niu Z, Diao H, Yu S, Jiao K, Du Q, Shu G. Investigation and design optimization of exhaust-based thermoelectric generator system for internal combustion engine. Energy Convers Manag 2014;85:85–101. https://doi.org/10.1016/J.ENCONMAN.2014.05.061.
[145] Kumar S, Heister SD, Xu X, Salvador JR, Meisner GP. Thermoelectric generators for automotive waste heat recovery systems part II: Parametric evaluation and topological studies. Journal of Electronic Materials 2013;42:944–55. https://doi.org/10.1007/S11664-013-2472-8.
[146] Tang ZB, Deng YD, Su CQ, Yuan XH. Fluid Analysis and Improved Structure of an ATEG Heat Exchanger Based on Computational Fluid Dynamics. J. Electron. Mater. 2014;44:1554–61. https://doi.org/10.1007/s11664-014-3472-z.
[147] Wang Y, Li S, Zhang Y, Yang X, Deng Y, Su C. The influence of inner topology of exhaust heat exchanger and thermoelectric module distribution on the performance of automotive thermoelectric generator. Energy Convers Manag 2016;126:266–77. https://doi.org/10.1016/j.enconman.2016.08.009.
[148] Wang X, Deng Y. Research on and Thermal Performance of the Heat Exchanger in Automotive Exhaust-Based Thermoelectric Generator. SAE Technical Paper 2014. https://doi.org/10.4271/2014-01-2594.
[149] Yuan X, Bai W, Deng Y, Su C, Liu X, Liu C, et al. Numerical investigation on the performance of an automotive thermoelectric generator integrated with a three-way catalytic converter. J Renew Sustain Energy 2016:8. https://doi.org/10.1063/1.4962028.
[150] Brito FP, Pacheco N, Vieira R, Martins J, Martins L, Teixeira J, et al. Efficiency improvement of vehicles using temperature controlled exhaust thermoelectric generators. Energy Convers Manag 2020;203:112255. https://doi.org/10.1016/j.enconman.2019.112255.
[151] Cao Q, Luan W, Wang T. Performance enhancement of heat pipes assisted thermoelectric generator for automobile exhaust heat recovery. Appl Therm Eng 2018;130:1472–9. https://doi.org/10.1016/J.APPLTHERMALENG.2017.09.134.
[152] Brito FP, Martins J, Hançer E, Antunes N, Gonçalves LM. Thermoelectric exhaust heat recovery with heat pipe-based thermal control. J Electron Mater 2015;44: 1984–97. https://doi.org/10.1007/s11664-015-3638-3.

[153] Jang JC, Chi RG, Rhi SH, Lee KB, Hwang HC, Lee JS, et al. Heat pipe-assisted thermoelectric power generation technology for waste heat recovery. J Electron Mater 2015;44:2039–47. https://doi.org/10.1007/s11664-015-3653-4.
[154] Pacheco N, Brito FP, Vieira R, Martins J, Barbosa H, Goncalves LM. Compact automotive thermoelectric generator with embedded heat pipes for thermal control. Energy 2020;197:117154. https://doi.org/10.1016/j.energy.2020.117154.
[155] Klein Altstedde M, Rinderknecht F, Friedrich H. Integrating phase-change materials into automotive thermoelectric generators. J Electron Mater 2014;43:2134–40. https://doi.org/10.1007/s11664-014-2990-z.
[156] Huang K, Yan Y, Wang G, Li B. Improving transient performance of thermoelectric generator by integrating phase change material. Energy 2021;219:119648. https://doi.org/10.1016/j.energy.2020.119648.
[157] Yang Y, Wang S, He W. Simulation study on regenerative thermoelectric generators for dynamic waste heat recovery. Energy Procedia 2019;158:571–6. https://doi.org/10.1016/j.egypro.2019.01.154.
[158] Zhao Y, Wang S, Ge M, Liang Z, Liang Y, Li Y. Performance investigation of an intermediate fluid thermoelectric generator for automobile exhaust waste heat recovery. Appl Energy 2019;239:425–33. https://doi.org/10.1016/J.APENERGY.2019.01.233.
[159] Elghool A, Basrawi F, Ibrahim TK, Habib K, Ibrahim H, Idris D. A review on heat sink for thermo-electric power generation: classifications and parameters affecting performance. Energy Convers Manag 2017;134:260–77. https://doi.org/10.1016/j.enconman.2016.12.046.
[160] Lei X, Wang Y, Deng Y, Su C, Liu X, Chen G. Combined numerical and experimental investigation on the optimum coolant flow rate for automotive thermoelectric generators. J Electron Mater 2019;48:1981–90. https://doi.org/10.1007/s11664-018-06879-9.
[161] Tete PR, Gupta MM, Joshi SS. Developments in battery thermal management systems for electric vehicles: a technical review. J Energy Storage 2021;35:102255. https://doi.org/10.1016/J.EST.2021.102255.
[162] Luo D, Yan Y, Wang R, Zhou W. Numerical investigation on the dynamic response characteristics of a thermoelectric generator module under transient temperature excitations. Renew Energy 2021;170:811–23. https://doi.org/10.1016/j.renene.2021.02.026.
[163] Li X, Xie C, Quan S, Shi Y, Tang Z. Optimization of thermoelectric modules' number and distribution pattern in an automotive exhaust thermoelectric generator. IEEE Access 2019;7:72143–57. https://doi.org/10.1109/ACCESS.2019.2919689.
[164] Baranowski LL, Jeffrey Snyder G, Toberer ES. The misconception of maximum power and power factor in thermoelectrics. J Appl Phys 2014;115:126102. https://doi.org/10.1063/1.4869140.
[165] Chen M, Rosendahl LA, Condra TJ, Pedersen JK. Numerical modeling of thermoelectric generators with varing material properties in a circuit simulator. IEEE Trans Energy Convers 2009;24:112–24. https://doi.org/10.1109/TEC.2008.2005310.
[166] Vadstrup C, Schaltz E, Chen M. Individual module maximum power point tracking for thermoelectric generator systems. J Electron Mater 2013;42:2203–8. https://doi.org/10.1007/s11664-013-2571-6.
[167] Hertzke P, Müller N, Schenk S. The global electric-vehicle market is amped up and on the rise. McKinsey&Company; 2020. p. 1–8.
[168] IEA. Global EV outlook 2019. Paris: IEA; 2019. https://www.iea.org/reports/global-ev-outlook-2019. n.d.
[169] Dabadie JC, Le Berr F, Salzgeber K, Prenninger P. Evaluation of TEG potential in hybrid electric vehicle by simulation. Veh Therm Manag Syst Conf Exhib 2011:261–71. https://doi.org/10.1533/9780857095053.4.261.
[170] Oetringer K, Kober M, Altstedde MK. Upgrading hybrid-vehicles with a thermoelectric generator. In: Proceedings of the 9th international conference on ecological vehicles and renewable energies (EVER); 2014. p. 1–5. https://doi.org/10.1109/EVER.2014.6844021.
[171] Wang R, Yu W, Meng X. Performance investigation and energy optimization of a thermoelectric generator for a mild hybrid vehicle. Energy 2018;162:1016–28. https://doi.org/10.1016/J.ENERGY.2018.08.103.
[172] Hussain QE, Brigham DR, Maranville CW. Thermoelectric exhaust heat recovery for hybrid vehicles. SAE Int J Engines 2009;2:1132–42. https://doi.org/10.4271/2009-01-1327.
[173] Kim SKSH, Won BC, Rhi SH, Kim SKSH, Yoo JH, Jang JC. Thermoelectric power generation system for future hybrid vehicles using hot exhaust gas. J Electron Mater 2011;40:778–83. https://doi.org/10.1007/s11664-011-1569-1.
[174] Fang W, Quan S, Xie C, Tang X, Ran B, Jiao Y. Energy optimization for a weak hybrid power system of an automobile exhaust thermoelectric generator. J Electron Mater 2017;46:6617–27. https://doi.org/10.1007/s11664-017-5688-1.
[175] Deng YD, Fan W, Ling K, Su CQ. A 42-V electrical and hybrid driving system basedon a vehicular waste-heat thermoelectric generator. J Electron Mater 2012;41:1698–705. https://doi.org/10.1007/s11664-012-2068-8.
[176] Lan S, Rouaud C, Stobart R, Chen R, Yang Z, Zhao D. The potential of thermoelectric generator in parallel hybrid vehicle applications. SAE Tech Pap 2017. https://doi.org/10.4271/2017-01-0189.
[177] Muralidhar N, Himabindu M, Ravikrishna RV. Modeling of a hybrid electric heavy duty vehicle to assess energy recovery using a thermoelectric generator. Energy 2018;148:1046–59. https://doi.org/10.1016/J.ENERGY.2018.02.023.
[178] Saufi Sulaiman M, Singh B, Mohamed W. Experimental and theoretical study of thermoelectric generator waste heat recovery model for an ultra-low temperature PEM fuel cell powered vehicle. Energy 2019;179:628–46. https://doi.org/10.1016/j.energy.2019.05.022.
[179] Abbasi V, Tabar VS. Measurement and evaluation of produced energy by thermoelectric generator in vehicle. Measurement 2020;149:107035. https://doi.org/10.1016/J.MEASUREMENT.2019.107035.
[180] Bjørk R, Sarhadi A, Pryds N, Lindeburg N, Viereck P. A thermoelectric power generating heat exchanger: part I – experimental realization. Energy Convers Manag 2016;119:473–80. https://doi.org/10.1016/J.ENCONMAN.2016.04.042.
[181] Bosch H. From modules to a generator: an integrated heat exchanger concept for car applications of a thermoelectric generator. J Electron Mater 2016;45:1606–12. https://doi.org/10.1007/s11664-015-4129-2.
[182] Choi Y, Negash A, Kim TY. Waste heat recovery of diesel engine using porous medium-assisted thermoelectric generator equipped with customized thermoelectric modules. Energy Convers Manag 2019;197:111902. https://doi.org/10.1016/J.ENCONMAN.2019.111902.
[183] Gou X, Xiao H, Yang S. Modeling, experimental study and optimization on low-temperature waste heat thermoelectric generator system. Appl Energy 2010;87:3131–6. https://doi.org/10.1016/J.APENERGY.2010.02.013.
[184] Hsu CT, Yao DJ, Ye KJ, Yu B. Renewable energy of waste heat recovery system for automobiles. J Renew Sustain Energy 2010;2:13105. https://doi.org/10.1063/1.3289832.
[185] Huang GY, Hsu CT, Fang CJ, Yao DJ. Optimization of a waste heat recovery system with thermoelectric generators by three-dimensional thermal resistance analysis. Energy Convers Manag 2016;126:581–94. https://doi.org/10.1016/J.ENCONMAN.2016.08.038.
[186] deok In B, ik Kim H, wook Son J, Hyung Lee K. The study of a thermoelectric generator with various thermal conditions of exhaust gas from a diesel engine. Int J Heat Mass Transf 2015;86:667–80. https://doi.org/10.1016/j.ijheatmasstransfer.2015.03.052.
[187] Karri MA, Thacher EF, Helenbrook BT. Exhaust energy conversion by thermoelectric generator: two case studies. Energy Convers Manag 2011;52:1596–611. https://doi.org/10.1016/J.ENCONMAN.2010.10.013.
[188] Kim TY, Kwak J, Kim B. Energy harvesting performance of hexagonal shaped thermoelectric generator for passenger vehicle applications: an experimental approach. Energy Convers Manag 2018;160:14–21. https://doi.org/10.1016/j.enconman.2018.01.032.
[189] Kim TY, Negash AA, Cho G. Waste heat recovery of a diesel engine using a thermoelectric generator equipped with customized thermoelectric modules. Energy Convers Manag 2016;124:280–6. https://doi.org/10.1016/J.ENCONMAN.2016.07.013.
[190] Kim TY, Negash A, Cho G. Experimental and numerical study of waste heat recovery characteristics of direct contact thermoelectric generator. Energy Convers Manag 2017;140:273–80. https://doi.org/10.1016/J.ENCONMAN.2017.03.014.
[191] Lan S, Yang Z, Stobart R. Winward E. The Influence of Thermoelectric Materials and Operation Conditions on the Performance of Thermoelectric Generators for Automotive. SAE Tech. Pap., SAE International 2016. https://doi.org/10.4271/2016-01-0219. https://www.sae.org/publications/technical-papers/content/2016-01-0219/.
[192] Li Z, Tan G, Cai J, Yang Z, et al. Thermoelectric Module Temperature Stability Control for the Vehicle Engine Exhaust Heat Recovery. SAE Technical Paper 2015. https://doi.org/10.4271/2015-01-0350. 2015-01-0350.
[193] Liu X, Deng YD, Li Z, Su CQ. Performance analysis of a waste heat recovery thermoelectric generation system for automotive application. Energy Convers Manag 2015;90:121–7. https://doi.org/10.1016/J.ENCONMAN.2014.11.015.
[194] Magnetto D. HeatReCar: first light commercial vehicle equipped with a TEG. In: 3rd International Conference Thermal Management for EV/HEV, Darmstadt, Germany, 24–26 June 2013; 2021. https://www.iqpc.com/media/8360/10686.pdf.
[195] Massaguer A, Massaguer E, Comamala M, Pujol T, González JR, Cardenas MD, et al. A method to assess the fuel economy of automotive thermoelectric generators. Appl Energy 2018;222:42–58. https://doi.org/10.1016/J.APENERGY.2018.03.169.
[196] Zhang Y, Cleary M, Wang X, Kempf N, Schoensee L, Yang J, et al. High-temperature and high-power-density nanostructured thermoelectric generator for automotive waste heat recovery. ENERGY Convers Manag 2015;105:946–50. https://doi.org/10.1016/j.enconman.2015.08.051.
[197] Temizer İ, İlkılıç C. The performance and analysis of the thermoelectric generator system used in diesel engines. Renew Sustain Energy Rev 2016;63:141–51. https://doi.org/10.1016/J.RSER.2016.04.068.
[198] Nour Eddine A, Sara H, Chalet D, Faure X, Aixala L, Cormerais M. Modeling and simulation of a thermoelectric generator using bismuth telluride for waste heat recovery in automotive diesel engines. J Electron Mater 2019;48:2036–45. https://doi.org/10.1007/s11664-019-06999-w.
[199] Ezzitouni S, Fernández-Yáñez P, Sánchez L, Armas O, Soto F. Effect of the use of a thermoelectric generator on the pumping work of a diesel engine. Int J Engine Res 2021;22:1016–27. https://doi.org/10.1177/1468087419868047.
[200] Ivanov K, Aleksandrov A. Design and Study of an automotive thermoelectric generator. In: Proceedings of the 7th international conference on energy

efficiency and agricultural engineering (EE&AE); 2020. p. 1–4. https://doi.org/10.1109/EEAE49144.2020.9279082.
[201] Kim TY, Kwak J, Kim B. Application of compact thermoelectric generator to hybrid electric vehicle engine operating under real vehicle operating conditions. Energy Convers Manag 2019;201:112150. https://doi.org/10.1016/J.ENCONMAN.2019.112150.
[202] Kunt MA, Gunes H. Comparing the recovery performance of different thermoelectric generator modules in an exhaust system of a diesel engine both experimentally and theoretically. Proc Inst Mech Eng Part D J Automob Eng 2020;234:183–90. https://doi.org/10.1177/0954407019837786.
[203] Negash AA, Choi Y, Kim TY. Experimental investigation of optimal location of flow straightener from the aspects of power output and pressure drop characteristics of a thermoelectric generator. Energy 2021;219:119565. https://doi.org/10.1016/j.energy.2020.119565.
[204] Ramírez R, Gutiérrez AS, Cabello Eras JJ, Hernández B, Duarte Forero J. Data supporting the evaluation of the energy recovery potential of thermoelectric generators in diesel engines. Data Br 2020;28. https://doi.org/10.1016/j.dib.2019.105075.
[205] Temizer I, Yuksel T, Can I, Alnak D. Analysis of an automotive thermoelectric generator on a gasoline engine. Therm Sci 2020;24:137–45. https://doi.org/10.2298/tsci180105096t.
[206] Zhang R, Zhang H, Wang X. Lateral comparison of the coupling parameters on the novel hexagonal shaped cross flow thermoelectric generator. Energy 2021;215:119163. https://doi.org/10.1016/j.energy.2020.119163.
[207] Karana DR, Sahoo RR. Thermal, environmental and economic analysis of a new thermoelectric cogeneration system coupled with a diesel electricity generator. Sustain Energy Technol Assess 2020;40:100742. https://doi.org/10.1016/j.seta.2020.100742.
[208] Quan R, Liu G, Wang C, Zhou W, Huang L, Deng Y. Performance investigation of an exhaust thermoelectric generator for military SUV application. Coatings 2018;8. https://doi.org/10.3390/coatings8010045.
[209] Aranguren P, Araiz M, Astrain D, Martínez A. Thermoelectric generators for waste heat harvesting: a computational and experimental approach. Energy Convers Manag 2017;148:680–91. https://doi.org/10.1016/J.ENCONMAN.2017.06.040.
[210] Baker C, Vuppuluri P, Shi L, Hall M. Model of heat exchangers for waste heat recovery from diesel engine exhaust for thermoelectric power generation. J Electron Mater 2012;41:1290–7. https://doi.org/10.1007/s11664-012-1915-y.
[211] Demir ME, Dincer I. Performance assessment of a thermoelectric generator applied to exhaust waste heat recovery. Appl Therm Eng 2017;120:694–707. https://doi.org/10.1016/j.applthermaleng.2017.03.052.
[212] Deng YD, Hu T, Su CQ, Yuan XH. Fuel economy improvement by utilizing thermoelectric generator in heavy-duty vehicle. J Electron Mater 2017. https://doi.org/10.1007/s11664-016-4996-1.
[213] Du Q, Diao H, Niu Z, Zhang G, Shu G, Jiao K. Effect of cooling design on the characteristics and performance of thermoelectric generator used for internal combustion engine. Energy Convers Manag 2015;101:9–18. https://doi.org/10.1016/j.enconman.2015.05.036.
[214] Durand T, Dimopoulos Eggenschwiler P, Tang Y, Liao Y, Landmann D. Potential of energy recuperation in the exhaust gas of state of the art light duty vehicles with thermoelectric elements. Fuel 2018;224:271–9. https://doi.org/10.1016/J.FUEL.2018.03.078.
[215] Espinosa N, Lazard M, Aixala L, Scherrer H. Modeling a thermoelectric generator applied to diesel automotive heat recovery. J Electron Mater 2010;39:1446–55. https://doi.org/10.1007/s11664-010-1305-2.
[216] He W, Wang S. Thermoelectric performance optimization when considering engine power loss caused by back pressure applied to engine exhaust waste heat recovery. Energy 2017;133:584–92. https://doi.org/10.1016/j.energy.2017.05.133.
[217] He W, Wang S, Lu C, Zhang X, Li Y. Influence of different cooling methods on thermoelectric performance of an engine exhaust gas waste heat recovery system. Appl Energy 2016;162:1251–8. https://doi.org/10.1016/j.apenergy.2015.03.036.
[218] Lan S, Yang Z, Stobart R, Chen R. Prediction of the fuel economy potential for a skutterudite thermoelectric generator in light-duty vehicle applications. Appl Energy 2018;231:68–79. https://doi.org/10.1016/J.APENERGY.2018.09.087.
[219] Ma X, Shu G, Tian H, Xu W, Chen T. Performance assessment of engine exhaust-based segmented thermoelectric generators by length ratio optimization. Appl Energy 2019;248:614–25. https://doi.org/10.1016/J.APENERGY.2019.04.103.
[220] Yu S, Du Q, Diao H, Shu G, Jiao K. Effect of vehicle driving conditions on the performance of thermoelectric generator. Energy Convers Manag 2015;96:363–76. https://doi.org/10.1016/j.enconman.2015.03.002.
[221] Yang H, Shu G, Tian H, Ma X, Chen T, Liu P. Optimization of thermoelectric generator (TEG) integrated with three-way catalytic converter (TWC) for harvesting engine ' s exhaust waste heat. Appl Therm Eng 2018;144:628–38. https://doi.org/10.1016/j.applthermaleng.2018.07.091.
[222] Zheng S, Fan W. Simulations of TEG-based vehicle power system's impact on the fuel economy of hybrid and conventional vehicles. SAE Tech. Pap. 2016. https://doi.org/10.4271/2016-01-0900.
[223] Garud KS, Seo JH, Patil MS, Bang YM, Pyo YD, Cho CP, et al. Thermal–electrical–structural performances of hot heat exchanger with different internal fins of thermoelectric generator for low power generation application, 143. Springer International Publishing; 2021. https://doi.org/10.1007/s10973-020-09553-7. Vol.
[224] Luo D, Wang R, Yu W, Sun Z, Meng X. Heating for and different analysis of energy recovery potential types of conventional vehicles with a thermoelectric generator of conventional vehicles with a thermoelectric generator Assessing the f. Energy Procedia 2019;158:142–7.
[225] Luo D, Wang R, Yu W, Zhou W. A novel optimization method for thermoelectric module used in waste heat recovery. Energy Convers Manag 2020;209:112645. https://doi.org/10.1016/j.enconman.2020.112645.
[226] Luo D, Wang R, Yu W, Zhou W. A numerical study on the performance of a converging thermoelectric generator system used for waste heat recovery. Appl Energy 2020;270:115181. https://doi.org/10.1016/j.apenergy.2020.115181.
[227] Shishov KA. Selection of the design of a hot heat exchanger of an automotive thermoelectric generator for an urban driving cycle. J Phys Conf Ser 2019;1410:6–12. https://doi.org/10.1088/1742-6596/1410/1/012240.
[228] Sunawar A, Garniwa I, Hudaya C. The characteristics of heat inside a parked car as energy source for thermoelectric generators. Int J Energy Environ Eng 2019;10:347–56. https://doi.org/10.1007/s40095-019-0311-2.
[229] Xiao GQ, Zhang Z. Coupled simulation of a thermoelectric generator applied in diesel engine exhaust waste heat recovery. Therm Sci 2020;24:281–92. https://doi.org/10.2298/tsci181112322x.
[230] Yang Y, Wang S, Zhu Y. Evaluation method for assessing heat transfer enhancement effect on performance improvement of thermoelectric generator systems. Appl Energy 2020;263:114688. https://doi.org/10.1016/j.apenergy.2020.114688.
[231] Zhang F, Cheng L, Wu M, Xu X, Wang P, Liu Z. Performance analysis of two-stage thermoelectric generator model based on Latin hypercube sampling. Energy Convers Manag 2020;221:113159. https://doi.org/10.1016/j.enconman.2020.113159.
[232] Dzulkfli MS, Pesyridis A, Gohil D. Thermoelectric generation in hybrid electric vehicles. Energies 2020;13. https://doi.org/10.3390/en13143742.

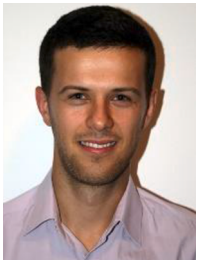

Nicolae Vlad BURNETE Dr. Nicolae Vlad Burnete is a member of the Romanian Society of Automotive Engineers and International Society of Automotive Engineers and Lecturer in the Automotive Engineering and Transports Department at the Technical University of Cluj-Napoca (TUCN). He received his Ph.D. in Mechanical Engineering from TUCN (2016), as well as an M.S. (2013) and an B.S. in Automotive Engineering (2011). He is currently a post-doctoral research fellow at TUCN where he is developing his thesis on "Increasing the global efficiency of internal combustion engines through waste heat recovery with thermoelectric generators". Dr. Burnete's research focus is on renewable energy solutions for a sustainable future. Dr. Burnete has been involved in multiple projects and research activities involving engine-fuel interactions, urban transport, biofuels, energy recovery and energy efficiency of vehicles. Dr. Burnete has published over 20 conference and peer reviewed articles and received several awards for his work.

Florin MARIASIU Dr. habil. Florin Mariasiu is full professor at Technical University of Cluj-Napoca (TUCN), Automotive and Transport Engineering. He received his PhD in Mechanical Engineering from TUCN (2003) as well as his habilitation degree in Mechanical Engineering (2015) from TUCN. Domains of research and interest are renewable and sustainable energetic solution for mechanical and thermal systems, electric and hybrid vehicles power sources, batteries thermal management and batteries in terms of applied and theoretical approaches. The results of dr.habil. Florin Mariasiu research activity can be resumed as 2 patents, 5 patent applications, 11 books, over 100 published scientific articles, over 200 citations and over 20 prizes and awards for research and innovation activity in fields of Mechanical and Automotive Engineering.

Christopher DEPCIK Dr. Christopher Depcik is an American Society of Mechanical Engineers Fellow and Professor in the Mechanical Engineering Department at the University of Kansas (KU). In addition, he has a Courtesy Appointment in the Aerospace Engineering Department. Prior to joining KU, he worked at the University of Michigan (UM) as a post-doctoral research fellow and lecturer. He received his Ph.D. in Mechanical Engineering from UM (2003), as well as an M.S. in Aerospace Engineering (2002), and an M.S. in Mechanical Engineering (1999). He received his B.S. in Mechanical Engineering from the University of Florida (1997). Dr. Depcik's laboratory conducts research revolving around a sustainable approach to energy and the transportation infrastructure. This includes analysis of electric vehicles, biofuels, combustion, and energy recovery potential. His group has published over 100-refereed articles and Dr. Depcik received the Society of Automotive Engineers Ralph R. Teetor Award for his transportation-related research and educational activities.

Istvan BARABAS Dr. Istvan Barabas is a Romanian Society of Automotive Engineers Fellow, member of public body of Hungarian Academy of Sciences and Professor in the Automotive Engineering and Transports Department at the Technical University of Cluj-Napoca (TUCN). He received his Ph.D. in Mechanical Engineering from TUCN (2003). His main research interests are biofuel & bioenergy, properties of fuel blends, and nano-additives for fuels and lubricating oils. He has published more than 150 conference and scientific journal papers. He is also the author of several books concerning automotive fuels. Dr. Barabas serves as a member of the editorial board of the Periodica Polytechnica Transportation Engineering and Technical Review journals and serves on the advisory or organizing committees of several international conferences.

Dan MOLDOVANU Dr. Dan Moldovanu is a member of Romanian Society of Automotive Engineers, International Society of Automotive Engineers, and International Federation of Automotive Experts. He is an Associate Professor in the Automotive Engineering and Transports Department at the Technical University of Cluj-Napoca (TUCN). He received his Ph.D. in Mechanical Engineering from TUCN (2011), M.S. in Mechanical Engineering (2009) and B.S. in Mechatronics (2008). Dr. Moldovanu is a member/researcher of the Testing, Certification and Research of Internal Combustion Engines Laboratory (TUCN), with focus on Internal combustion engines testing, HIL testing, and MATLAB simulation of automotive components. Dr. Moldovanu has published over 20 peer reviewed articles and received several awards for his publications. Dr. Moldovanu has been involved in projects and research activities involving engine-fuel interactions, cold start testing, biofuels and energy recovery.

COMPUTATIONAL FLUID DYNAMICS SIMULATION OF A SINGLE CYLINDER RESEARCH ENGINE WORKING WITH BIODIESEL

by

Dan MOLDOVANU* * *and Nicolae BURNETE

Automotive Department, Technical University of Cluj-Napoca, Cluj-Napoca, Romania

Original scientific paper
DOI: 10.2298/TSCI111004021M

The main objective of the paper is to present the results of the computational fluid dynamics simulation of a direct injection single cylinder engine using diesel, biodiesel, or different mixture proportions of diesel and biodiesel and compare the results to a test bed measurement in the same functioning point.
The engine used for verifying the results of the simulation is a single cylinder research engine from AVL with an open engine control unit, so that the injection timings and quantities can be controlled and analyzed.
In Romania, until the year 2020 all the fuel stations are obliged to have mixtures of at least 10% biodiesel in diesel. The main advantages using mixtures of biofuels in diesel are: the fact that biodiesel is not harmful to the environment; in order to use biodiesel in your engine no modifications are required; the price of biodiesel is smaller than diesel and also if we compare biodiesel production to the classic petroleum based diesel production, it is more energy efficient; biodiesel assures more lubrication to the engine so the life of the engine is increased; biodiesel is a sustainable fuel; using biodiesel helps maintain the environment and it keeps the people more healthy.

Key words: *computational fluid dynamics simulation, single cylinder research engine, biodiesel, rapeseed oil.*

Introduction

In the last years, computational fluid dynamics (CFD) modeling was improved to simulate 3-D flows, mixture formation, burning and pollutant formation for direct injection engines.

In the engine development process, CFD modeling of direct injection engine is used to analyze the interaction between the fuel and the motion of the intake air inside the combustion chamber. The scope is to minimize the prototyping time and to identify solutions with high success rate, in an early stage of the project. The success is based on the capability to make numerous studies, including different shapes for the combustion chamber, for the piston, for the admission pipes, in a relatively short time, based on the computational power [1-11].

In the last years, due to an intense world request, a lot of simulation models have been developed using CFD code. The continuous request for answers regarding direct injection engines, the characteristics, and performance of calculation systems, in many cases can't be satisfied with own codes. In this context, AVL FIRE is a world leader for the CFD simulation solutions, and can always be upgraded with own generated code.

The program used for simulation is AVL FIRE, and for the simulation, for the combustion model, Eddy break-up model was used, for the auto-ignition model Diesel_MIL (multiple ignition location), and for NO formation the original Heywood model.

* Corresponding author; e-mail: dan.moldovanu@auto.utcluj.ro

The Eddy break-up model is the typical example of mixed-is-burnt combustion model. It is based on the works [12-16] and can be found in all commercial CFD packages. The model assumes that the reactions are completed at the moment of mixing, so that the reaction rate is completely controlled by turbulent mixing. Combustion is then described by a single step global chemical reaction:

$$F + v_s\mathrm{O} \rightarrow (1 + v_s)P \tag{1}$$

in which F stands for fuel, O for oxidizer, and P for products of the reaction. Alternatively we can have a multistep scheme, where each reaction has its own mean reaction rate.

In AVL FIRE the mean reaction rate is written:

$$\overline{\rho \dot{r}_{\mathrm{fu}}} = \frac{C_{\mathrm{fu}}}{\tau_{\mathrm{R}}} \bar{\rho} \min\left(\bar{y}_{\mathrm{fu}}, \frac{\bar{y} O_x}{S}, \frac{C_{\mathrm{Pr}} \bar{y} \mathrm{Pr}}{1+S} \right) \tag{2}$$

The first two terms of the "minimum value of" operator "min" simply determine whether fuel or oxygen is present in limiting quantity, and the third term is a reaction probability which ensures that the flame is not spread in the absence of hot products. C_{fu} and C_{Pr} are empirical coefficients and τ_{R} is the turbulent mixing time scale for reaction.

The value of the empirical coefficient C_{fu} has been shown to depend on turbulence and fuel parameters. Hence, C_{fu} requires adjustment with respect to the experimental combustion data for the case under investigation [17].

Boundary definition

The simulations were made in order to understand in more detail the processes that occur and the behavior of the air-fuel mixture inside the combustion chamber.

The objectives are structured in the following way:

- investigation of the air flow inside the combustion chamber, to understand the effects that the intake pipes shape have on the flow and the effects of the bowl of the piston on the air-fuel mixture and on the flow structure,
- the study on the shape of the injection, and
- study of the swirl coefficient, injection parameters, pressure, temperature, and the combustion equivalence ratio in the combustion chamber.

All investigations were made in AVL FIRE, and the verification of the results was made in the Technical University of Cluj-Napoca, on the test bed from the automotive department.

The point chosen for simulation is 4000 rpm and an IMEP of 4 bar because it best represents the engine operation points.

The accuracy of the simulations depends on the prediction capability of the used models, adopted for injection simulation, propagation of the injection, burn, and pollutant formation.

The initial data regarding the dimensions of the single cylinder engine are presented in tab. 1. Table 2 presents the timings and quantities of the injected fuel.

In conformity with tab. 2, fig. 1 presents the injection laws for pilot and main injection. Due to the injector needle lift, the real injection law has looks a little different than the theoretical one; and because of the delay between the energizing of the injector and the actual needle lift, the injection used in the simulation is delayed, but the injected quantity remains the same (the area between the graph and the horizontal axis).

Table 1. Engine specifications

Type	Value	Unit
Bore	85	mm
Stroke	90	mm
Fuel system	Natural aspirated	–
Injection system	Common rail	–
Maximum speed	4200	rpm

Table 2. Injection timings

Injection time	SOI	EOI	Quantity [mm^3]	Quantity [mg]
Pilot	692	695	2.9	2.5
Main	701	725	23.83	20.1

SOI – start of injection; EOI – end of injection

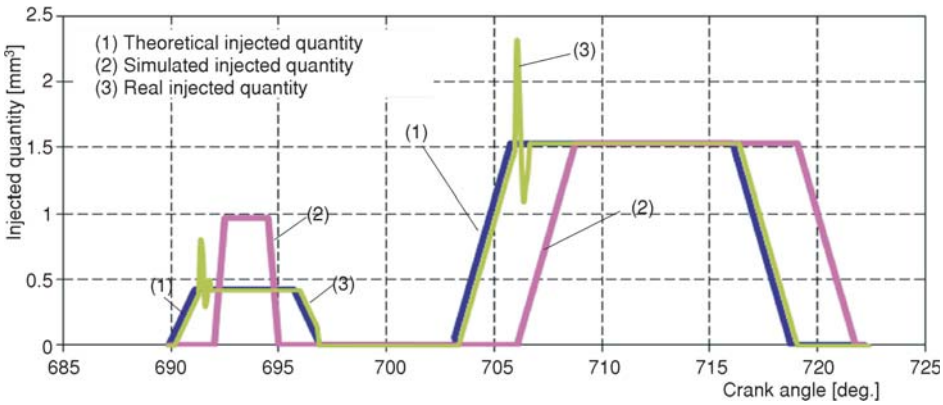

Figure 1. Theoretical, simulated, and real injection laws for pilot and main injection

The combustion chamber geometry and the created mesh are presented in fig. 2. The maximum number of cells in the moving mesh is 1.5 million.

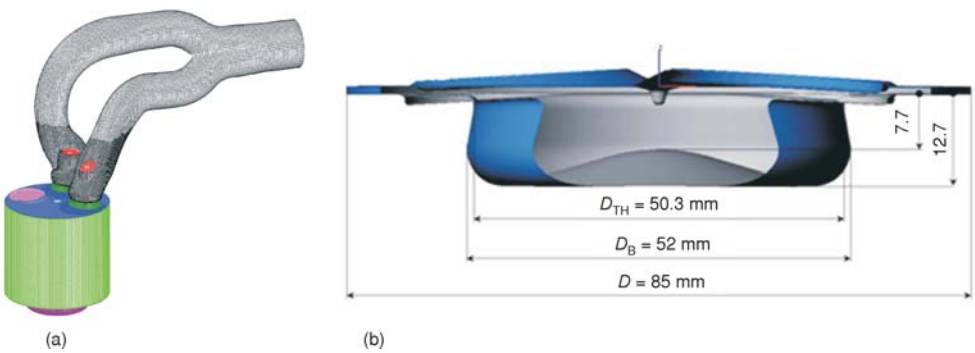

Figure 2. Used moving mesh (a) and the combustion chamber geometry (b)

Results and discussions

The obtained results were processed with the post-processing module AVL IMPRESS, using user defined programs and MS Excel.

Flow speeds

The flow speed of the air entering the combustion chamber is important to monitor for the filling of the chamber, to notice the air currents and to improve the flow parameters. Also the swirl coefficient was studied because it has a great influence on the injection process.

The results are presented in figs. 3 and 4, for the maximum opening of the intake valves.

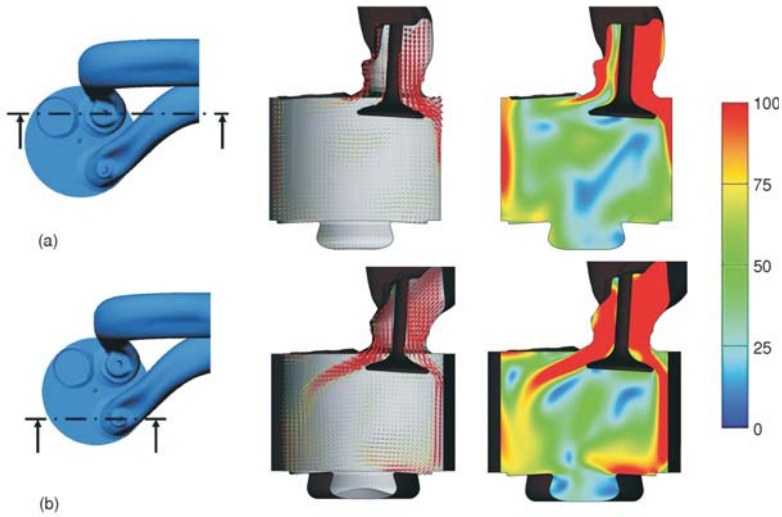

Figure 3. Vectorial and surface views of the flow velocities at 450° CA (a) in the helical port, (b) in the tangential port
(for color image see journal web site)

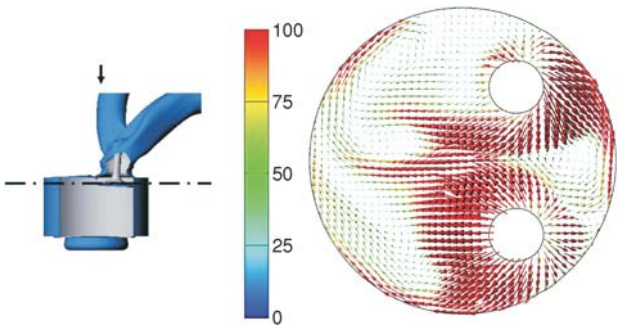

Figure 4. Top vectorial view of the flow velocities at maximum intake valves opening
(for color image see journal web site)

The role of the helical port can be seen better in the vectorial view, fig. 4:

– to create the proper swirl;
  and the role of the tangential port (better seen in the surface view, fig. 3):
– to ensure the correct air flow;
  that is why in the tangential port the red area with the speed of 100 m/s is bigger.

Swil coefficient

The swirl coefficient data were generated with the help of a function implemented in AVL FIRE. The swirl coefficient rises from 0° CA to 480° CA to a value of 2.4 and then decreases to 1.9 at 680° CA.

The most important points of the swirl coefficient are:

– intake valve closing (580° CA), where the swirl coefficient is 2.04, and
– injection start (692° CA), where the swirl coefficient is 2.09.

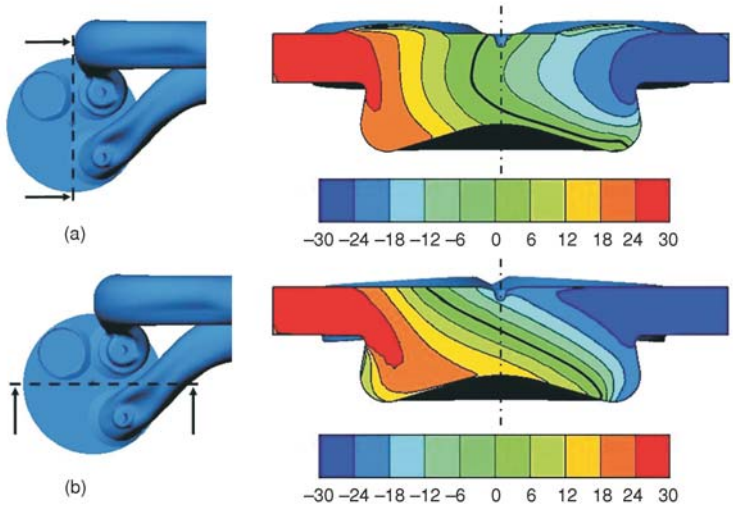

Figure 5. Swirl analysis (flow velocities) at 690 deg CA
(a) section perpendicular on Oy axis (b) section perpendicular on Ox axis
(for color image see journal web site)

It is important to know the shape of the flow at maximum intake valves opening (fig. 5), and to know the axis around which the air is swirling because this axis should coincide with the cylinder axis [18]. The axis analysis is presented in fig. 6.

By studying the swirl coefficient we can see that the swirl axis almost coincides with the cylinder axis, which is good, because it influences equally all the injection cones; fact also confirmed with the cuts perpendicular on the cylinder axis in fig. 6.

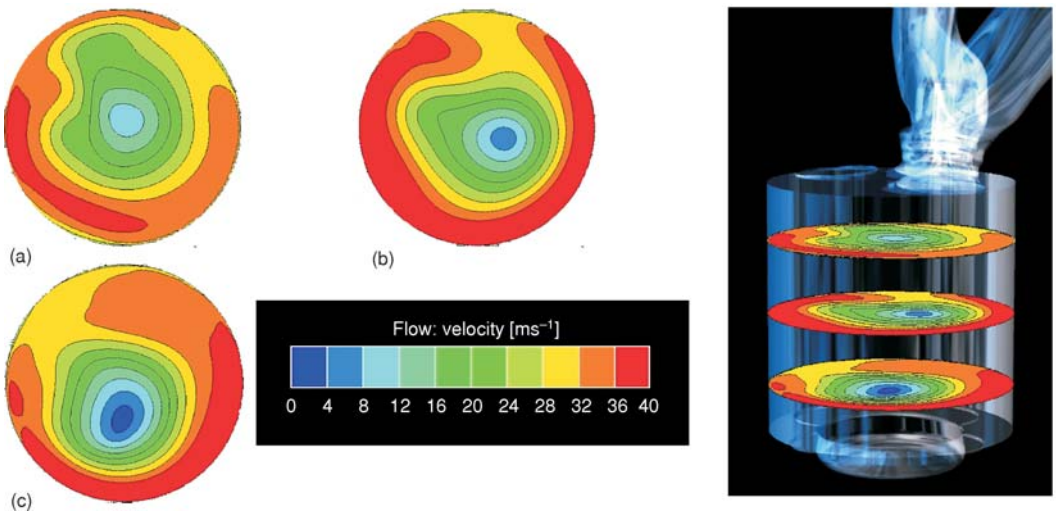

Figure 6. Rotation axis of the air flow in the combustion chamber; cut at (a) 1/4 stroke, (b) 1/2 stroke, and (c) 3/4 stroke (for color image see journal web site)

Combustion equivalence ratio

Figure 7 represents the variation of the combustion equivalence ratio during the pilot and main injection. The effect of the swirl can be seen, as the injection cones tend to rotate clockwise, which ensures a better air-fuel mixture, and there for a better combustion.

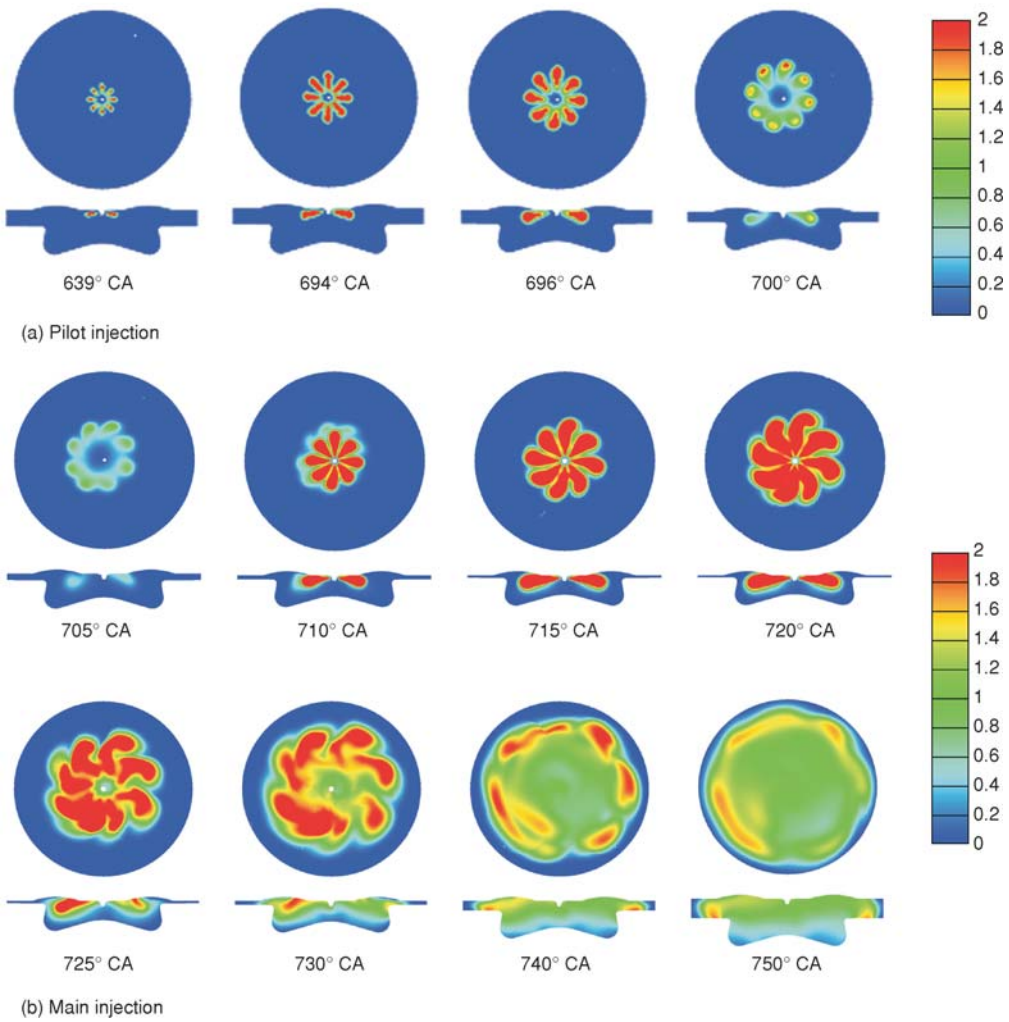

Figure 7. Evolution of the combustion equivalence ratio of the pilot and main injection
(for color image see journal web site)

Jet penetration

Simulations were made using diesel, B10 (10% rapeseed oil + 90% diesel), B20, and B50, the biodiesel blends have different lower calorific values and different densities, which are presented in tab. 3.

Because the density rises for B50, B20, and B10 in comparison to diesel, the penetration of the fuel, for the same injection pressure, is different, and it is presented in fig. 8. It can be

Table 3. Lower calorific value and density of different blends of biodiesel in comparison to diesel [19]

Fuel	Composition	Lower calorific value [kJkg^{-1}]	Density [kgm^{-3}]
Diesel	Diesel 100%	43200	830
B10	10% rapeseed + 90% diesel	42780	835
B20	20% rapeseed + 80% diesel	42360	840
B50	50% rapeseed + 50% diesel	41100	855

seen that the maximum penetration of the fuel jet when using B50 is 18 mm, in comparison to 15.2 mm for B20, 14.8 mm for B10, and 13.6 mm for diesel. Comparing the obtained results with the experimental research made by Mariasiu [19], it seems that the biofuels penetration is directly influenced by the turbulence of engine fluid inside the combustion chamber. The immediate effect is reducing of the smoke pollutant emissions.

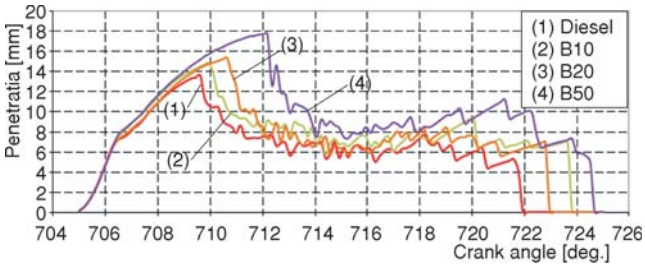

Figure 8. Fuel jet penetration using different blends of biodiesel

Cylinder pressure

The cylinder pressure is presented in fig. 9. The differences between diesel and biodiesel blends can be seen, because if the mixture contains more rapeseed oil, the lower calorific value of the obtained biodiesel decreases.

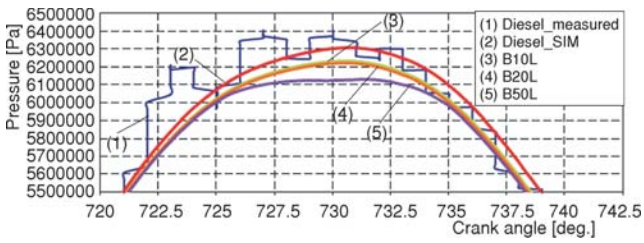

Figure 9. Cylinder pressure for diesel, B10, B20, and B50

The cylinder pressure was measured with a piezoelectric sensor placed in the combustion chamber and results were collected with an INDI Module from AVL.

The pressure inside the combustion chamber using pure diesel is 63.29 bar, for B10 it is 62.18 bar, for B20 it is 62.32 bar, and for B50 it is 61.26 bar; so the pressure decreases to 97% using B50 in comparison to pure diesel.

Temperature in the combustion chamber

The temperature inside the combustion chamber during the diesel and biodiesel burn is presented in fig. 10.

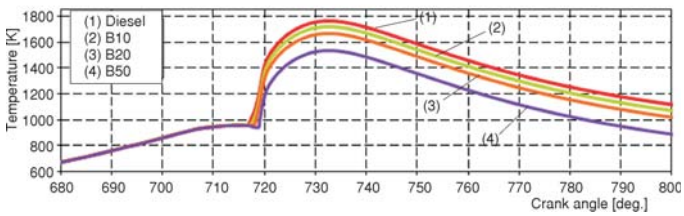

Figure 10. The temperature inside the combustion chamber using the biodiesel blends

The temperature inside the combustion chamber reaches from 1761 K (when using die-

sel) to 1534 K (when using B50), so the temperature decreases to 87% when using B50, to 94% when using B20, and to 97% when using B10 in comparison to diesel.

Conclusions

In the present study the flow velocities during the intake were analyzed. The role of the tangential and helical intake port were underlined, the swirl axis was also analyzed. The axis of the swirl is well centered so the influence on the fuel injection cones is uniform.

Also the diesel, B10, B20, and B50 combustion has been simulated and the equivalence ratio, cylinder pressure, cylinder temperature and fuel jet penetration were investigated.

The cylinder pressure for the diesel fuel was also measured on the test bed, because of the A and B constants from the Eddy break-up model used for the combustion. The constants were kept and the simulation was restarted using B10, B20, and B50, respectively; the pressure and temperature curves were extracted.

When using biodiesel blends, due to the higher density, the penetration increases with the percentage of biodiesel in diesel. But due to the decrease of the lower calorific value, the cylinder pressure drops to 97% and the temperature also drops to 87%. But the advantage when using biofuels is mainly the lower emissions [20-22].

The authors wanted to underline the importance of test bed measurements before simulating the processes inside the single cylinder research engine. The methodology of the research followed a few logical steps: first, the measurements on the test bed were made in a very well chosen working point, in order to obtain the best views for the movement of the air inside the cylinder; secondly, the surface of the cylinder head, piston head, injector tip, valves and other important surfaces were measured and built in a computer aided design software and imported in AVL FIRE; thirdly, the boundaries were named in order to create different cell sizes for different selections like the valve tips; forth step, we created the solver steering file where the inputs were the temperatures, pressures from the test bed in order to create the real simulation conditions.

After the simulation was done, all the necessary data were extracted and processed in order to be presented in a traditional way.

Also, the authors wanted to underline the advantages of using a simulation based on test bed measurements, like: by measuring the cylinder pressure, atmospheric pressure and temperature, and the sizes of the engine elements, the simulation was able to generate including the movement of the air inside the cylinder, and much more needed data, also the fuel can be changed easily and the simulation should run again to generate a new set of data.

Acknowledgments

This study was supported by the Technical University of Cluj-Napoca (Automotive department, and the PRODOC Ph. D. Project) in co-operation with AVL GmbH, Graz, Austria. The author gratefully acknowledges the support for this work from both sides.

Nomenclature

CA – crank angle
C_{fu}, C_{Pr} – empirical coefficients
D – piston diameter
D_B – piston bowl diameter
D_{TH} – piston throat diameter
deg. – degrees
F – fuel quantity
O – oxygen quantity
P – products of reaction quantity
τ_R – the turbulent mixing time scale for reaction

References

[1] Priesching, P., *et al*., 3-D-CFD Modeling of Conventional and Alternative Diesel Combustion and Pollutant Formation – A Validation Study, JSAE F&L 2007, JSAE 20077285, SAE paper 2007-01-1907, 2007
[2] Ranjbar, A., *et al*., Computational Study of the Effect of Different Injection Angle on Heavy Duty Engine, *Thermal Science, 13* (2009), 3, pp. 9-21
[3] Tatschl, R., *et al.*, FIRE – A Generic CFD Platform for DI Diesel Engine Mixture Formation and Combustion Simulation. International Multidimensional Modeling User's Group Meeting at the SAE Congress, Detroit, Mich., USA, 2001
[4] Tatschl, R., *et al*., A Comprehensive CFD Workflow for the Modeling of Gasoline DI Engines, The 1st National Congress on Fluids Engineering, Muju Resort, Korea, 2000
[5] ***, AVL FIRE Physics and Chemistry Help Manual
[6] Jafarmadar, S., *et al*., Numerical Investigation of the Effect of Fuel Injection Mode on Spray/Wall Interaction and emission Formation in a Direct Injection Diesel Engine at Full Load State, *Thermal Science, 14* (2010), 4, pp. 1039-1049
[7] Abe-El Aziz, M. S., Effect of Variable Viscosity and Suction/Injection on Thermal Boundary Layer of a Non-Newtonian Power-Law Fluids Past a Power-Law Stretched Surface, *Thermal Science, 14* (2010), 4, pp. 1111-1120
[8] Pitta, S. R., *et al.*, A Computational Fluid Dynamics Analysis on Stratified Scavenging System of Medium Capacity Two-Stroke Internal Combustion Engines, *Thermal Science, 12* (2008), 1, pp. 33-42
[9] Ganapathy, T., *et al.*, Artificial Neural Network Modeling of Jatropha Oil Fueled Diesel Engine for Emission Predictions, *Thermal Science, 13* (2009), 3, pp. 91-102
[10] Khalilarya, S., *et al*., Determination of Flow Pattern and its Effect on NO_x Emission in a Tangentially fired single chamber square furnace, *Thermal Science, 14* (2010), 2, pp. 493-503
[11] Kozic, M. S., *et al*., Numerical Simulation of Multiphase Flow in Ventilation Mill and Channel with Louvers and Centrifugal Separator, *Thermal Science, 15* (2011), 3, pp. 677-689
[12] Heywood, J. B., Internal Combustion Engine Fundamentals, Second Series, McGrawHill Book Company, New York, USA, 1988
[13] Magnussen, B. F., Hjertager, B. H., On Mathematical Modeling of Turbulent Combustion with Special Emphasis on Soot Formation and Combustion, *Proceedings*, 16th International Symposium on Combustion, Boston, Mass., USA, The Combustion Institute, Pittsburgh, Penn., USA, 1977, pp. 719-729
[14] Spalding, D. B., Combustion and Mass Transfer, Pergamon Press, Oxford, UK, 1979
[15] Pešić, R. B., *et. al*., Experimental Determination of Double Vibe Function Parameters in Diesel Engines with Biodiesel, *Thermal Science, 14* (2010), Suppl., pp. S197-S208
[16] Stojiljković, D., *et al.*, Mixtures of Bioethanol and Gasoline as a Fuel for SI Engines, *Thermal Science, 13* (2009), 3, pp. 219-228
[17] Mariasiu, F., Contemporary Diesel Engine (in Romanian), Sincron Publishing House, Cluj-Napoca, Romania, 2005
[18] Gunasekaran, J., Ganesan, V., Effect of Swirl and Tumble on the Stratified Combustion of a DISI Engine - A CFD Study, SAE technical paper 2011-01-1214, 2011
[19] Mariasiu, F., The Modeling of Fuel Injection in Compression Ignition Engines (in Romanian), Sincron Publishing House, Cluj-Napoca, Romania, 2001
[20] Burnete, N., *et al*., Biofuels – Alternative Energy Source in Romania, International Congress on Automotive and Transport Engineering, CONAT 2010, Vol III, ISSN 2069-0401, Paper no. CONAT20102064
[21] Burnete, N., *et al.*, Diesel Engines and Biofuels for Urban Transportation (in Romanian), Mediamira Publishing House, Cluj-Napoca, Romania, 2008
[22] Demirbas, A., Biodiesel, A Realistic Fuel Alternative for Diesel Engines, Springer Publishing House, Berlin, 2008

Paper submitted: October 4, 2011
Paper revised: January 5, 2012
Paper accepted: January 7, 2012

applied sciences

MDPI

Article

Simulink Model of a Thermoelectric Generator for Vehicle Waste Heat Recovery

Nicolae Vlad Burnete [1], Florin Mariasiu [1,*], Dan Moldovanu [1] and Christopher Depcik [2]

[1] Automotive Engineering and Transports Department, Technical University of Cluj-Napoca, 400641 Cluj-Napoca, Romania; nicolae.vlad.burnete@auto.utcluj.ro (N.V.B.); dan.moldovanu@auto.utcluj.ro (D.M.)
[2] Department of Mechanical Engineering, University of Kansas, Lawrence, KS 66045, USA; depcik@ku.edu
* Correspondence: florin.mariasiu@auto.utcluj.ro

Featured Application: The work presented in this study can be used in the design and development process of thermoelectric generators for vehicle waste heat recovery.

Abstract: More than 50% of the energy released through combustion in the internal combustion engine (ICE) is rejected to the environment. Recovering only a part of this energy can significantly improve the overall use of resources and the economic efficiency of road transport. One solution to recoup a part of this otherwise wasted thermal energy is to use thermoelectric generator (TEG) modules for the conversion of heat directly into electricity. To aid in development of this technology, this effort covers the derivation of a respectively simple steady-state Simulink model that can be utilized to estimate and optimize TEG system performance for ICEs. The model was validated against experimental data found in literature utilizing water cooling for the cold side. Overall, relatively good agreement was found with the maximum error in generated power around 10%. Following, it was investigated whether air can be used as a cooling medium. It was established that, at the same temperature as the water (18.4 °C), a flow velocity of 13.1 m/s (or 47.2 km/h) is required to achieve a similar cold junction temperature and power output. Subsequently using the model with air cooling, the performance of a TEG installed on a heavy-duty vehicle traveling at 50, 80, 90, and 120 km/h under different ambient temperatures was analyzed. It was determined that both a lower temperature and a higher flow velocity can improve power output. A further increase of the power output requires a larger temperature gradient across the module, which can be achieved by a higher heat input on the hot side.

Keywords: thermoelectric generator; thermoelectric module; waste heat recovery; internal combustion engine; steady-state model

check for updates

Citation: Burnete, N.V.; Mariasiu, F.; Moldovanu, D.; Depcik, C. Simulink Model of a Thermoelectric Generator for Vehicle Waste Heat Recovery. *Appl. Sci.* **2021**, *11*, 1340. https://doi.org/10.3390/app11031340

Academic Editor: Alberto Benato
Received: 18 January 2021
Accepted: 29 January 2021
Published: 2 February 2021

Publisher's Note: MDPI stays neutral with regard to jurisdictional claims in published maps and institutional affiliations.

Copyright: © 2021 by the authors. Licensee MDPI, Basel, Switzerland. This article is an open access article distributed under the terms and conditions of the Creative Commons Attribution (CC BY) license (https://creativecommons.org/licenses/by/4.0/).

1. Introduction

With the advent of the internal combustion engine (ICE) in the late 19th century and its continued development during the 20th century, humankind has benefited greatly from its use for transportation. In fact, the 20th century can be defined in one word: "Mobility"; local, regional, national, and international mobility of goods, people, and ideas. However, owing to its construction and general operation, the ICE manages to only partially transform fuel chemical energy into mechanical work. This is illustrated by the thermal efficiency of modern ICEs that generally only reaches 40–45%. This respectively low value of energy conversion directly influences the economic efficiency of the road transport process. For example, a 40 t freight vehicle with a payload of 25 t operating with an ICE has an overall transport process efficiency equal to 17–18% [1]. Furthermore, since transportation has a significant influence in both national and global economies, increasing transport process efficiency can immediately reduce operating costs while additionally helping to decrease greenhouse gas emissions.

Most of the thermal energy of the ICE (approx. 30%) is lost through the high temperature combustion exhaust gases that are discharged directly into the atmosphere. Therefore, one solution to increase overall efficiency is to recover, at least a part of this significant heat loss to the environment. For this purpose, research has targeted the design, development, and implementation of thermoelectric generator modules for directly converting heat into electricity, which can then be used in hybrid power systems to increase vehicle efficiency. Thermoelectric devices are environmentally friendly and have numerous other advantages including the lack of moving parts, the conversion of thermal energy directly into electrical energy, high reliability, as well as low maintenance requirements. The main disadvantage of such devices is their low efficiency owing to the small dimensionless figure of merit ($Z\overline{T}$) values currently found in commercial devices. However, there are promising solutions for achieving higher $Z\overline{T}$ values even at low to mid temperatures (<150 °C) [2].

The research efforts focused on identifying the potential for converting thermal energy into electricity, through thermoelectric generator (TEG) systems of different configurations and sizes, installed on the engine's exhaust path show that it is possible to obtain an electrical power output of approximately 200–1000 W, depending on vehicle type and operating conditions [3–6]. However, research has also shown that the vehicular use of TEG systems depends on driving conditions with negative effects found when conditions have a high changing frequency [7].

The development of numerical models investigating the efficient use of TEG systems centers mainly on: Operating temperatures, optimizing geometric dimensions [8], different materials in TEG construction [9], and design optimization of hot and cold side heat exchangers [10]. Furthermore, TEG system design focuses on the energetic efficiency of conductive and convective system types [11]. In this area, Fan et al. [12] proposed a numerical model to determine the optimum values for the thermocouple leg lengths and cross-sectional areas. Their analysis showed that, for given thermal boundary conditions, the maximum output power can be improved by optimizing the leg length or cross-sectional area. Other efforts by Yu et al. [13] developed a mathematical model to investigate the effects of different vehicle engine operating regimes (e.g., cold-start and different loads) on TEG performance. The major conclusion of their research was that TEG performance is influenced more by vehicle speed than by ambient temperature. Wang et al. [14] used a three-dimensional computational fluid dynamics simulation to analyze power output, temperature distribution, and pressure drop of a TEG system with different internal structures of the heat exchanger. Their model considered the coverage and placement of the thermoelectric modules on the heat exchanger surface. The primary outcome was that increasing the number of modules may eventually saturate the total power output. Du et al. [15] investigated the design of a cooling channel for a thermoelectric module using a CFD software program (Fluent). Their results showed that in general, the output power is higher when using liquid as cooling fluid compared to air.

The analysis of this literature shows that there is a wide variety of numerical models for TEG simulation with different types of sophistication. However, most models are usually only briefly presented, with little detailing of the underlying equations and of the implementation. Therefore, the aim of this study is to develop and validate a respectively simple steady-state Simulink model that can be utilized to estimate and optimize TEG system performance. The model is intended to aid in the design and development of thermal energy recovery systems for ICEs, but it can be applied in other areas as well. Employing the described model early in the design process can facilitate whether thermal energy recovery is feasible for the TEG system under specific operating conditions. Furthermore, the proposed Simulink model can be integrated into existing software solutions for the analysis of different energy sources and powertrains.

2. Thermoelectric Model Equations

A thermoelectric couple (TC) consists of p-type and n-type semiconductor legs that are connected thermally in parallel and electrically in series (Figure 1). When heat is applied

to produce electric current, the TC operates as a generator. If, however, current is applied at the terminals, then the TC operates as a heat pump. For this effort, the focus is on thermoelectric generation and the use of the model as a heat pump is left to future work.

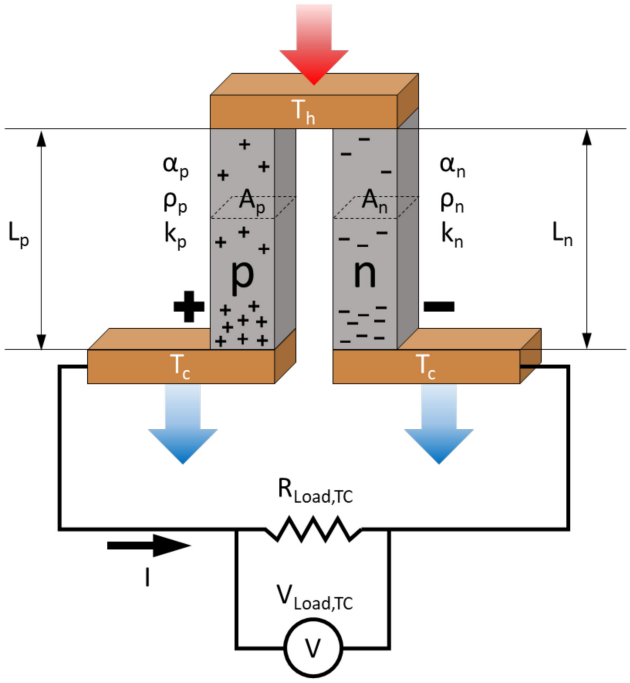

Figure 1. Thermoelectric couple operating as a generator.

If the two junctions of the TC are subjected to different temperatures ($\Delta T = T_h - T_c$ [K], where T_h [K]—hot side temperature, T_c—cold side temperature), a potential difference, proportional to the temperature variation, will appear ($V_{OC,TC}$ [V]—open circuit voltage, $V_{Load,TC}$ [V]—potential difference across a load connected to the TC):

$$V_{OC,TC} = \alpha_{TC} \cdot (T_h - T_c) \tag{1}$$

where α_{TC} [V/K] is the relative Seebeck coefficient:

$$\alpha_{TC} = \alpha_p - \alpha_n. \tag{2}$$

If the TC is connected to an external load with a resistance $R_{Load,TC}$ [Ω], a current flow will appear (I [A]). Consequently, the potential difference $V_{Load,TC}$ can be expressed as:

$$V_{Load,TC} = I \cdot R_{Load,TC}. \tag{3}$$

In addition, there is an internal electrical resistance of the TC, R_{TC} [Ω], which is defined based on the characteristics of the two legs: Electrical resistivity (ρ_p [Ωm]—electrical resistivity of the p-type leg, ρ_n [Ωm]—electrical resistivity of the n-type leg), length (L_p [m]—length of the p-type leg, L_n [m]—length of the n-type leg), and cross-sectional area (A_p [m^2]—cross-section area of the p-type leg, A_n [m^2]—cross-section area of the n-type leg).

$$R_{TC} = \rho_p \frac{L_p}{A_p} + \rho_n \frac{L_n}{A_n} \tag{4}$$

Knowing that the relation between $V_{Load,TC}$ and $V_{OC,TC}$ is

$$V_{Load,TC} = V_{OC,TC} - IR_{TC} \tag{5}$$

which results in a derivation of the current:

$$I = \frac{\alpha_{TC}(T_h - T_c)}{R_{TC} + R_{Load,TC}}. \tag{6}$$

This flow of current leads to three additional effects: Peltier heating or cooling, Joule heating, and the Thomson effect. The latter is relatively small and is usually neglected to simplify the analysis, as is the case in this study.

If current flows through the junction, heat must be continuously added or rejected to maintain a constant temperature. Furthermore, this heat flow is proportional to the current flow and changes direction if the current is reversed. This is called the Peltier effect and is defined by the Peltier coefficient $\pi_{TC,junction}$ [J/A]:

$$\pi_{TC,junction} = \frac{\dot{Q}_{junction}}{I} \tag{7}$$

where $\dot{Q}_{junction}$ [W] is the rate of heat absorption/rejection at the hot/cold junction. Using Kelvin relationships, the Peltier coefficient can be expressed based on the Seebeck coefficient, which is respectively easier to measure:

$$\pi_{TC,junction} = \alpha_{TC} T_{junction} \tag{8}$$

where $T_{junction}$ [K] is the temperature of the hot side and cold side junction. Thus, the rate of heat absorption/rejection at this junction can be expressed as:

$$\dot{Q}_{junction} = \alpha_{TC} I T_{junction}. \tag{9}$$

In addition to Joule heating, there is another irreversible phenomenon that accompanies the reversible thermoelectric effect, namely the conduction of heat. In a TC, heat conduction causes a transfer of heat from the hot side to the cold side as a means of achieving thermal equilibrium. Considering the thermal conductivities of the two legs (k_p [W/mK]—thermal conductivity of the p-type leg, k_n [W/mK]—thermal conductivity of the n-type leg), one can define the thermal conductance (K_{TC} [W/K]) of the TC:

$$K_{TC} = k_p \frac{A_p}{L_p} + k_n \frac{A_n}{L_n}. \tag{10}$$

Joule heating, $\dot{Q}_{Joule,h/c}$ [W], is the process where electrical energy is converted into thermal energy as current flows through a resistance. For a TC, Joule heating decreases the rate of heat absorption at the hot junction and increases the rate of heat transfer to the cold junction, in equal shares (i.e., half of the heat generated by the Joule effect passes to the hot side and the other half to the cold side) [16]:

$$\dot{Q}_{Joule,h/c} = \frac{1}{2} I^2 R_{TC}. \tag{11}$$

Neglecting the Thomson effect, by applying the first law of thermodynamics at the hot junction of a TC, the rate of heat absorption, $\dot{Q}_{h,TC}$ [W], is:

$$\dot{Q}_{h,TC} = \alpha_{TC} I T_h - \frac{1}{2} I^2 R_{TC} + K_{TC}(T_h - T_c) \tag{12}$$

whereas the rate of heat rejection, $\dot{Q}_{c,TC}$ [W], at the cold side is:

$$\dot{Q}_{c,TC} = \alpha_{TC} I T_c + \frac{1}{2} I^2 R_{TC} + K_{TC}(T_h - T_c). \tag{13}$$

Overall, the power delivered to the load, $P_{el,TC}$ [W], can be calculated in two ways:

$$P_{el,TC} = \dot{Q}_{h,TC} - \dot{Q}_{c,TC} \tag{14}$$

or as:

$$P_{el,TC} = I^2 R_{Load,TC}. \tag{15}$$

The thermoelectric performance of the material is assessed using the figure of merit [1/K]:

$$Z = \frac{\alpha^2}{\rho k} \tag{16}$$

which, for a TC becomes

$$Z_{TC} = \frac{\alpha_{TC}^2}{\left[\sqrt{\rho_p k_p} + \sqrt{\rho_n k_n}\right]^2}. \tag{17}$$

This figure of merit, like the thermoelectric parameters, is temperature dependent. However, often, average values are assumed with errors found to be below 10% of the true value [17].

The conversion (or thermal) efficiency of the TC is the ratio of the power output to the heat input at the hot side. To simplify the final expression, the following notations are employed for the load resistance ratio (m [-]) and Carnot efficiency (η_C [-]), respectively,

$$m = \frac{R_{Load,TC}}{R_{TC}} \tag{18}$$

$$\eta_C = 1 - \frac{T_c}{T_h}. \tag{19}$$

Thus, the conversion efficiency is:

$$\eta_{th} = \frac{\eta_C m}{(1+m) - \frac{1}{2}\eta_C + \frac{1}{2Z\overline{T}}(1+m)^2\left(1 + \frac{T_c}{T_h}\right)}. \tag{20}$$

Expressions of maximum parameters (current, voltage, power, and efficiency) are also introduced here due to their importance in determining TEG parameters, which will be shown later. The maximum voltage occurs at open circuit when I = 0:

$$V_{OC,TC,max} = \alpha_{TC}(T_h - T_c). \tag{21}$$

The maximum current, however, occurs at short circuit, where $R_{Load,TC}$ = 0; thus, leading to the following expression:

$$I_{max} = \frac{\alpha_{TC}(T_h - T_c)}{R_{TC}}. \tag{22}$$

To obtain the maximum power, it can be shown that the load resistance must equal the internal resistance (thus: m = 1), which leads to the following expression:

$$P_{el,max} = \frac{\alpha_{TC}^2 (T_h - T_c)^2}{4R_{TC}} \tag{23}$$

For the maximum efficiency, the conversion efficiency is differentiated with respect to m and set to 0. This leads to the following expression for the load resistance ratio:

$$m = \sqrt{1 + Z\overline{T}} \tag{24}$$

where $Z\overline{T}$ [-] is the dimensionless figure of merit ($\overline{T} = 1/2 \cdot (T_h + T_c)$ [K] is the average temperature across the TC). Consequently, the maximum conversion efficiency becomes:

$$\eta_{th,max} = \left(1 - \frac{T_c}{T_h}\right) \cdot \frac{\sqrt{1 + Z\overline{T}} - 1}{\sqrt{1 + Z\overline{T}} + \frac{T_c}{T_h}}. \tag{25}$$

Of additional high importance is the efficiency at maximum power (η_{mp}), or, in other words, at matching load resistance (m = 1). Based on Equation (20), η_{mp} is:

$$\eta_{mp} = \frac{\eta_C}{2 - \frac{1}{2}\eta_C + \frac{2}{Z\bar{T}}\left(1 + \frac{T_c}{T_h}\right)}. \tag{26}$$

The output of a single TC is generally small; e.g., well below 1 [W]. Therefore, many TCs are connected to form a thermoelectric module (TEM) (Figure 2); thus, increasing the power output. At this point it is worth recalling that a TEM can operate both as a generator (often designated with TEG in literature) and/or as a heat pump (usually TEC—thermoelectric cooler). In the present study, the TEM operates as a generator, but the notation of TEM is used to avoid confusion with the acronym TEG that involves the overall system including heat exchangers (shown later). The output of a TEM can be expressed based on the number of thermocouples (n_{TC} [-]) and the parameters of the TC, except for electrical current that is independent of the number of thermocouples. Thus, the total rate of heat absorption/rejection at the hot and cold sides are, respectively:

$$\dot{Q}_{h,TEM} = n_{TC}\left[\alpha_{TC} I T_h - \frac{1}{2} I^2 R_{TC} + K_{TC}(T_h - T_c)\right] \tag{27}$$

$$\dot{Q}_{c,TEM} = n_{TC}\left[\alpha_{TC} I T_c + \frac{1}{2} I^2 R_{TC} + K_{TC}(T_h - T_c)\right]. \tag{28}$$

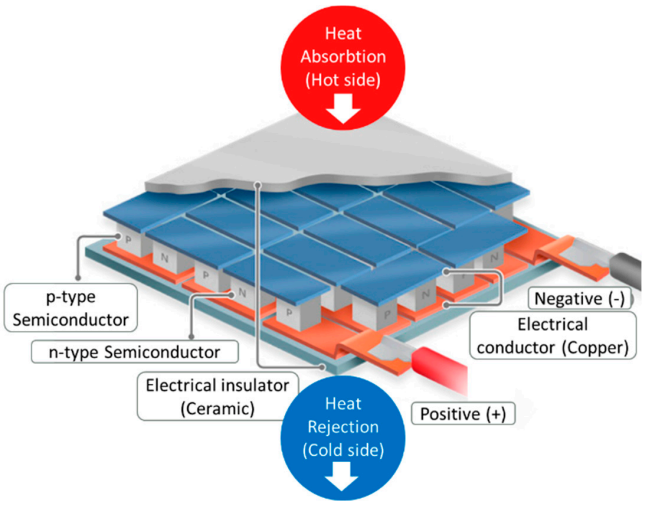

Figure 2. Thermoelectric module operating as a generator (based on [18]).

Using Equations (14), (27) and (28), the total power output of the module can be calculated:

$$P_{el,TEM} = n_{TC}\left[\alpha_{TC} I (T_h - T_c) - I^2 R_{TC}\right]. \tag{29}$$

3. TEM Properties Identification Model

Often TEM material properties are not available from the manufacturer and must be determined, which requires specialized equipment [19]. Furthermore, it is not always necessary to have high model accuracy throughout the entire operating range. For example, when estimating the performance of a TEM system in the preliminary design phase, it is helpful to have a respectively simple and physically based model that can be used to run parametric studies. To solve this issue, Lee et al. [20] and Zhang [21] proposed methods that use maximum parameter values, usually provided by manufacturers, to estimate the electrical resistivity, Seebeck coefficient, thermal conductivity, and the figure of merit. The authors call these effective parameters since, as compared to intrinsic material properties, they are determined at the system (TEM) level; thus, they account for the various losses caused by the manufacturing process (i.e., thermal and electrical contact resistances), the temperature dependency (due to the Thomson effect), as well as imperfect insulation (heat losses through radiation and convection). The basic idea is that, ideally, the

maximum current, voltage, power, and efficiency are functions of the material properties, the thermocouple geometry (area, length), and the temperatures of the two junctions (T_h, T_c).

3.1. Equations and Simulink Model

For the current study, the maximum parameters used to determine the outcomes are current, efficiency, and power (only three of the four maximum parameters presented in Equations (21)–(23) and (25) are required). By knowing the leg area ($A = A_p = A_n$) and length ($L = L_p = L_n$), the effective Seebeck coefficient and the effective electrical resistivity of the TC can be determined from Equations (22) and (23):

$$\rho^*_{TC} = \frac{4\left(\frac{A}{L}\right)P_{el,max}}{n_{TC}I^2_{max}} \tag{30}$$

$$\alpha^*_{TC} = \frac{4P_{el,max}}{n_{TC}I_{max}(T_h - T_c)}. \tag{31}$$

To determine the effective thermal conductivity, an additional parameter is required, namely the effective figure of merit which can be obtained from Equation (25):

$$Z^*_{TC} = \frac{1}{\overline{T}}\left[\left(\frac{1 + \frac{\eta_{max}}{\eta_C}\frac{T_c}{T_h}}{1 - \frac{\eta_{max}}{\eta_C}}\right)^2 - 1\right]. \tag{32}$$

Based on Equation (16), the effective thermal conductivity can be expressed as:

$$k^*_{TC} = \frac{{\alpha^*_{TC}}^2}{Z^*_{TC}\rho^*_{TC}}. \tag{33}$$

3.2. Model Validation

The model has been validated for two commercially available thermoelectric modules which are presented in Table 1. This data has been used in the Simulink model presented in Figure 3 to determine the effective parameters.

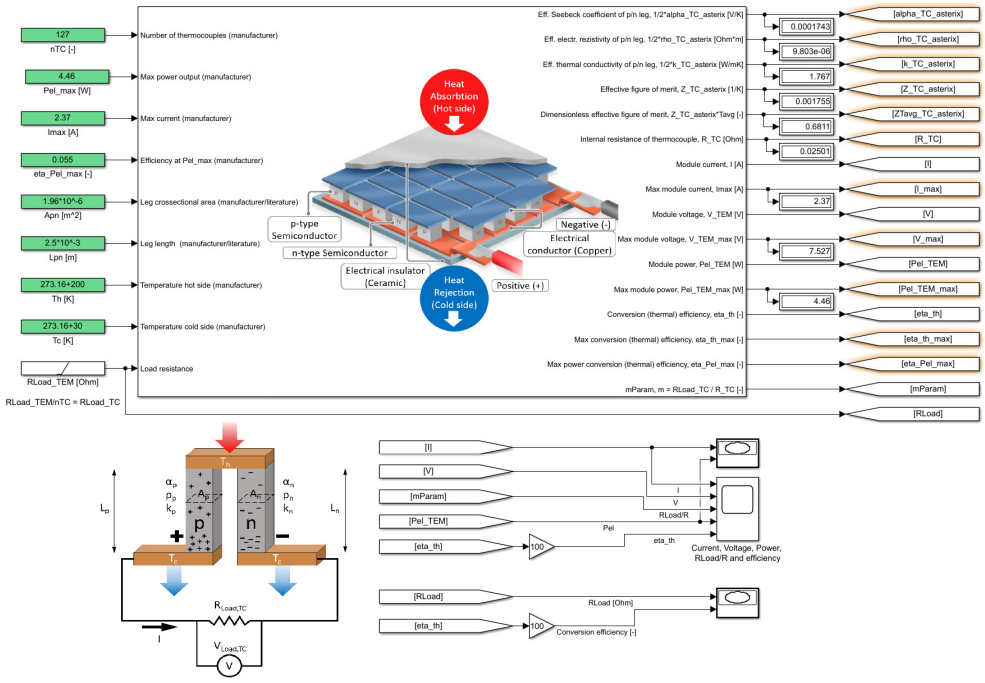

Figure 3. Simulink model for determining effective properties (values for TGM-127-1.4-2.5).

Table 1. Thermoelectric parameters of commercially available thermoelectric modules.

TEM	nTC [-]	Pel,max [W]	Imax [A]	ηmax [%]	Ap/n [mm^2]	Lp/n [mm]	Th [°C]	Tc [°C]
TGM-199-1.4-0.8 [22]	199	11.40	5.10	4.3	1.96	0.8	200	30
TGM-127-1.4-2.5 [23]	127	4.46	2.37	5.5	1.96	2.5	200	30

The effective parameters obtained with the model presented in Figure 3 were used to calculate the voltage, current, and power at matched load resistance conditions, as well as the power, current, voltage, and efficiency at the maximum temperature gradient for various values of the load resistance. The results show that there is a relatively good agreement between the measured and calculated values (Figures 4 and 5). The major differences appearing here can be attributed to the temperature dependency of the electrical resistivity, Seebeck coefficient, and thermal conductivity, which is not captured in the proposed model. Despite these differences, the predicted power output of the module is in relatively good agreement with the measured values. A possible reason for this result is that the maximum power was chosen as an input parameter in deference to the maximum voltage.

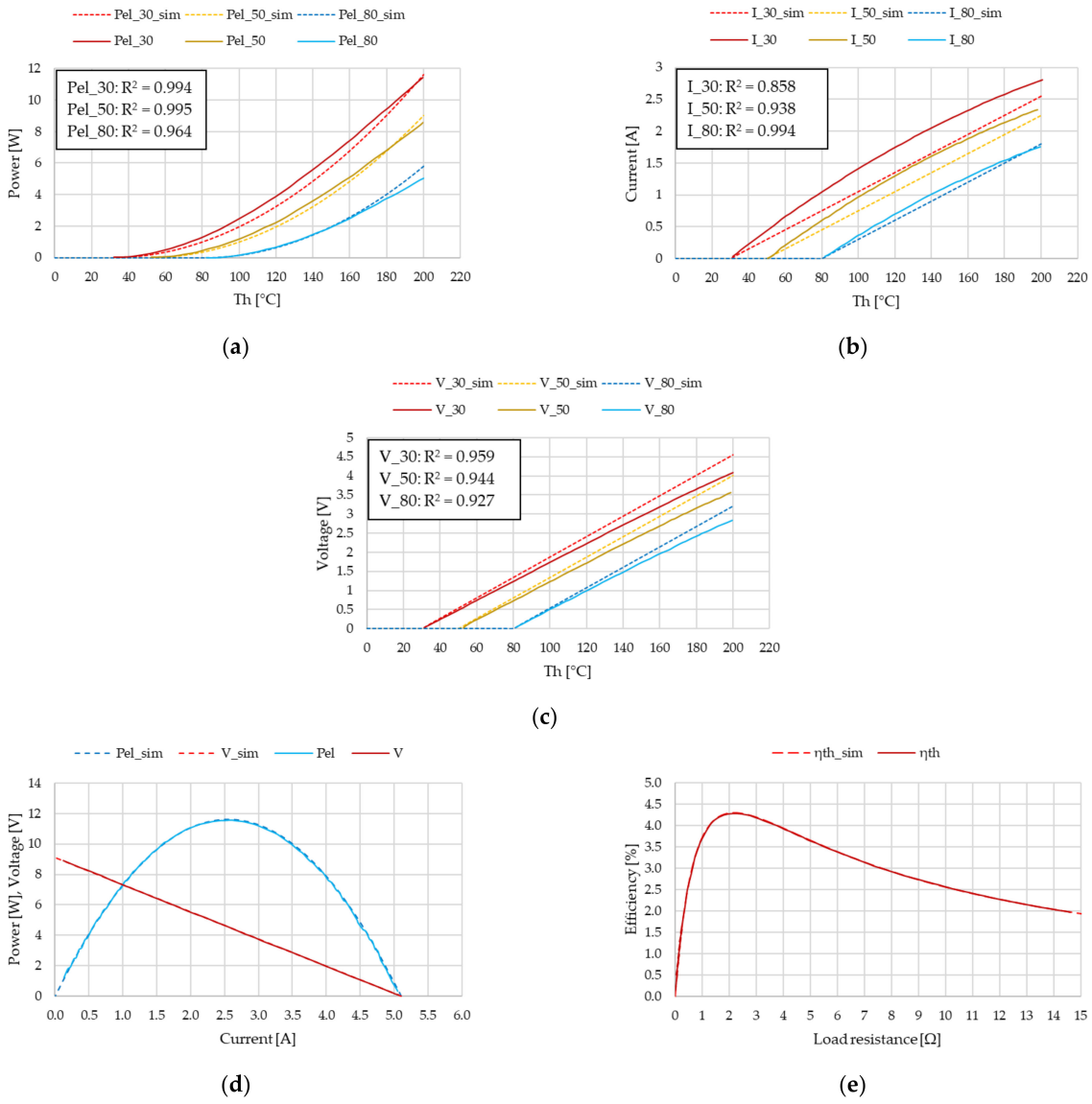

Figure 4. Manufacturer data compared to calculated data at matched load resistance conditions for TGM-199-1.4-0.8: (**a**) Module power; (**b**) module current; (**c**) module voltage; (**d**) module power and voltage with respect to current; and (**e**) module efficiency.

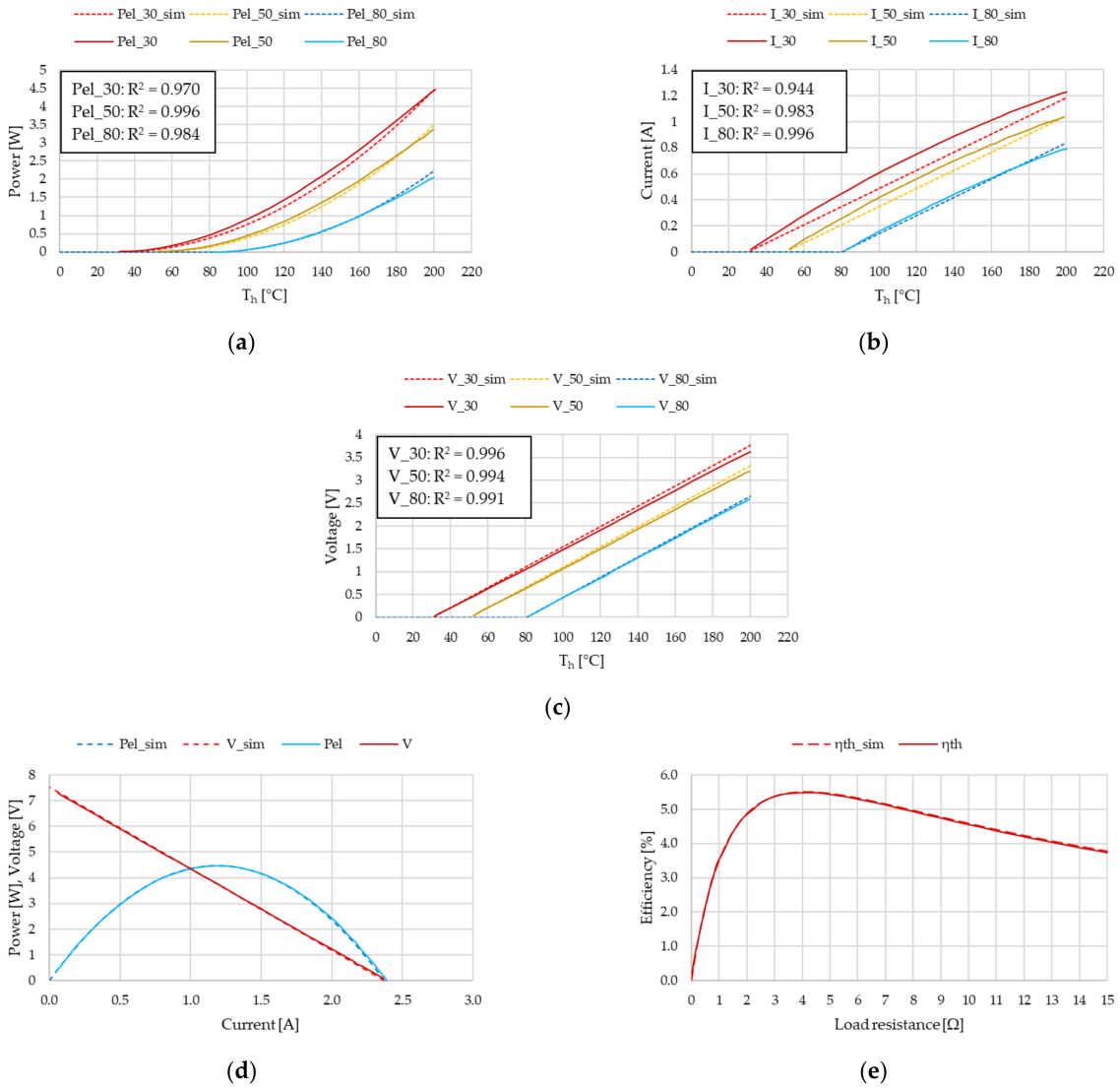

Figure 5. Manufacturer data compared to calculated data at matched load resistance conditions for TGM-127-1.4-2.5: (**a**) Module power; (**b**) module current; (**c**) module voltage; (**d**) module power and voltage with respect to current; and (**e**) module efficiency.

4. TEG Model for Exhaust Gas Waste Heat Recovery

For the current study, the system is analyzed under steady-state conditions. The domain is discretized along the flow direction in control volumes (CVs) having the same length as a TEM (Figure 6). Initially, only one control volume is considered for the calculation; however, a greater domain can be built by adding more control volumes with each taking input data from the previous CV. The changes in fluid properties with temperature are considered separately for each control volume and are defined at the mean CV temperature (average of inlet and outlet temperatures). For simplicity, thermoelectric parameters are considered constant, but the model can be readily updated with equations for these parameters, either from the literature or from the manufacturer.

Thermoelectric modules are often combined with heat exchangers (HX) to form thermoelectric generators (TEG), which are used to recover otherwise wasted thermal energy from the exhaust gases of ICEs. The fins of the HX allow for an increased heat transfer surface area, subsequently enhancing the amount of heat extracted through convection from the hot gases. This heat is then transferred through conduction to the TEMs. An

example of such a TEG with all relevant dimensions of the finned heat exchanger (L_{HX} [m]—heat exchanger length, W_{HX} [m]—heat exchanger width, H_{HX} [m]—heat exchanger height, $z_{HX,fin\text{-}spacing}$ [m]—heat exchanger fin spacing, $t_{HX,fin}$ [m]—heat exchanger fin thickness), as well as the positioning of the TEMs is presented in Figure 6. If the heat exchanger is covered with TEMs on both sides, the CV must be modified accordingly (Figure 7).

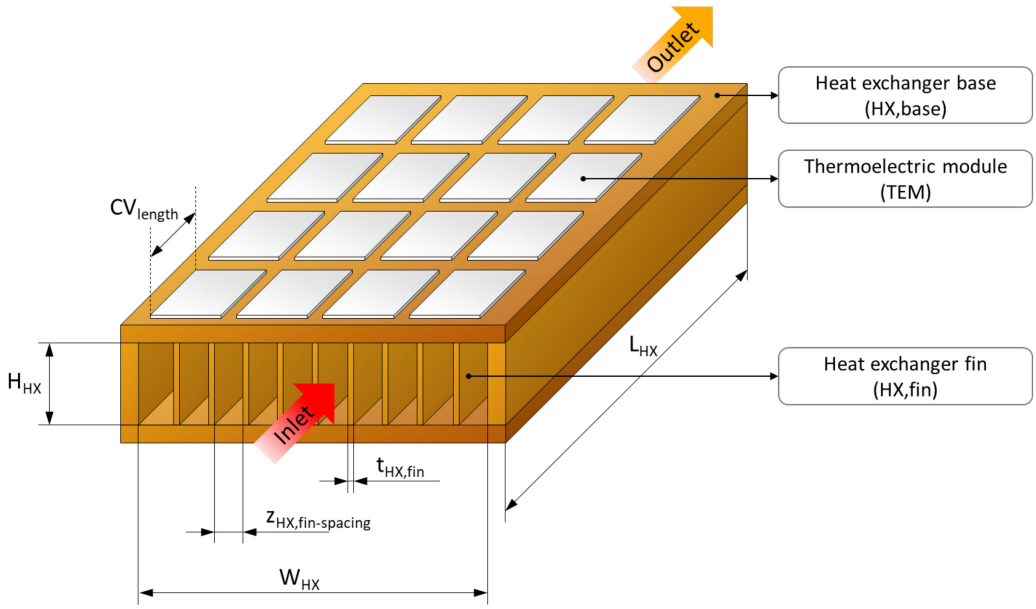

Figure 6. Hot side heat exchanger.

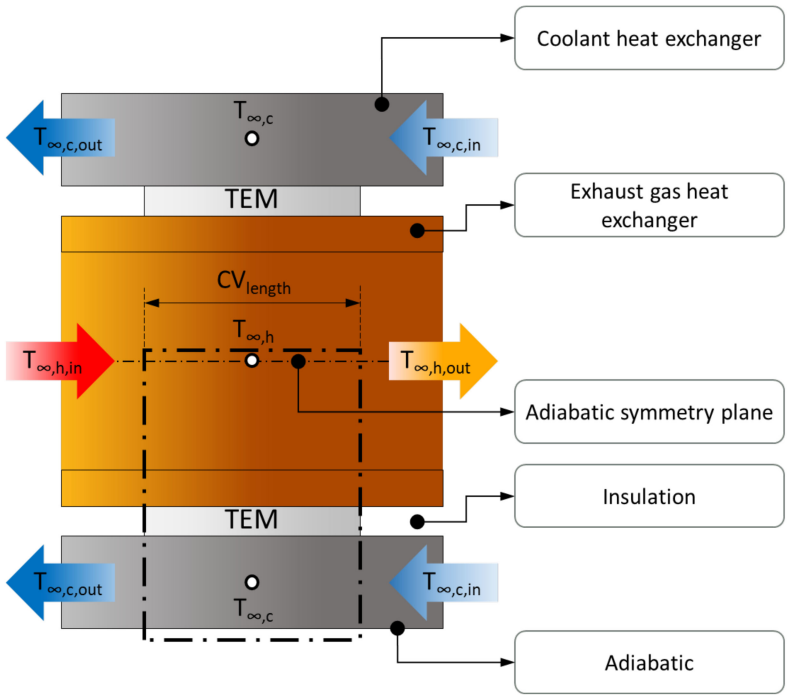

Figure 7. Side view of module section.

4.1. Equations and Simulink Model

The layering of the TEG, which will be used for calculating the amount of heat transferred to the hot side and from the cold side, is presented in Figure 8. The TEG is composed of two heat exchangers (hot and cold side), a thermal grease used to eliminate surface

imperfections in the interface area, and two ceramic plates acting as electric insulators. The electrical conductor height is relatively small and, since it has a respectively high thermal conductivity and low electrical resistivity, it was neglected in the present model.

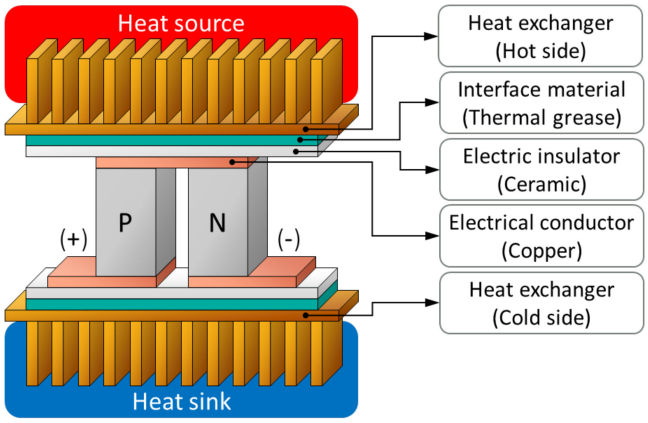

Figure 8. Integration of thermoelectric module in a thermoelectric generator.

As a first step, all relevant areas for the heat transfer are calculated starting from the area available for heat transfer in one TC ($A_{ht,TC}$ [m^2]):

$$A_{ht,TC} = A_p + A_n. \tag{34}$$

For a TEM with n_{TC} thermocouples, the area available for heat transfer ($A_{ht,TEM}$ [m^2]) will be:

$$A_{ht,TEM} = n_{TC}(A_p + A_n). \tag{35}$$

Thus, for a TEG with n_{TEM} [-] TEMs, the total area of the HX base in a control volume ($A_{ht,CV,base\text{-}TEM}$ [m^2]) available for heat transfer will be:

$$A_{ht,CV,base-TEM} = n_{TEM} n_{TC}(A_p + A_n). \tag{36}$$

The HX base area for one control volume ($A_{ht,CV,base}$ [m^2]) is defined as:

$$A_{ht,CV,base} = W_{Hx} \cdot L_{CV} \tag{37}$$

where L_{CV} is the length of the CV. The part of the HX base area that is not covered by TEMs, is considered to be insulated.

To calculate the amount of heat extracted from the hot gases, the total area ($A_{ht,CV,total}$) available for heat exchange with the hot gases in a control volume must be determined:

$$A_{ht,CV,total} = n_{fin}\left[2(t_{Hx,fin} + L_{CV})H_{Hx} + z_{Hx,fin-spacing}L_{CV}\right]. \tag{38}$$

Note that the equations presented are for a HX installed on the hot side, but the equations can also be used for an HX on the cold side.

To show the fraction of the HX base surface that is used for heat transfer to the TCs, a HX surface usage coefficient is proposed:

$$f_{Hx,Area} = \frac{A_{ht,CV,base-TEM}}{A_{ht,CV,base}}. \tag{39}$$

When only the flow velocity (V_{gas} [m/s]) is available, the crossflow area of the HX is required to compute the mass flow:

$$A_{Hx,cross} = n_{fin} z_{Hx,fin-spacing} H_{Hx} \tag{40}$$

consequently, the gas mass flow rate will be

$$\dot{m}_{gas} = \rho_{gas} V_{gas} A_{Hx,cross}. \tag{41}$$

If, however, the mass flow is available, then Equation (41) can be used to compute the gas flow velocity.

The next step is to determine the forced convection heat transfer coefficient between the gases and the HX surface. This is respectively difficult since the flow ranges from developing to fully developed. On this topic, Teertstra et al. [24] proposed and validated a model that uses a composite solution based on the limiting cases of flow between isothermal parallel plates. In the transitional flow region, an average Nusselt number is calculated as a function of the heat exchanger geometry and fluid flow velocity. To use this model, two conditions must be met: Air must be contained within the channels (this is achieved since a closed HX is considered) and the fin spacing must be considerably smaller than the fin height (high aspect ratio). The reduced Reynolds number has an experimental range of $0.2 \leq Re^* \leq 200$ [25] and is calculated as:

$$Re^*_{Hx,channel} = \frac{V_{gas} z_{Hx,fin-spacing}}{\mu_{gas}} \frac{z_{Hx,fin-spacing}}{L_{Hx}}. \tag{42}$$

The proposed equation for the Nusselt number is:

$$Nu_{Hx,channel} = \left[\left(\frac{Re^*_{Hx,channel} Pr_{gas}}{2} \right)^{-3} + \left(0.664 \sqrt{Re^*_{Hx,channel}} Pr^{\frac{1}{3}} \sqrt{1 + \frac{3.65}{\sqrt{Re^*_{Hx,channel}}}} \right)^{-3} \right]^{-\frac{1}{3}}. \tag{43}$$

If the flow is fully turbulent and Re * exceeds its range limits, then the Nusselt number can be calculated using the Gnielinski relation [26]:

$$Nu_{Hx,channel} = \frac{\frac{f_G}{8}(Re_{Hx,channel} - 1000) Pr_{gas}}{1 + 12.7\sqrt{\frac{f_G}{8}}\left(\sqrt[3]{Pr^2_{gas}} - 1\right)} \tag{44}$$

where $Re_{HX,channel}$ is the channel Reynolds number and f_G is the friction factor in turbulent flow in smooth tubes determined from the first Petukhov equation [27]:

$$Re_{Hx,channel} = \frac{V_{gas} z_{Hx,fin-spacing}}{\mu_{gas}} \tag{45}$$

$$f_G = \frac{1}{(0.79 \ln Re_{Hx,channel} - 1.64)^2}. \tag{46}$$

Knowing the Nusselt number, the gas-fin heat transfer coefficient can then be calculated with the following expression:

$$h_{gas-fin} = \frac{k_{gas}}{z_{Hx,fin-spacing}} Nu_{Hx,channel}. \tag{47}$$

To calculate the efficiency of the heat exchanger, as well as the thermal resistance, the efficiency of a single fin must be determined [28], along with the thermal resistances of all other intermediate layers. A single fin efficiency is calculated based on the m_{fin} parameter and the fin height, which, in this case is the same as the heat exchanger height:

$$m_{fin} = \sqrt{\frac{h_{gas-fin} \cdot 2(L_{Hx} + t_{Hx,fin})}{k_{Hx} L_{Hx} t_{Hx,fin}}} \tag{48}$$

$$\eta_{fin} = \frac{\tanh(m_{fin} H_{Hx})}{m_{fin} H_{Hx}}. \tag{49}$$

The next step is to calculate the overall effectiveness of the fin ($\eta_{o,fin}$ [-]), for which the area of a single fin (A_{fin} [m^2]) and the number of fins (n_{fin} [-]) must be known:

$$A_{fin} = 2H_{Hx}(L_{Hx} + t_{Hx,fin}) \tag{50}$$

$$\eta_{o,fin} = 1 - \frac{n_{fin}A_{fin}}{A_{ht,Hx,base}}(1 - \eta_{fin}). \tag{51}$$

Figure 9b shows the thermal resistance network used to calculate the hot (T_h [K]) and cold side (T_c [K]) junction temperatures along with the heat exchanger efficiency. To keep the model simple, and since it represents under 2% of the total heat transferred from the hot side [29], radiation losses are neglected. The resistances in Figure 9 are defined for all layers presented in Figure 8 based on their thickness ($t_{layer\text{-}name}$), thermal conductivity ($k_{layer\text{-}name}$), and surface area ($A_{layer\text{-}name}$). The equivalent gas-fin heat transfer resistance, and the thermal resistances of the base, grease, and ceramic are calculated according to Equations (52)–(55):

$$R_{th,fin,eq} = \frac{1}{\eta_{o,fin}h_{gas-fin}A_{ht,Hx,total}} \tag{52}$$

$$R_{th,Hx,base} = \frac{t_{Hx,base}}{k_{Hx,base}A_{ht,Hx,base}} \tag{53}$$

$$R_{th,grease} = \frac{t_{grease}}{k_{grease}A_{grease}} \tag{54}$$

$$R_{th,ceramic} = \frac{t_{ceramic}}{k_{ceramic}A_{ceramic}} \tag{55}$$

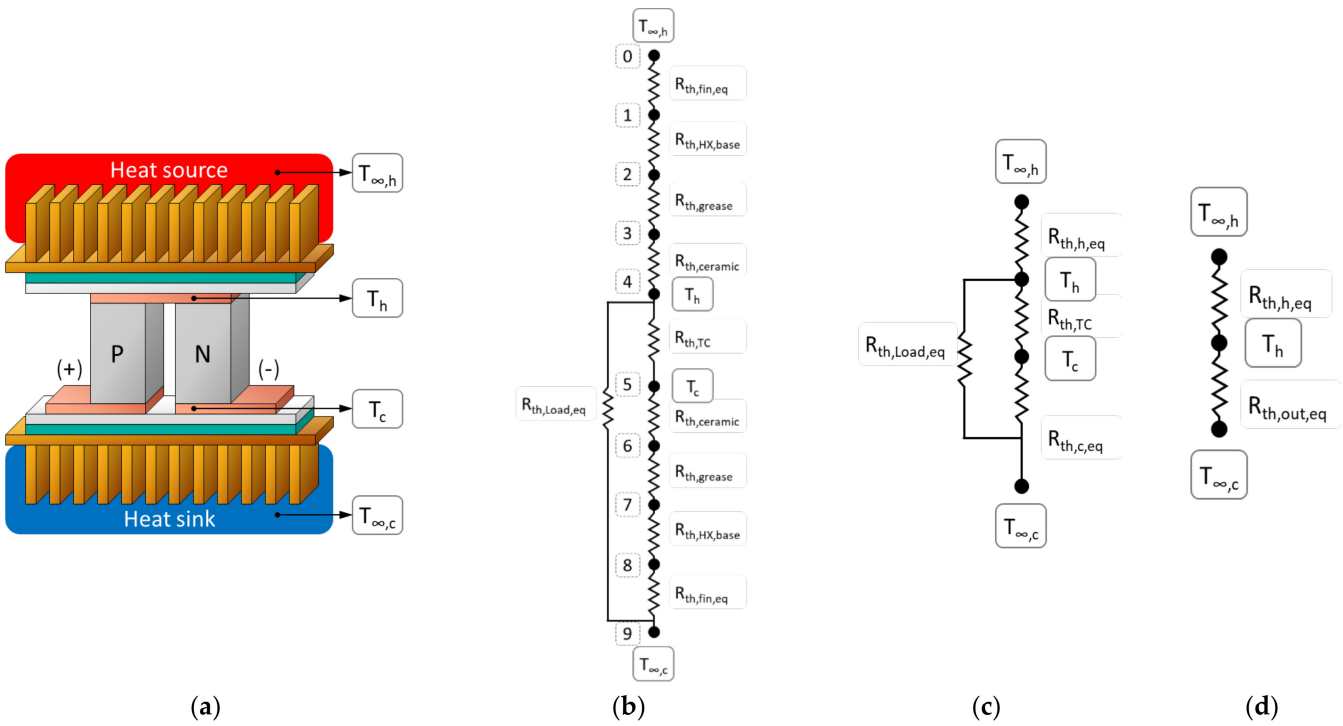

Figure 9. (**a**) Thermoelectric generator (TEG) temperatures of interest; (**b**) thermal resistance network for a CV; (**c**) simplified thermal resistance network for calculating T_c; and (**d**) simplified thermal resistance network for calculating T_h.

The equivalent thermal resistance of the TEM is calculated based on the hot and cold junction temperatures and the heat flow to the cold side:

$$R_{th,TEM} = \frac{T_h - T_c}{\dot{Q}_c}. \tag{56}$$

Similarly, an equivalent load resistance is defined based on the hot junction temperature and the temperature on the cold side ($T_{\infty,c} = 1/2 * (T_{\infty,c,in} + T_{\infty,c,out})$ [K], where $T_{\infty,c,in}$ and $T_{\infty,c,out}$ are the temperature of the gas at the cold side heat exchanger inlet and outlet respectively):

$$R_{th,Load,eq} = \frac{T_h - T_{\infty,c}}{P_{el,TEM}}. \tag{57}$$

Based on Equations (52)–(55), an equivalent thermal resistance of the hot side can be determined:

$$R_{th,h,eq} = R_{th,fin,eq} + R_{th,Hx,base} + R_{th,grease} + R_{th,ceramic}. \tag{58}$$

Similarly, the equivalent thermal resistance of the cold side is:

$$R_{th,c,eq} = R_{th,ceramic} + R_{th,grease} + R_{th,Hx,base} + R_{th,fin,eq}. \tag{59}$$

Often, an aluminum block is used to act as a thermal spreader that is placed between the HX and the TEM as in Figure 10. In this case, the thermal resistance of the base is replaced by the thermal resistance of the aluminum block:

$$R_{th,Al,block} = \frac{t_{Al,block}}{k_{Al,block} A_{Al,block}}. \tag{60}$$

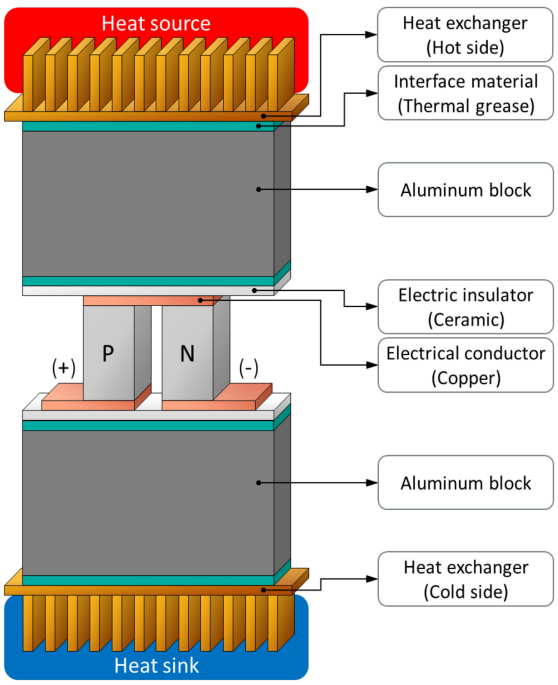

Figure 10. Integration of thermoelectric module in a thermoelectric generator.

It is important to note that, in such cases, the HX is usually also made of aluminum which allows for a simplification. Namely, the addition of the HX base thickness to the aluminum block thickness. They can, however, be introduced as separate blocks. In the present study, the former solution has been adopted.

For the case presented in Figure 10, the heat exchanger efficiency is defined as:

$$\eta_{Hx} = \left(\frac{1}{\eta_{o,fin}} + 2\frac{h_{gas-fin} A_{ht,Hx,total} t_{grease}}{k_{grease} A_{grease}} + \frac{h_{gas-fin} A_{ht,Hx,total} t_{Al}}{k_{Al} A_{Al}} \right). \tag{61}$$

To compute the junction temperatures, one more thermal resistance is needed, namely the equivalent thermal resistance of the out (output and heat rejection) side:

$$R_{th,out,eq} = \left(\frac{1}{R_{th,Load,eq}} + \frac{1}{R_{th,TC} + R_{th,c,eq}} \right)^{-1}. \tag{62}$$

Based on these resistances, the hot and cold side junction temperatures can be expressed with respect to $T_{\infty,h}$ ($T_{\infty,h} = 1/2 * (T_{\infty,h,in} + T_{\infty,h,out})$ [K], where $T_{\infty,h,in}$ and $T_{\infty,h,out}$ are the temperature of the gas at the hot side heat exchanger inlet and outlet respectively) and $T_{\infty,c}$:

$$T_h = \frac{R_{th,out,eq} T_{\infty,h} + R_{th,h,eq} T_{\infty,c}}{R_{th,out,eq} + R_{th,h,eq}} \tag{63}$$

$$T_c = \frac{R_{th,c,eq} T_h + R_{th,TC} T_{\infty,c}}{R_{th,c,eq} + R_{th,TC}}. \tag{64}$$

The amount of heat extracted from the hot gases can be determined from the CV inlet and outlet enthalpy represented by the heat capacity times the difference in temperature:

$$Q_{gas,Hx} = \dot{m}_{gas} c_{p,gas} (T_{\infty,h,in} - T_{\infty,h,out}). \tag{65}$$

However, in this effort, the outlet temperature is an output value. Neglecting the heat losses through radiation $Q_{gas,HX} = Q_h$, therefore, the outlet temperature is:

$$T_{\infty,h,out} = T_{\infty,h,in} - \frac{Q_h}{\dot{m}_{gas} c_{p,gas}}. \tag{66}$$

When installing a heat exchanger on the exhaust path of an ICE, there is also the issue of the increased backpressure that negatively influences engine performance and emissions. Consequently, the pressure drop must be estimated. Here, there are three effects that need to be considered: Viscous drag effects, flow expansion, and flow contraction. For a CV, the pressure loss due to this viscous drag effect is:

$$\Delta P_{loss,Hx} = \sum_{CV} f \frac{CV_{length}}{D_{hydr,channel}} \rho_{gas} \frac{V_{channel}^2}{2} \tag{67}$$

where f is the friction factor defined using the Churchill equation [30]:

$$f = 8 \left[\left(\frac{8}{Re_{channel}} \right)^{12} + \frac{1}{(A+B)^{1,5}} \right]^{\frac{1}{12}}. \tag{68}$$

The Churchill equation was chosen because it covers both developing and fully developed internal flows. The Reynolds number is calculated using Equation (45), while A and B are:

$$A = \left\{ -2.457 \ln \left[\left(\frac{7}{Re_{channel}} \right)^{0.9} + 0.27 \frac{\varepsilon_{surface}}{D_{hydr,channel}} \right] \right\}^{16} \tag{69}$$

$$B = \left(\frac{37350}{Re_{channel}} \right)^{16}. \tag{70}$$

To calculate A, two additional parameters are required, namely the surface roughness ($\varepsilon_{surface}$), which can be taken from literature and the channel hydraulic diameter ($D_{hydr,channel}$), which is calculated from the channel cross-sectional area and perimeter:

$$D_{hydr,channel} = \frac{2 z_{Hx,fin-spacing} H_{Hx}}{z_{Hx,fin-spacing} + H_{Hx}}. \tag{71}$$

For small gas density changes along the length of the heat exchanger, in case of n_{CV} control volumes ($CV_{length} = L_{HX}/n_{CV}$), Equation (67) can be simplified to:

$$\Delta P_{loss,Hx} = f\frac{L_{Hx}}{D_{hydr,channel}}\rho_{gas}\frac{V^2_{channel}}{2}. \quad (72)$$

Changes in the pipe cross-section area along the flow direction also lead to pressure losses by causing the flow to either expand or contract. To estimate these losses, the Borda-Carnot correlations are used [31]. These correlations require knowledge about cross-sectional areas, as well as the gas density and velocity. For a TEG installed on the exhaust pipe of an ICE (Figure 11), these cross-sectional areas are: Exhaust pipe upstream of the HX ($A_{inlet\text{-}pipe,cross}$ [m^2]), HX inlet ($A_{HX,inlet,cross}$ [m^2]) and outlet ($A_{HX,outlet,cross}$ [m^2]), as well as the exhaust pipe downstream of the HX ($A_{outlet\text{-}pipe,cross}$ [m^2]). Usually, TEG heat exchangers have a constant cross-section; thus, $A_{HX,inlet,cross} = A_{HX,outlet,cross} = A_{HX,cross}$. The inlet and outlet pipe cross-sectional areas are:

$$A_{inlet-pipe,cross} = \pi\frac{d^2_{inlet-pipe}}{4} \quad (73)$$

$$A_{outlet-pipe,cross} = \pi\frac{d^2_{outlet-pipe}}{4}. \quad (74)$$

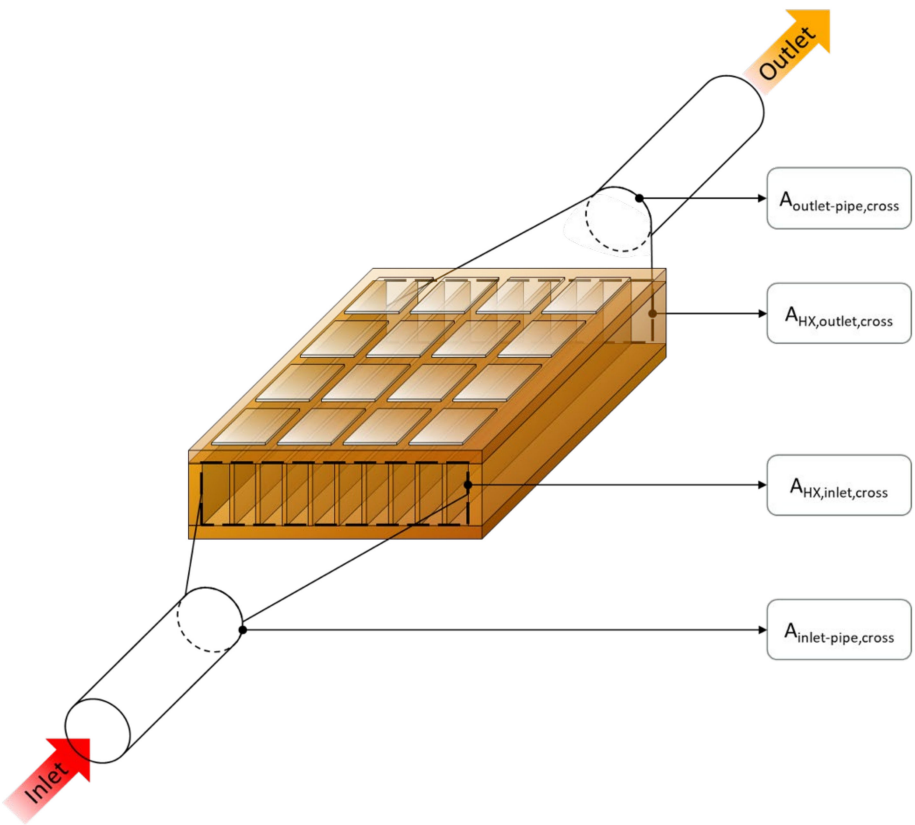

Figure 11. Areas used for calculating the pressure loss due to flow contraction and expansion.

The pressure loss due to flow expansion occurs before the HX, thus leading to the expression:

$$\Delta P_{loss,exp} = -\rho_{gas}\frac{A_{inlet-pipe,cross}}{A_{Hx,cross}}\left(1 - \frac{A_{inlet-pipe,cross}}{A_{Hx,cross}}\right)V^2_{gas} \quad (75)$$

whereas the pressure loss due to flow contraction occurs after exiting the HX:

$$\Delta P_{loss,contr} = \frac{1}{2}\rho_{gas}\left(\frac{1}{\mu_{contraction}} - 1\right)^2\left(\frac{A_{inlet-pipe,cross}}{A_{Hx,cross}}\right)^2 V_{gas}^2 \quad (76)$$

with $\mu_{contraction}$ as the contraction coefficient:

$$\mu_{contraction} = 0.63 + 0.37\left(\frac{A_{Hx,cross}}{A_{inlet-pipe,cross}}\right)^3. \quad (77)$$

It must be noted that the pressure losses due to flow expansion and contraction are calculated only for the HX inlet and outlet CVs, respectively.

4.2. Solution Method

The thermal circuit temperatures must be solved in an iterative manner due to the dependence of the thermal resistances on the terminal temperatures and thermoelectric properties. Therefore, before beginning the iterative calculation process, several temperatures must be estimated (i.e., T_h, T_c, $T_{\infty,h,out}$, and $T_{\infty,c,out}$). Using input data and these estimated temperatures, the thermal resistances together with the other parameters are evaluated. Then, the values of T_h, T_c, $T_{\infty,h,out}$, and $T_{\infty,c,out}$ are reevaluated and the convergence is checked based on the relative error value:

$$Error_{rel} = \sum\left|\frac{T_i - T_{i+1}}{T_i}\right| \quad (78)$$

If $Error_{rel}$ is below a set value (10^{-6} for this study), the calculation stops. If this is not the case, the initially guessed values are updated with the current results and the process starts again. The solution methodology flowchart for each CV is presented in Figure 12.

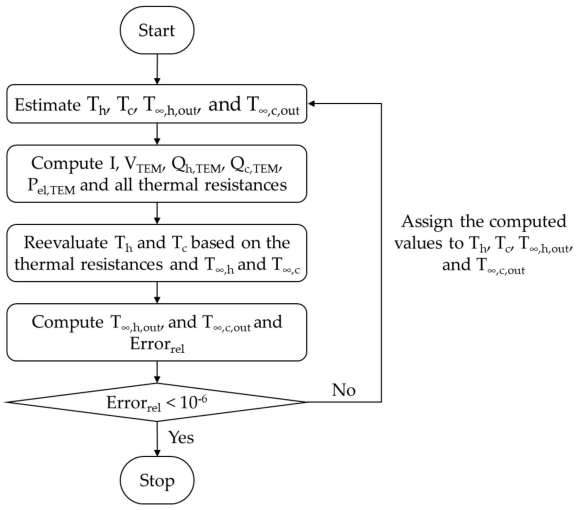

Figure 12. Solution methodology flow chart.

5. Results and Discussions

The model (Figure 13) was validated based on tests performed by Fagehi et al. [32]. In their work, Fagehi et al. [32] used a liquid (water) heat exchanger on the cold side which demanded a series of changes to the cold side heat exchanger model (not included in this study, but available upon request).

The comparison between the simulated and measured values is presented in Figure 14. Fagehi et al. [32] measured the junction temperatures, current, and voltage directly, while they calculated the power using two methods. The power designated with $P_{el_Temp_I}$ is calculated using the junction temperatures, electric current, and the ideal thermoelectric equations; whereas, $P_{el_V_I}$ was determined based on the measured voltage and current. Similar to the results of Fagehi et al. [32] the simulation results were closer to the power values

determined using the junction temperatures, electric current, and the ideal thermoelectric equations. The average and matched load resistance errors for the junction temperatures, power output, current, voltage, and efficiency are listed in Table 2. The possible causes of differences are: Measurement accuracy, the use of ideal equations, effective material properties, as well as constant values for both the thermoelectric properties and gas properties. In addition, this effort neglects the Thomson coefficient, radiative heat transfer, and the thermal spread resistance. Another possible source of error is the extraction of data from the graphs presented in literature by using a digital tool. Despite all the uncertainties, there is a reasonable agreement between the calculated and the measured values.

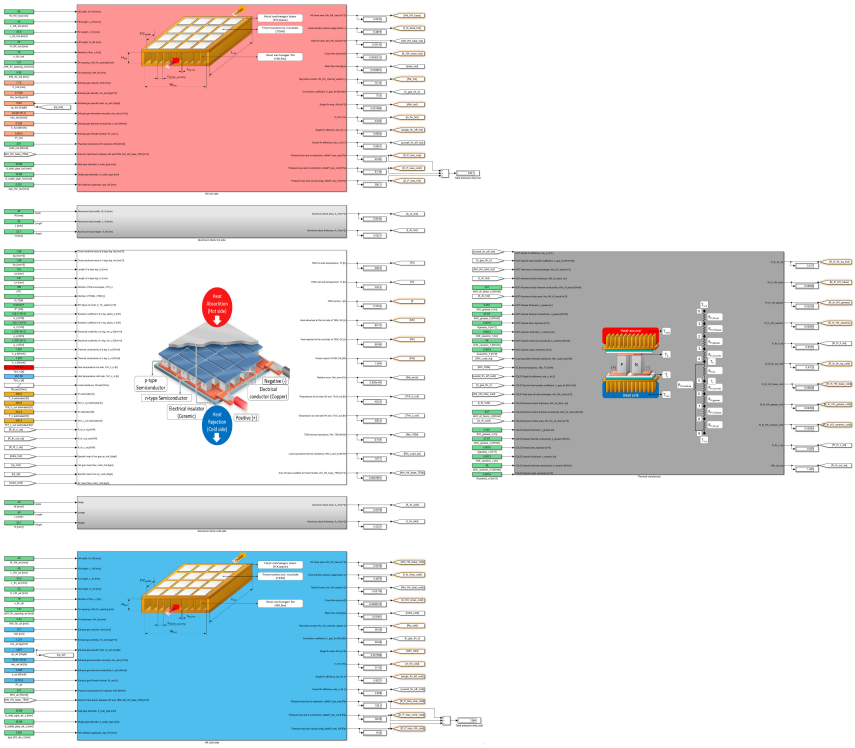

Figure 13. Simulink model with two heat exchangers (red—hot side and blue—cold side), aluminum blocks for thermal spread (light grey), the TEM between, and the thermal resistance network on right side.

Table 2. Comparison of calculated and measured values at peak measured power.

Parameter	T_h [°C]	T_c [°C]	P_{el} [W]	I [A]	V [V]	η_{th} [-]
Average error [%]	0.15	0.33	12.73/1.77	6.82	0.52	0.93
Error at matched load resistance [%]	0.11	0.45	10.46/3.50	2.99	0.38	1.8

As previously mentioned, Fagehi et al. [32] used a liquid (water) heat exchanger on the cold side. The same cold side temperature can be achieved by using air as the cooling fluid, but this poses an issue due to the very low thermal conductivity of air. This can be resolved by increasing the flow velocity and, to test this theory, the water cold side heat exchanger model (used only for the validation) was replaced with an air heat exchanger (similar to the one used on the hot side). Then, the air flow velocity on the cold side was adjusted to achieve a T_c value as close as possible to that obtained with the validated model (Figure 14). The required flow velocity was determined to be 13.1 m/s (or 47.2 km/h) and appears feasible for highway trucks and buses running at a constant speed. Here, the main advantages of utilizing air would be the lower weight and space requirements of the system, as well as a reduced complexity. Furthermore, a proper design of the flow passage to the cold side can allow for high air velocities; thus, leading to even greater temperature gradients than in the case of the liquid coolant solution. The main disadvantages of this solution are that the temperature gradient and, consequently, the power output depends

on vehicle speed and outside temperature (still less than the coolant temperature). Also, this solution is not feasible for stationary engines.

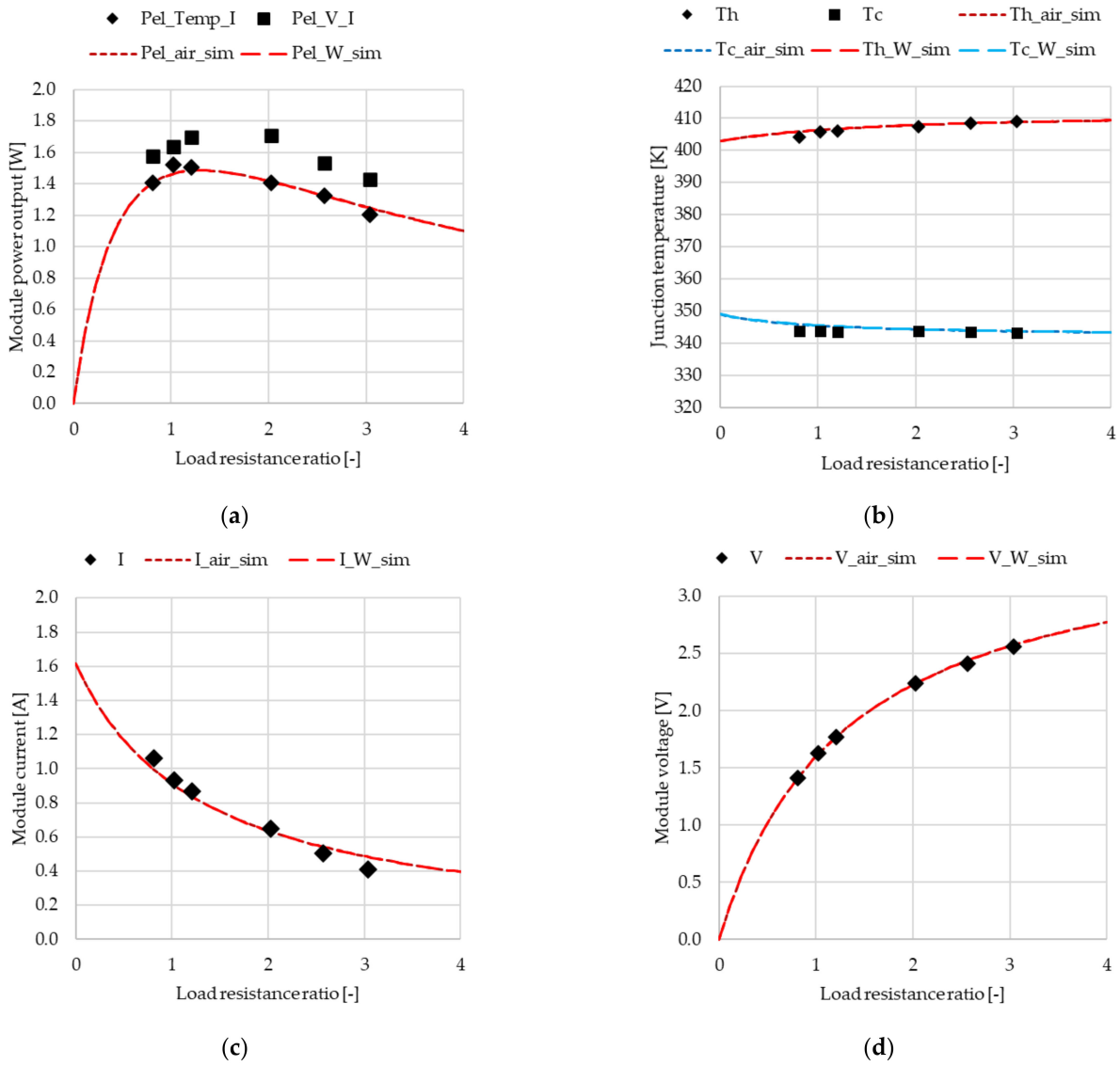

Figure 14. TEG model validation highlighting the difference between the simulated and measured values of (**a**) the electrical power output, (**b**) hot and cold junction temperatures, (**c**) current, and (**d**) voltage for two different types of cold side heat exchangers: Water (W_sim) and air (air_sim).

To test the possible output of such a TEG, 16 test cases (Table 3) were evaluated with varying air temperatures (T_{air}) and air flow velocities (V_{air}). For the hot side, the temperature of the exhaust gases was set at 250 °C with a flow velocity of 19.1 m/s (12 L engine running at 1500 min^{-1}, with an exhaust pipe diameter of 100 mm). For brevity, only the results for 50 and 90 km/h are presented here with the others are available upon request. Regarding case notation, "V" stands for velocity and "T" for temperature. The values following "V" and "T" are the velocity (in km/h) and temperature (in °C) values for that case (e.g., V50T-5 = velocity of 50 km/h and temperature of −5 °C). For this study it was assumed that the hot and cold side fluid temperatures and flow velocities are uniform and constant, but also that there is a uniform temperature distribution on the TEG and TEM surface. Furthermore, the simulation was performed for only one TEM. Consequently, when considering the desired number of TEMs this will result in an overprediction of the power output.

Table 3. Test cases for cold side heat exchanger using air as cooling fluid.

Case	$T_{air,-5}$ [°C]	$T_{air,10}$ [°C]	$T_{air,20}$ [°C]	$T_{air,30}$ [°C]
$V_{air,50}$ = 13.9 [m/s] $V_{air,80}$ = 22.2 [m/s] $V_{air,90}$ = 25.0 [m/s] $V_{air,120}$ = 33.3 [m/s]	−5	10	20	30

Table 4 and Figures 15 and 16 show the results for the two different velocities 50 and 90 km/h. Analysis of the results finds that both the higher air flow velocity on the cold side and a lower ambient temperature increase the output of the TEG. Decreasing the air temperature raises the temperature gradient and the power output, but also reduces the temperature of the hot side junction to that below the maximum allowable value of the TEM. This is because the hot side heat flow rate is constant. To further augment the output of the TEG, it would be necessary to increase the heat flow rate on the hot side (either by increasing the exhaust temperature or the flow velocity). Consequently, a high TEG output requires not only a good HX, but also a suitable heat extraction strategy.

Table 4. Results for cold side heat exchanger using air as cooling fluid.

Parameters	Case							
	V50T-5	V50T10	V50T20	V50T30	V90T-5	V90T10	V90T20	V90T30
P_{max} [W]	4.023	3.562	3.260	2.972	4.568	4.043	3.702	3.376
T_h [K]	449.2	453.5	456.4	459.3	444.6	449.0	452.1	455.2
T_c [K]	347.6	357.6	364.7	371.7	336.3	347.1	354.6	362.0
ΔT [K]	101.7	95.9	91.8	87.6	108.3	101.9	97.5	93.1

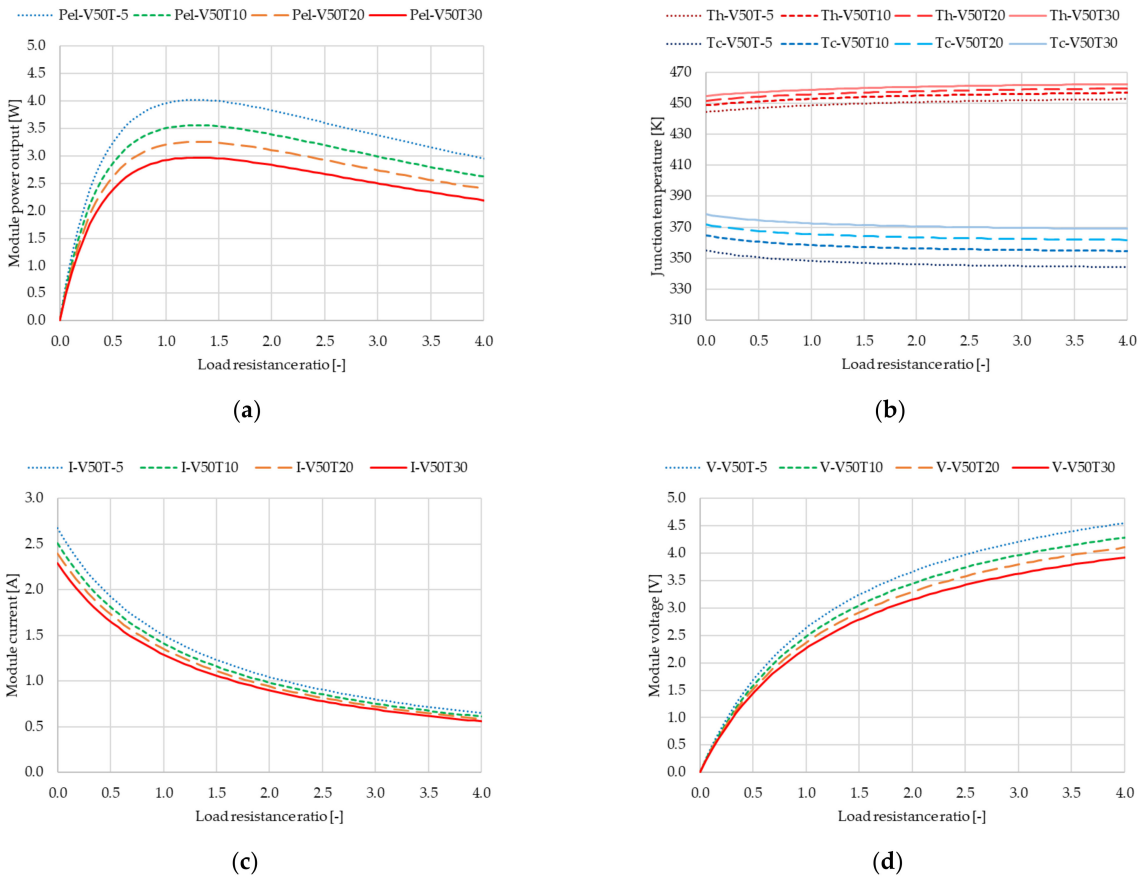

Figure 15. (**a**) Module power output, (**b**) junction temperature, (**c**) module current, and (**d**) module voltage with respect to the load resistance ratio for a velocity of 50 km/h at various temperatures (−5, 10, 20, and 30 °C).

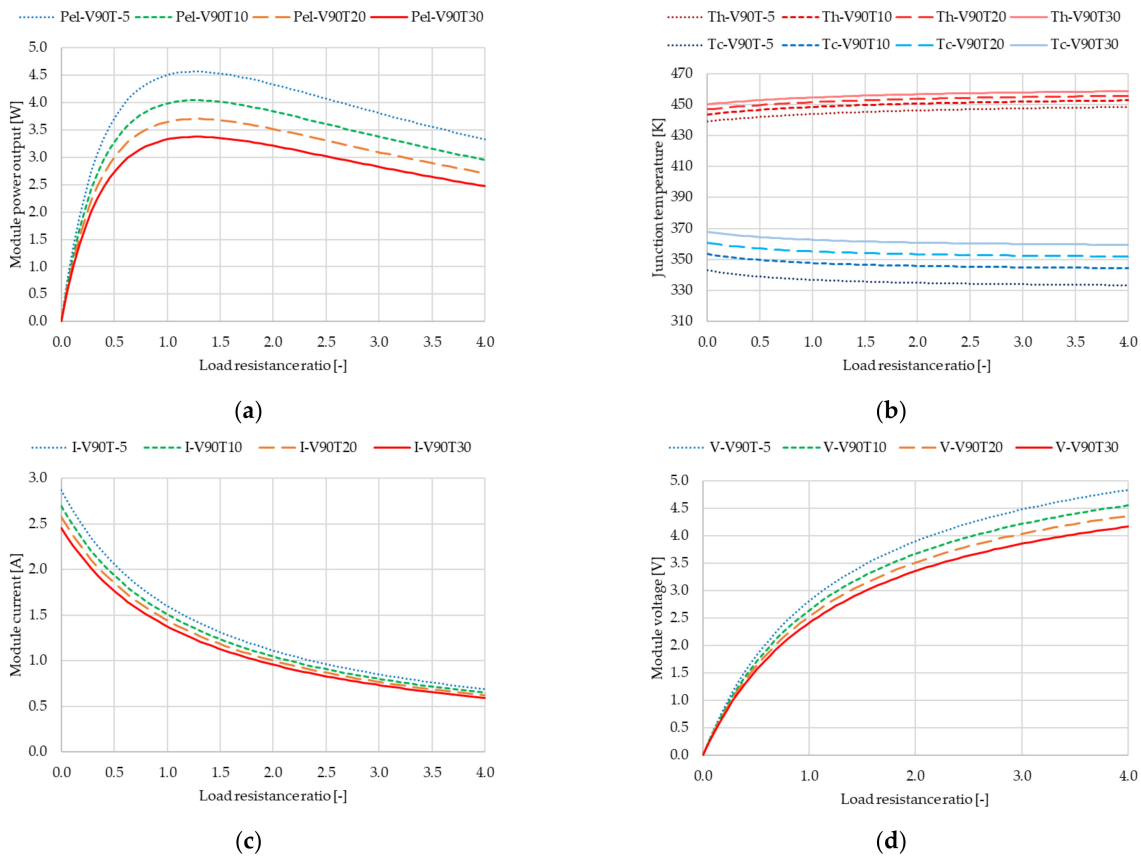

Figure 16. (**a**) Module power output, (**b**) junction temperature, (**c**) module current, and (**d**) module voltage with respect to the load resistance ratio for a velocity of 90 km/h at various temperatures (−5, 10, 20, and 30 °C).

6. Conclusions

Considering the vast amounts of wasted thermal energy from internal combustion engines, the study of thermoelectric power generation is necessary as a possibility to increase overall energy efficiency. Thermoelectric devices are environmentally friendly and have numerous other advantages including the lack of moving parts, high reliability, the direct conversion of thermal energy into electrical energy, as well as low maintenance requirements. However, the main disadvantage of such devices is their low efficiency owing to the small $Z\overline{T}$ values currently found in commercial devices.

In the present study, two Simulink models are presented (see Appendix A for detailed Simulink blocks). The first model was created based on the work of Lee et al. [20] to estimate thermoelectric parameters of a thermoelectric module. The validation showed that, even though the temperature dependency of the thermoelectric parameters was neglected, there is a relatively good agreement with experimental data.

Furthermore, a TEG model was proposed and validated for power output estimations in the case of exhaust gas thermoelectric generators. Model validation was accomplished using the results of Fagehi et al. [32]. For the validation, the cold side heat exchanger model was adapted to match the cooling method of the authors with reasonable agreement. The next step was to study the possibility of using air as the cooling fluid and to achieve the same cold side temperature, the flow velocity of the cold air was adjusted (an air velocity of 13.1 m/s showed a relatively good agreement).

After determining that similar results can be obtained with air as the cooling fluid, a parametric study was performed to show the potential of such a system for ICE exhaust coupling. The test conditions (used as input data for the cold side heat exchanger) consid-

ered a vehicle (with a respectively large engine capacity) traveling at different speeds (50, 80, 90, and 120 km/h) under dissimilar ambient air temperatures (−5, 10, 20, and 30 °C). The results showed that either a high air velocity or a low outside temperature leads to greater TEG power output. For the analyzed cases, the peak power output was 4.568 W for a temperature gradient of 108.3 K. It was also found that increasing the heat rejection on the cold side requires a simultaneous growth in heat input at the hot side to facilitate a favorable temperature gradient and, therefore, the power output of the TEG. Overall, this demonstrates that it is feasible to install an air-cooled TEG on a heavy-duty vehicle running at constant speed.

Author Contributions: Conceptualization, N.V.B.; methodology, N.V.B.; software, N.V.B. and D.M.; validation, F.M., C.D., and N.V.B.; formal analysis, N.V.B. and F.M.; investigation, N.V.B.; resources, N.V.B.; data curation, N.V.B. and D.M.; writing—original draft preparation, N.V.B.; writing—review and editing, N.V.B., F.M., and C.D.; visualization, N.V.B.; supervision, F.M.; project administration, N.V.B. All authors have read and agreed to the published version of the manuscript.

Funding: This research received no external funding.

Institutional Review Board Statement: Not Applicable.

Informed Consent Statement: Not Applicable.

Data Availability Statement: Not Applicable.

Acknowledgments: This paper was supported by the Project POCU/380/6/13/123927 "Entrepreneurial competences and excellence research in doctoral and postdoctoral programs-ANTREDOC", project co-funded by the European Social Fund.

Conflicts of Interest: The authors declare no conflict of interest.

Appendix A

Detailed Simulink blocks (Figures A1–A14). Please note that the values that can be seen in the figures were not necessarily used to validate the model. Also, the iterative temperature calculation loop is not included here.

Heat exchanger–hot side (similar for cold side)

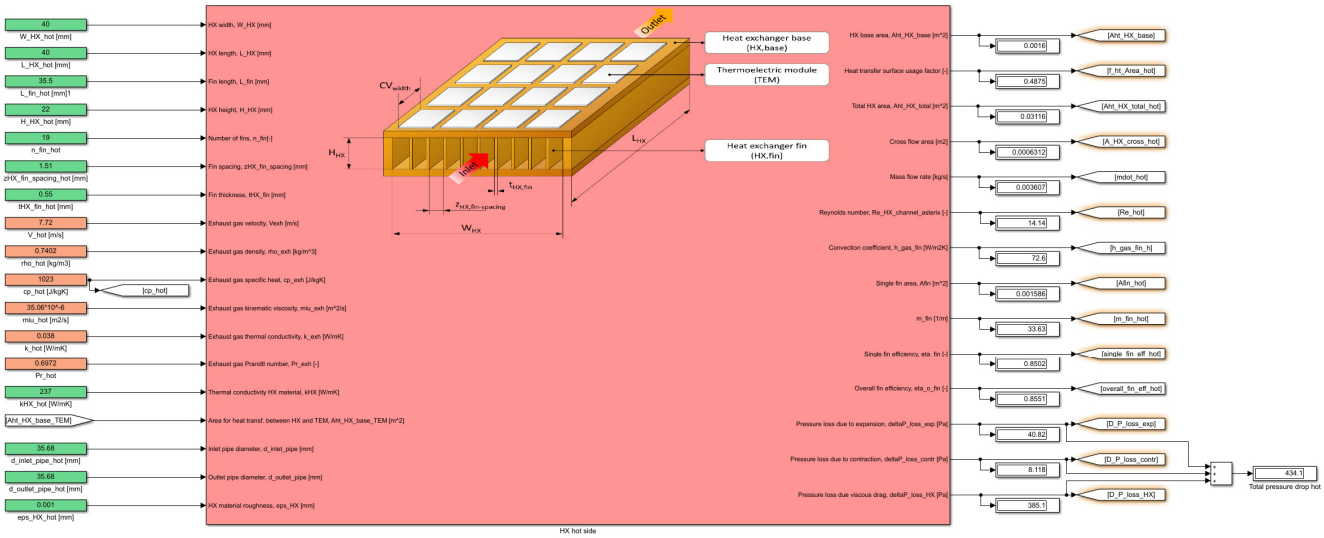

Figure A1. Hot side heat exchanger block.

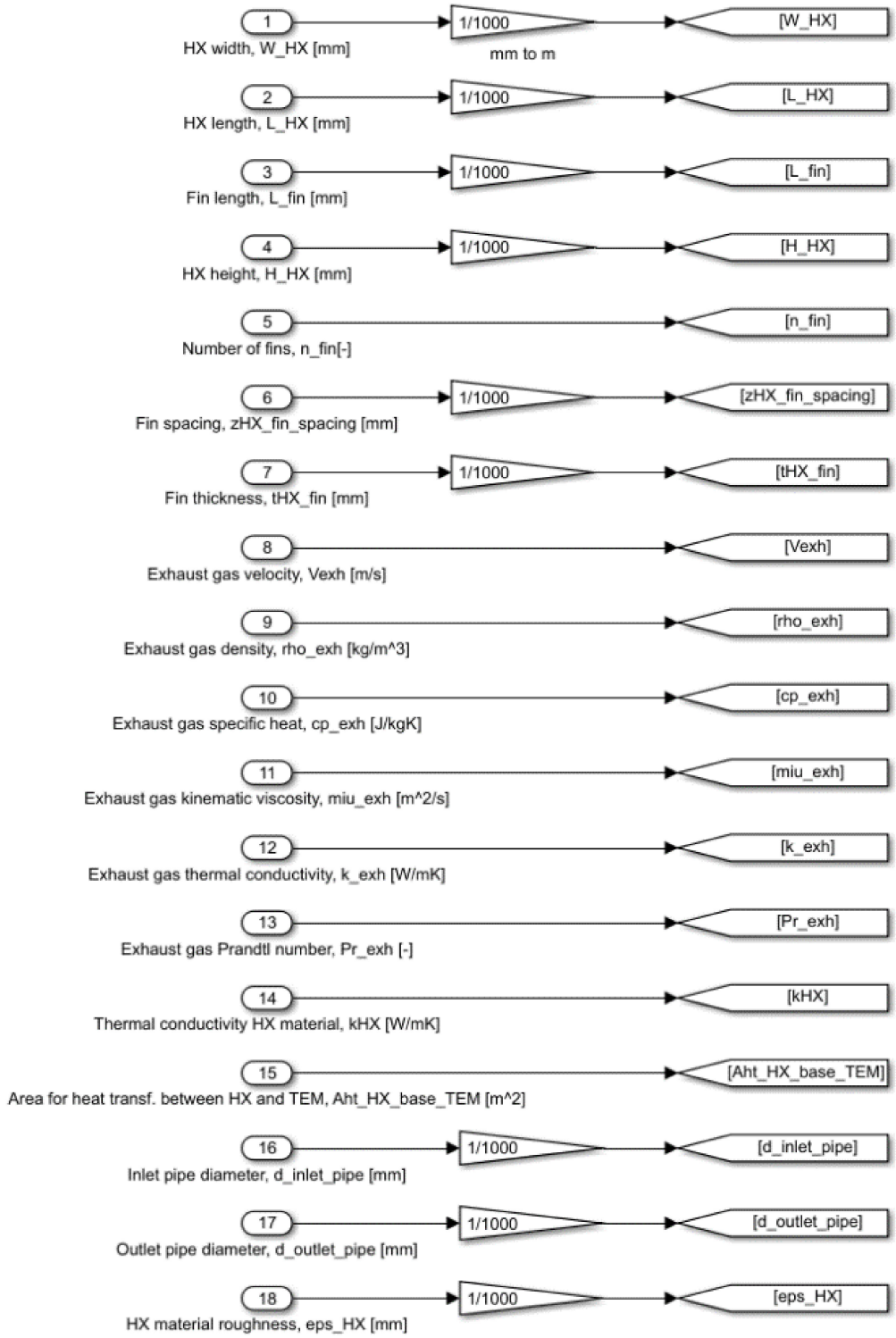

Figure A2. Hot side heat exchanger block—inputs.

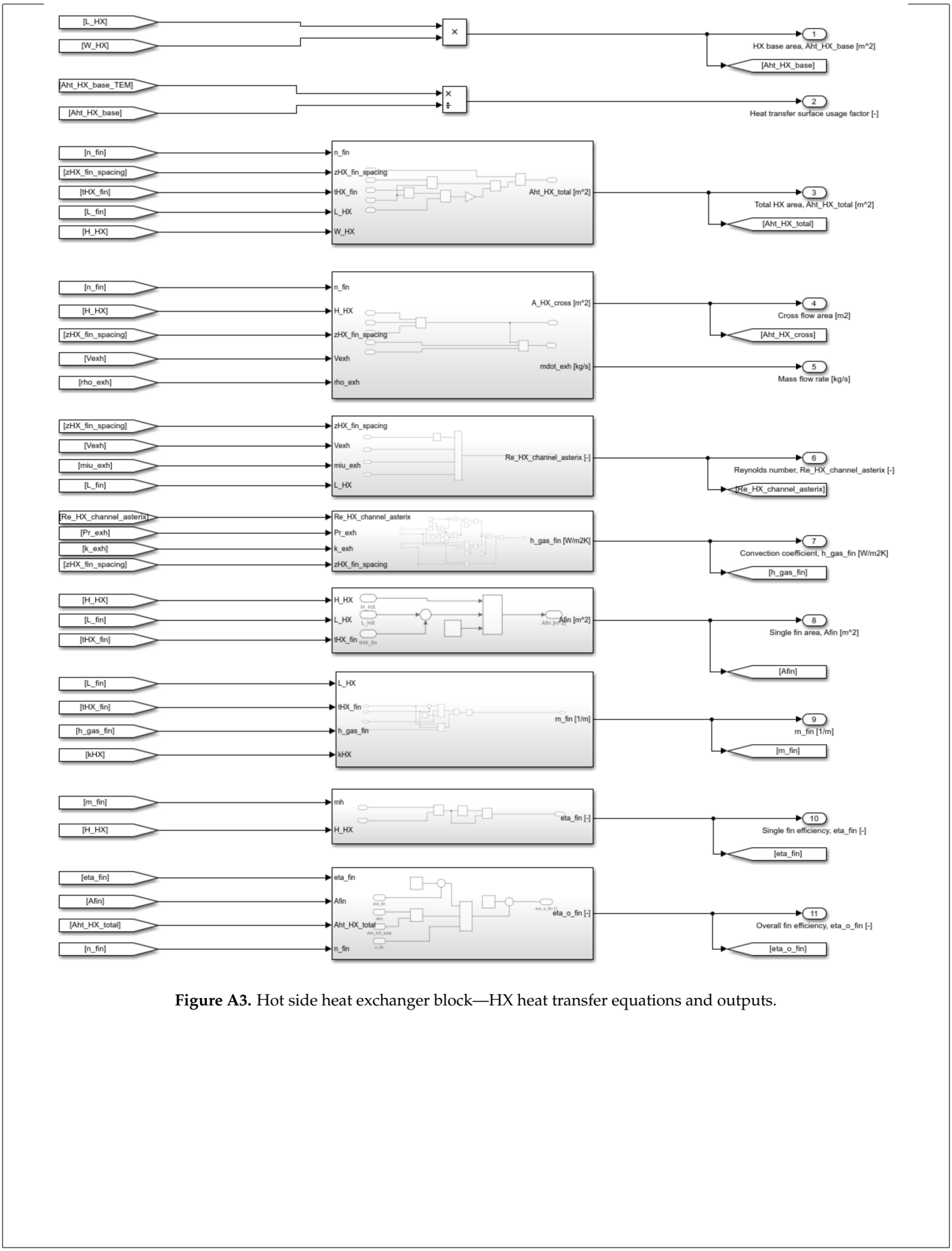

Figure A3. Hot side heat exchanger block—HX heat transfer equations and outputs.

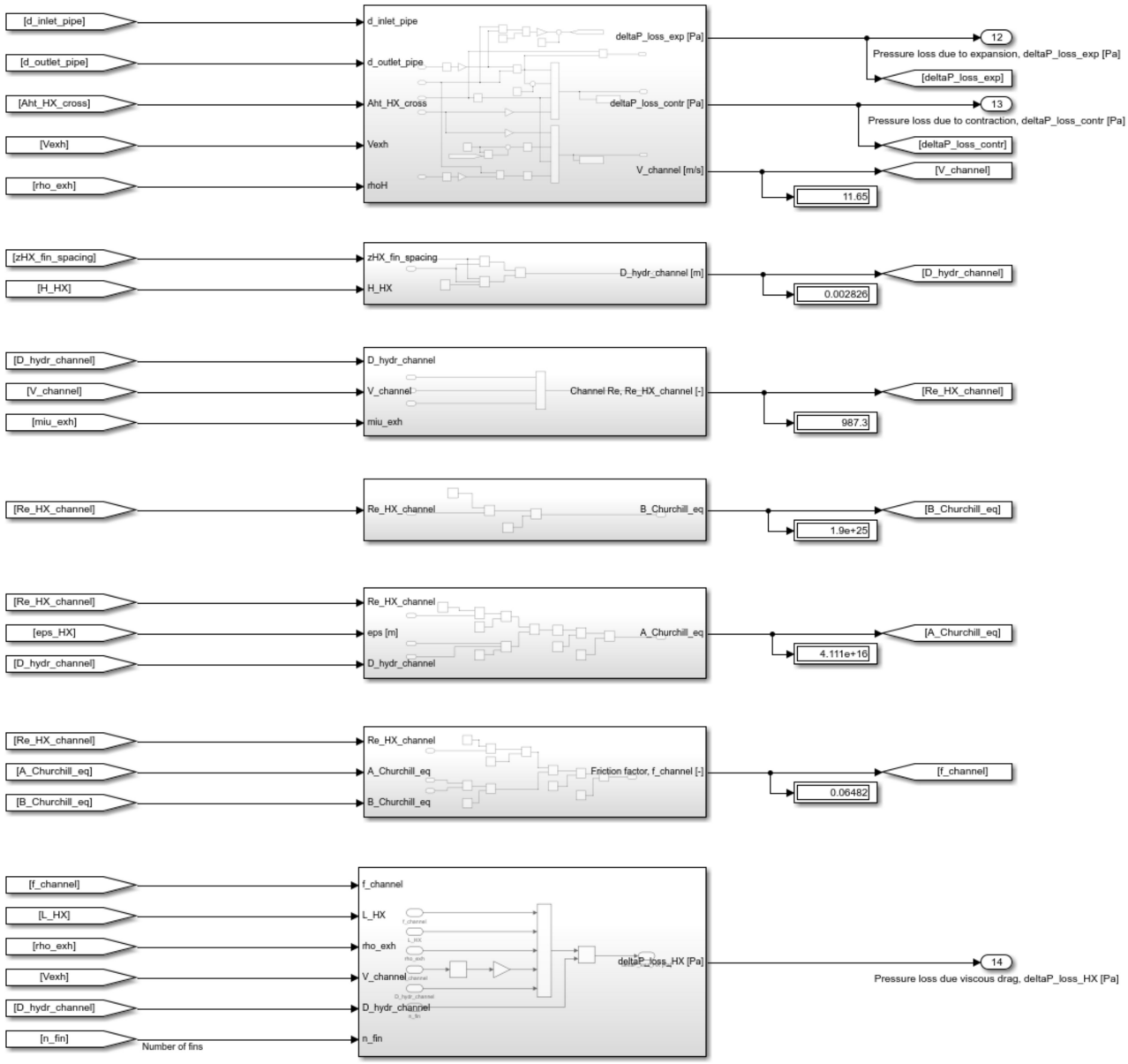

Figure A4. Hot side heat exchanger block—HX pressure drop equations and outputs.

Aluminum block—hot side (similar for cold side)

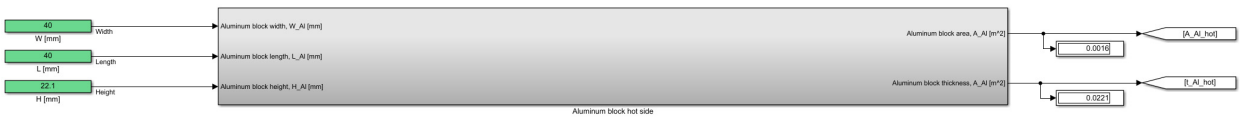

Figure A5. Aluminum block.

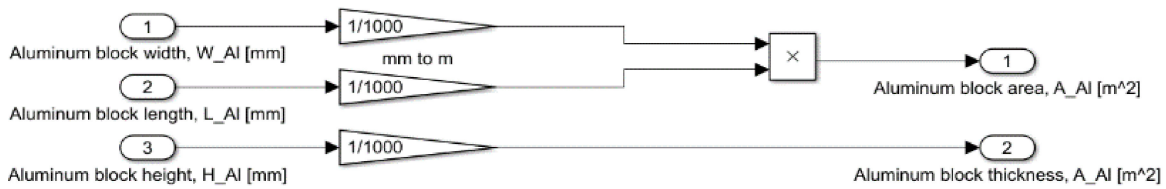

Figure A6. Aluminum block—equations.

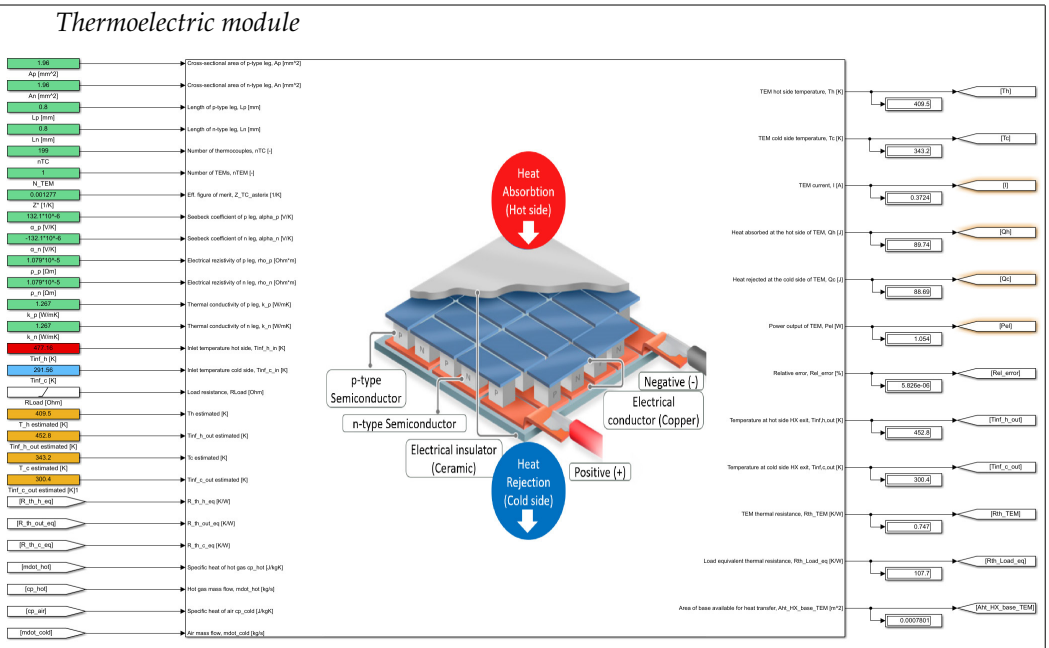

Figure A7. Thermoelectric module block.

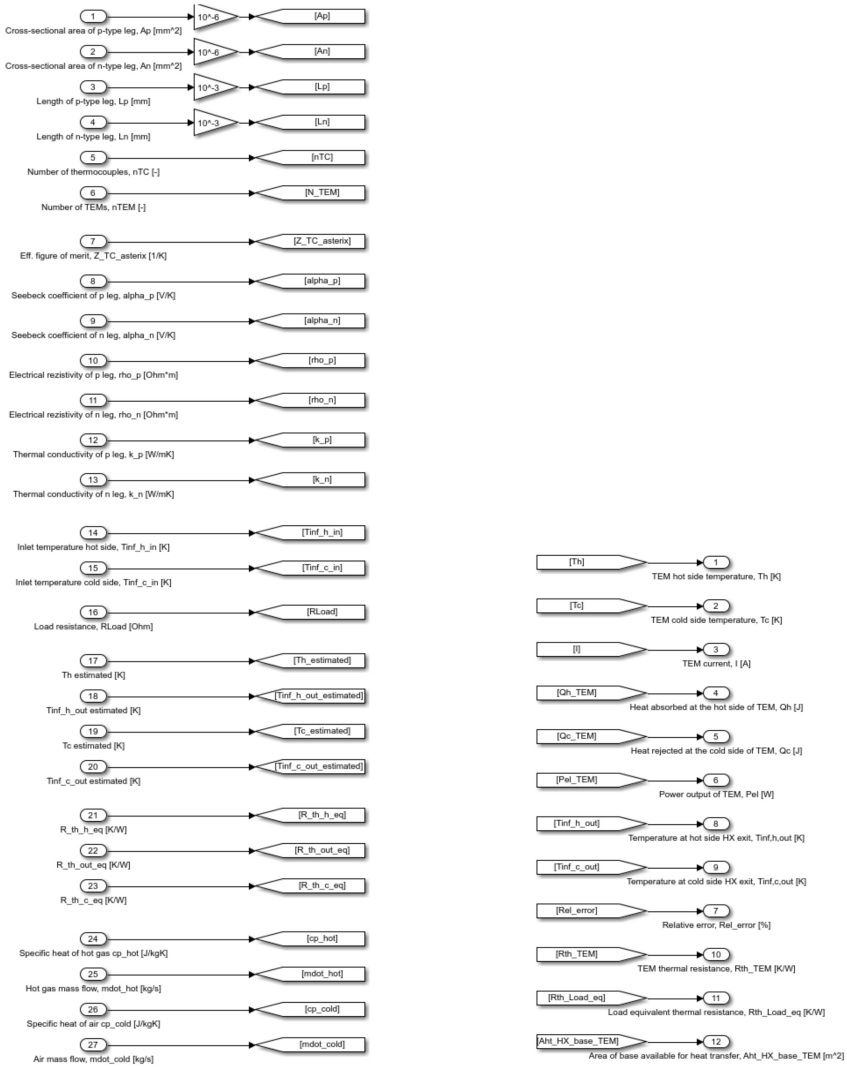

Figure A8. Thermoelectric module block—inputs and outputs.

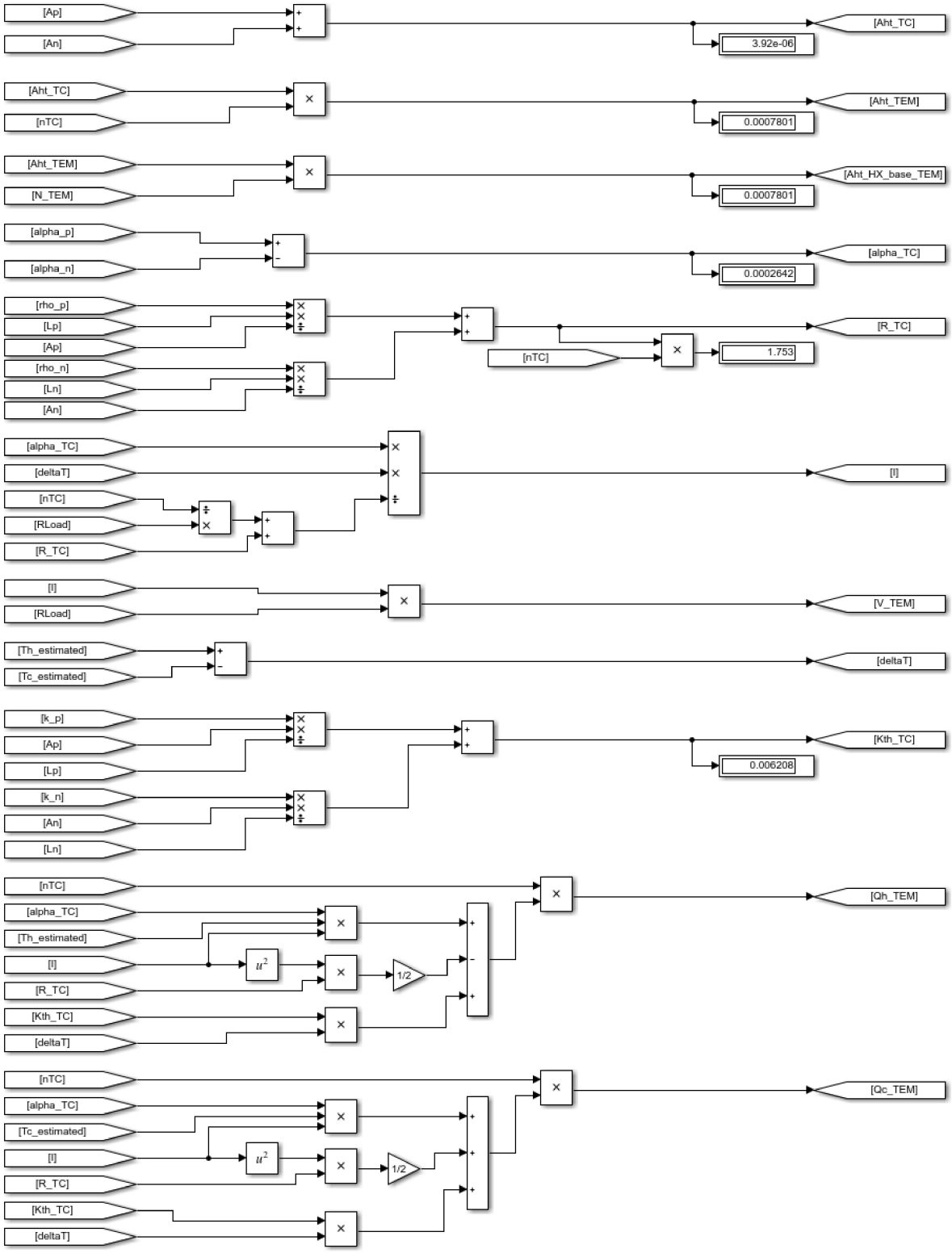

Figure A9. Thermoelectric module block—equations—part 1.

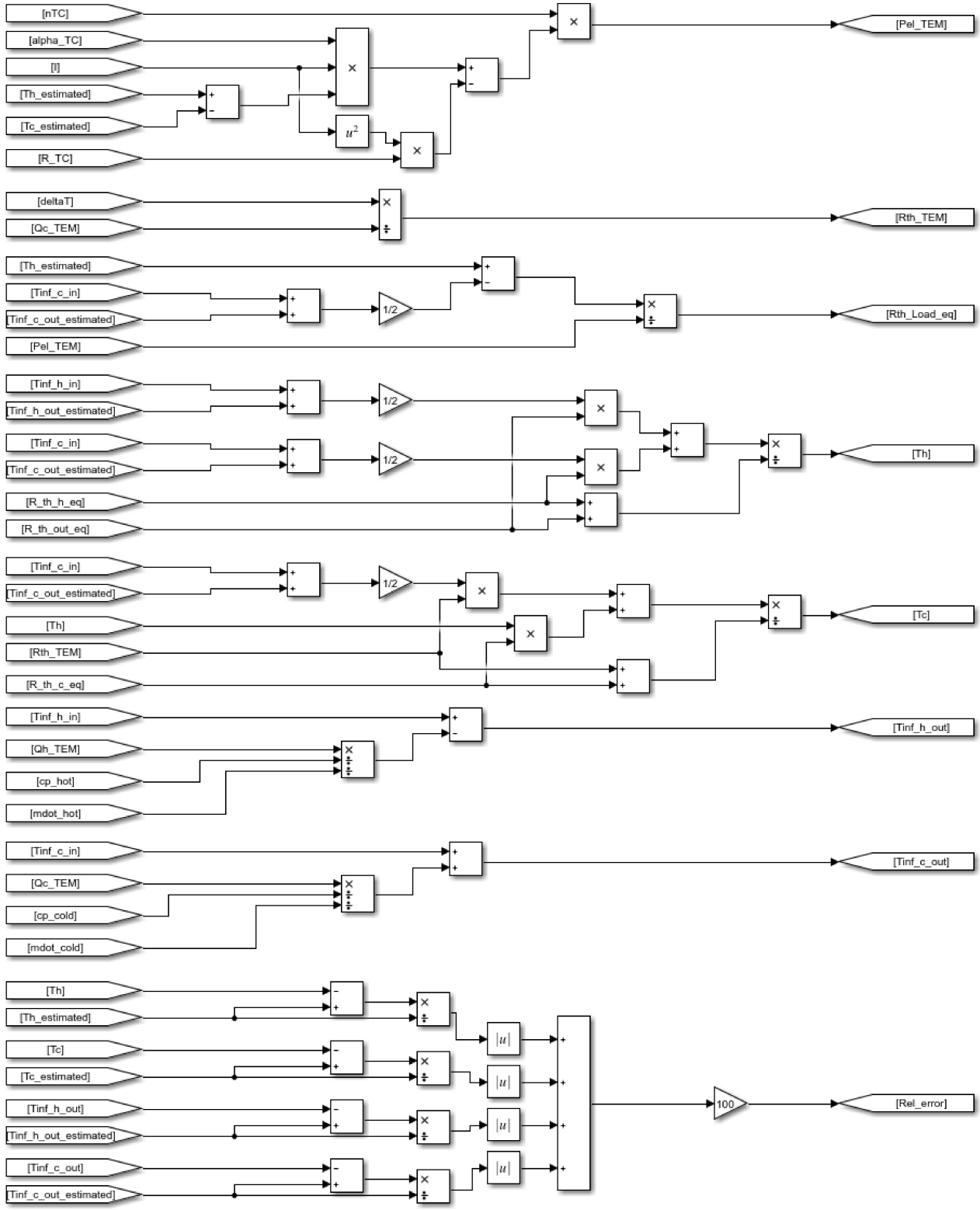

Figure A10. Thermoelectric module block—equations—part 2.

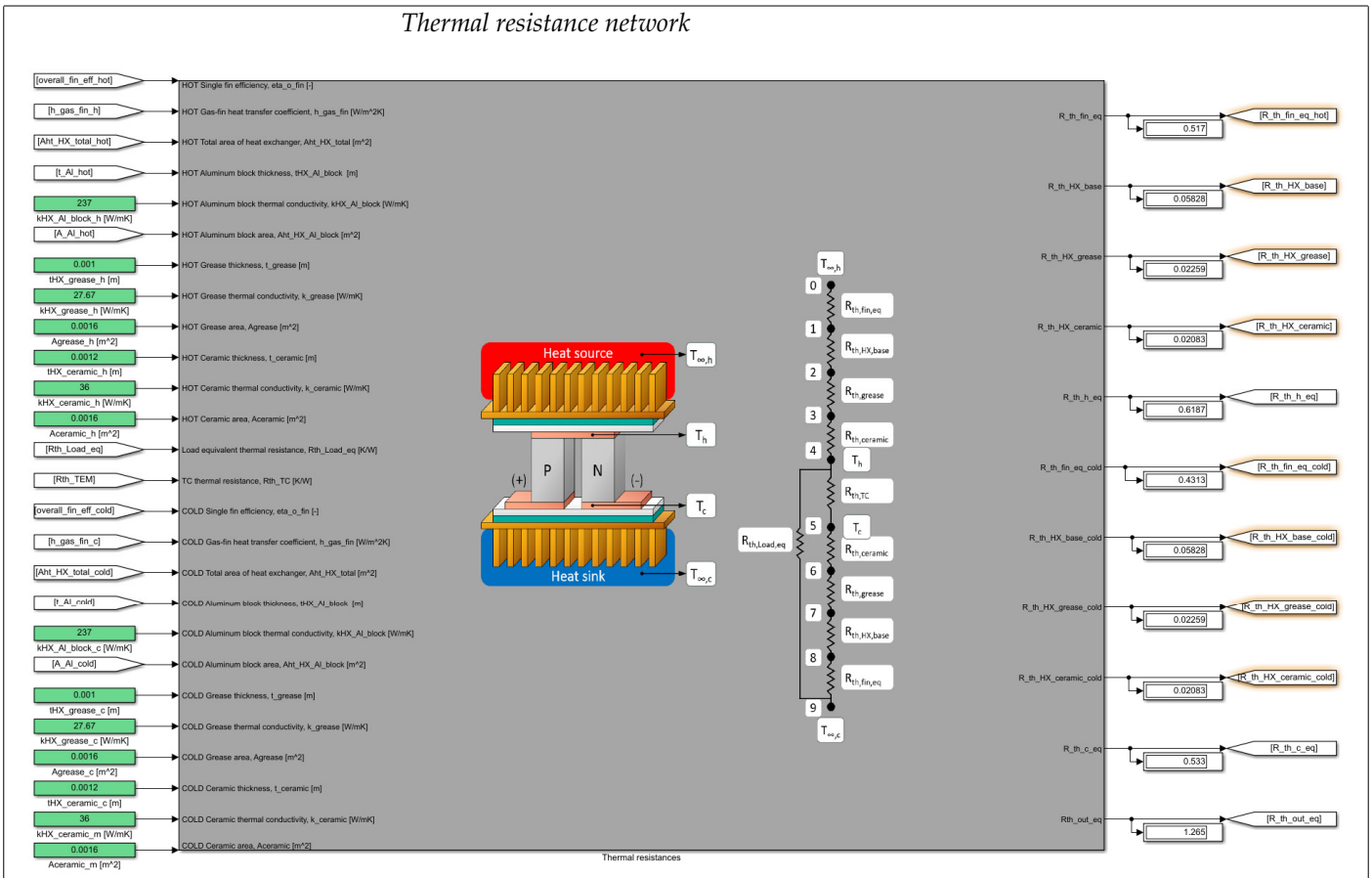

Figure A11. Thermal resistance network block.

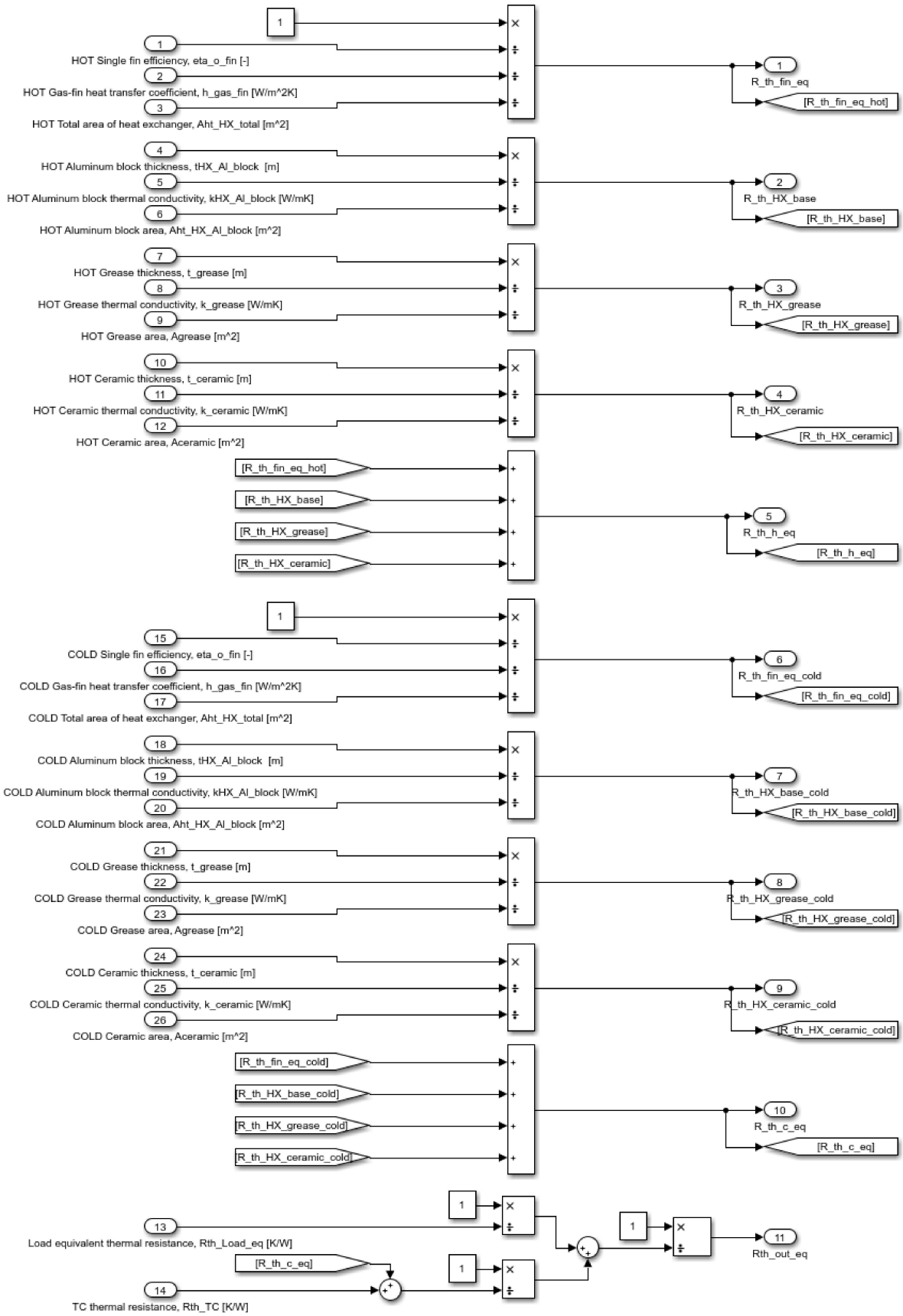

Figure A12. Thermal resistance network block—equations.

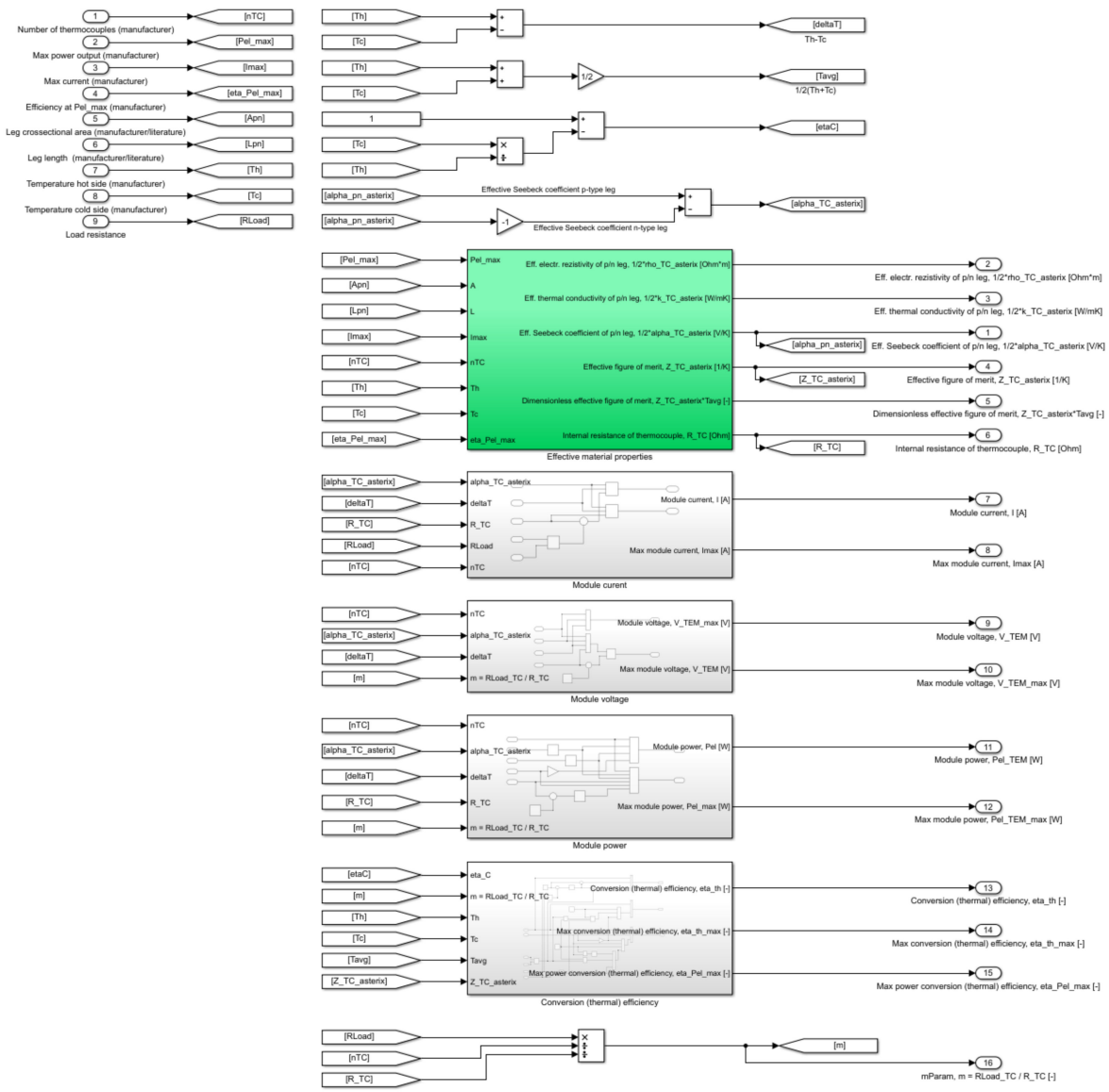

Figure A13. Effective properties model blocks (Figure 3)—equations.

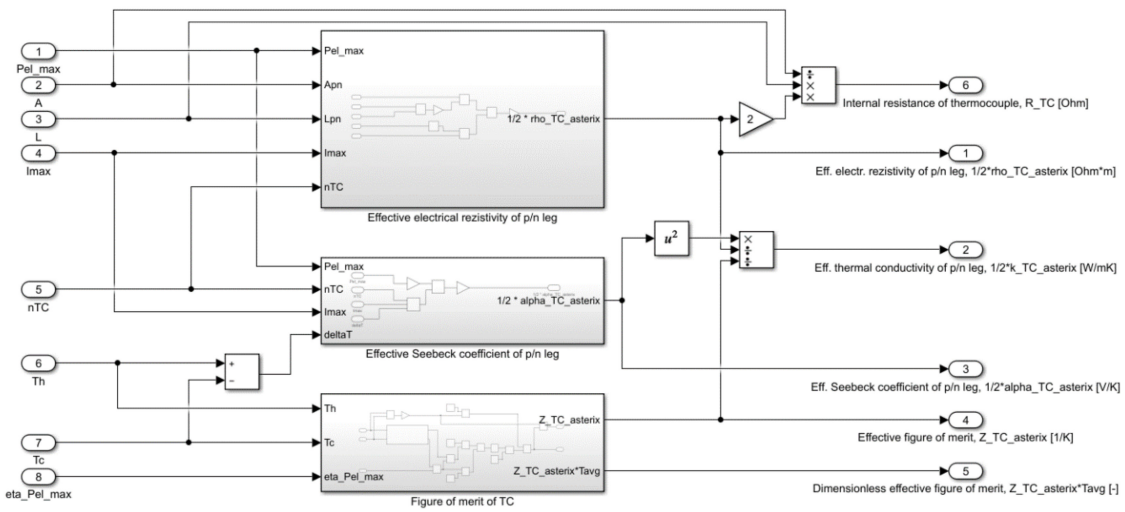

Figure A14. Effective properties model blocks (Figure 3)—Detail of the effective material properties block (Figure A13).

References

1. Hariram, A.; Koch, T.; Mårdberg, B.; Kyncl, J. A Study in Options to Improve Aerodynamic Profile of Heavy-Duty Vehicles in Europe. *Sustainability* **2019**, *11*, 5519. [CrossRef]
2. Márquez-García, L.; Beltrán-Pitarch, B.; Powell, D.; Min, G.; García-Cañadas, J. Large Power Factor Improvement in a Novel Solid–Liquid Thermoelectric Hybrid Device. *ACS Appl. Energy Mater.* **2018**, *1*, 254–259. [CrossRef]
3. Thacher, E.F.; Helenbrook, B.T.; Karri, M.A.; Richter, C.J. Testing of an automobile exhaust thermoelectric generator in a light truck. *Proc. Inst. Mech. Eng. Part D J. Automob. Eng.* **2007**, *221*, 95–107. [CrossRef]
4. Liu, X.; Deng, Y.D.; Li, Z.; Su, C.Q. Performance analysis of a waste heat recovery thermoelectric generation system for automotive application. *Energy Convers. Manag.* **2015**, *90*, 121–127. [CrossRef]
5. Yu, C.; Chau, K.T. Thermoelectric automotive waste heat energy recovery using maximum power point tracking. *Energy Convers. Manag.* **2009**, *50*, 1506–1512. [CrossRef]
6. Karri, M.A.; Thacher, E.F.; Helenbrook, B.T. Exhaust energy conversion by thermoelectric generator: Two case studies. *Energy Convers. Manag.* **2011**, *52*, 1596–1611. [CrossRef]
7. Yu, S.; Du, Q.; Diao, H.; Shu, G.; Jiao, K. Effect of vehicle driving conditions on the performance of thermoelectric generator. *Energy Convers. Manag.* **2015**, *96*, 363–376. [CrossRef]
8. Ma, X.; Shu, G.; Tian, H.; Yang, H.; Chen, T. Optimization of length ratio in segmented thermoelectric generators for engine's waste heat recovery. *Energy Procedia* **2019**, *158*, 583–588. [CrossRef]
9. Deng, Y.D.; Liu, X.; Chen, S.; Tong, N.Q. Thermal Optimization of the Heat Exchanger in an Automotive Exhaust-Based Thermoelectric Generator. *J. Electron. Mater.* **2013**, *42*, 1634–1640. [CrossRef]
10. Marvão, A.; Coelho, P.J.; Rodrigues, H.C. Optimization of a thermoelectric generator for heavy-duty vehicles. *Energy Convers. Manag.* **2019**, *179*, 178–191. [CrossRef]
11. He, W.; Wang, S.; Zhao, Y.; Li, Y. Effects of heat transfer characteristics between fluid channels and thermoelectric modules on optimal thermoelectric performance. *Energy Convers. Manag.* **2016**, *113*, 201–208. [CrossRef]
12. Fan, L.; Zhang, G.; Wang, R.; Jiao, K. A comprehensive and time-efficient model for determination of thermoelectric generator length and cross-section area. *Energy Convers. Manag.* **2016**, *122*, 85–94. [CrossRef]
13. Yu, S.; Du, Q.; Diao, H.; Shu, G.; Jiao, K. Start-up modes of thermoelectric generator based on vehicle exhaust waste heat recovery. *Appl. Energy* **2015**, *138*, 276–290. [CrossRef]
14. Wang, Y.; Li, S.; Zhang, Y.; Yang, X.; Deng, Y.; Su, C. The influence of inner topology of exhaust heat exchanger and thermoelectric module distribution on the performance of automotive thermoelectric generator. *Energy Convers. Manag.* **2016**, *126*, 266–277. [CrossRef]
15. Du, Q.; Diao, H.; Niu, Z.; Zhang, G.; Shu, G.; Jiao, K. Effect of cooling design on the characteristics and performance of thermoelectric generator used for internal combustion engine. *Energy Convers. Manag.* **2015**, *101*, 9–18. [CrossRef]
16. Goldsmid, H.J. *Introduction to Thermoelectricity*, 2nd ed.; Springer: Berlin/Heidelberg, Germany, 2016; ISBN 978-3-662-49255-0.
17. Rowe, D.M. *Thermoelectrics Handbook—Macro to Nano*; CRC/Taylor & Francis: Boca Raton, FL, USA, 2006.
18. Kumar, P.M.; Jagadeesh-Babu, V.; Subramanian, A.; Bandla, A.; Thakor, N.; Ramakrishna, S.; Wei, H. The Design of a Thermoelectric Generator and Its Medical Applications. *Designs* **2019**, *3*, 22. [CrossRef]
19. Wang, H.; McCarty, R.; Salvador, J.R.; Yamamoto, A.; König, J. Determination of Thermoelectric Module Efficiency: A Survey. *J. Electron. Mater.* **2014**, *43*, 2274–2286. [CrossRef]
20. Lee, H.; Attar, A.M.; Weera, S.L. Performance Prediction of Commercial Thermoelectric Cooler Modules using the Effective Material Properties. *J. Electron. Mater.* **2015**, *44*, 2157–2165. [CrossRef]
21. Zhang, H.Y. A general approach in evaluating and optimizing thermoelectric coolers. *Int. J. Refrig.* **2010**, *33*, 1187–1196. [CrossRef]
22. KRYOTHERM. TGM-199-1.4-0.8. Available online: https://kryothermtec.com/assets/dir2attz/ru/TGM-199-1.4-0.8.pdf (accessed on 4 January 2021).
23. KRYOTHERM. TGM-127-1.4-2.5. Available online: http://kryothermtec.com/assets/dir2attz/ru/TGM-127-1.4-2.5.pdf (accessed on 4 January 2021).
24. Teertstra, P.; Yovanovich, M.M.; Culham, J.R.; Lemczyk, T. Analytical forced convection modeling of plate fin heat sinks. In Proceedings of the Fifteenth Annual IEEE Semiconductor Thermal Measurement and Management Symposium (Cat. No.99CH36306), San Diego, CA, USA, 9–11 March 1999; pp. 34–41.
25. Lee, H. *Thermoelectrics: Design and Materials*; John Wiley & Sons: Hoboken, NJ, USA, 2016.
26. Gnielinski, V. New equations for heat and mass transfer in turbulent pipe and channel flow. *Int. Chem. Eng.* **1976**, *16*, 359–368.
27. Petukhov, B.S. Heat Transfer and Friction in Turbulent Pipe Flow with Variable Physical Properties. In *Advances in Heat Transfer*; Hartnett, J.P., Irvine, T.F., Greene, G.A., Cho, Y.I., Eds.; Elsevier: Amsterdam, The Netherlands, 1970; Volume 6, pp. 503–564. ISBN 0065-2717.
28. Cengel, Y.; Ghajar, A. *Heat and Mass Transfer: Fundamentals and Applications*, 6th ed.; McGraw-Hill Education: New York, NY, USA, 2020; ISBN 978-981-315-896-2.
29. Kumar, S.; Heister, S.D.; Xu, X.; Salvador, J.R.; Meisner, G.P. Thermoelectric Generators for Automotive Waste Heat Recovery Systems Part II: Parametric Evaluation and Topological Studies. *J. Electron. Mater.* **2013**, *42*, 944–955. [CrossRef]
30. Cengel, Y.; Cimbala, J. *Fluid Mechanics Fundamentals and Applications*, 4th ed.; McGraw-Hill Education: New York, NY, USA, 2017; ISBN 978-1259696534.
31. Bergman, T.; Adrienne, L.; Frank, I.; David, D. *Fundamentals of Heat and Mass Transfer*; John Wiley & Sons, Inc.: New York, NY, USA, 2011; ISBN 978-0470-50197-9.
32. Fagehi, H.; Attar, A.; Lee, H. Optimal Design of an Automotive Exhaust Thermoelectric Generator. *J. Electron. Mater.* **2018**, *47*, 3983–3995. [CrossRef]

IOP Conference Series: Materials Science and Engineering

PURPOSE-LED PUBLISHING™

PAPER • **OPEN ACCESS**

Comparative analysis of fuel cell and electric public for transport busses

To cite this article: H. Cărăușan *et al* 2022 *IOP Conf. Ser.: Mater. Sci. Eng.* **1256** 012041

View the article online for updates and enhancements.

You may also like

- Comparing productivity and feed-use efficiency between organic and conventional livestock animals
Ulysse Gaudaré, Sylvain Pellerin, Marc Benoit et al.
- Inverse design of electromagnetic metamaterials: from iterative to deep learning-based methods
Chen Ma, Zhenyu Wang, Hui Zhang et al.
- Reducing 4DCBCT imaging dose and time: exploring the limits of adaptive acquisition and motion compensated reconstruction
Benjamin K F Lau, Tess Reynolds, Paul J Keall et al.

This content was downloaded from IP address 193.226.5.163 on 07/07/2025 at 15:45

Comparative analysis of fuel cell and electric public for transport busses

H. Cărăușan, B. O. Varga, D. Moldovanu, A. A. Sirca

[1]Technical University of Cluj-Napoca, Department of Automotive Engineering and Transports, B-dul.Muncii 103-105, Cluj-Napoca, ROMANIA

horatiu.carausan@auto.utcluj.ro

Abstract. Current public transport systems have been in desperate need of modernization in the past decade. The pressing issue of climate change, alongside the ever-increasing strictness of emission standards, have guided public transport operators towards the use of alternative propulsion vehicles. The most popular option to conventional powered public transport vehicles have been BEBs (Battery Electric Busses). However, in the past years, FCEBs (Fuel Cell Electric Busses) have gained massive ground in this sector. The following paper aims to shed a light on the advantages and disadvantages of both technologies, in order to determine whether or not FCEBs represent a viable solution for the future.

1. Introduction

At this moment in time, humanity finds itself at a turning point in respect to dealing with one of the most critical challenges in its history. Pollution has become an extremely destructive consequence of the rapid pace of development and the continuous process of technical evolution found in all areas of activity. Unfortunately, society has developed in a direction deeply based on consumption and swift evolution, neglecting its efficiency in terms of energy management. This has put mankind on a collision course with disastrous long-term consequences for the environment so vital to our evolution.

One of the most viable resolutions to this problem, generated partly by the transport sector, is the implementation of widespread public transport alongside imposing traffic restrictions. In order to facilitate the adoption of public transport as a primary transport solution, several modern and sustainable transport vehicles must be endorsed as viable alternatives to personal transport vehicles.

Sustainability in the transport sector has become one of the biggest challenges on a European level, in the light of current environmental challenges. The paramount measures applied in these areas have been the introduction of stricter emissions regulations and the perpetual renewal of transport fleets all over the EU. The main sustainable options in regard to sustainable bus transport, have been BEBs (Battery Electric Busses) and FCEBs (Fuel Cell Electric Busses). Both technical solutions are based on the use of electrical energy as means of propulsion.

The fundamental difference between these classes of vehicles, is the means by which they store electrical energy. Both types use batteries in order to manage and contain the voltage necessary for propulsion, however, FCEBs use fuel cells as an energy buffer, reducing the strain of the battery, used mainly for power delivery. This feature make FCEBs less vulnerable to battery deterioration, drastically reducing the cost of operation.

Content from this work may be used under the terms of the Creative Commons Attribution 3.0 licence. Any further distribution of this work must maintain attribution to the author(s) and the title of the work, journal citation and DOI.
Published under licence by IOP Publishing Ltd

Battery powered busses have long been in use and currently represent the main solution for sustainable urban transport. The main differentiating factors between this kind of transport solutions are the chemistry of the batteries, charging power, battery capacity and range. The main type of battery used in the energy storage of battery electric busses, are Lithium-based (LFP, NMC, LTO). The chemical configuration of the batteries, dictate in turn, the range and energy consumption of BEBs. The average range of such busses varies around 150 km to 300 km depending on the size of the battery pack. The average energy consumption of such vehicles is of 1.3 kWh/km, depending on environment conditions, as well as vehicle load and usage rates. These known parameters, make BEBs, an obvious alternative to conventional fuel public transport busses [1].

Given the fact that BEBs were adopted on a large scale and in a relatively short time window, limited progress was made in the development of new battery technologies. This has led to a few shortcomings regarding the long-term operation of such busses. BEBs offer the possibility of drastically reducing local emissions and sound pollution at the cost of a difficult and complex recycling process. This significant disadvantage can be overcome by using an alternative way of buffering the energy needed for electric propulsion [2].

In this regard, hydrogen takes center stage, being one of the most efficient energy carriers available at the moment. It can be obtained by various means and can be used to store the required energy for long range operation of electric motors, by means of fuel cell usage. Presently, the most common methods of obtaining hydrogen, are steam reforming of natural gas and electrolysis. Both means present their own advantages and disadvantages, electrolysis being the more sustainable method of the two [3].

Fuel cells represent constructions capable of transforming hydrogen and oxygen into electricity, utilized to power tractive systems. They possess superior energy efficiency and emissions reduction capabilities. Having this transformation at hand, offers FCEBs the possibility to travel longer distances compared to conventional BEBs. In this way, energy storage is offset into specially designed tanks, capable of storing adequate amounts of hydrogen for extended ranges of operation [4].

There are several types of fuel cells available to the market, each presenting a series of advantages and disadvantages. The most used type of fuel cell is the Proton Exchange type (PEM). It uses a solid type of electrolyte in the form of an exchange membrane. PEM fuel cells operate in a narrow temperature range of 80-100 ºC and are capable of developing powers up to 100kW with an efficiency of around 40-60 %. This type of fuel cell has found broad use in the mobility industry, as it has a reduced startup time, alongside small packaging, and reduced weight. However, PEM fuel cells manifest a high sensitivity to humidity or dryness, as well as being influenced by water salinity and environment temperature. Other types of fuel cell technologies are: Alkaline (AFC), Phosphoric acid (PAFC), Molten carbonate (MCFC) and Solid oxide (SOFC). However, these types of fuel cells are not normally found in mobility applications, due to long start times and high costs of production and operation.[5] [6] [7].

In the elaboration of this paper, two main solutions of alternative public transport were modeled. The baseline is a completely electric bus, equipped with a Li-Ion battery pack and two hub-mounted electric machines. The fuel cell variant is also equipped with a smaller battery used for power delivery, in addition to a PEM fuel cell. This paper aims to highlight the key differences between these solutions, as well as to compare the way in which improvements to fuel cell technologies can help adopt this type of vehicle as a backbone of sustainable transport systems.

2. Material and Method

The purpose of this paper is to illustrate the differences in functionality of two buses that are similar in terms of construction but different in terms of energy management. In order to perform this analysis, AVL Cruise M, developed by AVL List GmbH has been used.

In order to perform the analysis, two vehicles produced by Solaris were modelled using AVL Cruise M. Solaris has developed and built a versatile public transport platform, found in multiple construction variants, the construction solution chosen being Urbino 12, a bus found in both fully

electric and fuel cell versions. Given the high degree of similarity between these vehicles, the focus of this paper will be to illustrate the functional differences, the structural part of the models being fundamentally similar. Of interest will be the way in which the range of these buses evolves, once they are subjected to identical test cycles. Before the actual modeling stage, it is important to define the various structural and functional characteristics of the vehicles considered. The data can be found in table 1.

Table 1. Constructive characteristics of the Solaris Urbino 12 busses [8]

Model			
Urbino 12 Electric		**Urbino 12 Fuel Cell**	
Kerb mass	13790 Kg	**Kerb mass**	11032 Kg
Maximum authorized mass	19000 Kg	**Maximum authorized mass**	19000 Kg
Length	12000 mm	**Length**	12000 mm
Width	2550 mm	**Width**	2550 mm
Frontal area	1.97 m^2	**Frontal area**	1.97 m^2
Friction coefficient	0.8	**Friction coefficient**	0.8
Battery power	350 kW	**Battery power**	100 kW
Motor	2 x ZF AVE 130	**Motor**	2 x ZF AVE 130
Motor power	2 x 150 kW	**Motor power**	2 x 150 kW
Fuel cell	-	**Fuel cell**	Ballard HD 60
Range	100 Km	**Range**	350 Km
Tank capacity	-	**Tank capacity**	28 – 37.5 kg H_2

The modelling process contained a series of parametrization processes. The models have a modular construction, every functional element of a BEV and FCEV being represented by a dedicated module. In order to obtain valid results, all components were modelled to the specifications published by the manufacturer. The electric model is composed of a battery pack, an ensemble of 2 ZF AVE 130 hub-mounted electric motors, a consumer module and a control functions subsystem. In addition to the components listed previously, the fuel cell variant of the Urbino 12 is equipped with a Ballard HD60 fuel cell.

The battery pack was configured having as reference the output power, voltage and current, in order to be as accurate as possible. The tractive system is composed of 2 electric motors, modelled after the real machines used by Solaris and manufactured by ZF. Each motor develops a peak power of 250 kW and a nominal voltage of 650V with a maximum current of 340A [9]. The control functions subsystem contains algorithms used for controlling each engine, as well as the calculation functions of range and performance of the vehicle. The functions used for implementing the test cycle, are also contained in this subsystem. The fuel cell model contains the Ballard HD60 fuel cell, as well as a dedicated function that controls the energy flow between the battery and the fuel cell.

The WLTC cycle has been chosen as the test cycle, being included in the AVL suite. This profile contains speeds close to those with which an urban bus would travel integrating the lower and upper limits between which the speed of the modeled vehicle must be located. In addition to these limits, the actual travel speed is included, along with gear shift points (if applicable).

In order to validate both models, their dynamic performance, energy consumption, battery state of charge and range were observed. Following the simulation, both models obtained performances similar to those declared by the manufacturer. The models can be observed in figure 1 and 2.

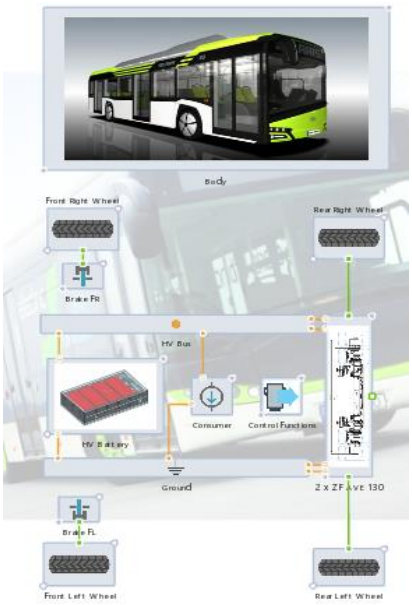

Figure 1. Urbino 12 Electric model

Figure 2. Urbino 12 Fuel Cell model

3. Results and Discussions

The first criterion analysed in case of the electric model, is the evolution of the range in relation to the travel speeds imposed by the test cycle. The results obtained are in line with the actual values provided by the manufacturers. At the end of the test cycle, a remaining range of 77.82 km was obtained. Considering the distance covered of 23.02 km, a total range of 100.84 km would be obtained, a value extremely close to range of 100 km declared by the manufacturer. However, range is influenced by a multitude of factors, its value varying depending on the environment temperature, the driving regime, the amount of energy recovered being also extremely important in defining the range of transport. The evolution of range in case of the electric model can be seen in figure 3.

The second metric analysed is the energy consumption of the vehicle. Following the simulation, an average consumption of 185.6 kWh/100km was obtained. This translates into 1.8 kWh/km, a value situated in the interval of 1-2 kWh/km declared by the manufacturer [10]. The evolution of energy consumption over the test cycle can be seen in figure 4.

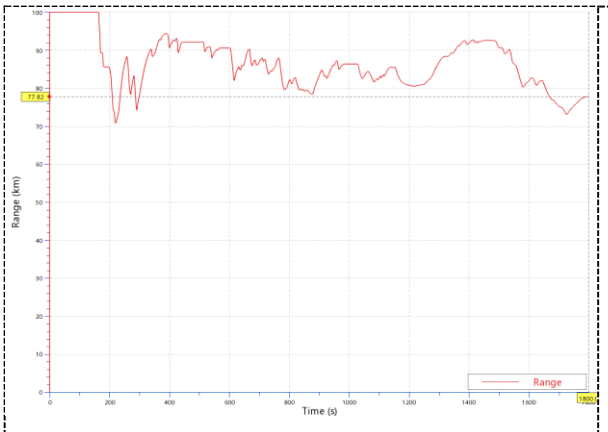

Figure 3. Evolution of range – Urbino 12 Electric

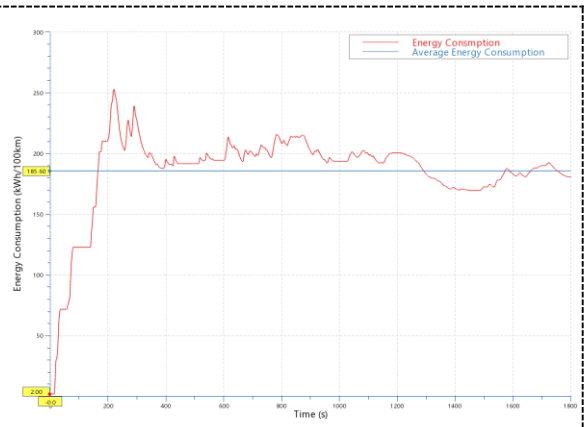

Figure 4. Battery energy consumption and average battery energy consumption – Urbino 12 Electric

In case of the fuel cell model, 5 different simulation cases were defined. Given the fact that PEM fuel cells are highly complex devices, their performance is affected by many variables. In order to showcase the improvement potential of this technology, 5 different simulation cases were created, the differentiating factor being catalyst layer thickness (measured in cm). The catalyst layer thickness is crucial as it represents the place where the electrochemical reactions associated to the generation of electricity take place. The thickness of this layer has a significant influence on the efficiency of the fuel cell. This influence is outlined through the simulation cases shown in table 2.

The first parameters analysed in the fuel cell model simulation were range and energy consumption. The results obtained after the electric model simulation, serve as a baseline for comparison. The evolution of these factors can be seen in figures 5 and 6. The data is presented in table 2.

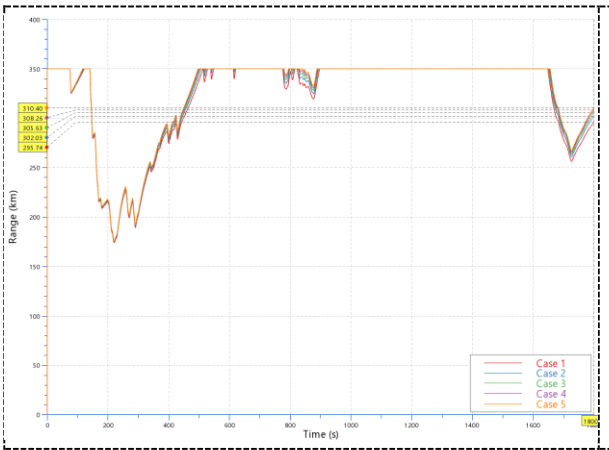

Figure 5. Evolution of range – Urbino 12 Fuel Cell

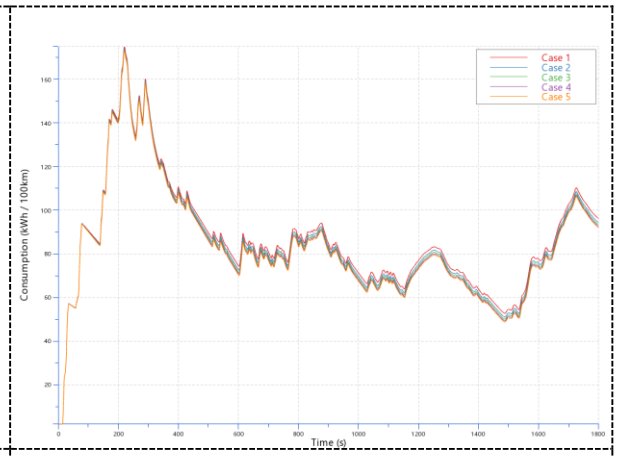

Figure 6. Battery energy consumption– Urbino 12 Fuel Cell

Table 2. Fuel cell model simulation results

	Simulation case				
	Case 1	**Case 2**	**Case 3**	**Case 4**	**Case 5**
Catalyst layer thickness (cm)	0.001	0.002	0.003	0.004	0.005
Remaining range (km)	295.74	302.03	305.63	308.26	310.40
Average battery energy consumption (kWh/100km)	86.63	85.24	84.42	83.83	83.35

The best way to compare these types of vehicles, is to take into consideration their overall energy consumption. In case of the BEBs, the only energy source is the battery, the overall energy consumption being identical to the battery energy consumption.

In case of the FCEBs on the other hand, there are two sources from which energy can be consumed: the battery pack and the fuel cell. The battery pack energy consumption is calculated by the software and can be seen in figure 6. However, the overall energy consumption of the vehicle represents a sum of the energy drawn from the battery and the energy resulted from the hydrogen mass reacted in the fuel cell. The hydrogen mass reacted can be seen in figure 7. The difference in the reacted hydrogen mass determined by the efficiency of the fuel cell. The difference in efficiency is determined by the catalyst layer thickness. The efficiency of the fuel cell in each case can be seen in figure 8.

Given the fact that 1 kg of hydrogen has the equivalent of 33.6 kWh, and the reacted mass can be extracted from the software, the overall energy consumption can be determined [12]. The data can be seen in table 3.

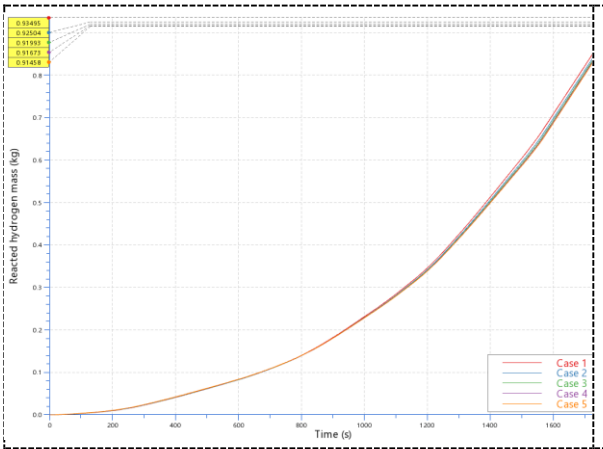

Figure 7. Reacted hydrogen mass – Urbino 12 Fuel Cell

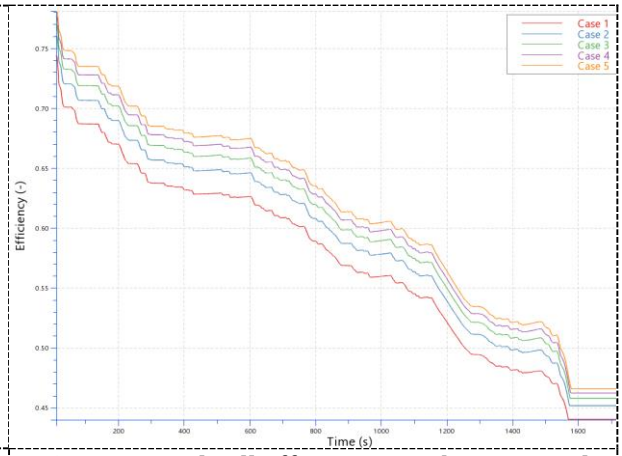

Figure 8. Fuel cell efficiency – Urbino 12 Fuel Cell

Table 3. Overall energy consumption

Distance travelled (km)	23.02				
Baseline - Urbino 12 Electric model					
Energy consumption (kWh/km)	1.8				
Total energy consumption (kWh)	41.436				
	Simulation case				
	Case 1	**Case 2**	**Case 3**	**Case 4**	**Case 5**
Fuel cell efficiency (%)	56	58	59	60.2	60.8
Average battery energy consumption (kWh/100km)	86.63	85.24	84.42	83.83	83.35
Hydrogen mass reacted (kg)	0.934	0.925	0.919	0.916	0.914
Energy resulted from the hydrogen mass reacted (kWh)	31.38	31.08	30.87	30.77	30.71
Total energy consumption (kWh)	51.17	50.70	50.29	50.06	49.88

4. Conclusions

In view of the aspects mentioned in this paper, as well as the data provided following the comparative analysis of the two solutions proposed the following can be concluded:

- Vehicles equipped with fuel cells offer a longer battery life, by their ability to keep their state of charge at a set threshold, the batteries being capable of going through fewer full charge cycles. The sustainability of fuel cell vehicles stems from their ability to use a variety of energy storage devices, having the ability of extending the life of their battery packs. At the same time, replacing battery packs and fuel cells involves lower costs than

electric vehicles. Vehicles with fuel cells are able to offer significantly more range than electric vehicles, using smaller battery packs with higher efficiency

- The range offered by fully electric solutions is much more vulnerable, being directly affected by the driving regime, the environmental conditions, as well as the surfaces on which the vehicle travel. In the case of fuel cell solutions, the evolution of range is far more predictable in terms of monitoring hydrogen consumption, the estimates being closer to real values.
- Following the simulations, the total energy consumption in case of the FCEB, was always higher than the consumption obtained following the BEB simulation. The lowest value of consumption obtained in the case of the fuel cell model is still higher by 8.45 kWh than the baseline value set by the electric model. However, due to the progress in terms of fuel cell manufacturing and technology, this difference can be soon overcome.
- The peak efficiency of the fuel cell contained in the models was of 60.8%, the lowest value being of 56%. The peak hydrogen mass reacted was registered in case number 1 as opposed to case number 5 which manifested the lowest amount of hydrogen reacted. Analysing the battery energy consumption in corelation with the hydrogen consumption, it can be stated that in the event of a significant improvement of fuel cell efficiency, the overall energy consumption of such vehicles cand be drastically reduced to a level that competes with or surpasses fully battery powered vehicles.

References

[1] Beckers C., Besselink I. J. M., Nijmeijer H. (2021). "*The State-of-the-Art of Battery Electric City Buses*", Conference: 34th International Electric Vehicle Symposium and Exhibition (EVS34), Nanjing, Jiangsu, China.

[2] Skeete J. P., Wells P., Dong X., Heidrich O., Harper G. (2020). "*Beyond the EVent horizon: Battery waste, recycling, and sustainability in the United Kingdom electric vehicle transition*", Energy Research & Social Science, Volume 69.

[3] Ajanovic, A., Glatt, A., & Haas, R. (2021). "*Prospects and impediments for hydrogen fuel cell buses."* Energy, 235,.

[4] Bethoux O. (2020). "*Hydrogen Fuel Cell Road Vehicles: State of the Art and Perspectives.",* Energies.

[5] Piyush Sharma, Pandey O.P. (2022). *"Chapter 1 - Proton exchange membrane fuel cells: fundamentals, advanced technologies, and practical applications"*, PEM Fuel Cells, Elsevier, Pages 1-24,

[6] Efficiency of Fuel Cell: Calculation Formula & Equation (2021) https://www.linquip.com/blog/efficiency-of-fuel-cell/

[7] U.S. Department of Energy. (2016). *"Comparison of Fuel Cell Technologies"* . Energy Efficiency & Renewable Energy https://www.energy.gov/sites/default/files/2016/06/f32/fcto_fuel_cells_comparison_chart_apr2016.pdf

[8] Solaris Urbino 12 Catalogue
https://www.solarisbus.com/public/assets/content/pojazdy/2021/2021/EN_Zeroemisyjne_1920_x_1080.pdf
[9] ZF Product Overview
https://www.zf.com/products/media/en/pim/tu___axle___transmission_systems_for_buses___coaches/chassis_7/TU_Product_Overview_202206_DE_EN_LowRes_Opt_pdf.pdf
[10] Iclodean C., Cordoș N., Todoruț A. (2019). "*Analysis of the Electric Bus Autonomy Depending on the Atmospheric Conditions".* Energies.
[11] Özdemir S. N., Taymaz I. (2019). "*Thickness effect of membrane and catalyst layer on the pem fuel cell performance"*, Conference: 4th International Energy&Engineering Congress, Gaziantep.
[12] Molloy P. (2019). *"Run on less with hydrogen fuel cells".*
https://rmi.org/run-on-less-with-hydrogen-fuel-cells/#:~:text=In%20electrical%20terms%2C%20the%20energy,as%20a%20gallon%20of%20diesel.

Analysis of the modes of operation of an electric vehicle on energy consumption

Dan Moldovanu
Automotive Engineering and Transports Department
Technical University *of Cluj-Napoca*
Cluj-Napoca, Romania
0000-0003-3039-1965

Florin Mariașiu
Automotive Engineering and Transports Department
Technical University *of Cluj-Napoca*
Cluj-Napoca, Romania
0000-0003-4054-518X

Bogdan Ovidiu Varga
Automotive Engineering and Transports Department
Technical University *of Cluj-Napoca*
Cluj-Napoca, Romania
0000-0002-7533-596X

Adela Ioana Borzan
Automotive Engineering and Transports Department
Technical University *of Cluj-Napoca*
Cluj-Napoca, Romania
0000-0002-7185-0999

Horațiu Cărăușan
Automotive Engineering and Transports Department
Technical University *of Cluj-Napoca*
Cluj-Napoca, Romania
0000-0002-0952-8157

Dan Doru Micu
Department of Electrotechnics and Measurements
Technical University *of Cluj-Napoca*
Cluj-Napoca, Romania
0000-0003-4921-7166

2023 10th International Conference on Modern Power Systems (MPS) | 979-8-3503-2682-6/23/$31.00 ©2023 IEEE | DOI: 10.1109/MPS58874.2023.10187463

***Abstract*— This manuscript presents a comprehensive analysis of the modes of operation of an electric vehicle (EV) and their impact on energy consumption. The study focuses on investigating the influence of three different drivers and three distinct road inclinations on the energy efficiency of an EV via simulation in MATLAB Simulink. The objective of this research is to gain a deeper understanding of the factors that affect energy consumption in various operational scenarios, ultimately contributing to the optimization of EV performance, range, and battery state of health (SOH). The obtained results (namely battery state of charge, battery current, motor torque) were analyzed in detail to assess the patterns associated with each driver type and road inclination scenario. Statistical techniques were employed to identify significant differences in energy efficiency among the various modes of operation. Additionally, insights were gained regarding the impact of driver behavior and road inclination on the EV's energy consumption.**

Keywords— electric vehicle, MATLAB Simulink, energy consumption, driver behavior, road inclination

I. Introduction

The introduction and large-scale use of electric vehicles in traffic (especially in the urban environment) represents the solution adopted at the global level for the reduction/elimination of pollution caused by the polluting emissions of internal combustion engines. From the very beginning, electric vehicle manufacturers had to solve the major problems (barriers) caused by customer requirements, especially related to the driving range for a full charge of the battery. For this reason, research has become numerous in the direction of increasing the energy efficiency of the battery through: the development of new materials and electrochemical technologies, intelligent command and control systems of energy flows, reducing the weight of vehicles, efficient thermal management systems, etc.

A simple bibliographic analysis of the articles published on the topic of increasing the performance of electric vehicles shows that there is a lack of studies and research related to the influence of the driver's driving style on the overall energy efficiency of the electric vehicle. The researches and studies published so far mainly refer to the analysis of the main factors of influence that influence the driver's behavior and to the way in which (using different techniques) fuel consumption can be reduced and implicitly the reduction of pollution.

The main links between driver behavior and fuel consumption underlined by different studies can be considered the following [1- 4]:

- acceleration and braking: Frequent and aggressive acceleration and braking consumes more fuel. Rapid acceleration and hard braking waste energy and increase fuel consumption. Smooth and gradual acceleration, as well as gentle braking, can improve fuel efficiency.
- speeding: Driving at high speeds increases aerodynamic drag and requires more fuel to maintain the vehicle's speed. Fuel efficiency tends to decrease significantly at higher speeds. Adhering to speed limits and driving within a reasonable speed range can help conserve fuel.
- idling: Keeping the engine running while the vehicle is stationary, such as during long periods of idling, wastes fuel. Turning off the engine when parked or waiting for extended periods can save fuel.
- constant speed: Consistently maintaining a steady speed, especially on highways, promotes fuel efficiency. Avoiding unnecessary speed fluctuations or sudden changes in speed can help conserve fuel.
- planning routes: Efficient route planning can reduce fuel consumption. Minimizing the distance traveled, avoiding congested areas, and choosing routes with fewer stops and traffic lights can improve fuel efficiency.
- vehicle maintenance: Neglecting vehicle maintenance, such as ignoring engine tune-ups, underinflating tires, or using poor-quality motor oil, can negatively impact fuel efficiency. Keeping the vehicle properly maintained helps optimize fuel consumption.

In addition to the technical approach to the problem of efficient use/exploitation of a vehicle (presented above), in general, it can be considered that several key factors influence driver behavior (Fig. 1) [5 – 9]:

- cognitive factors: Attention, perception, decision-making, and reaction time are cognitive processes that impact driver behavior. Distractions, fatigue, and impaired mental states (e.g., due to alcohol or drugs) can significantly affect these factors.

979-8-3503-2682-6/23/$31.00 ©2023 IEEE

Authorized licensed use limited to: Universitatea Tehnica din Cluj-Napoca. Downloaded on July 07,2025 at 14:47:36 UTC from IEEE Xplore. Restrictions apply.

▪ individual characteristics: Personal traits such as age, gender, experience, attitude, and risk perception can affect driver behavior. For example, younger and less experienced drivers may exhibit riskier behaviors compared to older and more experienced drivers.
▪ social and cultural factors: Cultural norms, social pressures, and peer influence can shape driver behavior. For instance, cultural attitudes towards speeding or seat belt usage can impact individual driver choices.
▪ environmental factors: Road and traffic conditions, weather conditions, and infrastructure design can influence driver behavior. Heavy traffic, poor road conditions, or adverse weather can increase stress levels and affect decision-making.
▪ legal and regulatory factors: Traffic laws, enforcement, and penalties play a role in shaping driver behavior. Strict enforcement and harsh penalties for traffic violations can act as deterrents and promote safer driving practices.
▪ Vehicle characteristics: The design, performance, and condition of a vehicle can impact driver behavior. Factors such as vehicle speed, handling capabilities, and advanced safety features can influence driver choices and actions.

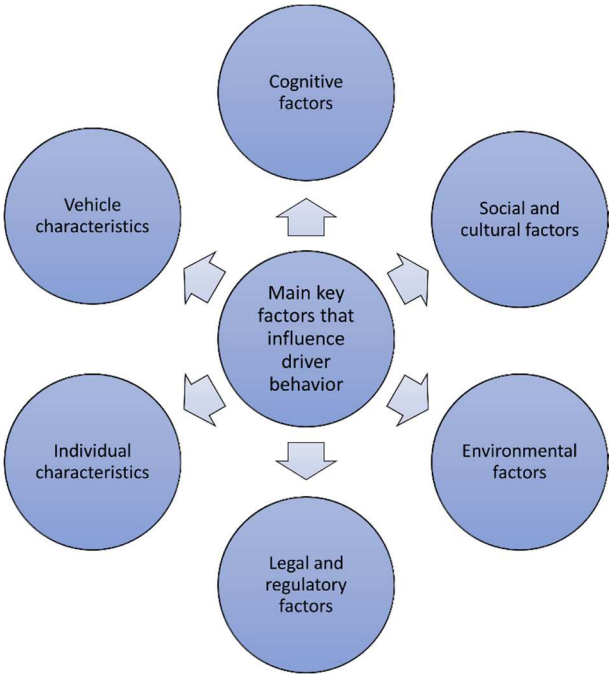

Fig. 1. Key factors that influence driver behavior

It is important to note that driver behavior is a complex interplay of these factors and can vary significantly among individuals, and in this context, the question arises whether the operating mode of a vehicle with an internal combustion engine has an effect or not when the driver switches to an electric vehicle.

In the case of electric vehicles, it is found that battery state of health (SOH) indicates a point of its lifetime and evaluates the health level of the present specific performance compared with the initial state, being an important factor in the operating time of an electric vehicle. One of the important factors regarding the functional degradation mechanism of the battery is the peak of the charge/discharge current [10 - 12].

The purpose of this article is to analyze the energy efficiency of an electric vehicle in a particular traffic case, by numerical computer simulation (MATLAB Simulink). Several scenarios are considered related to the departure from the spot (from the traffic light stop) for different situations of actuation of the accelerator pedal, in the mode: aggressive, normal and defensive. The analysis parameters taken into account were motor torque, battery state of charge and battery current; and the conclusions drawn were based on two major directions of analysis of the energy efficiency through the autonomy of the electric vehicle and the effect on the requests of the energy source (of the battery), conclusions that allowed issuing some solutions related to the studied problem.

II. SIMULATION MODEL

The simulation model is made in MATLAB Simulink (namely EvReferenceApplication from MATLAB Library, under University license), and consists of an electric vehicle made with:

▪ a longitudinal driver subsystem that uses the closed loop variant;
▪ the environment subsystem that includes the road gradient, wind velocity and atmospheric conditions;
▪ controller subsystem that includes the powertrain control module;
▪ passenger car subsystem, that has a Simscape electric plant with 3 degrees of freedom vehicle body, longitudinal wheel model, differential and the powertrain that consists of a mapped motor, the EV (electric vehicle) battery and all wheel drive;

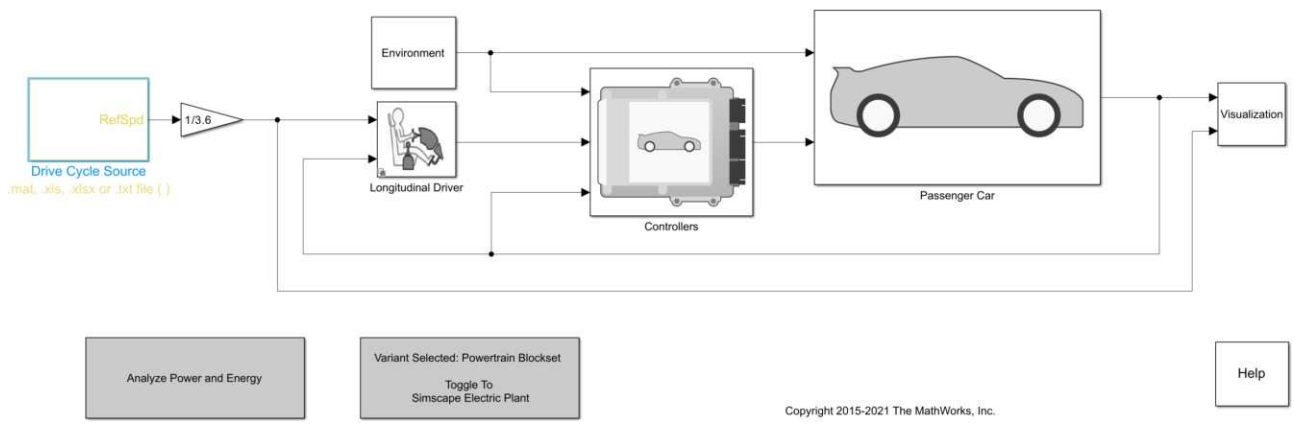

Fig. 2. Model used for simulation of the electric vehicle

Authorized licensed use limited to: Universitatea Tehnica din Cluj-Napoca. Downloaded on July 07,2025 at 14:47:36 UTC from IEEE Xplore. Restrictions apply.

The EV battery subsystem is a datasheet battery [13] that uses the following formula for the SOC calculation:

$$SOC\ [\%] = SOC_0[\%] + \frac{1}{C}\int_0^t I_b dt \qquad (1)$$

where SOC_0 is the initial charge of the battery, C is the rated capacity of the battery and I_b is the battery current.

The main input for the model, demand velocity in kilometers per hour, was changed using a signal builder block and sent to the driver that compares the demand velocity with the actual velocity of the vehicle and acts accordingly. The second input factor was the gradient of the road. Three gradients were considered, 0%, 5% and 10% respectively.

The simulation was run for three different drivers: aggressive, normal and defensive, with the three gradients. The demand velocity profiles for the three drivers were created (Fig. 3): for the normal driver (Velocity_dem_norm [km/h]), a linear demand of velocity from stand still to 100 kilometers per hour in 100 seconds, while for the aggressive driver (Velocity_dem_agr [km/h]), a parabolic with higher-than-normal velocity demand was used, but after 100 seconds demand stabilizes at 100 kilometers per hour, and for the defensive driver, a parabolic with lower-than-normal velocity demand was used (Velocity_dem_def [km/h]).

The state of health of the battery, is expressed in percentage and can be calculated as:

$$SOH\ [\%] = \frac{Q_{max}}{C} 100 \qquad (2)$$

where Q_{max} is the maximum available charge of the battery.

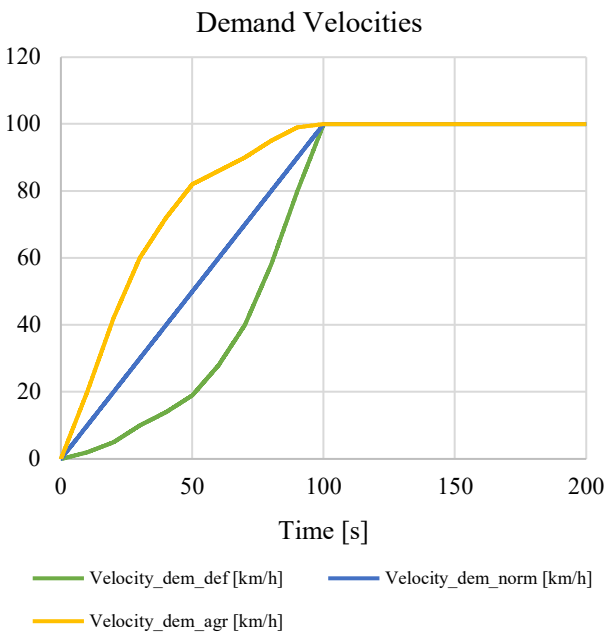

Fig. 3. Demand velocities for the three driver types

III. RESULTS

The simulation data were exported from Simulink to MATLAB workspace and processed.

All outputs have the following annotations:

- def – defensive driver;
- norm – normal driver;
- agr – aggressive driver;
- g0 – road gradient 0%;
- g5 – road gradient 5%;
- g10 – road gradient 10%.

Fig. 4 presents the motor torque for the three driver types, with a road gradient of 0%. It can be seen that for the aggressive driver, the torque demand is high at the beginning (first 20 seconds) of the cycle, with a maximum torque of 49.19 newton meters, and for the defensive driver, there is a high torque demand (max 56.01 newton meters) from second 80 to 100 of the simulation, while for the normal driver, the motor torque increases gradually from 24.61 newton meters to 38.6 newton meters. For all driver types, after 100 seconds, the motor torque stabilizes at 24.44 newton meters since the velocity demand is constant for all drivers.

Another output is the battery current (Fig. 5), for the three driver types on different road gradients.

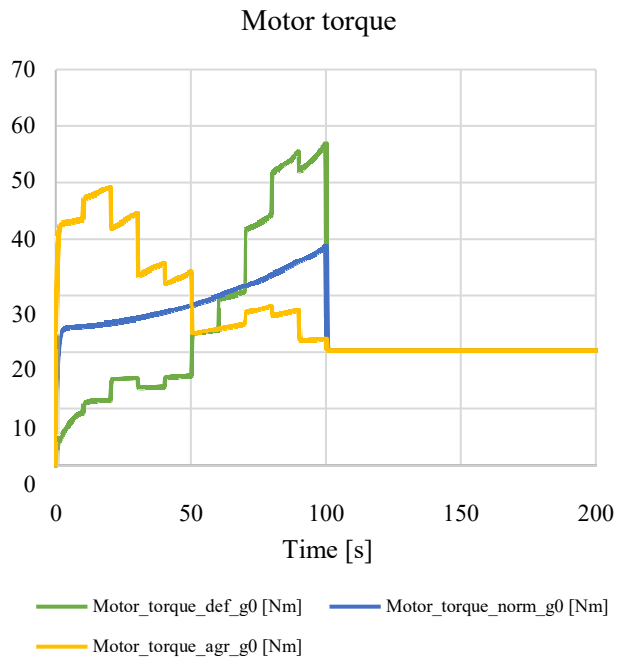

Fig. 4. Motor torque for the three driver types, with 0% road gradient

Table I presents the maximum values for the battery current in amperes.

TABLE I. MAXIMUM BATTERY CURRENT

Road gradient	Max battery current [A]		
	Aggressive driver	*Normal driver*	*Defensive driver*
0%	56.46	80.65	114.88
5%	161.50	187.60	228.71
10%	284.70	314.24	362.03

Fig. 6 presents the battery SOC for all simulations, all starting from 75% SOC.

Authorized licensed use limited to: Universitatea Tehnica din Cluj-Napoca. Downloaded on July 07,2025 at 14:47:36 UTC from IEEE Xplore. Restrictions apply.

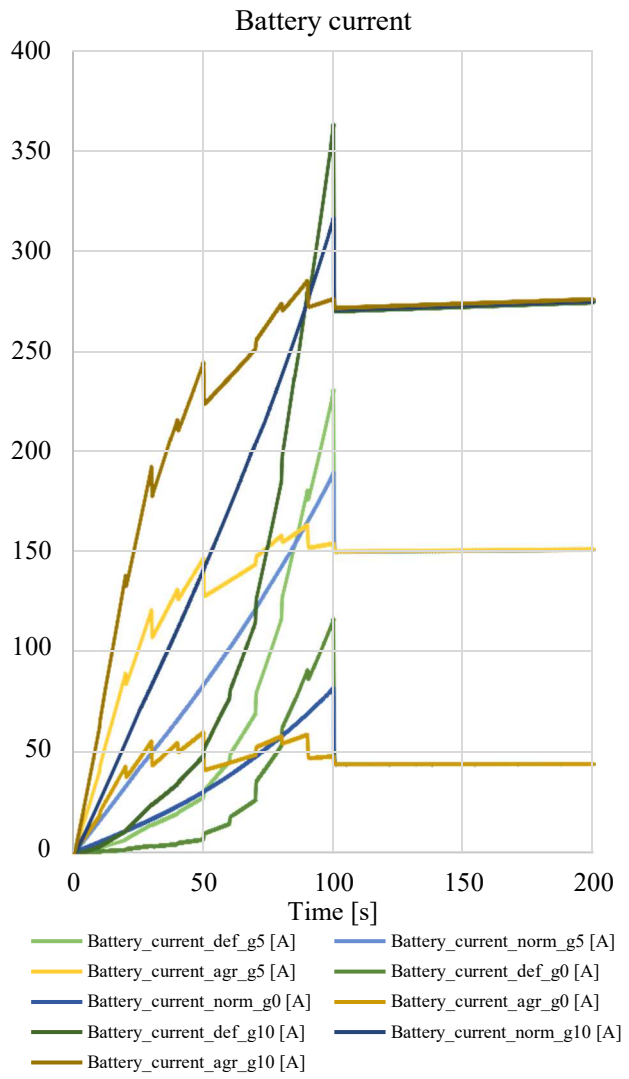

Fig. 5. Battery current for the three driver types with three road gradients

TABLE II. BATTERY SOC AFTER 200 SECONDS

Road gradient	Remaining battery SOC [-]		
	Aggressive driver	*Normal driver*	*Defensive driver*
0%	73.37	73.35	73.56
5%	69.98	70.56	71.06
10%	66.14	67.18	68.20

Fig. 7 presents the average battery current that was calculated for the given cycles.

IV. CONCLUSIONS

The expected conclusion of the simulations was that the defensive driver should be the best at preserving the battery, from the SOC and SOH perspective. Due to the imposed premises: all drivers must reach 100 kilometers per hour in 100 seconds, the conclusions are as follows:

- regarding the state of charge, at a road gradient of 0%, the SOCs are very similar no matter the behavior of the driver; for 5% and 10% road gradient, the defensive driver has the most SOC, but also has the biggest battery current requirement (228.71 amperes and 362.03 amperes respectively), which means that from a holistic point of view, the normal driver would exploit the vehicle in a better way, however, when looking at the average of the battery current values the defensive driver has the lowest values and therefor the recommendation stands – defensive drivers exploit electric vehicles in a more economical way;

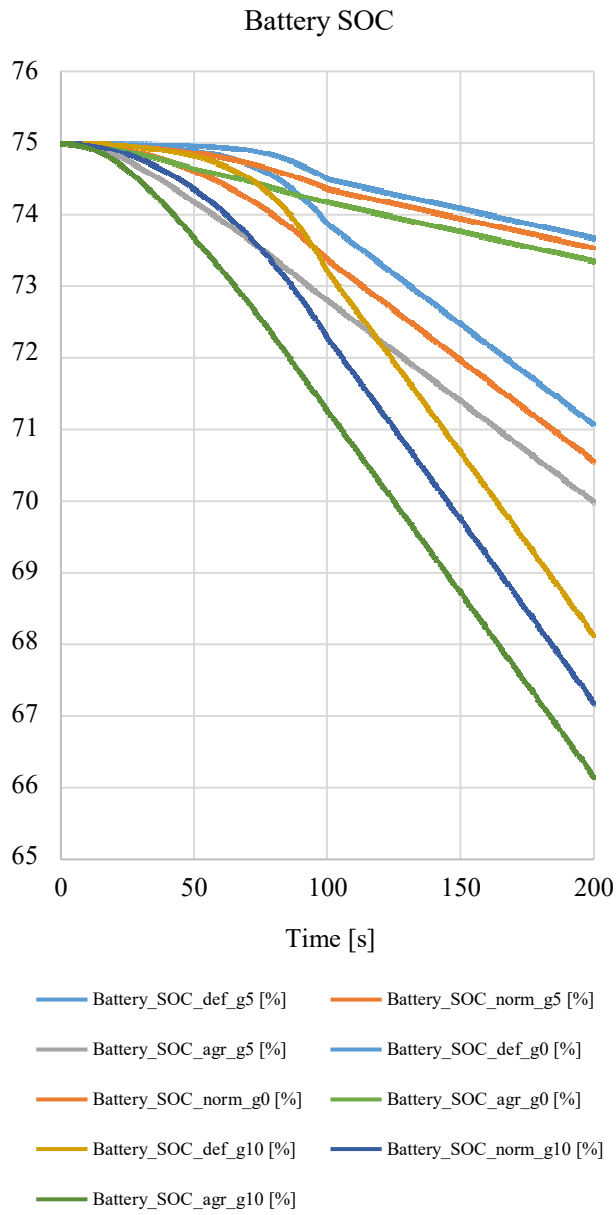

Fig. 6. Battery SOC for the three driver types with three road gradients

- regarding the state of health of the battery (SOH), since it is a measurement that indicates the level of degradation and remaining capacity of the battery, and is influenced by "SOC, temperature and the methods of charge and discharge" as mentioned by Li in [14], it can be concluded that in order to preserve the battery and prolong its life, the defensive driver is recommended so that the variations of the average battery current are smaller during exploitation; even though the defensive driver needs a higher torque towards the end of the acceleration and the aggressive driver uses high torque at the very beginning of the simulation.

For further development of the current manuscript, the imposed velocity will be kept at 100 kilometers per hour, but

Authorized licensed use limited to: Universitatea Tehnica din Cluj-Napoca. Downloaded on July 07,2025 at 14:47:36 UTC from IEEE Xplore. Restrictions apply.

the limit and the differences between the three drivers will be the maximum allowed acceleration, so that the defensive driver will take as long as it needs to reach the desired velocity. Also, a real urban driving scenario will be implemented with limited velocity to 50 kilometers per hour.

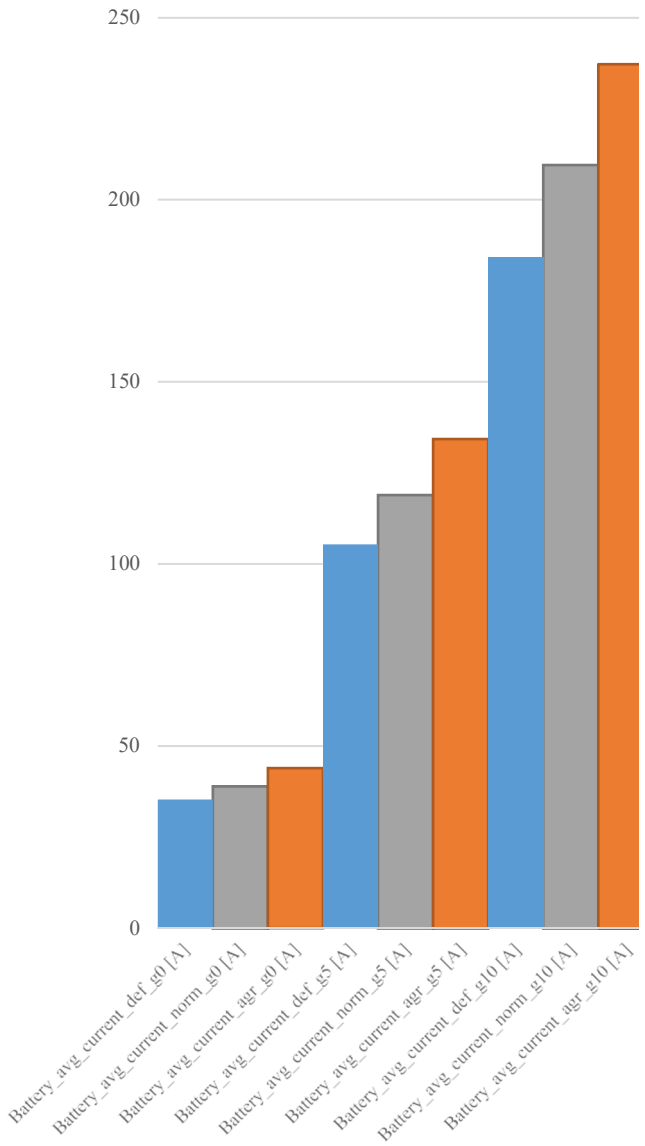

Fig. 7. Average battery current for the three driver types with three road gradients

ACKNOWLEDGMENT

This paper is supported by European Union's Horizon 2020 research and innovation programme under grant agreement No 101036871, project hOListic Green Airport (OLGA).

REFERENCES

[1] F. Zheng, J. Li, H. van Zuylen, and C. Lu, "ScienceDirect Influence of driver characteristics on emissions and fuel consumption ScienceDirect Influence of driver characteristics on emissions and fuel consumption ScienceDirect Influence of driver characteristics on emissions and fuel consumption," Transportation Research Procedia, vol. 27, no. 2, p. 0, 2017, doi: 10.1016/j.trpro.2017.12.142.

[2] Y. Ma and J. Wang, "Personalized Driving Behaviors and Fuel Economy Over Realistic Commute Traffic: Modeling, Correlation, and Prediction," IEEE Trans Veh Technol, vol. 71, no. 7, pp. 7084–7094, Jul. 2022, doi: 10.1109/TVT.2022.3171165.

[3] J. Gao et al., "Analysis of driving behaviours of truck drivers using motorway tests," Proceedings of the Institution of Mechanical Engineers, Part D: Journal of Automobile Engineering, vol. 234, no. 13, pp. 3103–3111, Nov. 2020, doi: 10.1177/0954407020925568/ASSET/IMAGES/LARGE/10.1177_0954407020925568-FIG11.JPEG.

[4] P. Ping, W. Qin, Y. Xu, C. Miyajima, and K. Takeda, "Impact of driver behavior on fuel consumption: Classification, evaluation and prediction using machine learning," IEEE Access, vol. 7, pp. 78515–78532, 2019, doi: 10.1109/ACCESS.2019.2920489.

[5] P. Yamin, S. Lahlou, S. Ortega, and V. Skrickij, "Local determinants of driving behaviours: Installation Theory interventions to reduce fuel consumption among truck drivers in Colombia," Transport, vol. 35, no. 6, pp. 616–634, Dec. 2020, doi: 10.3846/TRANSPORT.2020.14195.

[6] C. Chen, X. Zhao, Y. Yao, Y. Zhang, J. Rong, and X. Liu, "Driver's eco-driving behavior evaluation modeling based on driving events," J Adv Transp, vol. 2018, 2018, doi: 10.1155/2018/9530470.

[7] D. Hari, C. J. Brace, C. Vagg, J. Poxon, and L. Ash, "Analysis of a driver behaviour improvement tool to reduce fuel consumption," Proceedings - 2012 International Conference on Connected Vehicles and Expo, ICCVE 2012, pp. 208–213, 2012, doi: 10.1109/ICCVE.2012.46.

[8] E. M. Szumska and R. Jurecki, "The Effect of Aggressive Driving on Vehicle Parameters," Energies 2020, Vol. 13, Page 6675, vol. 13, no. 24, p. 6675, Dec. 2020, doi: 10.3390/EN13246675.

[9] E. Michelaraki, A. Kontaxi, P. Papantoniou, and G. Yannis, "Correlation of driver behaviour and fuel consumption using data from smartphones".

[10] M. Zhang et al., "A Review of SOH Prediction of Li-Ion Batteries Based on Data-Driven Algorithms," Energies 2023, Vol. 16, Page 3167, vol. 16, no. 7, p. 3167, Mar. 2023, doi: 10.3390/EN16073167.

[11] L. Yao et al., "A Review of Lithium-Ion Battery State of Health Estimation and Prediction Methods," World Electric Vehicle Journal 2021, Vol. 12, Page 113, vol. 12, no. 3, p. 113, Aug. 2021, doi: 10.3390/WEVJ12030113.

[12] D. Li, M. Zhimao, C. Mingsheng, and D. Jin, "Influence factors and identification of state-of-health for traction battery," IOP Conf Ser Mater Sci Eng, vol. 1043, no. 5, p. 52037, Jan. 2021, doi: 10.1088/1757-899X/1043/5/052037.

[13] "Lithium-ion, lithium-polymer, or lead-acid battery - Simulink." https://www.mathworks.com/help/autoblks/ref/datasheetbattery.html?searchHighlight=BattEv&s_tid=srchtitle_BattEv_3 (accessed May 30, 2023).

[14] D. Li, M. Zhimao, C. Mingsheng, and D. Jin, "Influence factors and identification of state-of-health for traction battery," *IOP Conf Ser Mater Sci Eng*, vol. 1043, no. 5, p. 52037, Jan. 2021, doi: 10.1088/1757-899X/1043/5/052037

Authorized licensed use limited to: Universitatea Tehnica din Cluj-Napoca. Downloaded on July 07,2025 at 14:47:36 UTC from IEEE Xplore. Restrictions apply.

Fuel 255 (2019) 115753

Contents lists available at ScienceDirect

Fuel

journal homepage: www.elsevier.com/locate/fuel

Full Length Article

Second law analysis of waste cooking oil biodiesel versus ULSD during operation of a CI engine

Jonathan Mattson[a], Nicolae Vlad Burnete[b,*], Christopher Depcik[a], Dan Moldovanu[b], Nicolae Burnete[b]

[a] University of Kansas, Dept. of Mechanical Engineering, 1530 W.15th Street, 3138 Learned Hall, Lawrence, KS 66045, USA
[b] Technical University of Cluj-Napoca, Dept. of Automotive Engineering and Transports, Bvd. Muncii 103-105, 400641 Cluj-Napoca, Romania

ARTICLE INFO

Keywords:
Waste cooking oil
Biodiesel
ULSD
Combustion analysis
2nd law analysis
Availability

ABSTRACT

Waste cooking oil (WCO) biodiesel is a sustainable option compared to ultra-low sulfur diesel (ULSD) due to its relatively low cost and carbon cycle recovery potential while not competing with food resources. Research on this fuel finds limited studies with little to no information regarding a second law heat release analysis and contrasting findings with respect to NO_x emissions. This effort rectifies these issues by performing experiments with ULSD and WCO biodiesel on a single cylinder compression ignition engine running at constant speed (2000 rpm) and various loads (0, 25, 50, 75, and 100% load). The combustion timing of WCO biodiesel was normalized to match the peak in-cylinder pressure timing of ULSD. Generally, WCO biodiesel demonstrated shorter ignition delays and, thus, quicker periods for the mixture formation while requiring more fuel (and greater CO_2 emissions) to match the load requirement. Subsequently, this cuts the premixed event short and induces diffusion-dominated combustion above that of operation with ULSD. WCO biodiesel primarily resulted in cooler peak temperatures, but longer periods of high temperatures that appear later in the combustion cycle where work extraction is more difficult; hence, lowering the 2nd Law efficiency. As a result, availability losses due to heat transfer increase, but this warmer in-cylinder environment mitigates losses due to entropy production. The emissions analysis highlights a more complete combustion of WCO biodiesel with lower CO and HC emissions. NO_x emissions are closely tied with in-cylinder temperatures and the amount of diffusion burn; hence, increasing or decreasing based on combustion behavior.

1. Introduction

Even though significant fossil fuel reserves are found every few years, in the long term their depletion is inevitable [1]. Furthermore, a well-to-wheel analysis of their production and usage highlights their hazardous emissions while also negatively affecting the climate by increasing the greenhouse gas effect. Nowadays, one accepted alternative to fossil fuels is the use of biofuels (e.g., biodiesel and bioethanol). Specifically, regions and/or countries like the European Union and Brazil are increasing their biofuel use and production as part of their ambition to decrease pollutant emissions and fossil fuel dependency [2].

Compared to fossil fuels, biofuels have a few advantages. In specific, they are biodegradable and can potentially produce lower hazardous combustion emissions [3–7]. Furthermore, since the carbon dioxide (CO_2) they emit during combustion is partially recirculated as it is consumed by growing plants, overall this leads to a cleaner process [8]. Possible feedstocks for producing biofuels are vegetable oils (neat or used) like rapeseed, sunflower, or palm oil along with animal fats, sugar cane, and a myriad of other plant and animal based options [4,9–14]. However, one must consider the food-fuel competition [15,16], as well as the impact on water resources, biodiversity, and the destruction of the soil [17] when considering a biofuel source.

Waste cooking oil (WCO) as a feedstock has a major advantage in that it can be acquired at a relatively low cost or even free of charge and does not compete with food resources. In addition, the conversion of WCO to a useable biofuel for compression ignition (CI aka diesel) engines is respectively straightforward. Over the years, various methods for producing biodiesel from oils have been proposed and tested: transesterification, response surface technology, two-step reaction process, enzymatic method, etc. [18]. Nowadays, the most common production methods are esterification and transesterification reactions

* Corresponding author.
E-mail addresses: jmattson@ku.edu (J. Mattson), nicolae.vlad.burnete@auto.utcluj.ro (N.V. Burnete), depcik@ku.edu (C. Depcik), dan.moldovanu@auto.utcluj.ro (D. Moldovanu), nicolae.burnete@auto.utcluj.ro (N. Burnete).

https://doi.org/10.1016/j.fuel.2019.115753
Received 16 January 2019; Received in revised form 30 June 2019; Accepted 2 July 2019
Available online 08 July 2019
0016-2361/ © 2019 Elsevier Ltd. All rights reserved.

Nomenclature

Abbreviation

*	exceptions apply
AC	air cooled
B5	95% Diesel + 5% Biodiesel (v/v)
B10	90% Diesel + 10% Biodiesel (v/v)
B20	80% Diesel + 20% Biodiesel (v/v)
B30	70% Diesel + 30% Biodiesel (v/v)
B40	60% Diesel + 40% Biodiesel (v/v)
B50	50% Diesel + 50% Biodiesel (v/v)
B70	30% Diesel + 70% Biodiesel (v/v)
B100	100% Biodiesel
BD	Biodiesel
BSFC	brake specific fuel consumption
BTE	brake thermal efficiency
CO	carbon monoxide
CO_2	carbon dioxide
CRatio	compression ratio
CR	common rail
NA	naturally aspirated
N/A	not available
NO_x	nitric oxides
p_{max}	peak cylinder pressure
Δp	pressure gradient
PM	particulate matter
ROHR	rate of heat release
rpm	revolutions per minute
T_{cyl}	in-cylinder temperature
T_{exh}	exhaust gas temperature
τ_{ign}	ignition delay
TC	turbocharged
UHC	unburnt hydrocarbons
WC	water cooled

because they can be accomplished with a minimum of equipment at a reasonable price [19]. As a result, the end cost of WCO biodiesel is relatively moderate while demonstrating a price reduction of up to 45% as compared to virgin oils [19,20]. Generally, this is consistent with one of the accepted strategies to reduce biofuel costs, namely the reduction of feedstock expenditures since they can account for 70–75% of the biofuel price [21]. Another advantage is that the pollution resulting from the disposal of cooking oil is avoided [8,22]. As an example of WCO's potential, de Araújo et al. [19] calculated that using the oil generated in households could cover 13% of the annual demand for biodiesel in Brazil.

One issue when using WCO as feedstock is that it has an increased amount of impurities (e.g., solid suspensions), free fatty acids, and water that can negatively influence the transesterification process when employing alkali catalysts [8,23,24]. In addition, the cooking process affects other properties like viscosity and specific heat; hence, WCO might need to undergo a pretreatment process to match suitable oil characteristics for the transesterification process [8,11]. However, there are alternative solutions for this process that allow an economically feasible production of biodiesel from WCO, such as enzyme catalysis [25,26], supercritical [27], and acid catalysis transesterification [6,28].

With respect to CI engine tests, there are numerous studies regarding the use of biodiesel obtained from various feedstocks (mostly virgin vegetable oils). However, papers covering biodiesel specifically obtained from WCO are respectively less common than the traditional feedstocks for the United States (soybean) [29] and Europe (rapeseed) [30]. From the available literature [13,31–49], of which those that include engine tests are highlighted in Table 1, the general conclusions that can be drawn are:

- While the wide variance in feedstocks seen along with the subsequent divergence in biodiesel fuel properties, fuel injection systems (e.g., mechanical versus common rail), and engine compression ratios does prevent direct comparison between all works, generally viscosity, flash point, cetane number, and density are greater for WCO biodiesel in comparison to the diesel fuels employed; whereas, energy content on both a mass and volumetric basis are less;
- Engine performance (power, torque) is slightly reduced, except for maximum power, where the decrease is considerable largely due to a poorer atomization process from a higher viscosity and worse volatility;
- Maintaining engine performance does grow the fuel consumption and CO_2 emissions because of the reduced lower heating value of biodiesel;
- Brake thermal efficiency is similar to that of diesel, with a few studies indicating an increase in efficiency when using biodiesel;
- Generally, nitrogen oxide (NO_x) emissions grew. However, some researchers found similar values or even a reduction in NO_x emissions. The main reasons for this increase are the slight advance of the combustion process due to a lower ignition delay and a higher oxygen content of the biodiesel, but other reasons were highlighted as well. This includes a greater adiabatic flame temperature and advanced start of injection (especially for pump-line-nozzle injection systems) when using biodiesel;
- Partial products of combustion, such as carbon monoxide (CO), Particulate Matter (PM), smoke opacity, and Total Hydrocarbon (THC) emissions, decrease considerably due to the greater oxygen content in biodiesel.

Examining these findings illustrates numerous CI engine studies focused on the performance of WCO biodiesel as compared to ULSD regarding combustion characteristics and pollutant emissions. While these papers may include a first law of thermodynamics heat release analysis, there is little to no information investigating an availability or second law of thermodynamics understanding. Therefore, this effort builds upon these earlier efforts by incorporating a second law heat release analysis and highlighting the availability extracted as work, lost due to heat transfer, destroyed by entropy generation, and retained by the exhaust. This helps to shed additional light on the seemingly contradictory findings with respect to NO_x emissions. As a result, a comprehensive understanding of WCO biodiesel in comparison to ULSD is determined.

2. Material and methods

The engine used for this study is a naturally-aspirated four-stroke AVL5402 single cylinder CI research engine. To simulate loading on the engine, it is coupled with an AVL DynaRoad202 dynamometer with engine and dynamometer specifications presented in Table 2. The testbed used for the study features an AVL Rapid Prototyping Engine Management System (RPEMS) and ETK7 engine management system that allows a flexible engine control. Specifically, this enables the user to change the injection timing and quantity for up to four injection sequences (pilot 1, pilot 2, main, and post injection), as well as the fuel pressure in the common rail. Here, only a main injection event was utilized. Furthermore, the testbed is equipped with a fuel conditioning unit for control of the experiments. This includes an AVL735 Fuel Mass Flow Meter for fuel flow and density (± 0.12% kg/h, ± 0.0005 g/cm^3) measurements along with an AVL753 Temperature Control unit for fuel

Table 1
Review of engine results obtained with WCO in comparison to pure diesel.

Ref.	Engine	Test conditions	Fuels	BTE	BSFC	p_{max}	Δp	ROHR	T_{cyl}/T_{exh}	τ_{ign}	NO_x	CO	CO_2	UHC	PM	Smoke
[36]	1-cylinder, NA, AC, 17:1 CRatio	1500 rpm 17.5 MPa injection pressure 0, 0.46, 1.65, 2.94, 3.69, 4.74, and 5.35 MPa *Feedstock*: N/A	Neat diesel, B5, B10, B20, B30, B50, B70, B100	↑*	↑	↓	N/A	N/A	T_{exh} ↑*	↓	↓	↓	N/A	↓*	N/A	↑*
[37]	1-cylinder, NA, AC, 17.5:1 CRatio	1500 rpm 0–100% load *Feedstock*: N/A	B10, B20, B30	↓	↑	N/A	N/A	N/A	T_{exh} ↑	N/A	↑	↓	↑	↓	N/A	↓
[38]	1-cylinder, NA, AC, 18.0:1 CRatio	2200 rpm 0.12, 0.24, 0.36, 0.48 MPa BMEP *Feedstock*: waste sunflower oil	B5, B10	↓	↑	–	↓*	↓*	N/A	↓	↑	–*	N/A	N/A	N/A	↓
[39]	1-cylinder, CR, 17.4:1 CRatio	1400 rpm 80, 160 MPa injection pressure 25…0 °CA (5 °CA swap) injection advance *Feedstock*: N/A	B100	N/A	↑*	N/A	N/A	↓	N/A	↑	↑	↓	N/A	N/A	N/A	↓
[40]	1-cylinder, NA, AC, 21.2:1 CRatio	0%, 20%, 40%, 60% and 80% of rated torque *Feedstock*: canola oil	ULSD, UCO BD, JP-8	↑	↑	↑	–	–	T_{cyl} ↑	↓	↑	↓	↑	↓	–	–
[41]	1-cylinder, CR, 17.4:1 CRatio	1400 rpm 80 MPa injection pressure 0.16…0.93 MPa BMEP 60…0 °CA (5 °CA swap) injection advance 10, 20, 30, 40, 50, 60 mg/stroke for ULSD 11, 22.1, 33.4, 44.3, 55.4, 66.2 mg/stroke for B100 *Feedstock*: N/A	Diesel, B100	N/A	↑	↓	N/A	↑	N/A	↑	↑*	↓*	N/A	↓*	N/A	↓*
[42]	1-cylinder, NA, WC, 16:1 CRatio	1500 rpm 27 °CA injection advance 20 MPa injector opening pressure 0…4.4 MPa BMEP *Feedstock*: palm oil	Diesel, WCO neat, WCO emulsion	↑*	N/A	↓	↓	↑	T_{cyl} ↓	↑	↓	↑	N/A	↑*	N/A	↑
[43]	1-cylinder, NA, WC, 17.5:1 CRatio	1000…3000 rpm at 200 rpm intervals 17, 18, 19, 20, 21, 22 MPa injection pressure 100% load **Power and torque also tested: ↓with BD percentage *Feedstock*: sunflower oil	Diesel, B10, B20, B30, B100	↓	↑	N/A	N/A	N/A	T_{exh} ↑	N/A	↑	↓	↑	↓	N/A	↓
[44]	4-cylinder, TC, CR, 18.0:1 CRatio	modes U10, C', F, G', H (Europe) *Feedstock*: mixture of olive, sunflower and palm oil	B30, B70, B100	–	↑	N/A	N/A	–	N/A	–	↓*	N/A	N/A	↓*	↓*	↓*
[45]	4-cylinder, TC, CR, 18.5:1 CRatio	800, 1200, 2400, 3600 rpm 25, 50, 100% load *Feedstock*: N/A	B5, B20, B40, B70, B100	↑ 50, 100% load	↑	↓	N/A	↓ (peak)	N/A	↓	↓*	↑	↓	↓*	N/A	N/A
[46]	4-cylinder, NA, in-line injection pump, 19.0:1 CRatio	Japanese 13-mode test cycle *Feedstock*: N/A	ULSD, B20, B50, B75, B100	↑* B20, B50, B75	↑	↑	N/A	↓	N/A	↓	N/A	N/A	N/A	N/A	↓	N/A

(*continued on next page*)

Table 1 (*continued*)

Ref.	Engine	Test conditions	Fuels	BTE	BSFC	p_{max}	Δp	ROHR	T_{cyl}/T_{exh}	τ_{ign}	NO_x	CO	CO_2	UHC	PM	Smoke
[47]	6-cylinder, TC, CR, 17.5:1 CRatio	1400 rpm and 1000, 1500, 2000 rpm 0.16, 0.32, 0.48, 0.64, 0.81, 0.97, 1.13, 1.30 MPa BMEP pilot + main injection up to 40% load *Feedstock*: non-edible animal and vegetable fat and oil	B100	↑*	N/A	↓	↓	↓*	T_{cyl} ↑*	↓	↑*	N/A	N/A	N/A	N/A	N/A
[48]	6-cylinder, TC, WC, Marine, 17.0:1 CRatio	1050, 1500 rpm 25%, 50% and 75% load *Feedstock*: N/A	ULSD, B70, B90, B100	N/A	N/A	↓	N/A	↓	T_{exh} ↓	↓	↓	N/A	N/A	N/A	N/A	N/A

Note: A study that could not be included in this table was performed by Shen et al. [49]. The authors measured with a Portable Emission System (PEMS) the real driving emissions of two light-duty (LD) and two heavy-duty (HD) diesel trucks (one China III and one China IV) running on neat diesel, B5, B20, and B100. The test routes included both highway (HW) and non-highway (NHW) roads near Beijing and had a total length of approximately 80 km. The authors reported a slight increase in fuel consumption for all vehicles when operated with blends or B100. On the other side, there was a decrease in CO (except HD-China IV), HC (except HD-China III B5), NO_x (except LD and HD-China III), and PM (except HD-China III and IV). By using blends, the authors noted a significant reduction in CO, HC, NO_x, and $PM_{2.5}$ compared to diesel operation in NHW conditions. For HW conditions, the values increased.

Table 2
Engine and dynamometer specifications.

Engine			
Model	AVL 5402	Bore	85 mm
Intake	naturally aspirated with tangential and swirl inlet ports	Stroke	90 mm
Cooling	water cooled	Fuel system	CR, direct injection Bosch CP4.1
Cycle	4-Stroke	Maximum injection pressure	180 MPa
Displacement	510.7 cm^3	Engine management system	AVL RPEMS + ETK7 (Bosch)
Number of cylinders	1	Rated power (aspirated)	6 kW
Compression ratio	17.1:1	Rated power (supercharged)	16 kW
Number of valves	2 + 2 (1 exhaust valve is deactivated to allow the installation of a combustion visualization system)	Rated speed	4200 rpm

AC-Dynamometer			
Model	AVL DynaRoad202	Nominal power (motor mode)	198 kW
Nominal power (generator mode)	220 kW	Nominal torque (motor mode)	473 Nm
Nominal torque (generator mode)	525 Nm	Maximum speed (motored/generator mode)	12 000 rpm

temperature control. Operating conditions are further regulated with the aid of an AVL577 conditioning unit that enables a control of the coolant flow and temperature (5–120 °C ± 1 °C) while also modulating the oil flow, temperature, and pressure. The engine load and speed were the same in all cases and were controlled by the PUMA automatic control system. The oil and coolant temperatures were maintained at 100 and 90 °C respectively by the oil/coolant conditioning system. The injected quantity was adjusted in order to match the engine load of the reference fuel.

The engine is equipped with a glow-plug type AVL GU22C pressure transducer (0 to 250 bar, linearity ± 0.3%, thermal sensitivity ± 1%) for in-cylinder pressure measurements at a variable sampling interval over an engine cycle. For this study, the authors opted for a sampling interval of 0.1 °CA (crank angle) between 30 °CA BTDC (before top dead center) and 70 °CA ATDC (after top dead center), and 1 °CA for the rest of the cycle. The pressure trace, which is an average of 101 thermodynamic cycles, was then analyzed using the first and second laws of thermodynamics to determine the rate of heat release and in-cylinder temperatures [50,51]. Additional sensors allow the measurement of the ambient temperature (accuracy ± 1.5 °C), pressure (accuracy ± 0.2%) and relative humidity (RH; accuracy ± 0.6% for 0–5% RH and ± 1% for 5–80% RH), intake air temperature (PT100; accuracy ± 0.15 + 0.002× temperature) and pressure (PTX 1400; accuracy ± 2% from −20 to 80 °C), as well as exhaust gas temperature and pressure (same as intake). The intake air mass flow is measured using a Sensyflow P thermal mass flow meter (accuracy ± 1% of reading; repeatability error ± 0.25% of reading).

Two fuels were used for this study: a locally purchased winter grade diesel, designated ULSD (with the properties specified according to the quality assurance sheet of the fuel, except for density that was measured using the AVL 735 and the energy content that was taken from the European Fuel Quality Legislation [2]), and a WCO biodiesel (produced according to the methodology presented by Cecrle et al. in [52]) with the main properties estimated to be similar to those presented in Table 4. For the tests, the engine was operated at 2000 rpm at five different loads: 0, 25, 50, 75 and 100% load. The ULSD was tested first, as a reference. For the WCO biodiesel, the injection quantity was increased to obtain the equivalent load, while the injection timing was adjusted to maintain the same crank angle position of the peak cylinder pressure for normalized combustion phasing between the test fuels (discussed later). The fuel injection pressure was the same in both cases and the test parameters are presented in Table 3. Ambient conditions were also controlled, with the following values measured during the tests: 28–35 °C ambient temperature, 973–981 mbar ambient pressure, 13.3–17.3% relative humidity, and 23–29 °C intake air temperature. Finally, the emissions were measured using a Bosch BEA350 system as follows: after the engine reached steady state, defined when engine oil and exhaust temperatures changed by less than one percent over a 60 s period, emission values for CO, CO_2, NO_x, and HC were recorded every 10 s for 1 min. The obtained values were averaged and converted to brake specific quantities (Eq. (1) [53]).

Table 4
Estimated properties of WCO biodiesel [52] and diesel fuel employed in this effort.

Property	m.u.	WCO biodiesel	ULSD
CN	–	52.8	min. 51
Energy content	kJ/kg	39,663	43,000
Density	kg/m^3 at 298.15 K	860*	826
Kinematic viscosity	cSt at 40 °C	6.560	2–4.5
Dynamic viscosity	cP at 40 °C	5.790	1.625–3.717
Oxygen content	wt %	10.5	N/A
H/C molar ratio	–	1.84	N/A

* The WCO biodiesel density was measured with the other WCO biodiesel properties estimated based on the prior work.

$$E_{P,i} = E_{V,\,i,dry} \cdot \frac{M_i}{M_{exh,dry}} \cdot \frac{\dot{m}_{exh,dry}}{P_{eff}} = E_{V,\,i,wet} \cdot \frac{M_i}{M_{exh,wet}} \cdot \frac{\dot{m}_{exh,wet}}{P_{eff}} \left[\frac{g}{kWh}\right] \tag{1}$$

where $E_{P,i}$ – pollutant mass referenced to P_{eff} in [g/kWh]; $E_{V,i}$ – exhaust emission value of component i as volume share [ppm]; M_i – mol mass of the component i, [kg/kmol]; M_{exh} – mol mass of the exhaust [kg/kmol]; $\dot{m}_{exh}$ – exhaust mass flow [kg/h].

3. Results and discussion

3.1. Non-normalized tests

The first efforts involved testing the WCO biodiesel without changing the injection timing as compared to ULSD operation. In specific, after setting the injection timing and pressure to the same ULSD test values, the injection quantity of WCO biodiesel was increased gradually until the BMEP of the engine was equated to that of ULSD. This led to an increase of 53.4, 49.1, 37.4, 39.8, and 35.0% in fuel mass injected for 0, 25, 50, 75, and 100% load, respectively, when using WCO biodiesel. This is largely due to its reduced energy content even though it has a greater density as highlighted in Table 4. In other words, since the engine injection system adds fuel on a volumetric basis, WCO biodiesel is being added at a reduced volumetric energy level of around 34,110 MJ/m^3 in comparison to 35,518 MJ/m^3 for ULSD.

As demonstrated in Fig. 1, employing the same injection timing for WCO biodiesel as ULSD led to an advance of the combustion process. To further elucidate on combustion timing differences, a comparison of the injection timings with the start of combustion using the 2nd derivative of pressure determined through the ROHR analysis (shown later) provides valuable insight about the ignition delay in Fig. 2. It was found that, except at 100% load, combustion of the biodiesel fuel started earlier than ULSD, both in the non-normalized (1.9 to 6.6 °CA advanced) and the normalized (1.8 to 4.2 °CA advanced) cases. This is due primarily to the larger cetane number (CN) of biodiesel, in spite of the increased injection delay (valid for common rail injection systems, but not for mechanical injection systems [54,55]), poorer atomization, and

Table 3
Test parameters used in this study.

Speed	Load	ULSD			WCO biodiesel			
		Quantity	Injection timing	Injection pressure	Quantity	Injection timing	Injection pressure	Normalized injection
rpm	%	mg	°CA BTDC	MPa	mg	°CA BTDC	MPa	°CA
2000	0	9	7.5	60	13.6	5.6	60	+1.9
	25	12.6	7.9	60	18.5	6.0	60	+1.9
	50	16.4	8.2	70	22.2	6.4	70	+1.8
	75	21.4	9.0	70	29.4	7.9	70	+1.1
	100	27.4	11.6	70	36.3*	12.4	70	−0.8

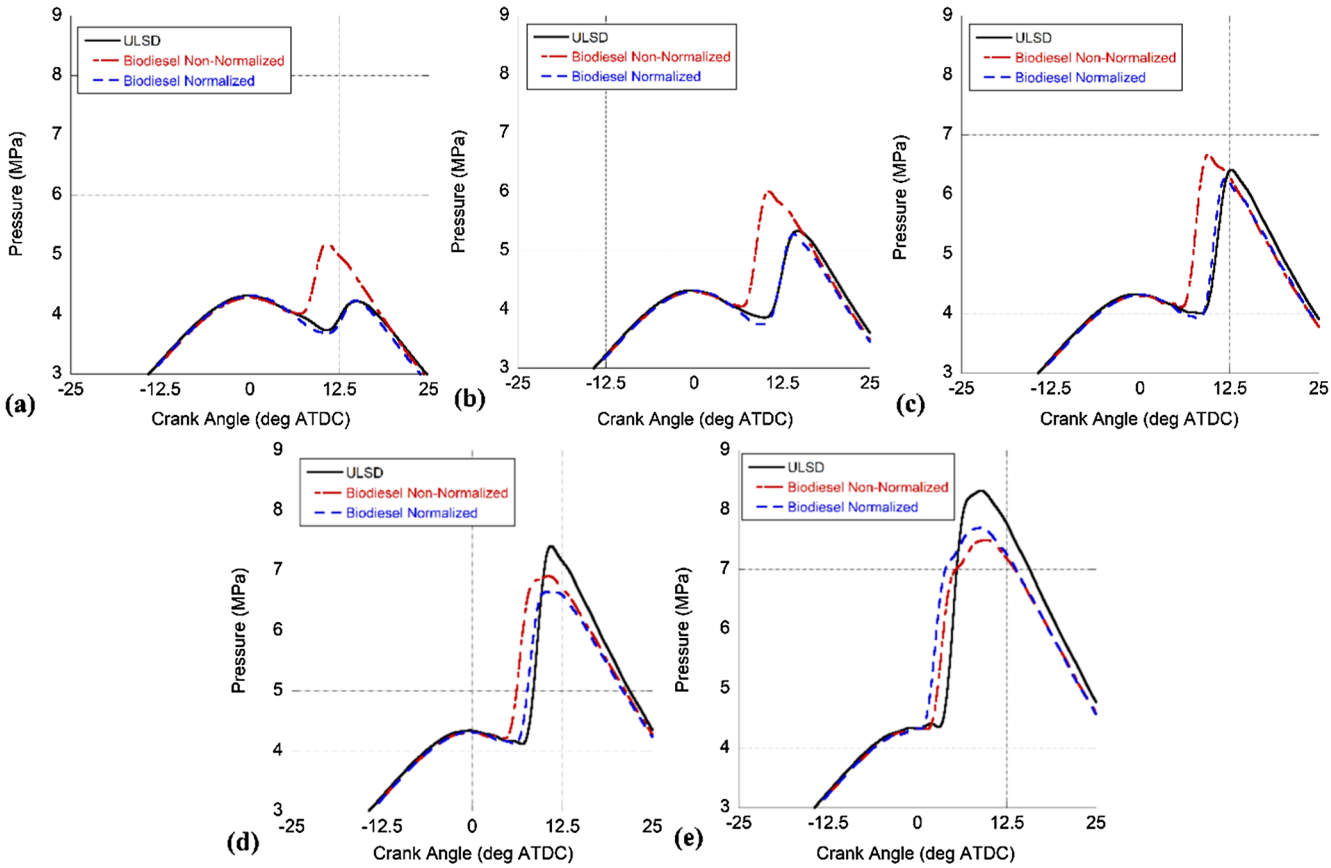

Fig. 1. Filtered in-cylinder pressure trace at (a) 0% load, (b) 25% load, (c) 50% load, (d) 75% load, and (e) 100% load for AVL 5402 engine.

lowered air-entrainment level, which occurs when changing from ULSD to biodiesel [39,41,56]. Moreover, the fuel bound oxygen in biodiesel additionally aids in achieving equivalence ratios in the flammability range faster than with ULSD promoting a reduced ignition delay. However, at 100% load, the start of combustion was somewhat comparable between ULSD, non-normalized (0.1 °CA advance) and normalized (1 °CA advance) biodiesel. Here, the need to add a significant amount of fuel to achieve the load required forces the injection process earlier into the compression stroke; hence, each case is given ample opportunity to mix prior to reaching combustion temperatures.

Since combustion that happens sooner results in an earlier heat release, this subsequently influences in-cylinder temperatures and exhaust emissions. Therefore, the rest of the analysis will primarily compare normalized WCO biodiesel and ULSD results by matching the peak pressure crank angle location to (mostly) remove the influence of combustion phasing. This WCO biodiesel normalization process resulted in an increase of 1.6, 0.9, 1.0, 0.7, 7.7% in fuel mass injected for 0, 25, 50, 75, and 100% load, respectively, in comparison to the non-normalized tests.

3.2. Normalized tests

Up to 50% load (Fig. 1a–c), delaying the injection timing and matching the BMEP requirements finds that the in-cylinder pressures between normalized biodiesel and ULSD are relatively similar to slightly lower. However, above 50% load (Fig. 1d, e), the peak cylinder pressures for normalized biodiesel drop significantly below that of ULSD. This is likely due to the increased viscosity of biodiesel inhibiting

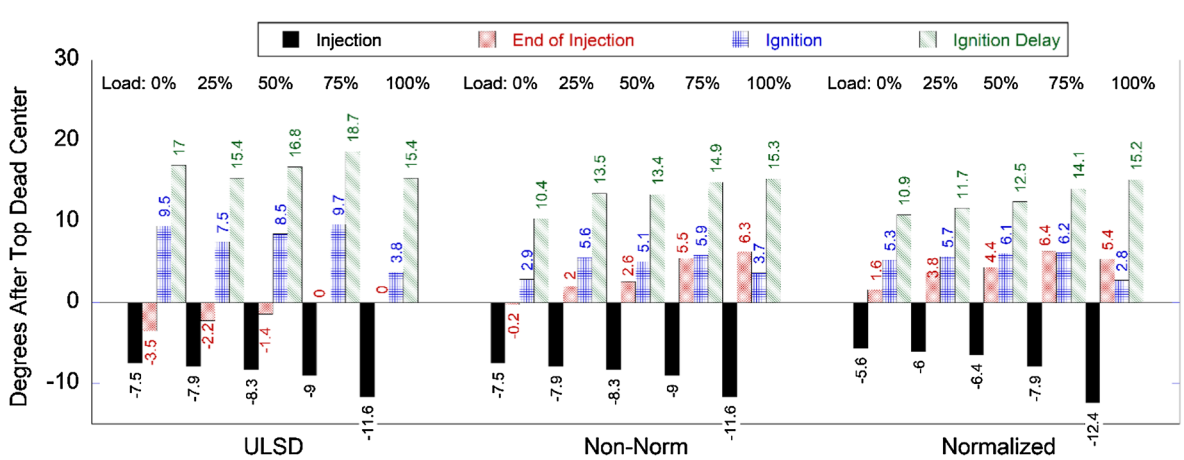

Fig. 2. Injection parameters relevant for the combustion process analysis.

fuel breakup and promoting diffusion burn as a greater level of fuel flow rate is needed to achieve these higher loads. Interestingly, unlike prior results in the literature [57,58], at 100% load the normalized biodiesel test requires an advanced injection timing in comparison to the non-normalized case. Reviewing these earlier efforts finds that they:

a) employ a higher compression ratio engine (21.2:1 for the Yanmar L100V compared to 17.1:1 for the AVL 5402);
b) the peak pressure for combustion happens sooner;
   - Yanmar L100V ignition occurs at 4–5 °CA ATDC with peak pressure at 10 °CA ATDC;
   - AVL 5402 ignition occurs 7.5–10 °CA ATDC and peak pressure at 12.5 °CA ATDC or later;
c) while the Yanmar L100V in question has been upgraded to a common rail electronic injection system, it operates at a respectively lower pressure of 45 MPa as opposed to 60–70 for the AVL 5402.

Here, the set base calibration of the AVL 5402 engine was supplied by the engine manufacturer and not determined as per the maximum thermal efficiency as accomplished for the previous work [59]. Therefore, biodiesel fuel is injected in a relatively less favorable environment for atomization and vaporization. Furthermore, this is compounded by a respectively lower compression ratio that results in a reduced pressure and temperature seen by the fuel as it enters the cylinder. Given biodiesel's higher viscosity, lower volatility, and reduced energy content, it has a more difficult time achieving the 100% load setting, subsequently requiring an earlier and longer injection event.

Two dissimilar kinds of behavior are seen for the Rate of Heat Release (ROHR): one for loads at or below 50% (Fig. 3a–c) and one for above 50% (Fig. 3d, e). Distinctively, below 50% load, the normalized biodiesel encounters a higher peak ROHR with apparently a shorter period of premixed energy liberation. As a result, the process indicates a strong proclivity towards constant volume combustion. Nonetheless, even with this seemingly more energetic and quicker heat release event, the in-cylinder pressures do not exceed that of ULSD. Investigating Fig. 2 demonstrates that, except for the 100% load case, all normalized biodiesel injection events begin closer to TDC. Therefore, the fuel injection process is seeing a greater in-cylinder pressure and temperature initially; hence, this should result in a lower spray penetration length (compared to the non-normalized case) but a more spread-out fuel spray that vaporizes quicker. Furthermore, engine coolant temperatures were found to be slightly higher during the biodiesel tests since combustion happens sooner and there is more time for heat transfer (80.4/80.6 °C for WCO compared to 78.2/79.8 °C for ULSD; seen in 2nd law analysis discussed later). Thus, this will additionally promote a slightly enhanced vaporization of the fuel. As a result, there appears to be a better mixing of fuel and air at the beginning of WCO biodiesel's fuel injection process. Combining this with its higher CN, more embedded oxygen (i.e., greater level of equivalence ratios in the flammability zone) and a greater adiabatic flame temperature results in a quicker and apparently more vigorous heat release. However, since significantly more biodiesel fuel must be added because of its reduced energy content, this grows the energy taken away from the working fluid via the latent heat of vaporization. As a result, the in-cylinder pressure and temperature (Fig. 4) drops below that of ULSD even as combustion is beginning (Fig. 1). Therefore, the biodiesel fuel added towards the end of the injection process sees slightly worse conditions while mixing and vaporizing less well (compounded by its greater viscosity), subsequently showing up as a less efficient diffusion burn (seen in Fig. 3), and increasing fuel consumption. Overall, while initially biodiesel burns more effectively, this is not sufficient to overcome a growth in diffusion burn resulting in lower in-cylinder pressures and temperatures. This discussion will be revisited when presenting the second law heat release analysis for further clarification.

After 50% load, the onset of diffusion burn behavior begins and there will be a reduction in efficiency proportional to the increase in

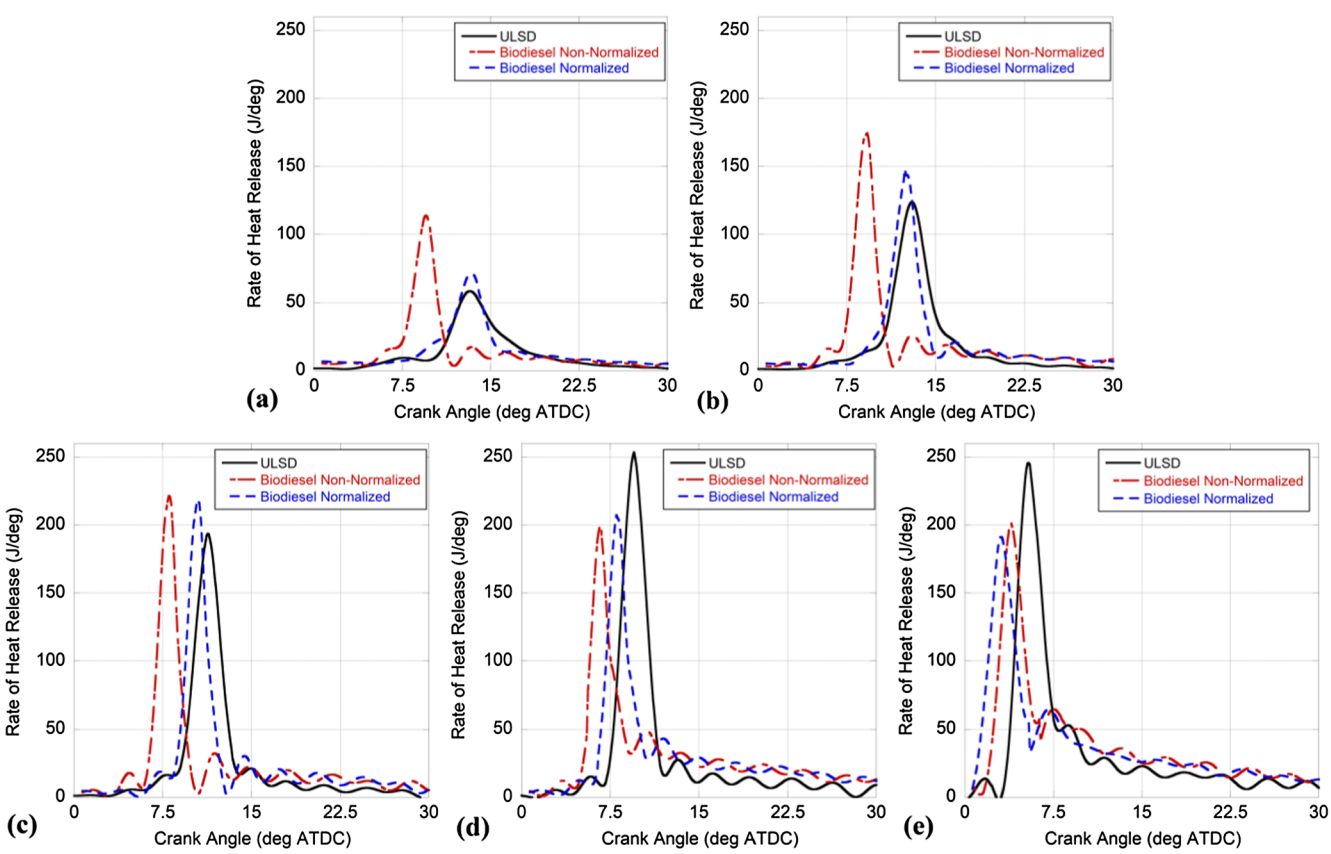

Fig. 3. Calculated Rate of Heat Release at (a) 0% load, (b) 25% load, (c) 50% load, (d) 75% load, and (e) 100% load for AVL 5402 engine.

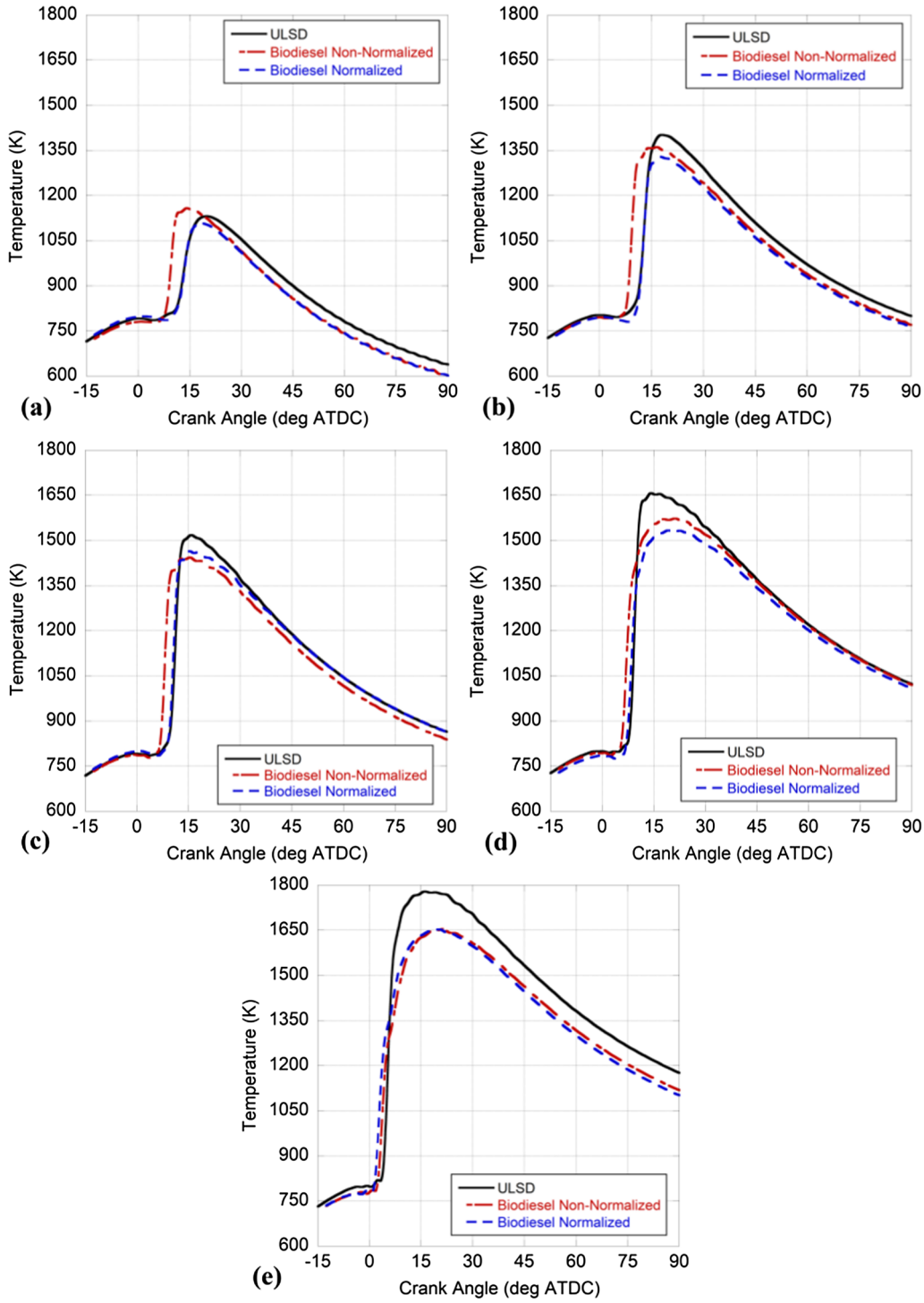

Fig. 4. Calculated in-cylinder temperatures at (a) 0% load, (b) 25% load, (c) 50% load, (d) 75% load, and (e) 100% load for AVL 5402 engine.

pressure trace width. This is due to a combination of a larger fuel mass injected and a poorer mixing of biodiesel with the air inside the combustion chamber, which leads to a greater amount of fuel that cannot be burnt during the premixed phase. Here, ULSD appears to remain largely pre-mixed because of its respectively lower viscosity and longer ignition delay resulting in an enhanced mixing process. As a result, the trend now switches with ULSD having a higher ROHR and shorter combustion event. Some diffusion burn is seen with ULSD at 100% load, but the amount is significantly less than biodiesel.

In Fig. 4, the global in-cylinder temperatures highlight that WCO biodiesel burns at a lower temperature than ULSD after combustion normalization for this engine. This trend of temperature largely follows that of pressure and its associated discussion since they are related through the ideal gas law. Interestingly, at 50% load, the normalized pressure for the WCO biodiesel process is less than the non-normalized case; whereas, the temperature is slightly higher. In this case, it appears that the longer ignition delay (Fig. 2) resulting from a later injection helps to prepare slightly more fuel for a premixed burn event that would have otherwise resulted in a diffusion burn. Hence, the peak ROHR is similar along with the temperatures. This greater level of premixed burn from a longer ignition delay is also seen at 75% load when comparing the normalized and non-normalized cases. However,

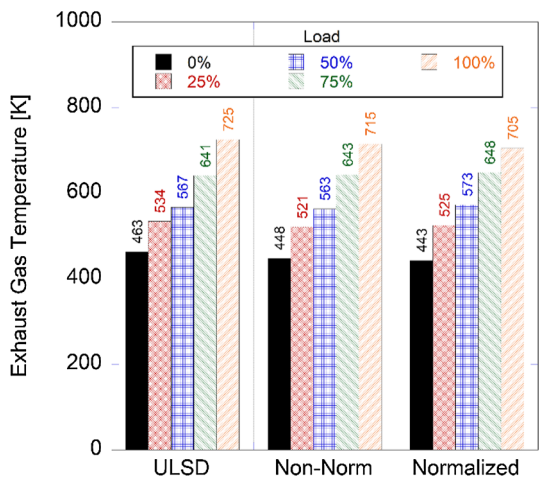

Fig. 5. Exhaust gas temperature for all cases.

since the normalized case is burning later in the cycle with more diffusion burn required to hit the load condition, the global in-cylinder conditions are less a function of the more energetic premixed spike. Therefore, both the temperature and pressure of the normalized case fall below the non-normalized case. Finally, at 100% load, since the normalized case injects fuel before the non-normalized case, this ignition delay trend is reversed, and the peak normalized ROHR is smaller. Overall, the significantly lengthened fuel injection process that adds the required amount of fuel at this load results in equivalent temperatures.

The analysis of the exhaust gas temperatures (Fig. 5) showed a similar evolution to that of the in-cylinder temperature with respect to load. However, even though the normalized biodiesel results all maintained a lower in-cylinder temperature than ULSD, higher exhaust temperatures for this fuel were seen for the 50% and 75% load cases. This is due to the larger amount of fuel used and subsequent shift towards diffusion burn when moving to biodiesel, even though the 50% load case had a greater premixed spike. Hence, more fuel is burning closer to the exhaust valve opening (EVO). At 100% load, this trend reverses as the normalized biodiesel was injected before ULSD; therefore, combustion is now happening further away from the EVO event.

This apparent contradiction between the higher biodiesel ROHR and its lower in-cylinder pressures and temperatures in comparison to ULSD can be clarified further by investigating the second law of thermodynamics heat release analysis in Fig. 6. While operation with biodiesel results in lower peak temperatures within the cylinder, it also causes a longer period of relatively higher temperatures. Generally, biodiesel undergoes a more complete combustion process; hence, the chemical potential availability of the fuel is successfully converted to thermal availability. However, as the load increases, this thermal availability is in the form of diffusion burn that happens later in the expansion stroke, where in-cylinder conditions are rapidly cooling and availability is more challenging to extract. Furthermore, the higher viscosity and lower volatility of biodiesel results in a worse mixing process, moving still more thermal availability production into the diffusion burn phase. Therefore, while fuel potential availability is more likely to be transformed via combustion, that availability is also less likely to be successfully extracted as work (Fig. 6a). As a result, this increases the amount of fuel availability lost to heat transfer (Fig. 6b) due to prolonged higher temperatures, but this simultaneously results in a decrease in internal entropy production (Fig. 6c). Therefore, availability retention increases as a fraction of total availability (Fig. 6d) that is exhausted to the atmosphere at the close of the cycle, which may find its way into a greater exhaust temperature (Fig. 5). In addition, the energy content of biodiesel influences the results; i.e., the engine requires more biodiesel fuel availability in order to meet the required load to make up for the fact that the availability is less optimally extracted as work.

Overall, biodiesel (mostly) demonstrates an earlier and greater level of premixed combustion; however, this occurs too early for the biodiesel fuel injected later that cannot prepare fast enough to join in on the premixed event. As a result, premixed combustion is limited in comparison to ULSD, and remaining fuel transitions from premixed (quasi-constant volume) combustion to diffusion (quasi-constant pressure) combustion; thus, peak pressures are limited. This added inefficient combustion adds availability later in the expansion stroke, where it is less easily extracted, subsequently lowering the 2nd law efficiency (Fig. 6a).

Unlike the prior efforts [50,51], the respectively lower compression ratio of this engine is not quite powerful enough to overcome some of these differences. In addition, this is worsened by the fact that combustion happens later in this engine under a less ideal temperature scenario. Finally, while the performance deviations between biodiesel and ULSD are generally reduced for higher loads where both fuels begin to encounter a greater level of diffusion burn, this engine begins having trouble in mixing biodiesel significantly earlier than with ULSD. In specific, biodiesel diffusion combustion begins to set in just beyond 50% load, whereas ULSD diffusion burn is put off until after 75% load (see Fig. 3c, d, and e). This results in still worsened performance for the biodiesel fuel, due to the biodiesel entering the less exergetically efficient diffusion phase at lower engine loads.

As a result of this decreasing overall efficiency, Fig. 7a shows the greater amount of availability that must be added when working with biodiesel, which in turn reflects the worsened fuel consumption. Generally, operation with biodiesel seems to require another 120–300 J of thermal availability present in the cylinder. In addition, the deviation in availability generally grows with engine load, highlighting the increasing gulf of performance between the two fueling strategies. In comparison to prior efforts, this is likely linked to the engine compression ratio. In specific, as the compression ratio increases, the importance of fuel viscosity on overall engine performance may decrease so long as the fuel is still able to adequately break up and vaporize. Hence, at higher compression ratios, the performance of an engine might become tied more to the quantity of fuel delivered and less on the quality of that fuel.

Of note, availability addition is related directly to the brake specific availability consumption (BSAC) in Fig. 7b that is the second law analog to brake specific energy consumption. Here, this highlights the amount of availability that is successfully converted to useful work for a given engine cycle. Thus, since the availability addition with biodiesel is higher than with ULSD, the BSAC is greater as well. Moreover, Fig. 7b highlights a more dramatic trend with WCO biodiesel illustrating its optimum operational point at 50% load (stated before: highest premixed burn without a significant diffusion burn phase). Hence, the engine appears to be more sensitive to changes in the fuel properties; again, reaffirming the prior statement that at respectively lower compression ratios, performance is tied more closely to fuel properties than fuel quantity.

In order to maintain engine performance when switching to WCO biodiesel operation, it is necessary to increase the injected fuel mass to compensate for its reduced volumetric energy content as compared to ULSD. Therefore, as more fuel is burnt at enhanced combustion efficiencies and because the H/C ratio of biodiesel is similar to that of ULSD, CO_2 emissions (a proxy for fuel consumption, and thus fuel availability addition) generally increase when using WCO biodiesel as presented in Fig. 8. However, even if the CO_2 emissions are higher, its overall greenhouse gas footprint can be lower when considering the CO_2 consumption of the plants used as its feedstock [8]. As with all fuels, the potential CO_2 advantages of WCO biodiesel could be enhanced further by properly matching the fuel injection parameters to the properties of this fuel.

Despite the mixture formation issues caused by a higher viscosity, the fuel bound oxygen content of WCO biodiesel has a beneficial effect

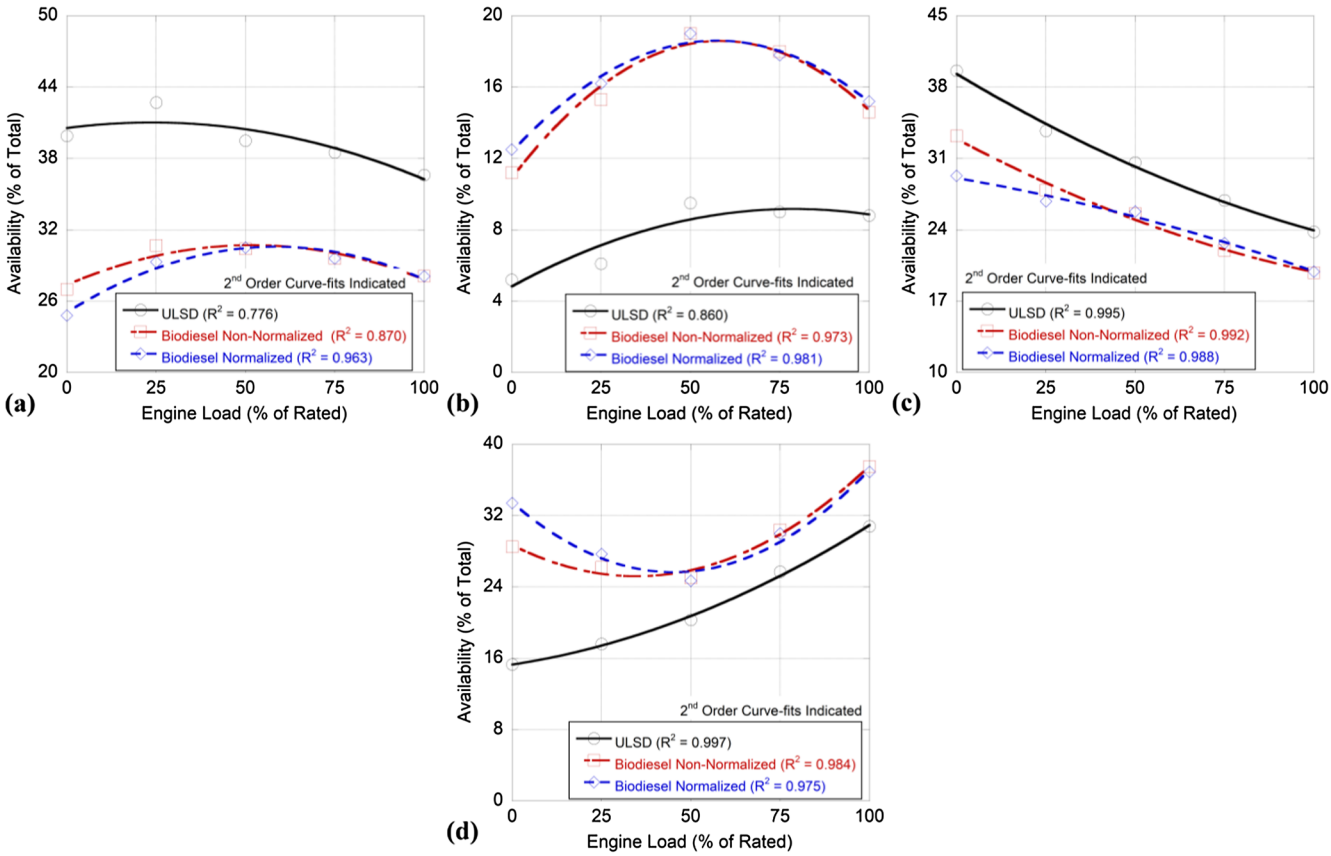

Fig. 6. Percentage of total thermal availability (a) extracted as work, (b) lost through heat transfer, (c) destroyed by entropy generation, or (d) retained by the exhaust at EVO for AVL 5402 engine.

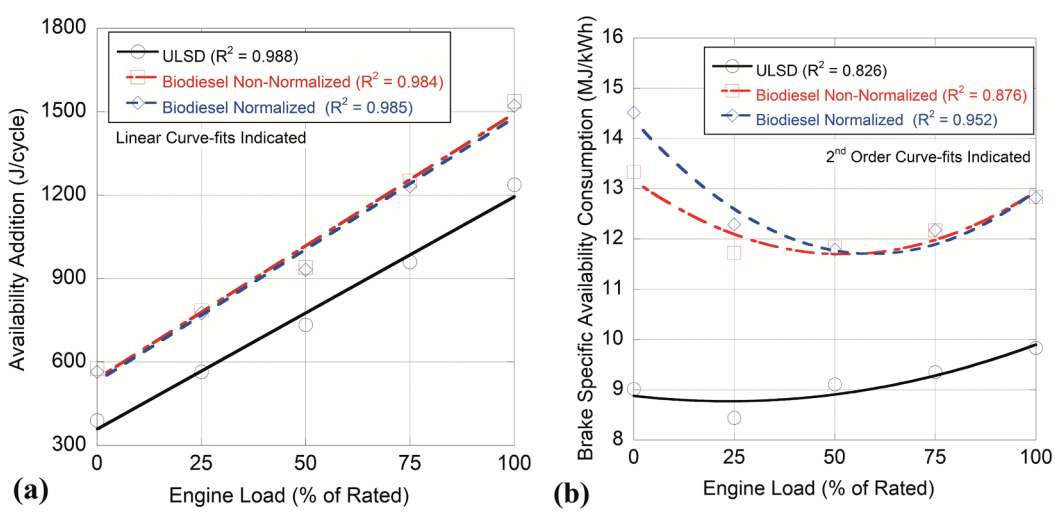

Fig. 7. (a) Total thermal availability and (b) brake specific availability consumption added to the cylinder for AVL 5402 engine.

on CO emissions in all cases as illustrated in Fig. 8. However, this benefit decreases in both the non-normalized and the normalized cases with the growth in engine load as the level of diffusion burn increases at greater equivalence ratios. Moreover, when normalizing the combustion phasing, the combustion process is shifted later in the expansion phase and, as a result, CO emissions increase compared to the non-normalized case. This is due to the slightly less favorable combustion environment, since the combustion time is slightly reduced, and the fuel mass somewhat increases. Since HC emissions emanate primarily from the diffusion burn phase, the trend of HC emissions follows that of CO in Fig. 8. Largely, HCs are formed due to a low oxidation rate at reduced temperatures or because of insufficient oxygen being available locally (poor mixing). As shown previously, in-cylinder temperatures are lower when using WCO biodiesel and its mixing process is respectively worse as compared to ULSD. However, its fuel bound oxygen provides some compensation along with locally higher adiabatic flame temperatures; thus, improving the engine out HC values. Again, analogous to CO, HC emissions are larger for the normalized case since combustion happens in a less advantageous situation. Furthermore, these greater CO and HC emissions are tied to the increased thermal availability present in the engine exhaust at EVO; i.e., any partial oxidation species present later in the engine cycle are essentially

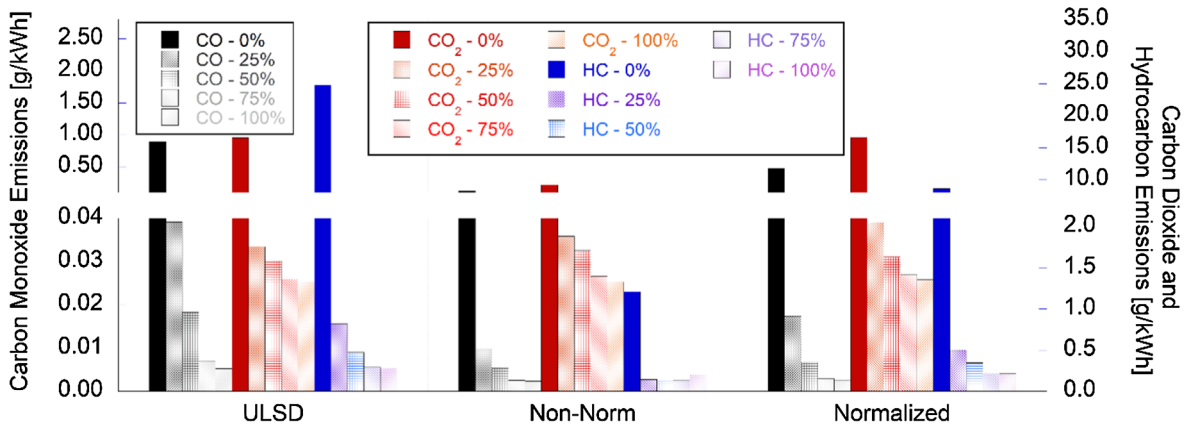

Fig. 8. Brake specific CO, CO_2, and HC emissions.

unconsumed potential availability. Here, they cannot be effectively extracted as work and do not have the time to be lost via heat transfer; hence, they are retained in the exhaust gases and expelled at EVO.

Fig. 9 presents the NO emissions and, unfortunately, NO_2 emissions were not available at the time of study. However, since NO_2 emissions are a respectively small fraction of NO_x emissions (e.g., 10–30% [60,61]), the trend of NO emissions will primarily represent that of NO_x. Here, to understand NO_x emissions trends, it is necessary to discuss engine load and calculated in-cylinder temperatures. At 0% and 25% load, there is an increase in NO emissions when using WCO biodiesel as shown in Fig. 9. For these cases, even though global in-cylinder temperatures are slightly lower for WCO biodiesel (note: greater in 0% non-normalized), the local availability of oxygen, higher adiabatic flame temperatures, and the fact that combustion happens closer to TDC in a mostly pre-mixed phase all leads to more favorable NO_x formation conditions. However, beginning at 50% load, the NO_x emissions of WCO biodiesel are smaller than those of ULSD with the lowest values for the normalized case (except at 100% load when biodiesel injection timing was advanced). The main reason behind this decrease is its considerably lower in-cylinder temperature. Therefore, as stated prior, even though the early stages of WCO biodiesel combustion happens in a more opportune environment for NO_x emissions, the prolonged fuel injection event due its reduced volumetric energy content and subsequent growth of diffusion burn combustion finds a less favorable situation. Hence, as more fuel burns later in the engine cycle, this reduces the temperature and time needed for thermal NO_x kinetics. Furthermore, WCO's respectively worse mixture formation required an increase in fuel availability; thus, combined with a later burning event (after in-cylinder temperatures have fallen below levels conducive to NO_x formation) results in more availability retained in the exhaust (Fig. 6d) and not towards energy release and NO_x emissions. Overall, NO_x is shown to both increase and decrease here in comparison to ULSD, depending on the precise conditions present within the cylinder, helping to highlight the disparity in literature findings (see Table 1).

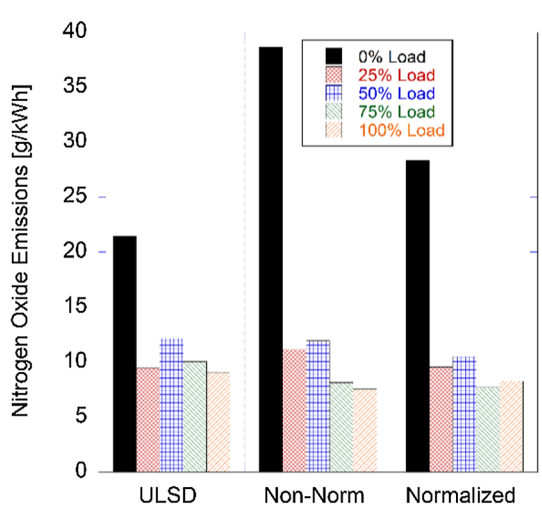

Fig. 9. Brake specific NO emissions.

4. Conclusions

Biofuels, and particularly biodiesels, represent an advantageous fuel due to their significantly reduced carbon emissions potential, thanks to their renewable nature. Waste cooking oil biodiesel is one such fuel while additionally having the advantage of not competing with existing food resources. However, its differing characteristics in comparison to petroleum-based diesel affects the injection timing along with the initiation of ignition and quality of combustion. Moreover, to understand where deficiencies in combustion behavior occur, it is necessary to examine the precise pathways by which fuel energy is lost. This requires the use of 2nd Law Heat Release modeling that can quantify losses in fuel availability due to heat transfer or internal irreversibilities in addition to energy lost during the exhaust event. In tandem with traditional modes of analysis via in-cylinder pressure and engine-out emissions measurement results in a greater understanding of the biodiesel combustion process.

Generally, WCO biodiesel's heightened Cetane Number results in a shorter ignition delay period, requiring delays in fuel injection timing to maintain optimal combustion timing. Furthermore, adding biodiesel results in a shortened period for the mixture to atomize, vaporize, and ignite. As a result, this offers a more opportune vaporization and mixing of the biodiesel injected early on in the fuel charge through its introduction at higher in-cylinder pressures. However, biodiesel's shortened ignition delay period and greater viscosity begins to hamper combustion, cutting the premixed event short and inducing diffusion-dominated combustion above that of diesel; hence, lowering the 2nd Law efficiency. Moreover, while biodiesel operation primarily results in cooler peak temperatures, it promotes longer periods of higher temperatures due to this shift towards diffusion burn and its embedded oxygen that facilitates greater combustion efficiency. These higher in-cylinder temperatures increase the loss of availability due to heat transfer; however, this does maintain a warmer in-cylinder environment that mitigates losses due to entropy production. Thus, biodiesel usage promotes a larger conversion of fuel potential to thermal availability, and maintains a higher fraction of this availability by limiting entropy production. Unfortunately, this availability addition occurs later in the engine cycle, making it more difficult to extract as work. Further optimization might be effective in reducing these drawbacks, particularly by increasing fuel injection pressures.

Biodiesel usage also results in a relatively similar emissions profile to operation with diesel. In specific, CO and HC emissions are each generally reduced, owing to the more thorough combustion of fuel. While the increased fuel usage results in heightened CO_2 emissions, this is offset by the fuel feedstock reabsorbing that carbon content when it is grown, bringing the fuel closer to carbon-neutrality. Finally, NO_x emissions are more closely tied with in-cylinder temperatures and the amount of diffusion burn; thus, they will either increase or decrease depending on combustion behavior.

Funding

This research did not receive any specific grant from funding agencies in the public, commercial, or not-for-profit sectors.

Declaration of Competing Interest

None.

References

[1] Shafiee S, Topal E. When will fossil fuel reserves be diminished? Energy Policy 2009;37:181–9. https://doi.org/10.1016/j.enpol.2008.08.016.
[2] The European Parliament and The Council of The European Union. Directive 2009/28/EC of the European Parliament and of the Council of 23 April 2009 2009.
[3] Zhang X, Peterson C, Reece D, Haws R, Moller G. Biodegradability of biodiesel in the aquatic environment. Trans Asae 1998;41:1423–30.
[4] Knothe G. Biodiesel and renewable diesel: A comparison. Prog Energy Combust Sci 2010;36:364–73. https://doi.org/10.1016/j.pecs.2009.11.004.
[5] Mudge SM, Pereira G. Stimulating the biodegradation of crude oil with biodiesel preliminary results. Spill Sci Technol Bull 1999;5:353–5. https://doi.org/10.1016/S1353-2561(99)00075-4.
[6] Zhang Y, Dubé MA, McLean DD, Kates M. Biodiesel production from waste cooking oil: 2. Economic assessment and sensitivity analysis. Bioresour Technol 2003;90:229–40. https://doi.org/10.1016/S0960-8524(03)00150-0.
[7] Speidel H, Lightner R, Ahmed I. Biodegradability of New Engineered Fuels Compared to Conventional Petroleum Fuels and Alternative Fuels in Current Use. In: Finkelstein M, Davison B, editors. Twenty-First Symp. Biotechnol. Fuels Chem. SE – 69, Humana Press; 2000, p. 879–97. doi:10.1007/978-1-4612-1392-5_69.
[8] Montefrio MJ, Xinwen T, Obbard JP. Recovery and pre-treatment of fats, oil and grease from grease interceptors for biodiesel production. Appl Energy 2010;87:3155–61. https://doi.org/10.1016/j.apenergy.2010.04.011.
[9] Demirbas A. Importance of biodiesel as transportation fuel. Energy Policy 2007;35:4661–70. https://doi.org/10.1016/j.enpol.2007.04.003.
[10] Agarwal AK. Biofuels (alcohols and biodiesel) applications as fuels for internal combustion engines. Prog Energy Combust Sci 2007;33:233–71. https://doi.org/10.1016/j.pecs.2006.08.003.
[11] Knothe G, Razon LF. Biodiesel fuels. Prog Energy Combust Sci 2017;58:36–59. https://doi.org/10.1016/j.pecs.2016.08.001.
[12] Atadashi IM, Aroua MK, Aziz AA. High quality biodiesel and its diesel engine application: a review. Renew Sustain Energy Rev 2010;14:1999–2008. https://doi.org/10.1016/j.rser.2010.03.020.
[13] Demirbas A. Progress and recent trends in biodiesel fuels. Energy Convers Manag 2009;50:14–34. https://doi.org/10.1016/j.enconman.2008.09.001.
[14] Burnete NV, Filip N, Barabás I. Diesel-Ethanol blends and their use in Diesel engines. J Automot Eng 2015:89.
[15] Escobar JC, Lora ES, Venturini OJ, Yáñez EE, Castillo EF, Almazan O. Biofuels: environment, technology and food security. Renew Sustain Energy Rev 2009;13:1275–87. https://doi.org/10.1016/j.rser.2008.08.014.
[16] Naylor RL, Higgins MM. The political economy of biodiesel in an era of low oil prices. Renew Sustain Energy Rev 2017;77:695–705. https://doi.org/10.1016/j.rser.2017.04.026.
[17] Organisation for Economic Cooperation and Development. Technology roadmap: biofuels for transport. OECD Publishing; 2011.
[18] Basha SA, Gopal KR, Jebaraj S. A review on biodiesel production, combustion, emissions and performance. Renew Sustain Energy Rev 2009;13:1628–34. https://doi.org/10.1016/j.rser.2008.09.031.
[19] Mandolesi de Araújo CD, de Andrade CC, de Souza e Silva E, Dupas FA. Biodiesel production from used cooking oil: A review. Renew Sustain Energy Rev 2013;27:445–52. https://doi.org/10.1016/j.rser.2013.06.014.
[20] Peters J, Thielmann S. Promoting biofuels: Implications for developing countries. Energy Policy 2008;36:1538–44. https://doi.org/10.1016/j.enpol.2008.01.013.
[21] Enweremadu CC, Mbarawa MM. Technical aspects of production and analysis of biodiesel from used cooking oil—A review. Renew Sustain Energy Rev 2009;13:2205–24. https://doi.org/10.1016/j.rser.2009.06.007.
[22] da S César A, Werderits DE, de Oliveira Saraiva GL, da S Guabiroba RC. The potential of waste cooking oil as supply for the Brazilian biodiesel chain. Renew Sustain Energy Rev 2017;72:246–53. https://doi.org/10.1016/j.rser.2016.11.240.
[23] Marmesat S, Rodrigues E, Velasco J, Dobarganes C. Quality of used frying fats and oils: comparison of rapid tests based on chemical and physical oil properties. Int J Food Sci Technol 2007;42:601–8. https://doi.org/10.1111/j.1365-2621.2006.01284.x.
[24] Gebremariam SN, Marchetti JM. Economics of biodiesel production: review. Energy Convers Manag 2018;168:74–84. https://doi.org/10.1016/j.enconman.2018.05.002.
[25] Gharat N, Rathod VK. Enzyme catalyzed transesterification of waste cooking oil with dimethyl carbonate. J Mol Catal B Enzym 2013;88:36–40. https://doi.org/10.1016/j.molcatb.2012.11.007.
[26] Waghmare GV, Rathod VK. Ultrasound assisted enzyme catalyzed hydrolysis of waste cooking oil under solvent free condition. Ultrason Sonochem 2016;32:60–7. https://doi.org/10.1016/j.ultsonch.2016.01.033.
[27] Aboelazayem O, Gadalla M, Saha B. Biodiesel production from waste cooking oil via supercritical methanol: optimisation and reactor simulation. Renew Energy 2018;124:144–54. https://doi.org/10.1016/j.renene.2017.06.076.
[28] Gaurav A, Ng FTT, Rempel GL. A new green process for biodiesel production from waste oils via catalytic distillation using a solid acid catalyst – Modeling, economic and environmental analysis. Green Energy Environ 2016;1:62–74. https://doi.org/10.1016/j.gee.2016.05.003.
[29] Energy Information Administration US. Monthly Biodiesel Production Report. Washington, DC: 2019.
[30] Phillips S, Flach B, Lieberz S, Lappin J, Bolla S. EU Biofuels Annual 2018:2018.
[31] He B-Q. Advances in emission characteristics of diesel engines using different biodiesel fuels. Renew Sustain Energy Rev 2016;60:570–86. https://doi.org/10.1016/j.rser.2016.01.093.
[32] Enweremadu CC, Rutto HL. Combustion, emission and engine performance characteristics of used cooking oil biodiesel—a review. Renew Sustain Energy Rev 2010;14:2863–73. https://doi.org/10.1016/j.rser.2010.07.036.
[33] Demirbas A. Political, economic and environmental impacts of biofuels: a review. Appl Energy 2009;86:S108–17. https://doi.org/10.1016/j.apenergy.2009.04.036.
[34] Jiaqiang E, Pham M, Zhao D, Deng Y, Le D, Zuoa W, et al. Effect of different technologies on combustion and emissions of the diesel engine fueled with biodiesel: a review. Renew Sustain Energy Rev 2017;80:620–47. https://doi.org/10.1016/j.rser.2017.05.250.
[35] Lapuerta M, Armas O, Rodríguez-Fernández J. Effect of biodiesel fuels on diesel engine emissions. Prog Energy Combust Sci 2008;34:198–223. https://doi.org/10.1016/j.pecs.2007.07.001.
[36] Attia AMA, Hassaneen AE. Influence of diesel fuel blended with biodiesel produced from waste cooking oil on diesel engine performance. Fuel 2016;167:316–28. https://doi.org/10.1016/J.FUEL.2015.11.064.
[37] Abed KA, El Morsi AK, Sayed MM, El Shaib AA, Gad MS. Effect of waste cooking-oil biodiesel on performance and exhaust emissions of a diesel engine. Egypt J Pet 2018. https://doi.org/10.1016/j.ejpe.2018.02.008.
[38] Can Ö. Combustion characteristics, performance and exhaust emissions of a diesel engine fueled with a waste cooking oil biodiesel mixture. Energy Convers Manag 2014;87:676–86. https://doi.org/10.1016/j.enconman.2014.07.066.
[39] Hwang J, Qi D, Jung Y, Bae C. Effect of injection parameters on the combustion and emission characteristics in a common-rail direct injection diesel engine fueled with waste cooking oil biodiesel. Renew Energy 2014;63:9–17. https://doi.org/10.1016/j.renene.2013.08.051.
[40] Mangus M, Depcik C. Comparison of ULSD, Used Cooking Oil Biodiesel, and JP-8 Performance and Emissions in a Single-Cylinder Compression-Ignition Engine. SAE Int J Fuels Lubr 2012;5:1382–94. https://doi.org/10.4271/2012-32-0009.
[41] Hwang J, Bae C, Gupta T. Application of waste cooking oil (WCO) biodiesel in a compression ignition engine. Fuel 2016;176:20–31. https://doi.org/10.1016/j.fuel.2016.02.058.
[42] Senthil Kumar M, Jaikumar M. A comprehensive study on performance, emission and combustion behavior of a compression ignition engine fuelled with WCO (waste cooking oil) emulsion as fuel. J Energy Inst 2014;87:263–71. https://doi.org/10.1016/j.joei.2014.03.001.
[43] Yesilyurt MK. The effects of the fuel injection pressure on the performance and emission characteristics of a diesel engine fuelled with waste cooking oil biodiesel-diesel blends. Renew Energy 2019;132:649–66. https://doi.org/10.1016/j.renene.2018.08.024.
[44] Lapuerta M, Herreros JM, Lyons LL, García-Contreras R, Briceño Y. Effect of the alcohol type used in the production of waste cooking oil biodiesel on diesel performance and emissions. Fuel 2008;87:3161–9. https://doi.org/10.1016/j.fuel.2008.05.013.
[45] An H, Yang WM, Maghbouli A, Li J, Chou SK, Chua KJ. Performance, combustion and emission characteristics of biodiesel derived from waste cooking oils. Appl Energy 2013;112:493–9. https://doi.org/10.1016/j.apenergy.2012.12.044.
[46] Wei L, Cheung CS, Ning Z. Influence of waste cooking oil biodiesel on combustion, unregulated gaseous emissions and particulate emissions of a direct-injection diesel engine. Energy 2017;127:175–85. https://doi.org/10.1016/j.energy.2017.03.117.
[47] Chen H, Xie B, Ma J, Chen Y. NOx emission of biodiesel compared to diesel: higher or lower? Appl Therm Eng 2018;137:584–93. https://doi.org/10.1016/j.applthermaleng.2018.04.022.
[48] Geng P, Mao H, Zhang Y, Wei L, You K, Ju J, et al. Combustion characteristics and NOx emissions of a waste cooking oil biodiesel blend in a marine auxiliary diesel engine. Appl Therm Eng 2017;115:947–54. https://doi.org/10.1016/j.applthermaleng.2016.12.113.
[49] Shen X, Shi J, Cao X, Zhang X, Zhang W, Wu H, et al. Real-world exhaust emissions and fuel consumption for diesel vehicles fueled by waste cooking oil biodiesel blends. Atmos Environ 2018;191:249–57. https://doi.org/10.1016/j.atmosenv.2018.08.004.
[50] Mattson J, Reznicek E, Depcik C. Second Law Heat Release Modeling of a

Compression Ignition Engine Fueled With Blends of Palm Biodiesel 2015:V06BT07A012. doi:10.1115/IMECE2015-51079.
[51] Mattson JMS, Depcik C. First and second law heat release analysis in a single cylinder engine. SAE Int J Engines 2016;9:536–45. https://doi.org/10.4271/2016-01-0559.
[52] Cecrle E, Depcik C, Duncan A, Guo J, Mangus M, Peltier E, et al. Investigation of the effects of biodiesel feedstock on the performance and emissions of a single-cylinder diesel engine. Energy Fuels 2012;26:2331–41. https://doi.org/10.1021/ef2017557.
[53] VDMA. Exhaust emission legislation Diesel and gas engines. 2017.
[54] Tat ME, Van Gerpen JH. Measurement of Biodiesel Speed of Sound and Its Impact on Injection Timing. 1617 Cole Boulevard Golden, Colorado 80401–3393: National Renewable Energy. Laboratory 2003.
[55] Boehman AL, Morris D, Szybist J, Esen E. The impact of the bulk modulus of diesel fuels on fuel injection timing. Energy Fuels 2004;18:1877–82. https://doi.org/10.1021/ef049880j.
[56] Mohan B, Yang W, Tay KL, Yu W. Experimental study of spray characteristics of biodiesel derived from waste cooking oil. Energy Convers Manag 2014;88:622–32. https://doi.org/10.1016/j.enconman.2014.09.013.
[57] Mangus M, Kiani F, Mattson J, Tabakh D, Petka J, Depcik C, et al. Investigating the compression ignition combustion of multiple biodiesel/ULSD (ultra-low sulfur diesel) blends via common-rail injection. Energy 2015;89:932–45. https://doi.org/10.1016/j.energy.2015.06.040.
[58] Mangus M, Kiani F, Mattson J, Depcik C, Peltier E, Stagg-Williams S. Comparison of Neat Biodiesels and ULSD in an Optimized Single-Cylinder Diesel Engine with Electronically-Controlled Fuel Injection. Energy Fuels 2014;28:3849–62. https://doi.org/10.1021/ef500417b.
[59] Mattson JMS, Mangus M, Depcik C. Efficiency and Emissions Mapping for a Single-Cylinder. Direct Injected Compression Ignition Engine 2014. https://doi.org/10.4271/2014-01-1242.
[60] Heywood JB. Internal combustion engine fundamentals. New York: Mcgraw-hill; 1988.
[61] Van Basshuysen R, Schäfer F, editors. Handbuch Verbrennungsmotor: Grundlagen, Komponenten, Systeme, Perspektiven. 8th ed. Springer Vieweg; 2017. doi:10.1007/978-3-658-10902-8.

IOP Conference Series: Materials Science and Engineering

PURPOSE-LED PUBLISHING™

PAPER • **OPEN ACCESS**

Preliminary results on nano-diamond and nano-graphite testing as additive for an engine lubrication oil

To cite this article: D Moldovanu *et al* 2020 *IOP Conf. Ser.: Mater. Sci. Eng.* **724** 012047

View the article online for updates and enhancements.

You may also like

- Influence of nano particles on the performance parameters of lube oil – a review
Anoop Pratap Singh, Ravi Kumar Dwivedi and Amit Suhane

- Wear and friction behavior of Al-TiB_2-nano-Gr hybrid composites fabricated through ultrasonic cavitation assisted stir casting
Suswagata Poria, Goutam Sutradhar and Prasanta Sahoo

- Nano-graphite field-emission cathode for space electric propulsion systems
Victor I Kleshch, Rinat R Ismagilov, Vsevolod V Mukhin et al.

This content was downloaded from IP address 193.226.5.163 on 07/07/2025 at 15:49

IOP Conf. Series: Materials Science and Engineering **724** (2020) 012047 doi:10.1088/1757-899X/724/1/012047

Preliminary results on nano-diamond and nano-graphite testing as additive for an engine lubrication oil

D Moldovanu[1], A Molea[1] and I Barabás[1]

[1]Technical University of Cluj-Napoca, Automotive Engineering and Transports Department, Bd. Muncii 103-105, Cluj-Napoca, Romania
Corresponding author: andreia.molea@auto.utcluj.ro

Abstract. An important amount of the fuel energy burned in an internal combustion engine is used to overcome the friction losses inside the engine. Developing advanced lubricants is one of the ways to improve the fuel efficiency and reducing the pollution caused by internal combustion engines. This paper presents tests done with 1% v/v nano-diamond and nano-graphite additives in engine oils, with bench tests on an air-cooled spark ignition engine (Honda GX 160) with a displacement of 118 cubic centimeters. Using the raw lubrication oil laboratory, tests were done to determine the viscosity, density and viscosity index using an Anton Paar SVM 3000 viscometer in comparison to the oil with nano-diamond and nano-graphite additives. The tests also revealed an average reduction in fuel consumption of 21% for the single cylinder engine in case of the oil with additives, for the entire speed range of the engine, showing a decrease of the fuel efficiency as the speed increases. The temperature of the exhaust manifold, outer side of the cylinder and the temperature of the oil pan were measured. By adding nano-diamond and nano-graphite additives to the lubricant oil, tests have revealed a reduction of the temperature of the exhaust manifold (with 11%), temperature on the outer side of the cylinder was reduced with 21% showing a clear friction reduction within the cylinder and piston-rings assembly. The temperature of the oil pan was reduced with 20%, showing a general reduction of the lubricating oil temperature which means a substantial reduction of the friction losses.

1. Introduction

An important amount of 33% of the fuel energy is used to overcome the friction losses in the car from which 35% is used to overcome the friction in the engine system. From this 12% of fuel energy, 45% is consumed in the piston assembly, 30% is consumed in bearings, seals, etc. (hydrodynamic lubrication), 15% is consumed in the valve train (mixed lubrication), and 10% is consumed by pumping and hydraulic viscous losses [1]. The less friction in the internal combustion engine the better fuel efficiency and less pollutant emission. The friction can be reduced using high performance engine oils.

Modern oils for internal combustion engines consist of a base oil (synthetic or semisynthetic) and an additive pack which could have a concentration up to 30-35% vol and it contains surface protective additives (anti-wear, corrosion and rust inhibitor, detergent, dispersant, friction modifier agents), oil performance improver additives (pour point depressant, seal swell agent, viscosity improver agents) and lubricant protective additives (anti-foaming, anti-oxidant, metal deactivator agents) [2].

During the past few years, various nano-materials have been studied as a new additive for lubricant oils, including polymers, metals, organic and inorganic materials [3].

In [4] the authors have studied the anti-scuffing property of lubricating oil and diamond nano-particles additive. They found out that 3% vol concentration of the diamond nano-particles had the most favourable effect on reducing the wear loss and the friction coefficient. Raina and Anand [5] have investigated the nano-diamond in combination with copper oxide and hexagonal boron nitride particles

Content from this work may be used under the terms of the Creative Commons Attribution 3.0 licence. Any further distribution of this work must maintain attribution to the author(s) and the title of the work, journal citation and DOI.
Published under licence by IOP Publishing Ltd

as an additive for poly-alpha-olefin. They observed a significant improvement in the lubrication properties of the base oil, the decrease of the friction coefficient was 15-25%.

Su et al. [6] have investigated the tribological properties of multi-walled carbon nanotubes with different sizes and volume fractions as an oil additive using a pin-on-disk friction and wear tester. They found that at 0.05% vol fraction the thin and short multi-walled carbon nanotubes could improve both friction-reducing and anti-wear properties of the oil more effectively than the thick and long multi-walled carbon nanotubes. Martorana et al. [7] have investigated the use of the dispersed fine graphite flake and carbon nanofiber in ethanol as a potential replacer of low pressure conventional hydraulic fluids in gear pump-driven hydraulic circuits. They found that both graphite and carbon nanofiber dispersions in ethanol within a concentration range of 195−1500 ppm can sustain hydraulic circuits with increases in pump efficiency.

Liu et al. [8] have conducted an investigation regarding the effects of nano-diamond additives in lubricating oil not only in a friction tester but also in a diesel engine. The authors ascertained a significant reduction of the friction coefficient of 30% and a slight increase on engine performances.

In our best knowledge the effect of the mixture of nano-diamond and nano-graphite as an additive for engine oil on the engine performances have not been investigated yet. The main goal of this article is to investigate the effect of this mixture on an internal combustion engine fuel consumption and friction.

2. Methodology

The test bench is presented in figure 1 and it consists of the internal combustion engine (I.C.E.) fitted with an external fuel tank, placed on an electronic scale (Gibertini Euromatic) to measure the fuel consumption. The speed of the engine was measured using an infrared tachometer (Lutron-DT 1236L), and the temperatures were measured with a digital infrared thermometer (ANENG AN550). For the Lutron-DT 1236L tachometer, the measurement range is 10 to 99999 rpm [9].

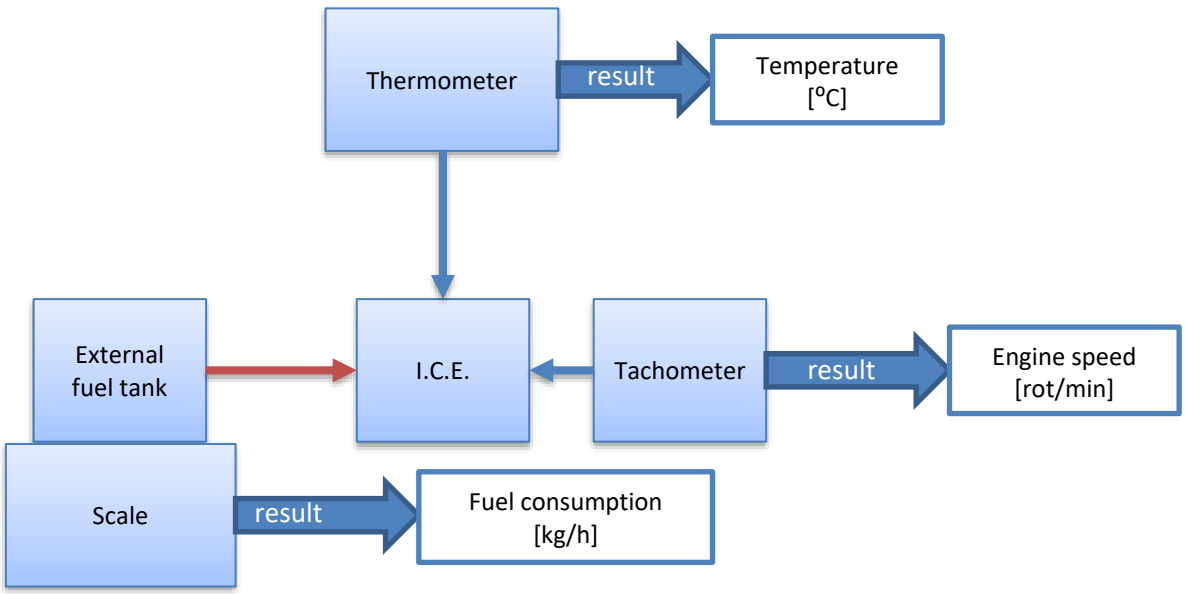

Figure 1. Used test bench sketch

The engine used for the tests was a Honda GX 160 single cylinder engine with the specifications presented in table 1.

Table 1. Honda GX 160 engine specifications.

Type	Single cylinder, 4 stroke
Displacement	163 cm^3
Bore x Stroke	68 x 45 mm
Max Power	3.6 kW @ 3600 rot/min
Max Torque	10.3 Nm @ 2500 rot/min
Cooling	Air cooled
Oil capacity	0.6 L
Fuel consumption	1.4 L/h @ 3600 rot/min

The used lubrication oil is Motul 5100 4T 10W-30, because it fulfils the API SL/SM standards. The standard properties of the lubrication oil are presented in table 2.

Table 2. Properties of Motul 5100 4T 10W-30.

Viscosity grade	SAE J 300	10W-30
Density at 20°C	ASTM D1298	0.871 g/cm^3
Viscosity at 40°C	ASTM D445	74.6 mm^2/s
Viscosity at 100°C	ASTM D445	11.5 mm^2/s
Viscosity index	ASTM D2270	147
Pour point limit	ASTM D97	-36°C
Flash point	ASTM D92	226°C
Total Base Number (TBN)	ASTM D2896	7.5 mg KOH/g

A commercially available ADDO nano-diamonds and nano-graphite particles, purchase from Plasma Chem, was used as additive. The additive contains 90% v/v motor oil and 10% v/v carbon nanoparticles, with an average of nano-particles size of 4-6 nm and this fulfils DIN EN ISO 6245 and DIN EN ISO 2160 standards. In order to prepare the oil with nano-diamonds and nano-graphite particles, a volume of 60 mL nano-additive was dispersed into 540 mL lubricant oil and the final concentration of the lubricant oil with additive was 1% v/v. The viscosity at 40°C and 100°C, viscosity index and density recorded with Stabinger viscometer SVM 3000 for the oil with nano-additve and the oil with nano-additives after used are presented in table 3.

Table 3. Properties of oil lubricant with nano-additives before and after use in engine.

Physicochemical properties	Oil with nano-additives before use	Oil with nano-additives after use
Density at 15°C	0.868 g/cm^3	0.867 g/cm^3
Viscosity at 40°C	62.175 mm^2/s	69.159 mm^2/s
Viscosity at 100°C	10.389 mm^2/s	11.178 mm^2/s
Viscosity index	156	154

The first test was done using as lubricant, only the Motul 5100 4T 10W-30 oil, with the engine speed variation from 1000 to 2500 rot/min in 100 rot/min steps, at zero load. The temperatures of the exhaust pipe (T_1 was chosen to monitor the temperature of the exhaust and therefore the fuel burn temperature loss), outer side of the cylinder (T_2 was chosen to evaluate the friction between the cylinder and the piston-rings assembly), exterior of the oil pan (T_3 was chosen to estimate the temperature of the lubricant itself) and the starter (T_4 was chosen as a reference temperature for the start of measurements) were measured, as seen in figure 2.

The second test was made using the same Motul 5100 4T 10W-30 oil, but with added nanomaterial additive (5 mL, the equivalent of 1%).

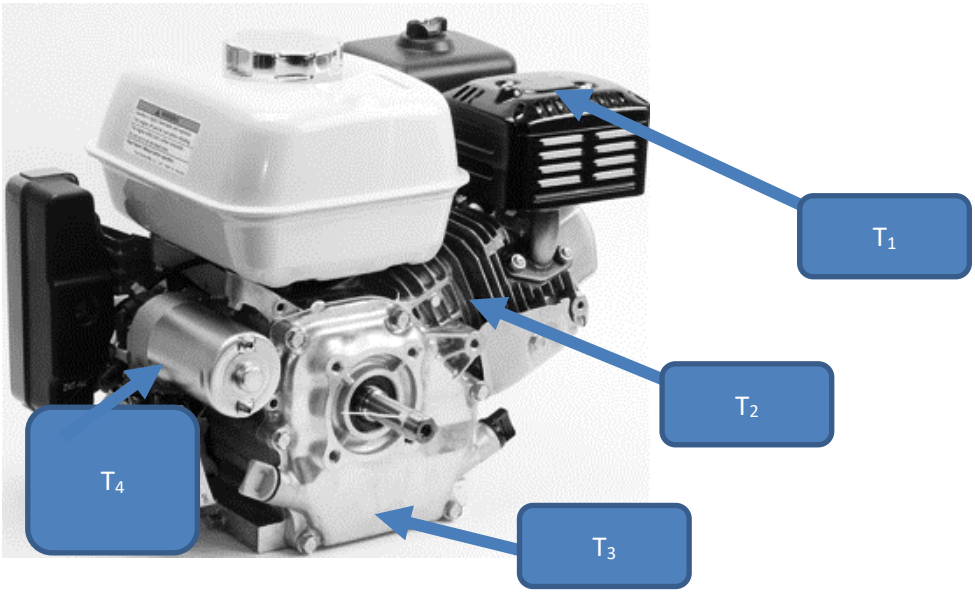

Figure 2. Measurements points for all temperatures

3. Results

First results that were extracted are the fuel consumptions for both tests, determined using the external fuel tank and scale. According with measurements, the variation of fuel consumption with speed presents a second order polynomial regression. The fuel consumption average (Fig. 3) when the oil lubricant with nano-additives was used (5.03 [kg/h]), decrease by 21% in comparrison with the average of fuel consumption when the standard oil lubricant was used (7.11 [kg/h]). This reduction is extremely high, but it is logical due to the fact that the engine was tested at zero load, where the engine only has to overcome the internal frictions, and no outer load is applied. This leaves more room for further investigations using the same additive but with an engine that can be loaded accordingly.

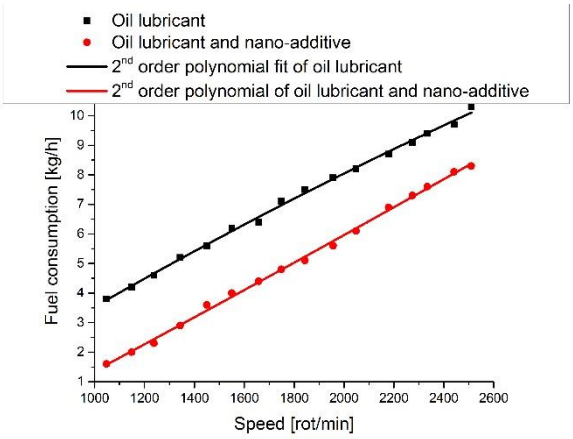

Figure 3. Fuel consumption versus speed

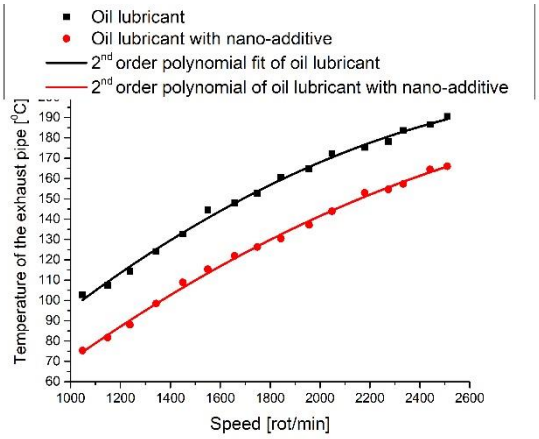

Figure 4. Temperature of the exhaust pipe versus speed

On the other hand, a reduction when nano-additives were used is explained thru the viscosity index. The results showed that the viscosity index of the oil lubricant increase with 6% when nano-additives are used (Tab. 3), which influence the fluid friction due to the formation of a better viscous film in the surface, leading to a reduction of the frictional losses. This reduction of power losses further enhances the automotive engine efficiency and our results are in agreement with [10] and [11].

The results shown in figure 4 indicate the variation of the temperature of the exhaust pipe (T_1) with speed. An increase of the temperature was observed for the oil lubricant with nano-additives. For the temperature of the exhaust pipe, an average value of 150°C was recorded for the standard lubricant oil while using the nano-additives, the average value of the temperature decreases to only 124°C, which indicates a better evolution of the temperature for the same testing time, i.e. better efficiency over time due to a lower friction coefficient.

The temperature of the outer side of the cylinder (T_2) also has second order polynomial variation, but the start temperature is around 45°C for the standard lubrication oil, and only around 37°C for the oil with nano-additive (Fig. 5). Due to the reduction of the frictions, the temperature of the outer side of the cylinder is reduced with 11% on the entire speed spectrum, when using nano-additives.

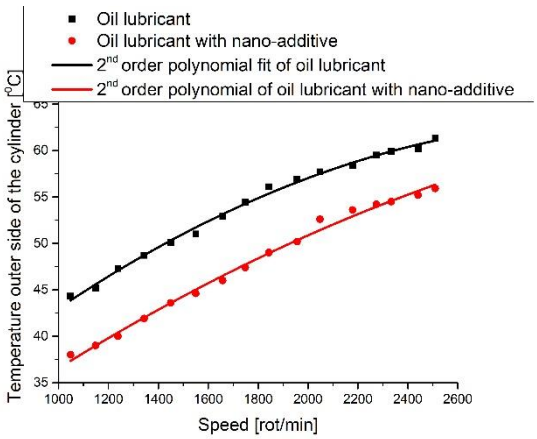

Figure 5. Temperature of the outer side of the cylinder versus speed

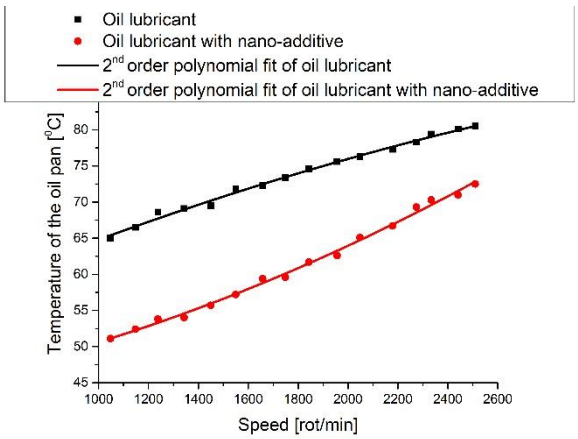

Figure 6. Temperature of the oil pan versus speed

Outside the oil pan (T_3), the temperature was monitored to understand the variation of the lubrication oil for both cases. By using the nano-additives instead of reaching an average value of 71°C, a value of 59°C was reached (Fig. 6) underlining the friction reduction with 20%.

4. Conclusions

The measurements were done with the increase of the speed at precise time intervals, with the same starting temperature of 25°C for the starter (neutral reference temperature zone).

Based on the present experimental investigations, the following conclusions can be drawn:

- ✓ by using nano-additives in the lubrication oil, an improvement of the physicochemical properties was observed, especially because of the decreasing of the viscosity and increasing of the viscosity index which lead to the formation of a better viscous film capable to reduce the frictions between the lubricated components;
- ✓ due to the reduced frictions, the fuel consumption was reduced by 21% at zero load;
- ✓ all the measured temperatures were reduced for the same exploitations of the engine.

Further investigations will be focused on loading the engine using a test bench, and the stabilization of the working temperature of the engine.

References

[1] Holmberg K Andersson P and Erdemir A 2012 *Tribol. Int.* **47** 221
[2] ***. Lubricant Additives - A Practical Guide. Available from: https://www.machinerylubrication.com/Read/31107/oil-lubricant-additives.
[3] Jatti VS and Singh TP *J. Mater. Sci. Technol.* 2015 29(2) 793
[4] Chu HY Hsu WC and Lin JF 2010 *Wear* **268(7)** 960
[5] Raina A. and Anand A *Appl. Nanosci.* 2017 **7(7)** 371
[6] Su Y, Tang Z, Wang G and Wan R 2018 *Adv. Mech. Eng.* **10(5)** 1.
[7] Martorana P, Bayer IS, Steele A and Loth E 2010 *Ind. Eng. Chem. Res.* **49(22)** 11363
[8] Liu H., Bai M and Qu Y 2012 *In: SAE-China, FISITA (eds) Proc. of the FISITA 2012 World Automotive Congress. Lecture Notes in Electrical Engineering*, Springer, Berlin, Heidelberg **190** 1313
[9] *** http://www.amt.cz/info/3/DT1236L.pdf
[10] Souza de Carvalho M.J, Seidl P, Pereira Belchior CR and Sodre JR 2010 *Tribol. Int.* **43** 2298
[11] Ali MKA Xianjun H, Mai L, Bicheng C, Turkson RF and Qingping C *Wear* 2016 **364-365** 270

EFFECTS OF BIOETHANOL ULTRASONIC GENERATED AEROSOLS APPLICATION ON DIESEL ENGINE PERFORMANCES

by

Florin MARIASIU* *, *Nicolae V. BURNETE, Dan MOLDOVANU, Bogdan O. VARGA, Calin ICLODEAN, and Levente KOCSIS

Department of Automotive Engineering and Transports, Technical University of Cluj-Napoca, Cluj-Napoca, Romania

Original scientific paper
DOI: 10.2298/TSCI140703108M

In this paper the effects of an experimental bioethanol fumigation application using an experimental ultrasound device on performance and emissions of a single cylinder Diesel engine have been experimentally investigated. Engine performance and pollutant emissions variations were considered for three different types of fuels (biodiesel, biodiesel-bioethanol blend and biodiesel-fumigated bioethanol). Reductions in brake specific fuel consumption and NO_x pollutant emissions are correlated with the use of ultrasonic fumigation of bioethanol fuel, comparative to use of biodiesel-bioethanol blend.

Considering the fuel consumption as Diesel engine's main performance parameter, the proposed bioethanol's fumigation method, offers the possibility to use more efficient renewable biofuels (bioethanol), with immediate effects on environmental protection.

Key words: *biodiesel, bioethanol, pollutant emissions, ultrasound, Diesel engines*

Introduction

The extensive use of Diesel engines as a power source for transportation, agriculture, industry, and construction owes much to their well-defined advantages, when compared to other internal combustion engines. Diesel engines have a better thermal efficiency, torque, and fuel economy [1-2].

According to [3], the global CO_2 equivalent of greenhouse gas emissions *budget* is less than 750 Gt before reaching the 2 °C global warming limit. In order to achieve the desired limits of pollution alternative energy sources must be considered. Because the transport industry is a major contributor to global warming a lot of effort is put into developing environmental-friendly vehicles. As a means to impact the whole vehicle park, research and development projects must also include fuels. This paper focuses on the superior use of bioethanol as renewable energy source for Diesel engines running in dual-fuel mode, using a novel fumigation technique.

Kujawski and Zielinski [4], Dincer [5], and Nag [6] shown that the renewable characteristics of biofuels can partly replace fossil fuels, and may help reduce green-house gas emissions (CO_2, N_2O and NO_x), promote a sustainable rural development and improve income distri-

* Corresponding author; e-mail: florin.mariasiu@auto.utcluj.ro.

bution. Biofuels ability to reduce greenhouse pollutant emissions is due to the presence of oxygen in their molecular composition. The oxygen content contributes to better air-fuel mixture combustion, leading to reduced emissions [7, 8].

However, a better fuel burning process leads to an increase in NO_x pollutant emissions. The NO_x emission formation mechanism strongly depends on the combustion temperature and the oxygen concentration. As a direct consequence, the formation rate will decrease if the in-cylinder combustion peak temperature is reduced [9-12]. The complexity and high number of factors influencing the combustion process, Johnson [13] show that NO_x emissions are more difficult to control than other pollutants. The peak temperature in the cylinder can be reduced with multiple injection strategies, the use of exhaust gas re-circulation technique and/or using ethanol or an ethanol-water emulsion as an additive to the fuel [14, 15].

Bioethanol is a renewable energy source made of plant materials. First generation bioethanol is produced by distillation from crops such as corn, wheat, sugar cane and sugar beet. Improved technologies have made it possible to produce non-food competitive second-generation bioethanol (cellulosic ethanol) from a wider range of feedstocks including agricultural residues, energy crops or woody raw material [16].

Bioethanol (ethanol) combustion in Diesel engines represents a challenge due to its significantly different properties compared to diesel fuel: poorer ignition properties (low cetane number), higher heat of vaporization, higher oxygen content, lower stoichiometric A/F ratio, lower heating value, and higher H/C ratio. However, with altered fuel characteristics and adequate engine adaptations or a modified combustion process, it is possible to take advantage of its more efficient compression ignited, compared to spark ignited, combustion [17]. Nowadays, there many solutions for using (bio)ethanol in Diesel engines like: direct injection of alcohol-diesel fuel blends, fumigation, glow-plug assisted ignition or addition of ignition improvers, each of them with its own constraints and challenges to overcome [17-19]. The main problems are: ethanol-diesel fuel miscibility, combustion control and the amount of engine modifications required [20]. More and more researchers are focusing their studies on dual fuel technologies for Diesel engines. In the following, some of the most recent researches in this field are presented briefly.

Hansdah and Murugan [21] studied the effects of fumigating ethanol obtained from *maduca indica* flower and was determined that the ignition delay increases for all of the studied flow rates by about 2-4 °CA at full load. Compared to normal diesel fuel operation, NO_x and smoke emissions were lower while CO and HC emissions slightly increased. The study also revealed an increased brake thermal efficiency.

Imran *et al*. [22] published a review of the literature concerning ethanol use in Diesel engines. The study concluded that break specific fuel consumption (BSFC) increases when using alcohol fumigation, which can be attributed to the lower calorific value of ethanol. The thermal efficiency with ethanol fumigation in Diesel engines is lower than that of diesel at low loads but at medium and high loads it surpasses it. The results regarding NO_x emissions compared to neat diesel varied between cited authors, but a common conclusion was that NO_x formation strongly depends on the combustion temperature and the oxygen concentration present in the combustion process. All cited authors reported an increase in HC and CO emission believed to be a cause of the lower combustion temperature. On the other hand, CO_2, smoke, and PM emissions significantly reduced.

Fraioli *et al*. [20] focused on the distribution and temporal evolution of chemical intermediates like OH, HCO, and CO in the combustion chamber and is influence on the combustion process. Was determined that ethanol fumigation causes wider auto ignition areas, a slower rate

of heat release and an increased combustion duration with respect to a direct injection n-heptane reference case.

The tests performed by Gargiulo *et al.* [23] lead to the conclusion that ethanol fumigation is very effective for reducing the number of emitted particles and that the chemical-physical characteristics of soot vary with the amount of injected ethanol.

Sarjovaara *et al.* [24] tested the influence of charge air temperature on combustion for an engine running with E85 fuel fumigation and direct diesel fuel injection at 1500 min^{-1} for two different loads. A major conclusion was that the maximum acceptable rate of E85 fuel decreased with charge air temperature. In comparison to normal diesel fuel operation, ignition delay increased, except for higher loads, and air temperatures, where E85 fuel auto-ignition occurred. The NO_x emissions decreased at low loads but increased at higher loads. The total hidro-carbon (THC) and CO emissions where slightly higher for all operating regimes, in contrast to smoke number which was lower in all cases.

Goldsworthy [25] tested the use of aqueous ethanol fumigation in a heavy-duty marine Diesel engine with two-stage injection operating at constant speed, for two different loads. It was observed that with ethanol addition, the injection is retarded by the electronic control unit (ECU) and that early combustion rates increase, which translates into a slightly improved thermal efficiency. The CO emissions increased during these tests except for low loads and moderate ethanol rates up to 10% energy content. The NO_x emissions performed as expected and decreased with the addition of ethanol. It was noted also that for an ethanol content in energy higher than 30%, knock phenomenon occurs.

Testing ethanol-water mixtures fumigation in a single cylinder engine, Morsy [26] noted that NO_x emissions and exhaust temperature decreased with the addition of ethanol-water mixtures except for pure ethanol. The CO and HC increased for all of the performed tests. Due to the lower energy content of ethanol, the BSFC increased but was noted a small improvement of thermal and exergy efficiency.

Bodisco and Brown [27] investigated inter-cycle variability of in cylinder pressure parameters in an ethanol fumigated common rail Diesel engine. Their study showed that substitutions by energy content up to 30% at full load and 20% at half load have only a minimal effect on the pressure parameters and the inter-cycle variability. At full load, higher ethanol substitutions lead to a decrease of the ignition delay and an increase in the inter-cycle variability.

Based on previous experiments it can be concluded that the general tendency when using ethanol fumigation in Diesel engines is that NO_x and PM emissions decrease while HC and CO pollutants emission increase [14, 28-31]. Few of the presented studies highlighted and some even minimized the importance of the major disadvantages of ethanol use in CI engines:

– the necessity of a separate fueling system and the associated control and command devices (with associated economic costs),
– the corrosive effect of ethanol,
– for values above 15% ethanol in blend, ethanol-biodiesel (diesel) blends are unstable,
– the use of anhydrous ethanol with high purity (99.2-99.6%) requires supplementary technological operations (and also a higher energy consumption), and
– the low cetane number and lubricity (lubricating characteristics) of ethanol.

To eliminate those shortcomings, the present paper proposes a new approach regarding the ethanol fumigation process. Based on previous experiments [32] that studied the effect of external energy (ultrasonic and microwave irradiation) on IC engines performance fueled with biofuel blends, a new evaporation process was proposed involving a device that performs an almost instant evaporation of bioethanol using ultrasounds. The application of ultrasound en-

ergy to the vegetable oil and in biofuel causes cavitation (under specific conditions). This is because the expansion and contraction of the transfer media create the conditions necessary for generating local droplets of very high temperature and pressure (instantaneous vaporization due to the cavitation process). Depending on the specific conditions of the ultrasonic process, the so formed droplets can be converted into a fine mist, using a current of air.

Figure 1. AVL 5402 engine test bed
1 – AVL 5402 research engine, 2 – DynoRoad 202 dyno, 3 – ECU AVL RPEMS ETK7 engine management system, 4 – FTIR equipment for pollutants analyse, 5 – AVL visioscope system, 6 – AVL 577 engine oil and coolant conditioning unit

Material and methods

To study the effect of ultrasonic fumigation of bioethanol on the performance of a DI Diesel engine and the resulting pollutant emissions characteristics, an experimental AVL 5402 optical DI Diesel engine test bed was used (fig. 1). The 5402 AVL engine is an experimental, four-stroke, common rail DI mono-cylinder engine, which has the main characteristics presented in tab. 1. The IC engine testing cell consists of an engine dynamometer, which is coupled to a research engine and related equipment. The DynoRoad 202 dynamometer is an asynchronous (AC) machine equipped with a converter power module insulated gate bipolar transistor (IGBT) for direct connection to the voltage power source. The power module uses a hybrid interface that facilitates control over engine torque and speed.

Table 1. Technical characteristics of the AVL 5402 engine

Parameter	Value	U.M.
Type	4-stroke, vertical single cylinder	–
Bore × Stroke	85 × 90	mm
Displacement	510.7	cm^3
Combustion type	DI single injector	–
Continuous rating output	6 (at 4200 min^{-1})	kW
Fuel injection pressure	1800	bar
Compression ratio	17.5 : 1	–
High pressure system	Common Rail CP4.1 Bosch	–
Engine management system	AVL-RPEMS + ETK7 Bosch	–
Cylinder pressure	50	MPa
Inlet valve open	8	° bTDC
Inlet valve close	226	° aTDC
Exhaust valve open	128	° aTDC
Exhaust valve close	18	° aTDC

The electronic control equipment consists of an AVL RPEMS management system comprising the electronic control unit ETAS ETK 7.1 and a CAN interface data bus. Engine load is controlled using the AVL throttle actuator control and the drive of the actuator. Lubricating oil and engine coolant conditioning is performed by the AVL577 conditioning unit, which controls the flow, temperature and pressure of both fluids set in the Puma Open operating system (control panel).

The AVL 735 measures the hourly fuel consumption and allows the conditioning of the fuel temperature.

Pollutant formation processes and emission intensity inside the combustion chamber were optical recorded and analyzed using AVL visioscope and AVL fourier transform infrared (FTIR) equipment. The AVL visioscope system provides optical access in the combustion chamber, which allows the investigation of the injection and combustion processes. The system incorporates the latest image recording technology in the field of internal combustion engines, and gives the possibility of optical investigation and recording of the phenomenon inside the engine cylinder (for *e. g*. flames temperature inside the combustion chamber and pollutants formation process).

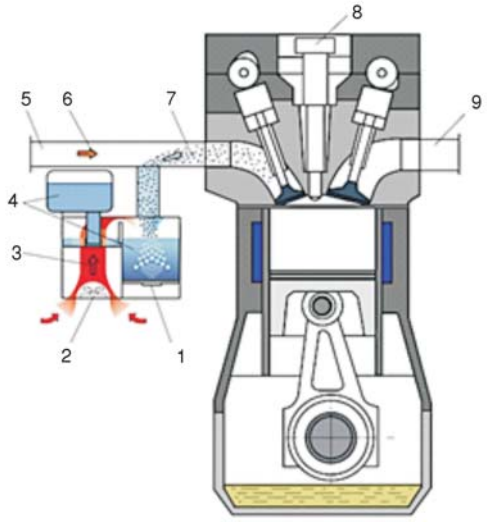

Figure 2. Schematic principle of ultrasonic fumigation process:
1 – ultrasonic emitter, 2 – fan, 3 – air, 4 – bioethanol, 5 – intake pipe, 6 – intake pipe air stream, 7 – fumigated bioethanol, 8 – fuel injector, and 9 – exhaust pipe

The experimental ultrasound based instantaneous fumigation system was manufactured by modifying a low-power ultrasonic electronically controlled air humidifier AOS 7146 type (Plaston AG, Swiss), 25 W power, 35 Hz frequencies, 24/220V AC. A plastic pipe (Polytetrafluoroethylene high density, 10 mm long, 30 mm in diameter) connected the exhaust orifice of the ultrasonic device with the engine's air intake manifold. The connection pipe was positioned at 30 mm ahead of the engine's inlet manifold. This positioning offered the advantage that the fumigated fluid was uniformly mixed with the intake air and reduced the possibility of condensation in the air intake pipe. The fumigated bioethanol mass flow was measured (and controlled) using a system consisting of an electronic weighing scale (Kingship GEW 6 type) coupled with an electronic timer. Using the engine test bed electronic control panel interface, the power of the ultrasonic emitter (fumigation intensity) was correlated with the open position of throttle valve (fig. 2).

The experiment focused on achieving the same quantity of fuel inside of combustion chamber taking into account the particularities of the used fuels and the different fueling methods. The mass flow of fumigated bioethanol was correlated with engine's loads regimes using the control and operating panel. The engine management system (ETAS ETK 7.1 with open ECU) allows modifications of the injection maps and therefor, the injection of a reduced quantity of fuel for the biodiesel injection + fumigated bioethanol (B5FE) experimental case. Detailed methodology is described in previous works of authors [33] and specific engine's management maps are presented in fig. 3.

In accordance with mandatory EU directives, a mixture of minimum 5% by volume of diesel mineral fuel and biodiesel (methyl ester) is sold at gas stations. So, what users usually call as *diesel fuel* is actually a blend of 95% diesel fuel and 5% methyl ester (biodiesel). The experimental works considered three types of fuels: B5 (diesel fuel + 5% rapeseed methyl ether biodiesel), B5E15 (95% BD fuel + 15% bioethanol blend), and B5FE (BD fuel + fumigated bioethanol). Physicochemical properties of the fuels used in the experiment are presented in tab. 2, and the bioethanol fuel is grain based and produced by a double distillation process.

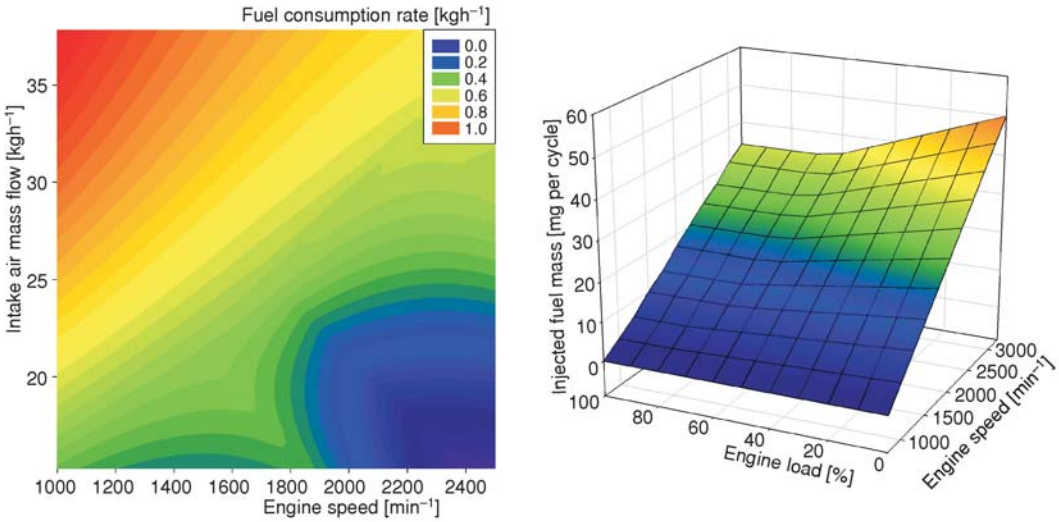

Figure 3. AVL 5402 engine's management maps for B5 case

Table 2. Physico-chemical characteristics of the tested fuels

Parameter	UM	Fuel		
		Bioethanol	B5	B5E15
Lower heating value	MJ/kg	28.60	42.38	40.27
A/F ratio	–	9.00	14.47	13.64
Density (at 20 °C)	kg/m^3	789.00	842.52	834.83
Carbon	%	52.14	86.03	80.88
Hidrogen	%	13.13	13.43	13.37
Oxigen	%	34.73	0.54	5.75
Molar mass	g/mol	46.07	213.23	188.80
Viscosity	mm^2/s	1.04	2.81	2.56

As the engine's manufacturer recommends, the measurements were taken after the engine warm-up period, when the engine enters the steady--state operating mode. The engine was run at the constant speed of 1800 min^{-1} while the dynamometer was used to load the engine. Engine loads at 20, 40, 60, and 80% correspond to 0.12, 0.22, 0.34, respectively, 0.42 MPa of brake mean effective pressure. The experimental tests were performed ten times for each considered fuel at each considered engine loads, and the results of those repetitions were averaged to reduce the level of uncertainty.

Results and discussion

To compare the performances of the three different fuel types in the Diesel engine, the BSFC was considered as the main comparison parameter. As seen in fig. 4 the measured values of BSFC decreased with increasing engine load for all tested fuels. That trend was expected since there are differences of heating value of biodiesel (B5), biodiesel-bioethanol blend (B5E15), and B5FE fuels. The average differences of BSFC parameter for B5E15 blend and B5FE fuel is with +13.4% and +5.0%, respectively, higher than in B5 case. This is due to the more specific homogeneity of A/F mixture (for ultrasonic fumigated bioethanol), and also because the amount of the bioethanol inside of combustion chamber play an important role in the combustion phas-

ing and combustion rate. It is generally considered that a rapid rate of heat is released (due to the increase of the ignition delay), with immediate effects on reducing the heat loss from the engine to the cylinder (and further, to the engine coolant) [21, 26]. A small quantity of the bioethanol will be consumed in the premixed combustion phase (during the early part of the biodiesel combustion process) and further, the remnant bioethanol is burned later in the combustion process as it continuous mixes with the formed hot products (in the expansion stroke) with direct influence on rate of heat release quantity during an engine cycle [25].

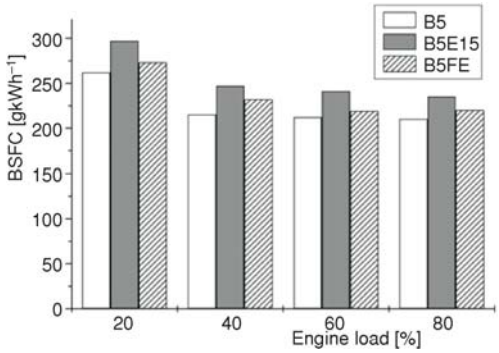

Figure 4. The BSFC *vs.* engine loads

The pollutant emissions considered in the experimental tests were NO_x, CO, and THC. The results are presented in figs. 5 to 9.

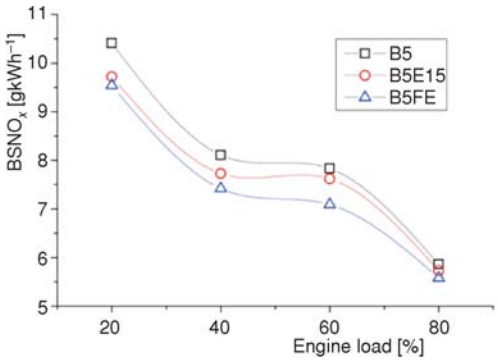

Figure 5. NO_x emissions *vs.* engine loads

The chemical reactions between nitrogen and oxygen that cause the formation of NO_x are possible only at high temperatures. The effect of the fumigated bioethanol on reducing the peak temperature in the ignition and combustion process is responsible for lower NO_x emission production (fig. 5). This effect is possible due to the intense latent heat of evaporation for bioethanol (in-cylinder temperature at the end of compression stroke drop substantially). A maximum (and major) reduction of 9.45% was achieved for 60% engine load, and the average reduction (for all considered loads) was –8.01%, respectively, –4.37% for B5E15 fuel comparative to B5 fuel. The temperature reduction inside of combustion chamber (and consequently as direct effect on NO_x formation process) using ultrasonic bioethanol fumigation technique is presented in fig. 6 using captured optical images from combustion chamber.

The effect of combined processes is responsible for higher CO emissions using fumigated bioethanol. The combustion parameters (the ignition delay, the latent heat of vaporization process and combustion duration) lead to lower engine cycle temperatures, with the effect of an inhibited oxidation process of CO to CO_2. The cooling effect of bioethanol vaporization inside the combustion chamber can also be responsible for increased CO production.

The increase of engine loads increases also the CO emissions level (fig. 7), data confirmed by experimental investigations done by other researchers [14, 29, 31, 32, 34]. Comparatively, the average emission of CO pollutant for the fumigation process (B5FE case) is with +4.34% higher than that in the case of the blended fuel B5E15, and also with +22.3% higher than in the case of the B5 fuel. The lowest values of CO emission for tested fuels were obtained for 40% engine load case, and the higher values of CO emissions for higher engine loads confirm the effect of engine load on CO pollutant production.

In case of THC emission the major reasons for production in case of bioethanol use are the slow rate of vaporization and the possibilities of biodiesel-bioethanol mixture positioning in

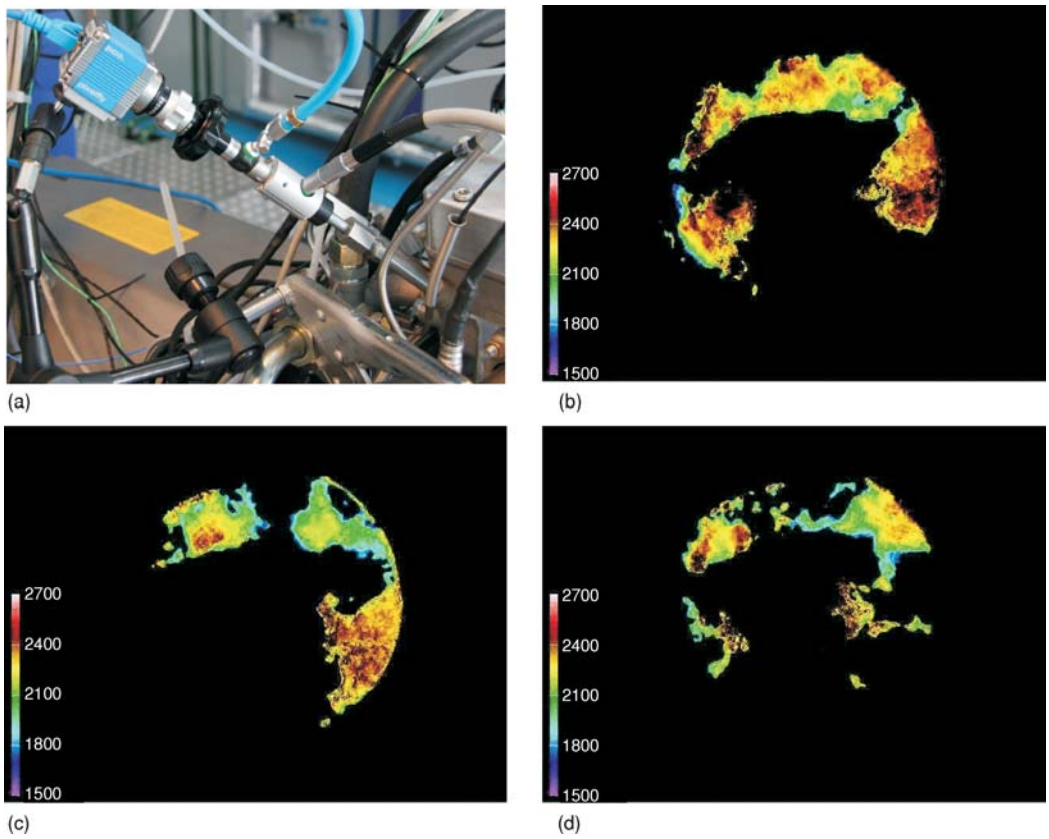

Figure 6. Thermal images of combustion process for considered fuels at 8 °CA aTDC; (a) Visioscope equipment, (b) B5 case, (c) B5E15 case, (d) B5FE case

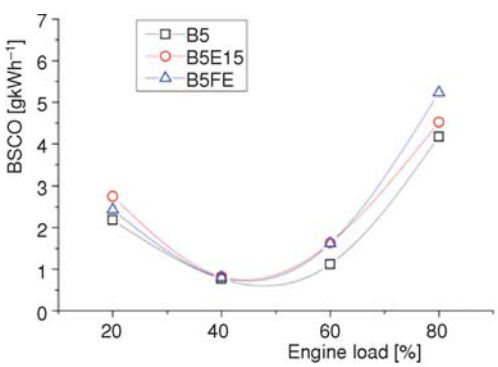

Figure 7. The CO emissions *vs.* engine loads

available spaces between the piston, liner and piston top ring during the intake and compression strokes. At can be see in fig. 8, some bioethanol mixture or liquid droplets were trapped inside the crevice during the intake and compression strokes prior to diesel injection and react with pumped lubricating oil inside of combustion chamber. Further, the burn of this mixture (bioethanol and lubricating oil) increase THC emissions.

Beside those factors, the lowered combustion temperature caused by the bioethanol vaporization also leads to incomplete combustion of fuel (especially near the walls of the combustion chamber) and thereby also can causes increased THC emissions (fig. 8). Due to their poor ignition properties, these mixtures are partially oxidized during combustion process, and the unburned products are discharged from the cylinder leading to a

high THC level. It is also possible that, during the valve overlap duration, a small amount of unburned bioethanol may directly escape into exhaust gases, where start a diffusive combustion process and increase of THC emission measured at the exhaust tail pipe end.

Still, the THC emissions production decrease with the increasing of engine loads for all considered fuels, due to a rapid vaporization rate of bioethanol caused by higher thermal load of cylinder. Comparative, the average experimental results shown that THC pollutants are with 12.3% (for B5FE) and 14.2% (for B5E15) higher that in the case of using B5 fuel (fig. 9). For small loads the THC emissions present major differences between fuels but with increasing of engine loads the values have relative same values (for 60 to 80% engine load regimes).

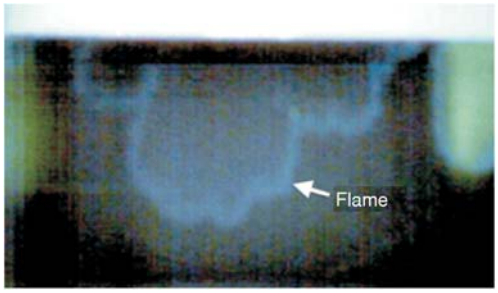

Figure 8. The bioethanol-lubricating oil mixture burning process in spaces between piston, liner, and piston top ring

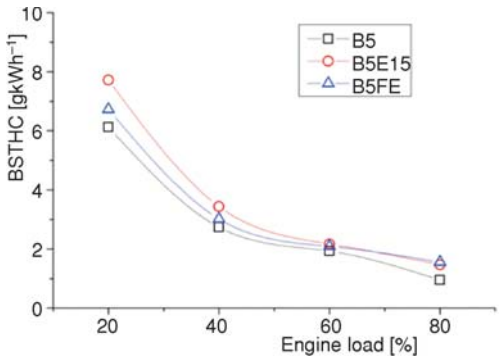

Figure 9. The THC emissions *vs.* engine loads

Conclusions

This paper presents an experimental study of the effects of bioethanol fumigation (as form of aerosols) on the performance (BSFC) and pollutant emissions of a DI single cylinder Diesel engine. The proposed fumigation method is based on the possibilities to intake into engine cylinder a quantity of bioethanol in form of ultrasonic generated aerosols.

Based on the results from the experiments, the following major conclusions and observations can be drawn.

- A simple and easy to use device was developed to realize the fueling fumigation process in form of aerosols, for a dual-fuel DI Diesel engine.
- The use of bioethanol as aerosols form in Diesel engine fueling process offers a major reduction of NO_x (when compared to biodiesel and biodiesel-bioethanol blend fuels). Water from the bioethanol enters the combustion chamber and lowers the combustion process peak temperature, causing a decrease of NO_x emissions. Strong correlation with the results from the literature was achieved, in conditions of a using this novelty fumigation fueling technique.
- The use of modern investigation apparatus offer the possibility to highlight the effects of mixture positioning in available spaces between the piston, liner and piston top ring on THC pollutant's formation and production.
- When compared to the B5E15 blend, the proposed fumigation procedure using ultrasound-generated aerosols (B5FE) leads to reduced BSFC (–7.45%), a decrease in NO_x (–3.8%) and THC (–1.63%) pollutant emissions while the level of CO (+11.1%) emissions increase.

- Further experiments are necessary to determine the effects of bioethanol ultrasonic generated fumigation technique on particulate emissions.

Acknowledgment

This work was supported by the strategic grant POSDRU/159/1.5/S/137070 of the Ministry of National Education, Romania, co-financed by the European Social Fund – Investing in People, within the Sectorial Operational Program Human Resources Development 2007-2013 and "UTCN Competitie interna 2014-2015 Program" grant.

References

[1] Desantes, J., *et al*., Influence on the Fuel Characteristics on the Injection Process in a D. I. Diesel Engine, SAE paper 980802, 1998
[2] Lakshminarayanan, P. A., Aghav, Y. V., *Modelling Diesel Combustion* (Mechanical Engineering Series), Springer, Berlin, Germany and The Netherlands, 2010
[3] ***, IPCC – Intergovernmental Panel on Climate Change, Summary for Policymakers: Climate Change 2013: The Physical Science Basis, Contribution of the Working Group I to the Fifth Assessment Report of the Intergovernmental Panel on Climate Change. Cambridge, Cambridge University Press, New York, USA, 2013
[4] Kujawski, W., Zielinski, L., Bioethanol – One of the Renewable Energy Sources, *Environmental Protection Engineering, 32* (2006), 1, pp. 143-150
[5] Dincer, K., Lower Emissions from Biodiesel Combustion, Energy Sources, Part A: Recovery, *Utilization, and Environmental Effects, 30* (2008), 10, pp. 963-968.
[6] Nag, A., *Biosystems Engineering*, McGraw-Hill, New York, USA, 2010
[7] Moldovanu, D., Burnete, N., Computational Fluid Dynamics Simulation of a Single Cylinder Research Engine Working with Biodiesel, *Thermal Science, 17* (2013), 1, pp. 195-203
[8] Tomic, M., *et al.*, Effects of Fossil Diesel and Biodiesel Blends on the Performances and Emissions of Agricultural Tractor Engines, *Thermal Science, 17* (2013), 1, pp. 263-278
[9] Heywood, J. B., *Internal Combustion Engines Fundamentals*, McGraw-Hill International Editions, Singapore, 1988
[10] Lu, X., *et al*., Simultaneous Reduction of NO_x Emission and Smoke Opacity of Biodiesel-Fueled Engines by Port Injection of Ethanol, *Fuel, 87* (2008), 7, pp. 1289-1296
[11] Maiboom, A., Tauzia, X., NO_x and PM Emissions Reduction on an Automotive HSDI Diesel Engine with Water-In-Diesel Emulsion and EGR: An Experimental Study, *Fuel, 90* (2011), 11, pp. 3179-3192
[12] Szybist, J. P., *et al.*, Evaluation of Formulation Strategies to Eliminate the Biodiesel NO_x Effect, *Fuel Processing Technology, 86* (2005), 10, pp. 1109-1126
[13] Johnson, T. V., Diesel Emission Control Technology 2003 in Review, SAE Technical Paper 2004-01-0070, 2004
[14] Abu-Qudais, M., *et al*., The Effect of Alcohol Fumigation on Diesel Engine Performance and Emissions, *Energy Conversion and Management, 41* (2000), 4, pp. 389-399
[15] Di, Y., *et al.*, Comparison of the Effect of Biodiesel-Diesel and Ethanol-Diesel on the Particulate Emissions of a Direct Injection Diesel Engine, *Aerosol Science and Technology, 43* (2009), 5, pp. 455-465
[16] ***, European Biofuels Technology Platform, Bioethanol use in Europe and Globally, 2015, Web: accessed 9 May 2015, www.biofuelstp.eu.
[17] Ma, J., *et al*., An Experimental Study of HCCI-DI Combustion and Emissions in a Diesel Engine with Dual Fuel, *International Journal of Thermal Science, 47* (2008), 9, pp. 1235-1242
[18] Papagiannakis, R. G., *et al*., Emission Characteristics of High Speed, Dual Fuel, Compression Ignition Engine Operating in a wide Range of Natural Gas/Diesel Fuel Proportions, *Fuel, 89* (2010), 7, pp. 1397-1406
[19] Kousoulido, M., *et al.*, Effect of Biodiesel and Bioethanol on Exhaust Emissions, European Topic Centre on Air and Climate Change, Technical Paper, Feb, 2008.
Web: http://acm.eionet.europa.eu/docs/ETCACC_TP_2008_5_biofuels_emissions.pdf
[20] Fraioli, V., *et al*., Ethanol Effect as Premixed Fuel in Dual-Fuel CI Engines: Experimental and Numerical Investigations, *Applied Energy, 119* (2014), Apr., pp. 394-404
[21] Hansdah, D., Murugan, S., Bioethanol Fumigation in a DI Diesel Engine, *Fuel, 130* (2014), Aug., pp. 324-333

[22] Imran, A., *et al*., Review on Alcohol Fumigation on Diesel Engine: A Viable Alternative Dual Fuel Technology for Satisfactory Engine Performance and Reduction of Environment Concerning Emission, *Renewable and Sustainable Energy Reviews, 26* (2013), Oct., pp. 739-751
[23] Gargiulo, V., *et al*., Chemico-Physical Features of Soot Emitted from a Dual-Fuel Ethanol-Diesel System, *Fuel, 150* (2015), June, pp. 154-161
[24] Sarjovaara, T., *et al*., Effect of Charge Air Temperature on E85 Dual-Fuel Diesel Combustion, *Fuel, 153* (2015), Aug., pp. 6-12
[25] Goldsworthy, L., Fumigation of a Heavy Duty Common Rail Marine Diesel Engine with Ethanol-Water Mixtures, *Experimental Thermal and Fluid Science, 47* (2013), May, pp. 48-59
[26] Morsy, M. H., Assessment of a Direct Injection Diesel Engine Fumigated with Ethanol/Water Mixtures, *Energy Conversion and Management, 94* (2015), Apr., pp. 406-414
[27] Bodisco, T., Brown, R. J., Inter-Cycle Variability of In-Cylinder Pressure Parameters in an Ethanol Fumigated Common Rail Diesel Engine, *Energy, 52* (2013), Apr., pp. 55-65
[28] Yao, C., *et al*., Experimental Study on the Effect of Gaseous and Particulate Emission from an Ethanol Fumigated Diesel Engine, *Science China Technological Science, 53* (2010), 12, pp. 3294-3301
[29] Chauhan, B. S., *et al*., Experimental Studies on Fumigation of Ethanol in a Small Capacity Diesel Engine, *Energy, 36* (2011), 2, pp. 1030-1038
[30] Zhang, Z. H., *et al*., Effect of Fumigation Methanol and Ethanol on the Gaseous and Particulate Emissions of a Direct-Injection Diesel Engine, *Atmospheric Environment, 45* (2011), 11, pp. 2001-2008
[31] Surawski, N. C., *et al*., Gaseous and Particle Emissions from an Ethanol Fumigated Compression Ignition Engine, *Energy Conversion and Management, 54* (2012), 1, pp. 145-151
[32] Mariasiu, F., Experimental Results Regarding Biodiesel Fueled CI Engine Functional Performances (in Romanian), *Biodiesel Magazin, 5* (2008), pp. 30-34
[33] Iclodean. C. D., Mariasiu, F., Possibility to Increase Biofuels Energy Efficiency used for Compression Ignition Engines Fueling, *TEM Journal, 3* (2014), 1, pp. 36-41
[34] Alpetkin, E., *et al*., Using Waste Animal fat Biodiesel-Bioethanol-Diesel Fuel Blends in a DI Diesel Engine, *Fuel, 157* (2015), Oct., pp. 245-254

Paper submitted: July 3, 2014
Paper revised: June 25, 2015
Paper accepted: July 20, 2015